Mathematical Problems in Engineering

Computational Intelligence and Renewable Energies

Lead Guest Editor: Saeid Jafarzadeh Ghoushchi
Guest Editors: Araz Darba, Dimitar V. Bozalakov, and Ramin Ranjbarzadeh

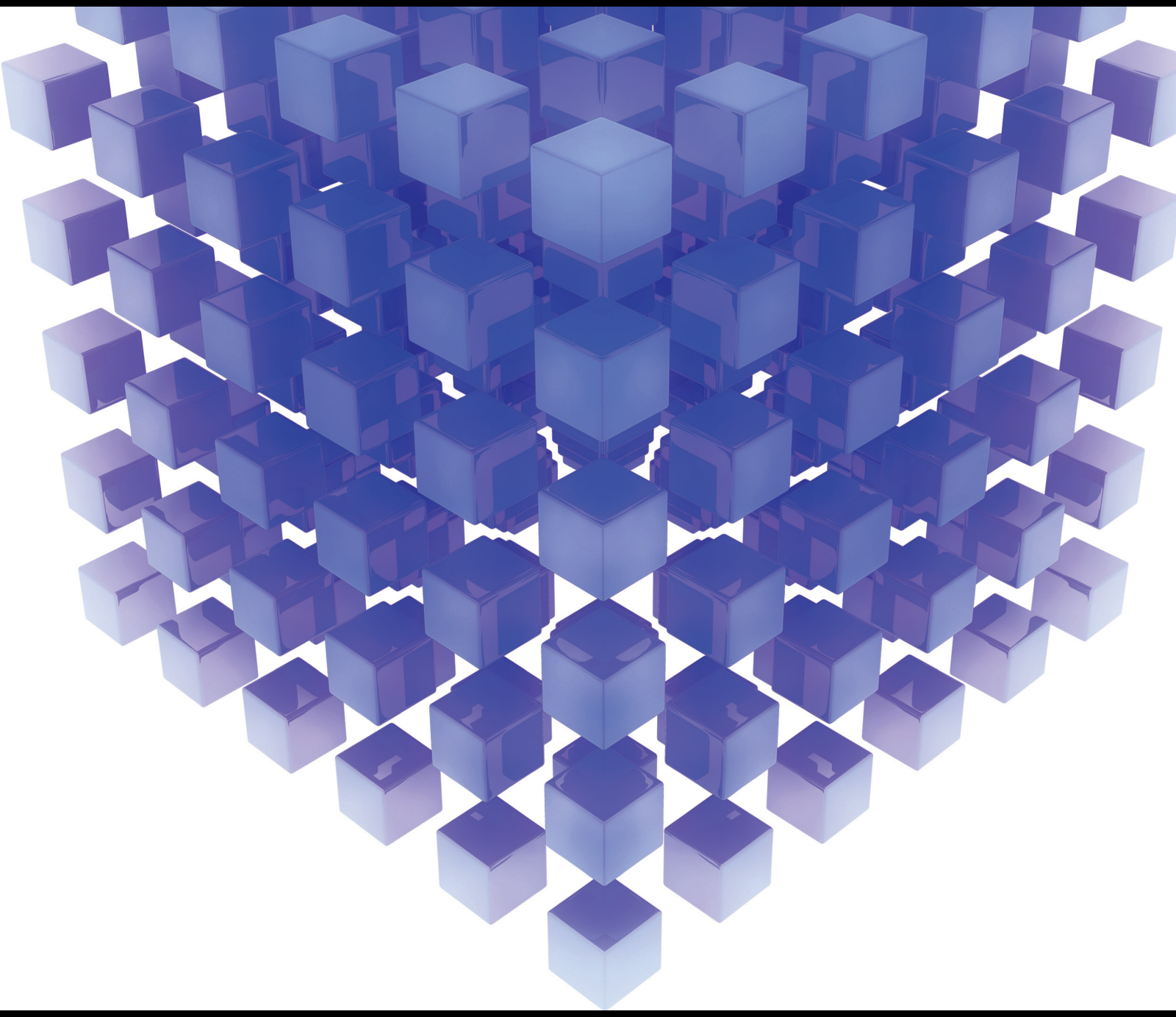

Computational Intelligence and Renewable Energies

Mathematical Problems in Engineering

Computational Intelligence and Renewable Energies

Lead Guest Editor: Saeid Jafarzadeh Ghoushchi
Guest Editors: Araz Darba, Dimitar V. Bozalakov, and Ramin Ranjbarzadeh

Contents

Hindawi
Mathematical Problems in Engineering
Volume 2022, Article ID 5726108, 11 pages
https://doi.org/10.1155/2022/5726108

Research Article

Carbon Market Evaluation Based on Random Walk Hypothesis in China

Tian Zhang[1] and Shaohui Zou[1,2]

[1]*School of Energy Xi'an University of Science and Technology, Xi'an 710054, China*
[2]*Energy Economy and Management Research Center, Xi'an University of Science and Technology, Xi'an, China*

Correspondence should be addressed to Shaohui Zou; ztzh91719@163.com

Received 30 January 2022; Revised 20 April 2022; Accepted 30 June 2022; Published 20 July 2022

Academic Editor: Araz Darba

According to the proposal of Kyoto protocol, carbon dioxide emission rights are traded as a commodity, and carbon emission trading market emerges as the times require. As the world's largest carbon emitter, China has established eight pilot markets for carbon emission trading. Selecting the closing price of eight carbon trading markets from the establishment to June 23, 2020, this paper analyzes the daily, weekly, and monthly return series data, using the first-order autoregressive process to adjust the daily income series to eliminate the weak trading market effect and then comprehensively uses the traditional variance ratio test and multiple variance ratio test to analyze the weak-form market efficiency of the eight carbon trading markets. The empirical results show that most of the carbon trading markets are non-weak-form market efficiency, and only Tianjin, Shanghai, and Hubei markets are weak-form market efficiency under the daily trading data. However, with the increase of carbon holding period, the weak-form market efficiency continues to strengthen. It shows that liquidity, quantity, and information transparency are important factors that affect the market efficiency.

1. Introduction

The climate change caused by the greenhouse gas effect not only affects the economic prosperity and development of all countries, but also threatens the ecological environment on which human beings rely for survival. Global warming has become a major problem that the international community urgently needs to cooperate to solve. After the Kyoto protocol was signed in 1997, carbon dioxide emission rights were regarded as a kind of trading goods; thus the carbon emission rights trading market appeared. Following the pace of energy conservation and emission reduction in the world, China actively undertakes more responsibility for emission reduction and has issued a number of policies to promote low-carbon economy. The domestic carbon trading market started late. Since 2013, China has successively established eight carbon trading markets in Beijing, Tianjin, Shanghai, Hubei, Guangdong, Shenzhen, Chongqing, and Fujian. By August 2020, the cumulative trading volume of carbon markets in China's pilot provinces and cities is more than 400 million tons, and the cumulative turnover is more than 9 billion yuan. It has effectively promoted the work of the pilot provinces and cities to cope with climate change and control greenhouse gas emissions [1].

2. Literature Review

In the capital market, "market efficiency" means that the relevant information inside and outside the market is completely reflected by the price, or various resources in the market are reasonably allocated and effectively utilized. The basic function of capital market is to distribute the ownership of capital in economic activities. The efficient market hypothesis holds that, in the stock market with sound laws, good functions, high transparency, and full competition, all valuable information has been timely, accurately, and fully reflected in the stock price trend, including the current and future value of enterprises, unless there is market

manipulation. Otherwise, it is impossible for investors to obtain excess profits higher than the average level of the market by analyzing the past prices.

In 1970, Fama put forward "efficient market hypothesis," which holds that if the price completely reflects all the available information in a market, it can be called an efficient market. According to the available information set, three types of efficient markets are defined: weak, semistrong, and strong [2]. In the weak-form efficient market, trading will not produce price fluctuations due to historical information, so investors can not obtain excess returns by virtue of historical information. In other words, the weak efficient market should conform to the "random walk" process. It will not achieve the expected purpose to analyze and predict the future market price trend by using the current or historical price, and the transaction price will not be easily influenced by speculation and other nonmarket factors.

Carbon emission trading market is a global emerging financial market. Foreign scholars have studied more the mechanism, rules, price factors, and risks of carbon market. Kruger and others called the EU carbon emission system "a great new policy experiment" and attached great importance to China's carbon emission trading market and regarded it as "the third big policy experiment" [3]. Chevalier uses OLS method and recursive CUSUM process to study the price volatility of EU carbon market based on the EU daily price [4]. Convery studied the mechanism and performance of the EU carbon market, at the same time, which gives other countries much significant advice for establishing carbon market [5]. Shaohui Zou and Tian Zhang applied both VAR-GARCH-DCC and VAR-GARCH-BEKK models to study the correlation and dynamic volatility spillover between green investing market, coal market, and CO_2 emissions [6].

In the past, the research field of market efficiency mainly focused on the stock market, securities market, and futures market. The main research methods of market efficiency were unit root process, random run test, sequence correlation test, capital asset pricing model, and variance ratio test [7–13]. Montagnoli uses the method of variance ratio test to test the market efficiency of holding period of 2, 5 and 10 days in the first and second stages. The research results confirm the conclusion of them. It shows that the second stage of EU carbon trading market is weak efficient market [14]. Based on the cost of holding hypothesis, Charles et al. studied the factors that affect the efficiency of the EU market and found that, even in the case of structural change, the futures price, spot price, and interest rate are cointegrated, and the lack of cost of holding is the main reason for market inefficiency [15]. In addition, based on the practical research of international carbon emission market, more and more scholars put forward targeted suggestions for the problems and obstacles in the process of promoting market development in China. The research suggests that China's carbon market should promote the development of relevant financial business from the aspects of improving the regulatory system, trading platform, and professional organization team [16–19].

On the basis of the existing research, this paper makes the following three contributions: (1) select the daily data, weekly data, and monthly data of eight pilot markets to conduct a full sample study; (2) the weak-form efficiency of carbon trading market defined as the idea that the carbon price fully reflects all the information related to carbon emissions; (3) comprehensive use of traditional variance ratio test and multiple variance ratio test for detailed empirical research.

3. Variance Ratio Tests

3.1. Lo-MacKinlay (1988) Test. The test method of variance ratio is proposed by Lo and MacKinlay (1988). Lo and MacKinlay variance ratio test is also known as the traditional variance ratio test, which allows the series to obey non-normal distribution and heteroscedasticity [20]. If the daily return series of carbon trading price obeys martingale process, the variance of daily return series increases linearly with time: the variance of period K is k times that of period 1. If the daily return series of carbon trading price obeys martingale process, the variance of daily return series increases linearly with time: the variance of period K is k times that of period 1. The series obeys independent and identical distribution (independent identical distribution) which is the premise of the series obeying martingale process.

The null assumption is that the daily return series have martingale process, that is, $VR\ (k) = 1$. If $VR\ (k) > 1$; it means that the carbon trading price fluctuates greatly; if $VR\ (k) < 1$, it indicates that the carbon trading price tends to be stable. $r_{1i,t}$ is the daily return series of carbon price in carbon trading market i at time t; $r_{2i,t}$ is the weekly return series of carbon price in carbon trading market i at time t; $r_{3i,t}$ is the monthly return series of carbon price in carbon trading market i at time t. i represents Beijing, Shenzhen, Shanghai, Guangdong, Tianjin, Hubei, Chongqing, and Fujian carbon markets, respectively, $T \longrightarrow \infty$. The variance ratio statistic equation is as follows:

$$\mathrm{VR}(k) = \frac{\left\{(1/T_k)\sum_{t=k+1}^{T}\left(x_{i,t} + x_{i,t-1} + \cdots + x_{i,t-k} - k\mu\right)^2\right\}}{\left\{(1/T)\sum_{t=1}^{T}\left(x_{i,t-1} - \mu\right)^2\right\}}, \tag{1}$$

where x is the adjusted return series; $\mu = (1/T)\sum_{t=1}^{T} x_{i,t}$; and k is the order of lags. The traditional variance ratio test results are divided into the same variance test and the different variance test. The same variance test formula is as follows:

$$M_1 = (\mathrm{VR}(k) - 1)\left(\frac{2(2k-j)(k-1)}{3kT}\right)^{-(1/2)}. \tag{2}$$

M_1 is asymptotically normal independent identically distributed. The premise of heteroscedasticity test is that there is heteroscedasticity in series, and the test statistic M_2 is expressed as

$$M_2 = (\mathrm{VR}(k) - 1)\left(\sum_{j=1}^{k-1}\left[\frac{2(k-j)}{k}\right]^2 \delta_j\right)^{-(1/2)}, \tag{3}$$

where j is the holding period.

$$\delta_j = \frac{\left\{\sum_{t=j+1}^{T}\left(x_{i,t}-\mu\right)^2\left(x_{i,t-1}-\mu\right)^2\right\}}{\left\{\left[\sum_{t=1}^{T}\left(x_{i,t}-\mu\right)^2\right]^2\right\}}. \quad (4)$$

The heteroscedasticity test also obeys the asymptotic normal distribution. If the statistic exceeds the critical value, the zero hypothesis that the return sequence obeys martingale process is rejected; that is, the market is a weak-form market efficiency; otherwise, the zero hypothesis is accepted. However, the traditional variance ratio test has the following three problems. First, the sample size is distorted due to the asymptotic normal distribution. The second is whether the original hypothesis is valid for all K. The third is the arbitrary selectivity of K value.

3.2. Nonparametric Test. Wright proposed the rank sum sign nonparametric test method of regression series, which solved the problem of sample size distortion [21]. When the sample size is small, the sample size has its own distribution, so it is necessary to test the nonnormality and instability. The results show that the method has better test effect. The null hypothesis: The return series follows martingale process. The rank test equation is as follows:

$$R_1 = \left[\frac{(1/T_K)\sum_{t=k+1}^{T}\left(r_{1i,t}+r_{1i,t-1}+\cdots r_{1i,t-k}\right)^2}{(1/T)\sum_{t=1}^{T} r_{1i,t}^2} - 1\right] \times\left(\frac{2(2k-1)(k-1)}{3kT}\right)^{-(1/2)}, \quad (5)$$

$$R_2 = \left[\frac{(1/T)\sum_{t=k+1}^{T}\left(r_{2i,t}+r_{2i,t-1}+\cdots r_{2i,t-k}\right)^2}{(1/T)\sum_{t=1}^{T} r_{2i,t}^2} - 1\right] \times\left(\frac{2(2k-1)(k-1)}{3kT}\right)^{-(1/2)}. \quad (6)$$

In this paper, r is used to express the rank of return series as follows:

$$r_{1i,t} = \frac{r_{i,t} - T + 1/2}{\sqrt{(T-1)(T+1)/12}}, \quad (7)$$

$$r_{2i,t} = \Phi^{-1}\frac{r_{i,t}}{T+1}. \quad (8)$$

Using rank test instead of M_1 test value in traditional variance ratio, the test result is not limited by sample size and heteroscedasticity, which is more convincing than traditional variance ratio test result. Wright's research shows that, even in the presence of heteroscedasticity, sign test has relative accuracy. The test equation is as follows:

Table 1: Sample description.

Markets	Total obs.	Daily	Weekly	Monthly	Time range
Beijing	1361	980	301	80	2013/11/29–2020/06/23
Shenzhen	1959	1525	350	84	2013/06/18–2020/06/23
Shanghai	1274	927	273	74	2013/11/26–2020/06/23
Guangdong	1676	1286	313	77	2013/12/19–2020/06/23
Tianjin	791	575	165	51	2013/12/16–2020/06/23
Hubei	1827	1445	308	74	2014/04/28–2020/06/23
Chongqing	713	500	160	53	2014/06/19–2020/06/23
Fujian	637	478	125	34	2017/01/09–2020/06/23

$$s_1 = \left[\frac{(1/T_K)\sum_{t=k+1}^{T}\left(s_{i,t}+s_{i,t-1}+\cdots+s_{i,t-k}\right)^2}{(1/T)\sum_{t=1}^{T} s_{i,t}^2} - 1\right] \times\left(\frac{2(2k-1)(k-1)}{3kT}\right)^{-(1/2)}, \quad (9)$$

where $S_t = 2\mu(x_t, 0) = 2H(x_t) - 1$, $H(x_t) = \begin{cases} 1, & \text{if } x_t > 0, \\ 0, & \text{if others.} \end{cases}$. S_t is independent identically distributed. If the statistic exceeds the critical value, the null hypothesis is rejected; otherwise, the null hypothesis is accepted.

3.3. Belaire-Franch and Contreras Test. Lo-MacKinlay variance ratio test and Wright variance ratio test are both single variance ratio tests. Compared with single variance ratio test, multiple variance ratio test has better effect. The specific reasons are as follows: When single variance ratio test is used, different difference sequences (i.e., different K) are selected to test whether the price series is a random walk process. If one or several difference series fail the statistical test, it can be considered that the sequence is not a random walk. Using single variance ratio test requires every difference series to pass statistical test, which will lead to overtest. In order to overcome this problem, Chow and Denning (1993) [22] proposed the idea of multiple variance ratio test. The statistics are as follows:

$$\mathrm{MV}(k_i) = \sqrt{t}\,\max\left|M(k_i)\right|, \quad (10)$$

where $M(k_i)$ is the Lo-MacKinlay test statistic.

Because the variance ratio statistics involved in the multiple variance ratio test proposed by Chow and Denning are based on the Lo-MacKinlay statistics, it has defects (the Lo-MacKinlay test statistics only conform to the asymptotic normality). Belaire and Contreras (2004) proposed an extended multiple variance ratio test [23]. Compared with Chow Denning's idea of multiple variance ratio test, the

Table 2: Summary statistics for carbon returns.

Markets		Obs.	Mean	Max	Min	Std. Dev.	Skewness	Kurtosis	Jb	Prob.
Daily	Beijing	979	0.000581	0.208055	−0.28305	0.07052	−0.66715	6.39830	543.707	≤0.001
	Shenzhen	1524	0.000090	2.29131	−2.25700	0.26145	0.166762	32.6348	55774.4	≤0.001
	Shanghai	926	0.000421	0.928461	−0.83873	0.07566	0.707451	45.3227	69188.2	≤0.001
	Guangdong	1285	−0.000614	0.116748	−0.23985	0.04857	−0.31575	3.47739	33.5559	≤0.001
	Tianjin	574	−0.00019	0.728239	−0.69314	0.06675	−0.07345	50.6190	54233.3	≤0.001
	Hubei	1444	0.000012	0.095602	−0.16664	0.02913	−0.18032	6.70875	835.408	≤0.001
	Chongqing	499	−0.000319	0.296493	−0.34465	0.13772	−0.22478	1.83857	32.2483	≤0.001
	Fujian	477	−0.002984	0.09575	−0.12557	0.06677	−0.15165	1.91883	25.0608	0.00004
Weekly	Beijing	300	0.001895	0.580654	−0.60244	0.12046	−0.68315	10.5841	742.331	≤0.001
	Shenzhen	349	0.000395	1.975343	−2.18505	0.32217	0.266869	21.2358	4839.90	≤0.001
	Shanghai	272	0.001299	0.928461	−0.83873	0.13321	0.288869	17.9285	2529.53	≤0.001
	Guangdong	312	−0.00252	0.333588	−0.37533	0.10025	−0.45340	5.70132	105.552	≤0.001
	Tianjin	164	−0.000757	0.728239	−0.69314	0.12149	0.194269	16.7178	1286.92	≤0.001
	Hubei	307	6.48E-05	0.335658	-0.46585	0.06751	−0.90303	18.2558	3018.87	≤0.001
	Chongqing	159	−0.001003	0.908177	−0.91821	0.32830	−0.23368	3.43784	2.71715	0.25702
	Fujian	124	−0.011705	0.477209	−0.52697	0.17200	−0.28249	4.42132	12.0867	0.00237
Monthly	Beijing	79	0.007198	0.381411	−0.42166	0.12282	−0.14361	5.43681	19.8177	0.00005
	Shenzhen	83	0.001661	0.675129	−0.63141	0.24671	0.098871	3.52679	1.09496	0.57840
	Shanghai	73	0.004841	0.928461	−0.48954	0.22110	0.947128	6.62387	50.8586	≤0.001
	Guangdong	76	−0.010347	0.615746	−0.50945	0.17946	−0.01568	5.29328	16.6570	0.00024
	Tianjin	50	−0.000059	0.728239	−1.19001	0.25581	−1.67923	11.7680	183.661	≤0.001
	Hubei	73	0.000273	0.525929	−0.29318	0.11319	1.376033	9.52035	152.353	≤0.001
	Chongqing	52	−0.003066	1.302343	−1.43408	0.60350	−0.00233	2.91958	0.01405	0.99299
	Fujian	33	−0.043104	0.975409	−0.96369	0.35809	0.153695	4.37134	2.71571	0.257212

main difference lies in the choice of basic statistics: Wright's rank sum signed statistics replace Lo-MacKinlay statistics.

The statistics of Belaire-Franch and Contreras are as follows:

$$\begin{aligned} \mathrm{CD}(R_1) &= \max_{1\le i\le m}\left|R_1(k_i)\right|, \\ \mathrm{CD}(R_2) &= \max_{1\le i\le m}\left|R_2(k_i)\right|, \\ \mathrm{CD}(S_1) &= \max_{1\le i\le m}\left|S_1(k_i)\right|. \end{aligned} \tag{11}$$

The above analysis shows that Belaire-Franch and Contreras statistics have better effect than Lo-MacKinlay statistics and Wright statistics. Furthermore, Wright statistics are more effective than Lo-MacKinlay statistics. But in order to better compare the three variance ratio test ideas, the results of these three test methods in the empirical part is listed.

4. Data Sources and Summary Statistics

4.1. Data. This paper studied the daily, weekly, and monthly data of carbon market price in detail. The sample information is summarized in Table 1. All the time series data in this paper can be found on China carbon emissions trading All the data can be:found on Official website of 8 pilot carbon markets: http://www.cerx.cn/; https://www.bjets.com.cn/article/jyxx/; https://www.cneeex.com/; http://www.cnemission.com/; https://www.chinatcx.com.cn/list/43.html; http://www.hbets.cn/; https://tpf.cqggzy.com/; https://www.hxee.com.cn/. it's also free. The data involves 7716 daily, 1995 weekly, and 527 monthly observations. In this paper, the returns of the series are calculated as

$$x_t = 100 \times \ln\left(\frac{P_t}{P_{t-1}}\right). \tag{12}$$

In the formula above, P_t denotes carbon price at time t and log is the natural logarithm.

4.2. Summary Statistics. The descriptive statistics of income series from Beijing, Shanghai, Guangdong, Hubei, Shenzhen, Chongqing, and Fujian carbon exchanges to June 23, 2020, are shown in Table 2. The mean value of the eight carbon trading market return series is around 0, which means that the carbon price is fixed for a period of time and the market is not active. From the fluctuation range of daily income series, that is, the difference between the maximum and the minimum, the minimum difference is 0.22132, and the maximum difference is 4.548318, indicating that the long-term volatility of carbon price is large. In terms of standard deviation, the standard deviation of monthly return series is larger than that of daily return series and weekly return series. The standard deviation of monthly return rate of Chongqing carbon trading market is 0.603508, which is larger than that of Guangdong, Beijing, Hubei, Tianjin, Fujian, Shenzhen, and Shanghai carbon trading markets, indicating that the price volatility of Chongqing carbon trading market is greater than that of other seven cities.

The carbon trading markets in Beijing, Guangdong, Hubei, Tianjin, Chongqing, and Fujian all show negative skewness and high kurtosis, among which the negative skewness indicates that the carbon trading market returns have a thick tail on the left. The skewness of Shenzhen and Shanghai carbon trading markets is 0.166762 and 0.707451,

Table 3: VR test daily returns.

Market		$k=2$	$k=5$	$k=10$	$k=30$
Beijing	L-M	0.461103***	0.234983***	0.118685***	0.057705***
	z-Statistic	−8.543156	−6.946726	−5.572058	−4.389915
Tianjin	L-M	0.39803**	0.183431**	0.089899*	0.062416
	z-Statistic	−2.485202	−2.15884	−1.861805	−1.487925
Shanghai	L-M	0.493802***	0.239946***	0.110478***	0.057196***
	z-Statistic	−3.010141	−2.922434	−2.837119	−2.684569
Shenzhen	L-M	0.33162***	0.14837***	0.089614***	0.045523**
	z-Statistic	−5.855641	−4.370003	−3.257013	−2.492294
Guangdong	L-M	0.495881***	0.24509***	0.121924***	0.062874***
	z-Statistic	−13.14374	−10.95438	−8.489376	−6.375676
Hubei	L-M	0.438173***	0.216592***	0.120986***	0.058237***
	z-Statistic	−11.23657	−9.326487	−7.594706	−6.188488
Chongqing	L-M	0.628142***	0.354641***	0.192052***	0.103572***
	z-Statistic	−7.126948	−6.645722	−5.402258	−4.128351
Fujian	L-M	0.562276***	0.314032***	0.170541***	0.088683***
	z-Statistic	−7.537041	−6.63919	−5.265964	−4.05519

respectively, which indicates that the right side of the normal distribution is thick tailed. For monthly data, the skewness of return series in Beijing, Guangdong, Chongqing, and Tianjin markets is left to the normal distribution, while the other four markets are opposite. The return series of 8 carbon trading markets show the characteristics of peak and thick tail, and they have the characteristics of abnormal distribution. It further shows that the market can not fully reflect the market information, which leads to information accumulation.

5. Empirical Results

5.1. Empirical Test of Lo-MacKinlay

5.1.1. The Daily Data Results. The test results of traditional variance ratio (Lo-MacKinlay) of daily return series of 8 carbon trading markets are shown in Table 3. According to the treatment method of weak trading market by Ibikunle et al. [24], this paper adjusts the daily return series of eight carbon trading markets. If the statistics of two or more holding periods are larger than the critical value, the null hypothesis of martingale process is rejected, that is, non-weak-form market.

The results show that Beijing, Shanghai, Shenzhen, Guangdong, Hubei, Chongqing, and Fujian markets all refuse the null hypothesis during the holding period. Therefore, Beijing, Shanghai, Shenzhen, Guangdong, Hubei, Chongqing, and Fujian carbon markets are non-weak-form market. The null hypothesis is accepted only when the holding period is 30 days in Tianjin carbon market; also, the statistics of the other three holding periods are higher than the critical value to varying degrees, and the null hypothesis of martingale process is rejected. In the daily return series of Tianjin carbon market, the statistics of three holding periods are greater than the critical value, which indicates that Tianjin carbon market has not reached the weak-form market efficiency. However, when the holding period is 30 days, the statistics are not significant, which indicates that the weak-form efficiency trend of the market is gradually increasing.

To sum up, the statistics of carbon markets in Beijing, Shanghai, Shenzhen, Guangdong, Hubei, Chongqing, and Fujian are greater than the critical value in varying degrees and do not reach the weak-form market efficiency level; Tianjin carbon trading market is a non-weak-form market efficiency, but the trend of weak-form market efficiency is increasing.

5.1.2. The Weekly Data Results. This paper used variance ratio test to do empirical research on weekly return series. The frequency of weekly data is lower than that of daily frequency data. The test results of traditional variance ratio (Lo-MacKinlay) of weekly return series of 8 carbon trading markets are shown in Table 4.

It can be seen from Table 4 that each holding period of weekly return series of Beijing and Guangdong carbon trading markets rejects the original hypothesis at the significance level of 1%, indicating that Beijing and Guangdong carbon trading markets are non-weak-form market efficiency. At the significance level of 10%, the weekly return series of Shanghai, Hubei, Chongqing, and Fujian carbon markets reject the original hypothesis, indicating that these four markets are non-weak-form market efficiency. The test results show that the weekly return series data of Tianjin and Shenzhen carbon trading markets only accept the null hypothesis when the holding period is 30 days, and other holding periods reject the null hypothesis.

5.1.3. The Monthly Data Results. From Table 5, some important implications were obtained. For pilots in Beijing, Tianjin, Shanghai, Shenzhen, Guangdong, and Hubei, we can reject the zero hypothesis of random walk, which illustrates these pilots are non-weak-form market efficiency,

Table 4: VR test weekly returns.

Market		$k=2$	$k=4$	$k=8$	$k=16$
Beijing	L-M	0.654493***	0.373247***	0.179679***	0.222856***
	z-Statistic	−3.568279	−3.168659	−3.232521	−2.132748
Tianjin	L-M	0.508498**	0.199109**	0.102121*	0.040291
	z-Statistic	−2.115261	−2.035371	−1.905071	−1.505145
Shanghai	L-M	0.410908***	0.168162*	0.084994**	0.037706*
	z-Statistic	−2.855362	−2.393971	−2.209673	−1.75355
Shenzhen	L-M	0.397243***	0.118289**	0.064635*	0.027196
	z-Statistic	−3.037446	−2.443292	−1.886342	−1.276251
Guangdong	L-M	0.51726***	0.243247***	0.132656***	0.05559***
	z-Statistic	−4.920838	−4.574642	−3.663555	−2.844785
Hubei	L-M	0.545944***	0.174654***	0.094933**	0.033483*
	z-Statistic	−3.192883	−2.873131	−2.466674	−1.957215
Chongqing	L-M	0.588219***	0.305006***	0.153959***	0.0544*
	z-Statistic	−3.8407	−3.266235	−2.675175	−1.729808
Fujian	L-M	0.663552***	0.342464***	0.15692***	0.075063**
	z-Statistic	−2.89223	−3.28576	−2.821544	−2.20439

Table 5: VR test monthly returns.

Market		$k=2$	$k=4$	$k=5$	$k=8$
Beijing	L-M	0.429718***	0.191804**	0.093079**	0.039567*
	z-Statistic	−3.26232	−2.352633	−1.843054	−1.285965
Tianjin	L-M	0.447671**	0.145181*	0.116835*	0.037386*
	z-Statistic	−1.68352	−1.555983	−1.320808	−1.133245
Shanghai	L-M	0.547518**	0.286775**	0.124463*	0.099739*
	z-Statistic	−2.572429	−2.211541	−1.852491	−1.383688
Shenzhen	L-M	0.526742***	0.271877***	0.175267**	0.086916 *
	z-Statistic	−3.4036	−2.931565	−2.135711	−1.655951
Guangdong	L-M	0.477374**	0.165066**	0.103202*	0.045582*
	z-Statistic	−2.54605	−2.046049	−1.580276	−1.113698
Hubei	L-M	0.381251**	0.264047**	0.126275**	0.082816*
	z-Statistic	−2.544513	−1.885446	−1.76267	−1.484773
Chongqing	L-M	0.579718**	0.233738**	0.129381*	0.060139
	z-Statistic	−2.283644	−2.017855	−1.568811	−1.023908
Fujian	L-M	0.318991**	0.190508	0.074262	0.429526
	z-Statistic	−2.296156	−1.489103	−1.249386	−0.559659

Table 6: Multiple variance ratio test daily returns.

Market		$k=2$	$k=5$	$k=10$	$k=30$
Beijing	MV*	0.855219***	0.765296**	0.5791**	0.327714***
	z-Statistic	−2.582753	−2.326537	−2.835249	−3.254458
Tianjin	MV*	0.823469	0.754047	0.688023	0.671746
	z-Statistic	−0.851179	−0.776355	−0.774332	−0.636679
Shanghai	MV*	0.891813	0.721833	0.617111	0.652238
	z-Statistic	−0.644325	−1.049579	−1.175289	−0.940869
Shenzhen	MV*	0.545556***	0.304225***	0.187486***	0.129181**
	z-Statistic	−4.946023	−4.195001	−3.219969	−2.415345
Guangdong	MV*	0.977622	0.939453	0.865519*	0.694647**
	z-Statistic	−0.580622	−0.854024	−1.2375	−1.962708
Hubei	MV*	0.896629	0.884268	0.865104	0.687674
	z-Statistic	−2.184306	−1.388532	−1.127249	−1.921894
Chongqing	MV*	1.338718***	1.774427***	2.16038***	2.312009***
	z-Statistic	6.591535	8.155265	7.88103	6.062376
Fujian	MV*	1.245093***	1.553289***	1.726864***	1.520605**
	z-Statistic	4.455762	5.410534	4.547625	2.227063

Table 7: Multiple variance ratio test weekly returns.

Market		$k=2$	$k=4$	$k=8$	$k=16$
Beijing	MV*	0.481274***	0.16136***	0.07543**	0.027335**
	z-Statistic	−4.547082	−3.59526	−2.975808	−2.011372
Tianjin	MV*	0.938769	0.769341	0.586697	0.484148
	z-Statistic	−0.258347	−0.566016	−0.845348	−0.799943
Shanghai	MV*	0.762357	0.648489	0.795515	1.014917
	z-Statistic	−1.182321	−1.075543	−0.493368	0.03044
Shenzhen	MV*	0.638717**	0.242447**	0.172405*	0.100163
	z-Statistic	−2.344503	−2.411365	−1.764301	−1.207583
Guangdong	MV*	0.912492	0.726244**	0.623283	0.477681
	z-Statistic	−1.059057	−1.801725	−1.632179	−1.558962
Hubei	MV*	0.874062	0.625463*	0.590202	0.692027
	z-Statistic	−1.18299	−1.654001	−1.281003	−0.778588
Chongqing	MV*	0.588219***	0.402421***	0.196758**	0.09251*
	z-Statistic	−3.8407	−3.223077	−2.878752	−2.238048
Fujian	MV*	0.663552***	0.342464***	0.15692***	0.075063**
	z-Statistic	−2.89223	−3.28576	−2.821544	−2.20439

while Chongqing and Fujian pilots are weak-form market efficiency.

Obviously, the empirical results of monthly returns are better than the results of daily data and weekly data. The results show that the carbon market price series of Chongqing and Fujian obey a random walk process. It can be seen that the monthly return series can overcome the disadvantage of thin daily return.

5.2. Multiple Variance Ratio Test

5.2.1. The Daily Data Results. The purpose of this test is to solve the problem of sample size distortion caused by the traditional variance ratio test, which is more credible than the traditional variance ratio test. In the multiple variance ratio test, the null hypothesis VR $(k) = 1$ holds for all k values, and the alternative hypothesis VR (km) $\neq 1$ holds for some holding periods, where $m = 1, \ldots, m$. Kim uses traditional variance ratio and Chow and Denning test as reference and introduces wild bootstrap into variance ratio test and sets the repetition times equal to 1000 [23, 24]. Because MV statistics have the characteristics of approximate sampling distribution, the problem of sample distortion caused by less sample size is solved. The multiple variance ratio test results of daily return series of 8 carbon trading markets are shown in Table 6.

The multiple variance ratio test method solves the problem of K arbitrary selection with the optimal lag time. The test results of multiple variance ratio are shown in Table 5. Beijing, Shenzhen, and Fujian carbon markets reject the null hypothesis at the significance level of 10%, indicating that Beijing, Shenzhen, and Fujian carbon trading markets are non-weak-form market efficiency. Tianjin, Shanghai, and Hubei carbon trading markets are weak-form market efficiency with insignificant holding periods at 1%, 5%, and 10%. The daily return series of Chongqing carbon trading market rejects the original hypothesis at the level of 1%, indicating that Chongqing carbon trading market is a non-weak-form market efficiency. The test results show that the original hypothesis is rejected only when the holding period is 10 days or 30 days, while the null hypothesis is accepted in other holding periods.

5.2.2. The Weekly Data Results. In this part, this paper used multiple variance ratio test to study the weekly returns of 8 carbon markets. The multiple variance ratio test results are shown in Table 7.

It can be seen from Table 7 that the carbon markets in Beijing, Chongqing, and Fujian reject the null hypothesis at the level of 10% significance. The research results show that the carbon markets in Beijing, Chongqing, and Fujian are non-weak-form market efficiency. Each holding period of weekly return series of Tianjin and Shanghai carbon trading markets is not significant at the level of 1%, 5%, and 10%, and they are weak-form market efficiency. The test results show that the weekly return series data of Shenzhen carbon trading market only accept the null hypothesis when the holding period is 30 days, and other holding periods reject the null hypothesis.

5.2.3. The Monthly Data Results. In our research, we also test the monthly returns using multiple variance ratio test. The empirical test results are shown in Table 8.

From Table 8, obviously, the null hypothesis of random walk in Tianjin and Shanghai, Shenzhen, Guangdong, Hubei, and Chongqing markets can be accepted, which illustrates these pilots are weak-form market efficiency; however, Beijing and Fujian markets are non-weak-form market efficiency.

5.3. Discussion

5.3.1. Carbon Price Volatility. Large price fluctuation and price instability are the prominent factors of the low efficiency of carbon market. Figure 1 shows the price fluctuation characteristics of eight carbon markets from the first trading

Table 8: Multiple variance ratio test monthly returns.

Market		$k=2$	$k=4$	$k=5$	$k=8$
Beijing	MV *	0.695192 * *	0.480591 *	0.343364	0.211074
	z-Statistic	−2.072848	−1.69775	−1.459785	−1.119355
Tianjin	MV *	0.739338	0.399241	0.415626	0.668487
	z-Statistic	−0.938343	−1.308469	−1.011917	−0.412345
Shanghai	MV *	1.093257	1.180996	1.190165	1.191703
	z-Statistic	0.465174	0.528045	0.380225	0.278525
Shenzhen	MV *	0.957645	0.880725	0.466108	0.464588
	z-Statistic	−0.357585	−0.469223	−1.371396	−0.804113
Guangdong	MV *	0.770781	0.683639	0.755878	1.100152
	z-Statistic	−1.519169	−0.87732	−0.459207	0.120964
Hubei	MV *	0.893936	1.075171	1.123346	1.315522
	z-Statistic	−0.555874	0.220587	0.27472	0.436051
Chongqing	MV *	1.059403	0.899872	0.691642	0.68386
	z-Statistic	0.349964	−0.28344	−0.584621	−0.351965
Fujian	MV *	0.450513 * *	0.256212	0.27613	0.127265
	z-Statistic	−1.985703	−1.608904	−1.102051	−1.021691

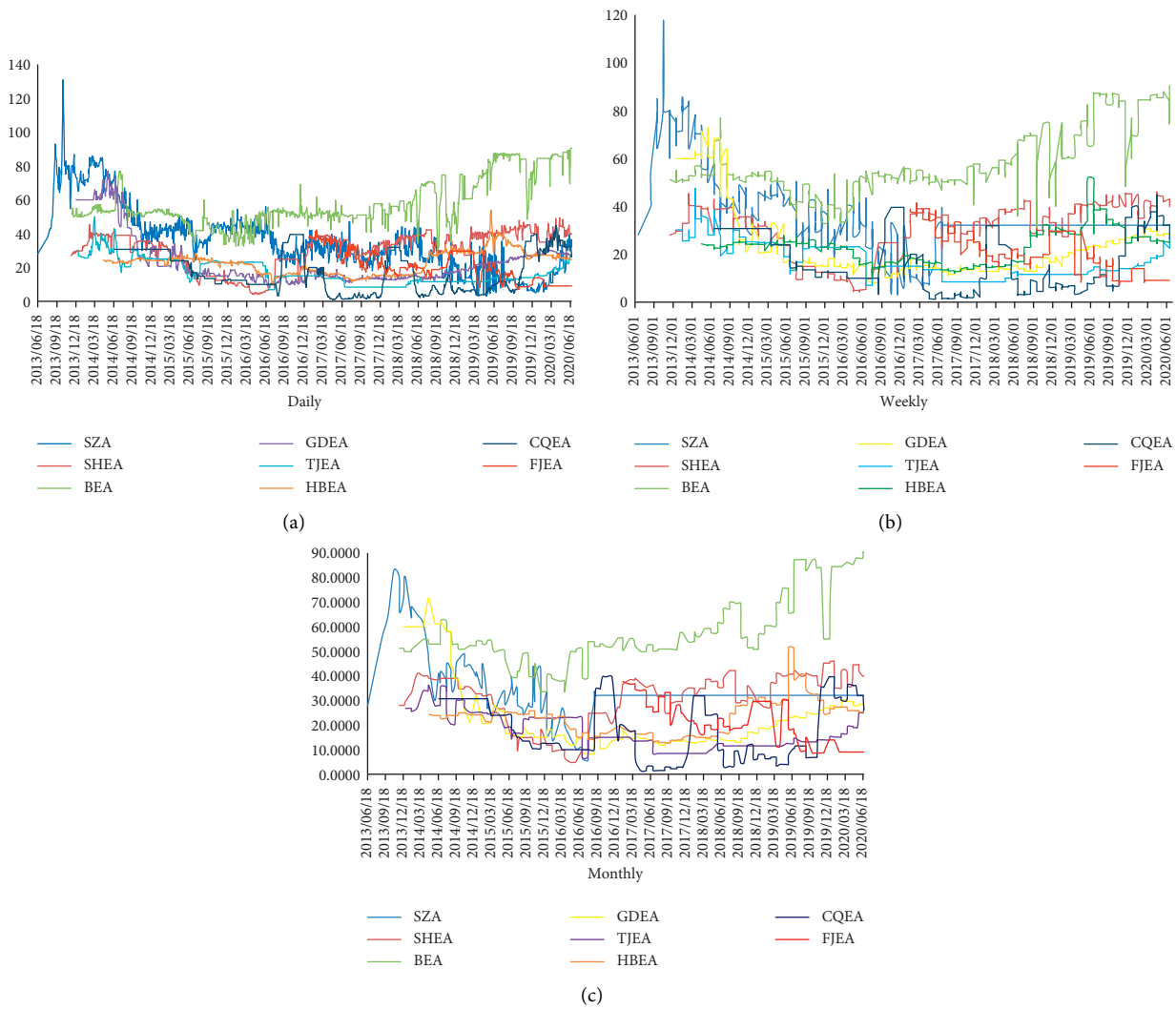

Figure 1: Price volatility of 8 pilots: (a) Daily. (b) Weekly. (c) Monthly.

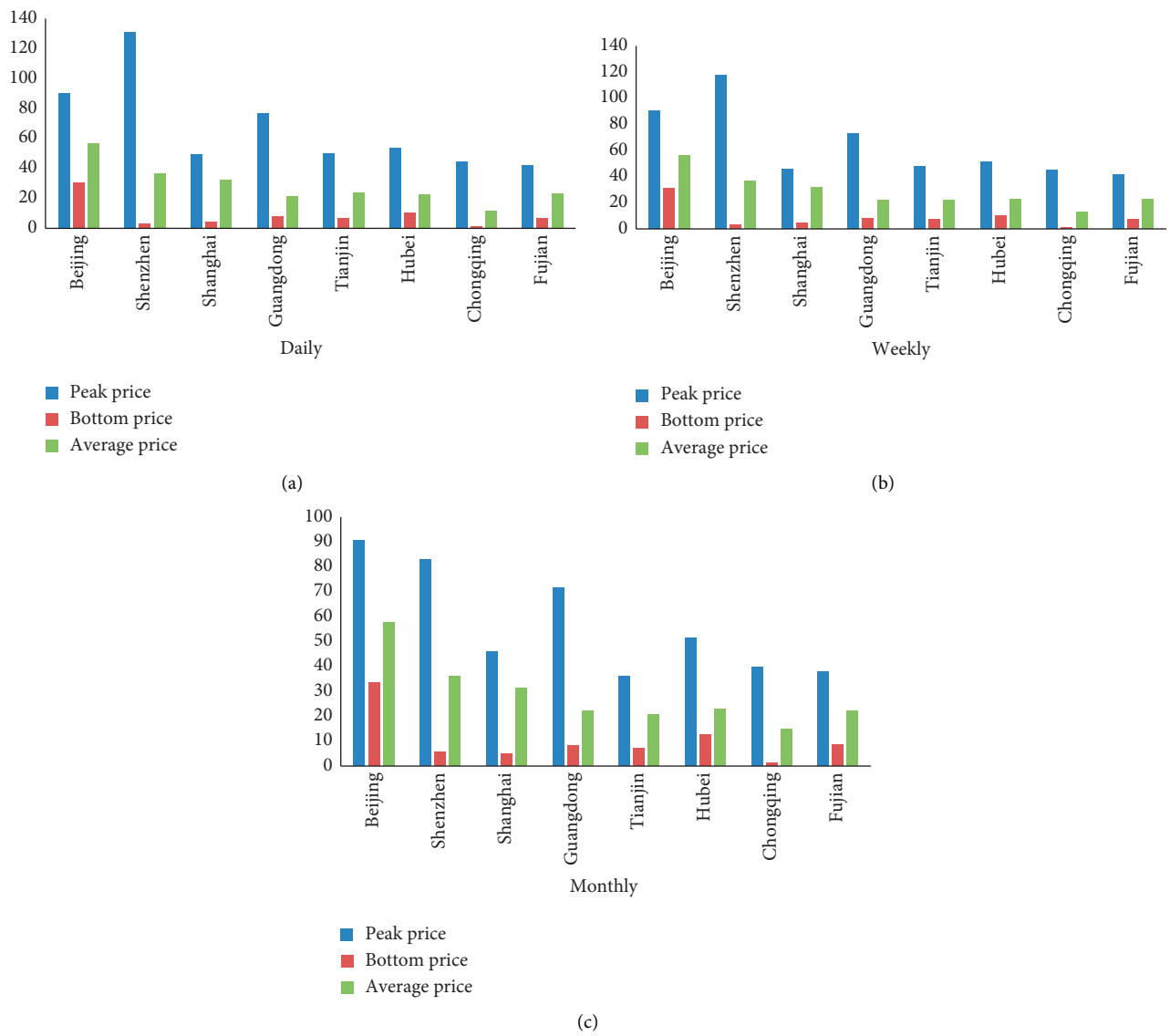

Figure 2: The average, peak, and bottom prices of the eight pilot ETS. (a) Daily. (b) Weekly. (c) Monthly.

day to June 23, 2020. The results show that the prices of China's eight carbon markets are very different.

As can be seen from Figure 1, the price of carbon market fluctuates sharply. By the middle of October 2013, the price in Shenzhen had reached a high level of 120 yuan/ton and then dropped sharply, with the price approaching 80 yuan/ton. In the year of 2017, the lowest price is approached to 20 yuan/ton. From 2013 to May 2016, the price of carbon market in Shanghai showed a downward trend, with a fluctuation range of 5–50 yuan/ton, showing an overall upward trend. From Figure 1, it can see that the prices of 8 pilots have similar fluctuation trend whenever it is daily data, weekly data, or monthly data.

5.3.2. Liquidity and Trading Volume. Liquidity is an important indicator to measure the development activity and maturity of the financial market. The stronger the liquidity is, the more attractive it is to all kinds of participating institutions, and the more perfect the price discovery function of the market is.

Transaction prices in an efficient financial market should contain fully available information, which has no empirically verifiable effect on predicting future prices or returns. In this research, this paper calculated the peak price, bottom price, and average price of 8 carbon markets.

Figure 2 shows the average price, peak price, and bottom price of China's eight carbon markets. In terms of the daily peak price, Shenzhen ranked the highest, at 130 yuan/ton, followed by Beijing and Guangdong where the prices were 87 yuan/ton and 78.91 yuan/ton, respectively. Regarding the bottom price, most of the prices are less than 10 yuan/ton. Beijing had the highest at 32 yuan/ton. Nationwide, the average price of carbon market is 25.68 yuan/ton. For the monthly data, Beijing had the highest at 90.5 yuan/ton; Tianjin, Chongqing, and Fujian's are lower, at 36.17 yuan/ton, 39.74 yuan/ton, and 37.74 yuan/ton, respectively.

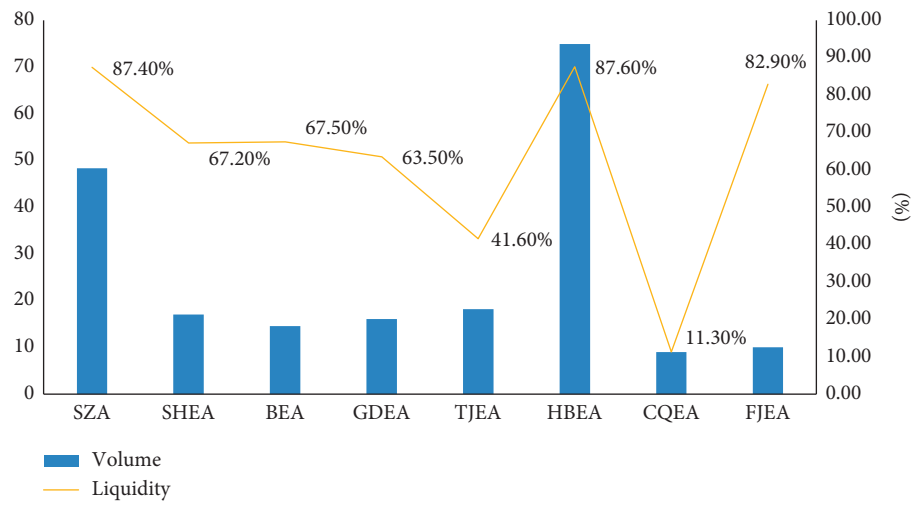

Figure 3: The liquidity and volume of the eight carbon markets.

At present, the pilot carbon markets of the eight provinces and cities are still in the early stage of market development, and the liquidity is generally weak. It can only make a preliminary analysis on the trading activity of the eight pilot carbon markets according to the ratio of the trading volume of the spot secondary market to the total amount of its quota. Lack of market liquidity is also the main problem in China's carbon market. Figure 3 shows the liquidity and trading volume of China's carbon market. The eight carbon markets are strikingly different. From our research, it can be concluded that these transactions have been carried out almost every day since Hubei ETS was launched. The trading frequency and activity of carbon market in Hubei Province are the highest among the eight carbon markets. The liquidity of Hubei market is as high as 87.6%, followed by Shenzhen and Fujian, indicating that Hubei and Shenzhen markets are active.

6. Conclusion

Weak-form market efficiency is a good performance of market operation. The basic judgment on the weak efficiency of carbon market is of great significance for building a national unified carbon market. In the empirical analysis, based on the data availability and effectiveness, the paper selects the closing price data of Beijing, Shanghai, Guangdong, and Hubei carbon trading markets from the establishment to June 23, 2020, to test the market weak-form efficiency test. Based on the sample period from June 18, 2013, to June 23, 2020, this paper tests the efficiency of all carbon markets in China (Beijing, Tianjin, Shanghai, Shenzhen, Guangdong, Hubei, Chongqing, and Fujian) and analyzes the factors influencing the efficiency.

The empirical results show that there are significant differences in carbon price levels among domestic carbon markets, and the development of domestic carbon market is unbalanced. The empirical results show that China's carbon market does not achieve weak-form efficiency. At the same time, Tianjin, Hubei, and Shanghai are rich in carbon resources, stable carbon prices, and strong market liquidity, forming a weak efficiency market. On the whole, the market is gradually implemented. In addition, liquidity, trading volume, carbon price, and allocation subsidies also affect market efficiency. The results show the following:

(1) There are many days when the carbon trading volume is zero, and the domestic carbon market is weak.

(2) The daily return series of carbon price follow non-normal distribution, with obvious characteristics of peak and thick tail. Carbon price can not truly reflect market supply and demand and is easier to be manipulated, resulting in higher market investment risk.

(3) The results of validity test are different with different carbon holding periods, and the weak-form efficiency of carbon trading market is phased. The price of carbon trading guides the behavior of the participants, and the weak efficiency of the market plays an important role in the healthy operation of the market. Compared with the research results of the first stage of non-weak efficiency of EU carbon trading market, China's carbon markets have achieved initial success by learning from the successful experience of foreign carbon trading markets and combining with the actual situation in China, which has laid the foundation for building a unified national carbon trading market [25-26].

Data Availability

The data used to support the findings of this study are available from the corresponding author upon request.

Conflicts of Interest

The authors declare that there are no conflicts of interest.

Authors' Contributions

All authors contributed equally to this work. All authors read and approved the final manuscript.

Acknowledgments

This research was supported by the National Social Science Foundation of China (NSSFC) under Grant no. 19GBL183.

References

[1] "Ministry of Ecology and Environment: The cumulative transaction volume of carbon emission trading pilot provinces and cities exceeds 400 million tons," 2020, https://baijiahao.baidu.com/s?id=1681787982070773140&wfr=spider&for=pc.

[2] E. Fama, "Efficient market hypothesis: a review of theory and empirical work," *Journal of Finance*, vol. 25, no. 2, 1970.

[3] J. Kruger, W. E. Oates, and W. A. Pizer, "Decentralization in the EU emissions trading scheme and lessons for global policy," *Review of Environmental Economics and Policy*, vol. 45, 2007.

[4] J. Chevallier, "Detecting instability in the volatility of carbon prices," *Energy Economics*, vol. 33, no. 1, pp. 99–110, 2011.

[5] F. Convery, D. Ellerman, and C. D. Perthuis, "The European carbon market in action: lessons from the first trading period interim report," *Working Papers*, vol. 5, no. 2, pp. 215–233, 2008.

[6] S. Zou and T. Zhang, "Correlation and dynamic volatility spillover between green investing market, coal market, and CO2 emissions: evidence from shenzhen carbon market in China," *Advances in Civil Engineering*, vol. 2022, Article ID 7523563, 13 pages, 2022.

[7] X. Dai, J. Yang, and Q. Zhang, "Weak form efficiency test of Chinese stock market: based on unit root method," *Systems Engineering*, vol. 78, no. 11, pp. 23–28, 2005.

[8] D. Xu and Z. Lv, "Statistical test on the efficiency of Shenzhen stock market," *The Journal of Quantitative & Technical Economics*, vol. 20, no. 006, pp. 158–160, 2003.

[9] X. Chen, "Research on the efficiency of dynamic beta coefficient of Chinese stock market," *Asia Pacific economy*, vol. 8, no. 4, 2014.

[10] M. Laurence, F. Cai, and S Cai, "Weak-form efficiency and causality tests in Chinese stock markets," *Multinational Finance Journal*, vol. 1, no. 4, pp. 291–307, 1997.

[11] X. Zhang and Z. Zhang, "Futures market efficiency theory and empirical test," *Chinese Journal of Management Science*, vol. 6, pp. 1–5, 2005.

[12] L. Jia and X. Wang, "An Empirical Study on the efficiency of China's stock market -- a test method based on variance ratio," *Economic Survey*, vol. 33, no. 1, pp. 137–140, 2010.

[13] C. Dong and weiqi Liu, "Research on stock return reversal effect and its relationship with bid ask spread," *Journal of Management Sciences in China*, vol. 21, no. 6, pp. 171–182, 2016.

[14] A. Montagnoli and F. P. D. Vries, "Carbon trading thickness and market efficiency," *Energy Economics*, vol. 32, no. 6, pp. 1331–1336, 2010.

[15] A. Charles, O. Darné, and J. Fouilloux, "Market efficiency in the European carbon markets," *Energy Policy*, vol. 60, no. sep, pp. 785–792, 2013.

[16] B. Guo and R. Zhou, "Analysis on price cycle and volatility characteristics of China's carbon trading market," *Statistics and decision*, vol. 12, no. 21, pp. 154–157, 2016.

[17] L. Zhao, C. fan, and H. Wang, "Time varying spillover effects of carbon market and energy market in China: an Empirical Study Based on Spillover index model," *Journal of Beijing Institute of Technology (Social Sciences Edition)*, vol. 23, no. 01, pp. 28–40, 2021.

[18] J. Liu, J. Liang, and C. Xia, "Research on Spillover Effects of China's carbon market, domestic coking coal market and EU carbon market," *Journal of Industrial Technological Economics*, vol. 39, no. 09, pp. 88–95, 2020.

[19] C. Sun, "Research on price volatility spillover effect of China's carbon market and EU carbon market," *Journal of Industrial Technological Economics*, vol. 37, no. 03, pp. 97–105, 2018.

[20] A. W. Lo and A. C. Mackinlay, "Stock market prices do not follow random walks: evidence from a simple specification test," *Review of Financial Studies*, no. 1, pp. 41–66, 1988.

[21] J. H. Wright, "Alternative variance-ratio tests using ranks and signs," *Journal of Business & Economic Statistics*, vol. 18, no. 1, p. 1, 2000.

[22] K. V. Chow and K. C. Denning, "A simple multiple variance ratio test," *Journal of Econometrics*, vol. 58, no. 3, pp. 385–401, 1993.

[23] J. Belaire-Franch and D. Contreras, "Ranks and signs-based multiple variance ratio tests," 2004.

[24] G. Ibikunle, A. Gregoriou, and N. R. Pandit, "Price discovery and trading after hours: new evidence from the world's largest carbon exchange," *International Journal of the Economics of Business*, vol. 20, no. 3, pp. 421–445, 2011.

[25] J. H. Kim, "Wild bootstrapping variance ratio tests," *Economics Letters*, vol. 92, no. 1, pp. 38–43, 2006.

[26] J. Zhou, X. Huo, B. Jin, and X. Yu, "The efficiency of carbon trading market in China: evidence from variance ratio tests," *Environmental Science and Pollution Research*, vol. 26, no. 14, Article ID 14372, 2019.

Hindawi
Mathematical Problems in Engineering
Volume 2022, Article ID 5680635, 10 pages
https://doi.org/10.1155/2022/5680635

Research Article

Machine Learning Based Prediction of Output PV Power in India and Malaysia with the Use of Statistical Regression

Ojaswa Yadav,[1] **Ramani Kannan**,[1] **Sheikh T. Meraj**,[1] **and Ammar Masaoud**[2]

[1]*Department of Electrical and Electronic Engineering, Universiti Teknologi PETRONAS, Seri Iskandar32610, Perak, Malaysia*
[2]*Faculty of Mechanical and Electrical Engineering, Al Baath University, Homs 22743, Syria*

Correspondence should be addressed to Ammar Masaoud; ammarshz123@gmail.com

Received 28 March 2022; Accepted 17 June 2022; Published 15 July 2022

Academic Editor: Ramin Ranjbarzadeh

Climate change and pollution are serious issues that are driving people to adopt renewable energy instead of fossil fuels. Most renewable energy technologies rely on atmospheric conditions to generate power. Solar energy is a renewable energy source that causes the least environmental damage. Solar energy can be converted to electricity, which necessitates the use of a PV system. This study presents a design, which analyses the output power performance of PV, using machine learning technique in India and Malaysia; using this, we would get the predicted amount of solar power using different weather conditions for both India and Malaysia. This study is divided into two sections, such as the data collection section and the implementation system. Dataset was collected from a weather NASA website, which took various weather parameters, based on which the model will be evaluated. The proposed research work is developed using ANN and is an amalgamation of statistical regression and neural networks, which help the model to get high accuracy by helping the model learn more complex relationships between parameters, which is able to evaluate the output power performance of photovoltaic cells with different environmental condition parameters in India and Malaysia. The ANN models are found to successfully predict PV output power with root mean square error (RMSE) of 1.5565, which was used as a measure of our model's accuracy. This ANN model also outperforms other models available in the literature. This will have a noteworthy contribution in scaling the PV deployment in countries such as India and Malaysia and will increase the share of PV power in their national power production, as it would give the industry and the two countries an idea as to how the predicted output PV power would vary based on weather conditions, such as temperature.

1. Introduction

The basic necessity of a human being is electricity or power. Electrical energy is essential for us to be able to go about our everyday lives without encountering any difficulties. Electrical energy may be obtained from a variety of sources, including wind, fossil fuels, hydropower, solar power, and nuclear and coal power. Renewable and nonrenewable energy are the two forms of energy.

Due to the massive consumption of fossil fuels in recent decades, global warming and the energy crisis have had a significant impact on government economic policy, climatic conditions, and energy security issues, motivating the development and use of alternative, sustainable, and clean energy sources to replace current energy production [1]. The entire world was compelled to focus on the utilization of renewable energy resources in order to avoid an emergency power outage, cut CO_2 emissions, and maintain pollution control. However, equipping such energy resources is a significant challenge, and as a result, we cannot entirely rely on the amount of renewable energy generated for the national power grid. One way to reduce future greenhouse gas emissions is to employ solar energy. Photovoltaic (PV) may offset 50% of all future development in thermal energy generation, reducing yearly worldwide carbon dioxide emissions by 10% in 20 years and 32% in 50 years, compared to predicted increases [2].

Photovoltaic power forecasting is a vital feature for large-scale integration into the conventional energy system that is both reliable and cost-effective. Furthermore, photovoltaic

(PV) power forecasting is necessary for reorganizing and installing large PV producing stations, power system stabilization, green power business, and power disturbance warning on self-governing power systems. As of February 28, 2021, India's installed solar power capacity, which includes both ground and roof-mounted plants, was 39,083 MW. From April 2019 through March 2020, solar power output totalled 50.1 TWh, or 3.6 percent of total power generation. In January 2022, renewable energy generation reached 13.15 billion units (BU), up from 11.51 BU in January 2021. By 2030, the government hopes to have installed renewable energy capacity of around 450 gigawatts (GW), with solar accounting for roughly 280 GW (almost 60%) [3]. Malaysia's yearly average daily solar radiation, on the other hand, ranges from 4.21 kWh/m^2 to 5.56 kWh/m^2. During the forecast period of 2022–2027, the Malaysia renewable energy market is predicted to grow at an annual rate of 8.5 percent. The COVID-19 epidemic has had a minor impact on Malaysia's renewable energy sector, since the government has postponed ambitious solar bids, including a 1 GW procurement in 2020 [4, 5]. These countries intend to increase their contribution to renewable energy (RE) over time. Because of its abundance, solar energy is the focus of renewable energy. In order to assess and analyse PV performance in terms of forecasting output PV power with minimal error, the impacts of important environmental factors on PV performance must be examined.

The main objective of this manuscript is achieved by developing a machine learning model based on statistical regression method. Statistical models are created by analysing historical data. Among them are time-series models, satellite data-based models, sky image-based models, artificial neural networks (ANN) models, and wavelet analysis-based models. This approach is selected for the study because of its high accuracy, novelty, and ease of use. We were able to make an ANN model, which is simple to understand, easy to use, and highly accurate with a root mean square error (RMSE) of 1.5565. The lesser the RMSE the better trained a model is considered. This model was also able to outperform various older regression models. Implementation of the ANN model has made it possible to calculate PV power in countries such as India and Malaysia with high accuracy in this manuscript, authors have reported the following new contributions:

(1) Developing a PV power prediction system algorithm to accurately predict the output solar power in the countries of India and Malaysia, since till now, no research based on these two countries combined have been done.

(2) Comparison of different machine learning based models and techniques to find the best one suited for our needs.

(3) Development of a model, which could outperform various old regression models.

(4) Exploring ANN carefully and finding the best prediction model, which could be made using our knowledge to help and provide the lowest RMSE, when compared with other models.

2. Related Literature

Several recent studies have reported on several methods for forecasting and estimating PV output power. The literature on PV plant power production estimation offers different types of models in detail, which are demonstrated in Table 1. In Reference [6], a phenomenological model is used, which is a scientific model that represents the actual relationships between events in a way that is consistent with fundamental theory but is not generated directly from theory. To put it another way, a phenomenological model is not based on basic principles. A phenomenological model makes no attempt to explain why the variables interact in the manner they do, instead focusing on describing the connection, assuming that the link continues beyond the observed values, which gives it a major drawback.

Various hybrid models for predicting PV power have grown in popularity. For example, reference [7, 8] suggested a method for power forecasting that incorporates three forecasting modules: two models for numerical weather forecasting and other one for AI based models, but this could become extremely complicate, since it would require a lot of resources and also because three different modules were used, which would make them difficult to understand. Reference [9] proposed a two-stage method, where, first, the clear-sky model approach is used to normalize the solar power, and then, adaptive linear time-series models are applied for prediction. This method, however, can also be used for short time predictions, and the accuracy decreases significantly around dusk and dawn. Reference [10] combines two well-known methods: the seasonal autoregressive integrated moving average technique (SARIMA) and the support vector machines method (SVMs), but it could only be used to determine short term PV power. The goal of these hybrid models for PV power forecasting is to take use of the strengths of each model to achieve worldwide forecasting performance, to establish the optimal weight between online data and meteorological forecasts, for example, many statistical and AI-based approaches are used.

Deterministic methods, based on physical events, attempt to forecast PV plant output by utilizing software such as PVSyst and System Advisor Model (SAM) to consider the electrical model of the PV devices that make up the plant. The electrical, thermal, and optical properties of PV modules were modelled using a deterministic method in [11–14]. The majority of published research on PV power forecasting focuses solely on deterministic forecasting, i.e., point forecasting. In certain cases, deterministic forecasting approaches fail to account for the uncertainties in PV power data.

Recently, there has been a lot of interest in probabilistic PV power forecasting models that can quantitatively explain these uncertainties [13, 15]. Using an ensemble of deterministic forecasters is one of the most common methods for creating probabilistic uncertainty. The primary drawback of ensemble-based PV power forecasting models is their high computing cost, which may pose a real-time difficulty in practice. Another shortcoming of deterministic and

Table 1: Characteristics of prediction models used for forecasting PV output power.

Objective	Advantage	Disadvantage	Reference
Forecast of PV	Highly versatile, made up of four different modules. High accuracy	Not easy to understand. Needs high computing power	[6]
Forecast of PV power	Physics inspired, and uses stochastic to increase efficiency. Uses three separate modules, two for numerical forecasting and other for AI based models.	Data collection is tougher than other methods. Solution is long and complicated.	[7, 8]
Solar power forecasting	Uses adaptive and linear time series. Easy to implement	Low accuracy during dusk and dawn	[9]
Estimate PV power	Hybrid model uses SARIMA and SVM methods. Good accuracy	Extremely complex to execute	[10]
Forecast PV plant output	Uses a physical model with software such as PVSyst and SAM	Deterministic forecasting is common. Fails to account for uncertainties in PV power data. High computing cost	[11, 12, 14]
Solar PV forecasting	Presents sate of the art PV power forecasting technique using extreme learning method	Can lead to over fitting. Uncertain performance of the model	[13, 15]
PV performance	Increased accuracy. Use of physical systems to get data	Expensive during setting up and can get complex	[16–18]
PV power forecasting	Predicted the solar irradiance using machine learning techniques, rather than PV power itself	More complexity. Did not get the PV power	[15, 20–23]
PV power forecasting	Increased accuracy	Uses expensive and restricted equipment	[24, 25, 28, 29]
PV power prediction	High accuracy. Simple model to understand	Data collection is done on hardware basis and would be expensive	[26]

probabilistic PV power forecasting techniques is their shallow learning models.

In [16], for the cities of Kuala Lumpur and Lucknow, researchers examined the capabilities and outputs of 8 MW solar mono-Si and poly-Si PV systems. PVsyst software was used to run the simulations. The findings provided light on the impact of temperature variations, the sun's location in relation to the Earth's horizon, and the impact of mono-Si vs poly-Si systems. In [17], a grid-tied 100 kWp solar photovoltaic power plant, erected on an institute's building rooftop in Bhopal, India, was simulated and energy analysed. The study sheds light on the performance of solar power plants connected to the medium-term grid in real-world settings in central India. The plant's standard performance ratio and capacity factor were discovered to be 80.72 percent and 19.27 percent, respectively; [18] included a comprehensive investigation of the PV plant's performance over time and estimated the energy output based on key meteorological data gathered from a solar radiation resource assessment (SRRA) station established at the PV power plant's site. The wet seasons have an impact on solar output and performance, which is a common occurrence in the humid tropical area. Based on various meteorological characteristics, a regression model of solar production for all seasons was created.

Insights into the features of data relationships and the relevance of particular qualities in datasets are provided by machine learning [19]. Jawaid et al. [11] examined several ANN algorithms without revealing the characteristics of the prediction model or their numerical performance. Several additional studies used machine learning approaches to estimate solar irradiance rather than PV power [20–22]. Some studies [23] focused solely on the training and testing of a single machine learning model for PV power prediction. Using a minimal input dataset, an adaptive ANN was utilised to simulate and size a standalone PV plant [24, 25]. The many components that make up a PV power system, as well as their output signals, were modelled using an ANFIS [7].

Artificial neural networks (ANN), support vector machines (SVM), multiple linear regression (MLR), and adaptive neuro-fuzzy inference system (ANFIS) are examples of statistical and machine learning algorithms that function without any prior knowledge of the system under investigation [26, 27]. Statistical learning algorithms provide several benefits. They can, first and foremost, operate with incomplete data. Secondly, they can generalize and make predictions once they've been trained. Their characteristics allow them to be utilised in a variety of situations. Different machine learning (ML) methods have been studied for output power prediction of renewable energy sources. References [15, 20, 22] predicted the solar irradiance using machine learning techniques, rather than PV power itself. However, due to increased complexity, the use of a convolution neural network was not useful. References [28–31] used satellite images, sky imaging and methods to increase the accuracy, but the data collection method was expensive and restricted. The method is also more expensive.

3. Proposed Model and Working Principle

Machine learning based photovoltaic (PV) performance forecast with various environmental conditions parameters for India and Malaysia is used. Artificial neural network (ANN) based regression technique has been used to calculate the predicted power generated by photovoltaic cells. In the proposed method, the division of data would be random, with a ratio of 70:30 for training and validating. Moreover, statistical regression technique would be used for ANN.

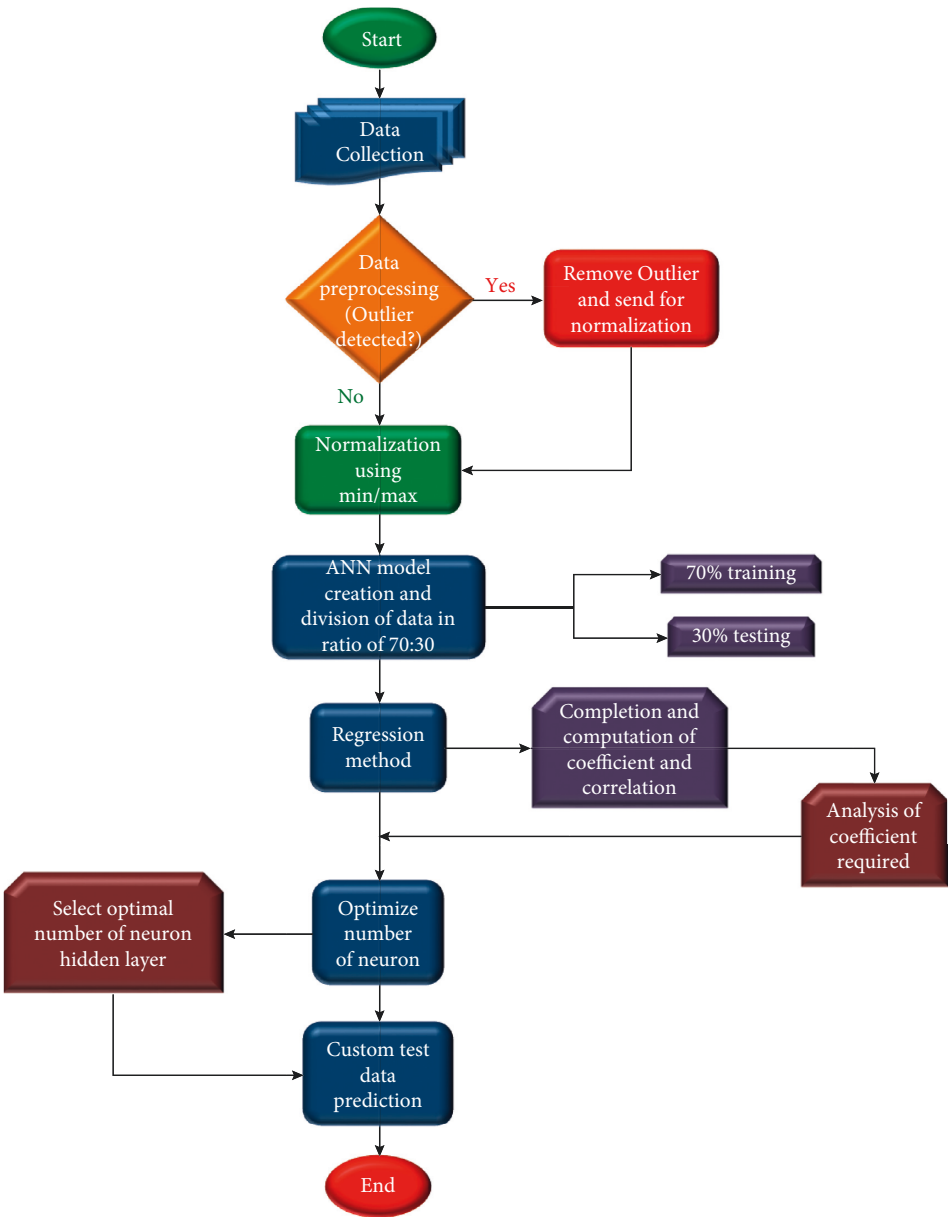

Figure 1: Flowchart of the proposed ANN model for predicting PV output.

Levenberg Marquardt method is used to conduct the training of the dataset. The performance of the proposed method is verified using mean squared error (MSE).

This study makes use of statistical regression method. Generally, the study of historical data is used to create statistical models. Time-series models, satellite data-based models, sky image-based models, artificial neural networks (ANN) models, and wavelet analysis-based models are among them. Due to its high accuracy, novelty, and easy usage, this method is selected in this manuscript. The flowchart of the proposed model is illustrated in Figure 1.

4. Reading of Datasheet

The dataset collected from the Internet was stored as an excel file and then sent to MATLAB. This included importing the data and reading the dataset as a CSV file [15]. The dataset consisted of weather information and readings for the entire countries by taking out the averages, and currently no specific locations were chosen. For this research, knowing the load and capacity of the plant was not necessary and is something, which can be added to the project on a later stage.

5. Data Prepossessing

After importing the data, the preprocessing of the data is initiated. This included removing missing values and dropping the nonrelevant columns. Once the nonrelevant columns have been removed, the process is continued by detecting and removing the outlines. To sum it up, the procedure will detect outliers based on factors such as wind

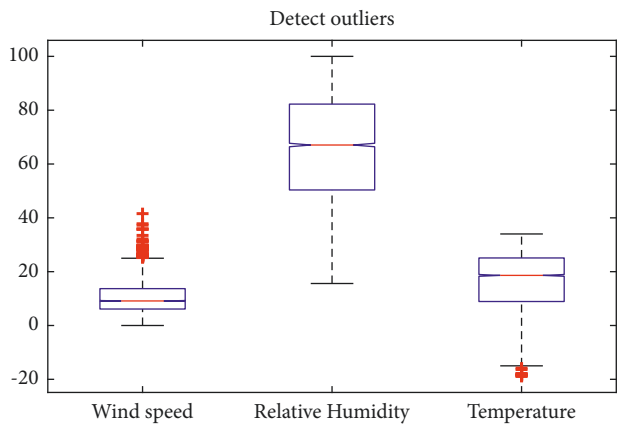

Figure 2: Detection of outliers.

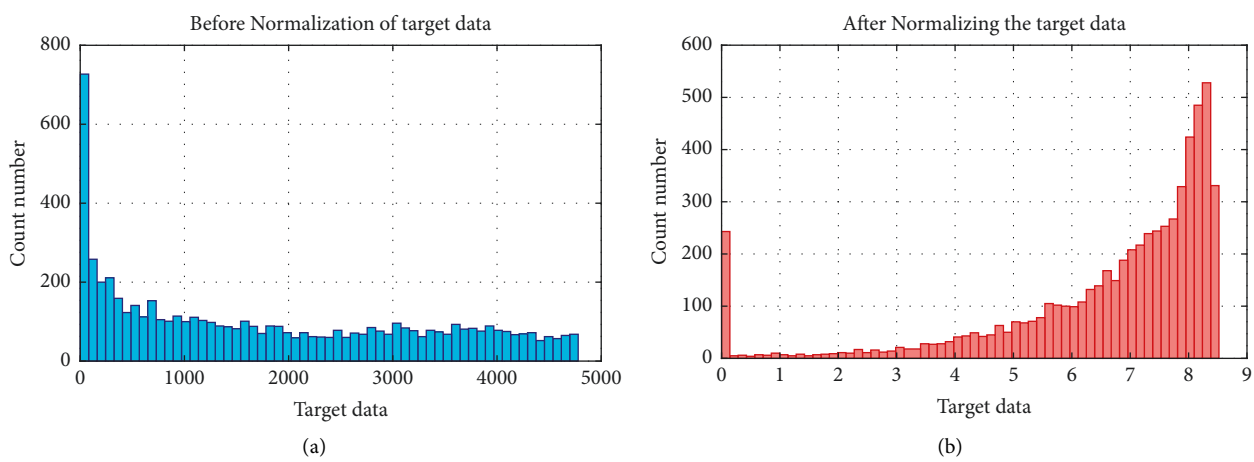

Figure 3: Normalization process of the targeted data: (a) before normalization; (b) after normalization.

speed, relative humidity, and temperature, make a threshold and range and check for outliers, as shown in Figure 2.

6. Normalization or Scaling

The process of arranging data in a database is known as normalization. It is used to reduce the amount of redundancy in a relationship or group of relationships. It is also used to get rid of unnecessary features like insertion, update, and deletion anomalies. Scaling is the process of measuring and assigning numbers to items based on predetermined principles. Scaling, in other terms, is the act of placing measurable things on a continuum using a continuous succession of numbers, to which they are allocated. In the proposed method, normalization and scaling have been performed and the results are shown in Figure 3.

7. Correlation between Solar Power and Temperature

Here, a relation describes the degree to which two variables move in coordination with one another. The two variables that have been selected in this case are solar power and the temperature in India and Malaysia. The results are combined,

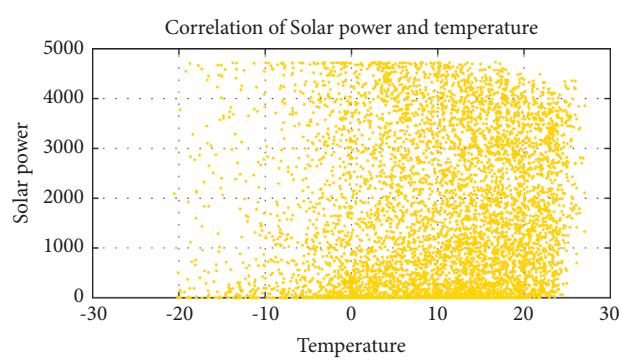

Figure 4: Correlation between solar power and temperature.

calculated, and graphically illustrated in Figure 4. Since, in this figure, the two variables are moving in the same direction with respect to one another, it can be stated that temperature and solar power are in a positive corelation to one another.

Variety of basic and common regression and prediction models: in this work, the ANN was also used to predict daily PV output power, which is a very popular machine learning tool for classification and regression application. With a layered structure (input, hidden, and output layers), the ANN attempts to recreate machine learning in a manner

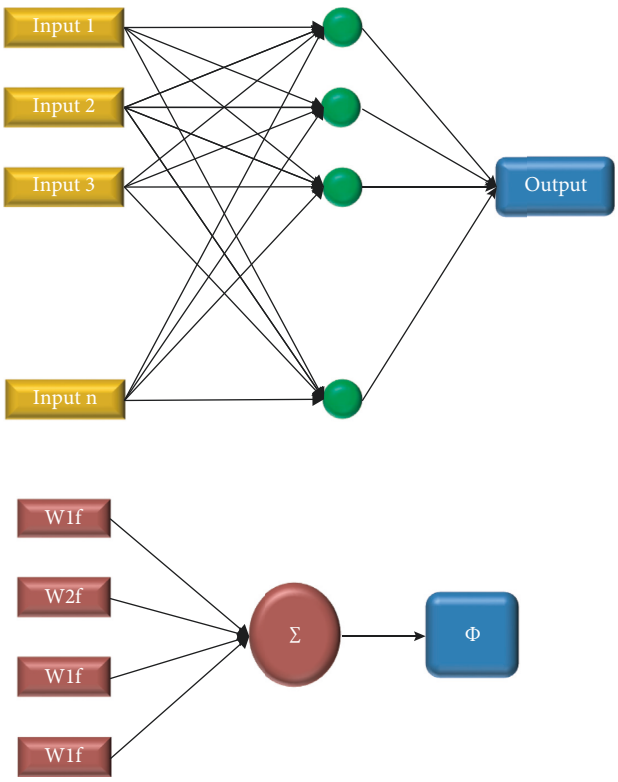

Figure 5: Proposed ANN model.

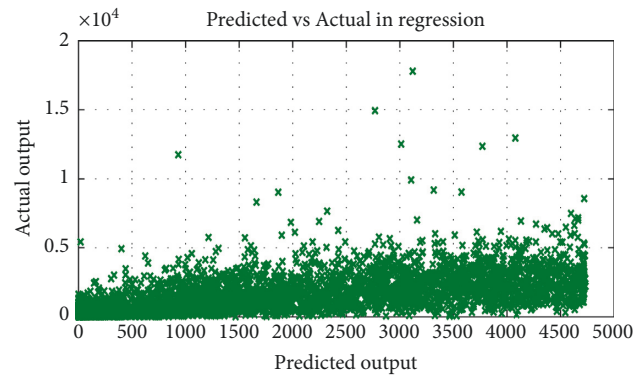

Figure 6: Predicted vs actual output.

comparable to that of the human brain. Artificial neurons are used to model ANNs, with each neuron receiving a set of inputs. These inputs are subjected to the activation function, which results in a neuron activation level (neuron output value), and learning knowledge is delivered in the form of training inputs and output pairs. The proposed model of ANN is shown in Figure 5. Some of the features of the proposed ANN are listed as follows:

(1) *Model Creation*. The hidden layers taken here are 30, the dataset has been divided into a ratio of 70 for testing and 30 for validating.

(2) *Performance*. We start training our model and check its performance.

(3) *Visualize the Prediction from ANN Model*. Visualize the prediction from ANN model Figure 6, depicts a graph, which is plotted to illustrate the actual vs predicted model for the artificial neural network designed here after completion of the program.

(4) *Custom Test Data Prediction*. Here, we calculate and store the predicted solar power in both the countries combined.

8. Analysis

To assess the efficacy of machine learning algorithms for PV output power prediction, many statistical studies were conducted. Various evaluation criteria are widely used to compare the performance of models: (i) The correlation coefficient, which determines the linear relationship between two variables; (ii) mean absolute error (MAE), which is calculated by averaging the absolute difference between two variables; (iii) mean square error (MSE) calculates and aggregates the square discrepancy between target and projected values; (iv) root mean square error (RMSE) is the square root of MSE and identical to MAE except that it averages the squares of the difference before finding the square root, giving greater mistakes more weight. Here, for the calculation of accuracy, MSE and RMSE were considered as the main factors to measure the success of the model.

$$\begin{aligned} r &= \mathrm{Con}(X,Y)\sigma x\sigma y, \\ \mathrm{MAE} &= n \times n(X-Y), \\ \mathrm{MSE} &= 2n \times P(X-Y), \\ \mathrm{RMSE} &= 2n \times rP(X-Y), \\ r_2 &= 1-\mathrm{MSE}, \\ \mathrm{MSE} &= \sum (X-Y)^2. \end{aligned} \tag{1}$$

9. Results and Discussion

The dataset used consists of parameters such as relative humidity, wind speed, temperature. Our machine learning technique was based on statistical regression method, which makes use of historical data to find the results. Our dataset was collected from a website link available of NASA's web page [32]. This method was used for its high accuracy and noncomplexity. Figure 7 summarizes the progress of our model and consists of the number of epochs, time taken to train, the performance of the model, gradient of model, Mu, and the validation check.

The validation performance is used to ensure that the system performs consistently and accurately over a wide range of characteristics by checking the performance of our system at different stages, as shown in Figure 8, the best training performance was observed at different epochs for different techniques. Out of the various models developed by the ANN using the different set of features, the best epochs were obtained at 6 epochs, respectively, with a value of 2.4228. This could be used in future to derive the model for predicting the PV power.

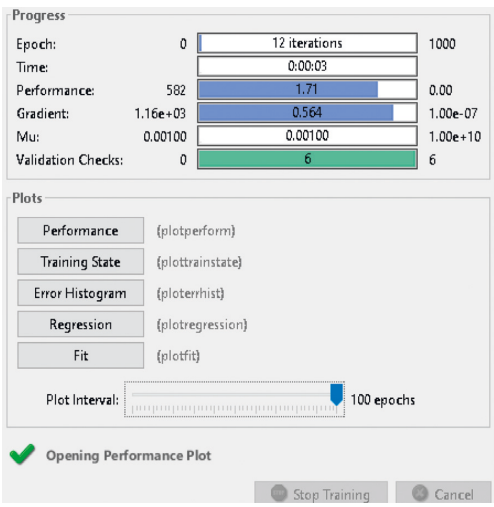

Figure 7: Performance of neural network.

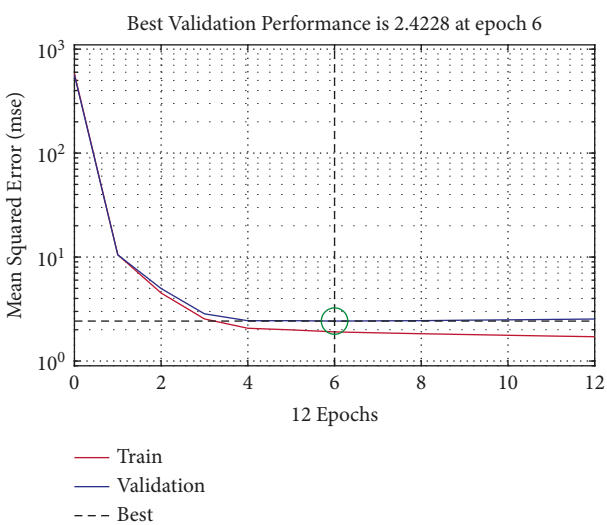

Figure 8: Performance of neural network.

Figure 9 shows the error histogram (a histogram of error between the target value and predicted value after training a feed forward neural network) with 20 bins, where bins represent the vertical bars in the graph. Total error from each neural network ranges from −7.054 to −4.794. Each vertical bar represents the number of samples from corresponding dataset, which lies in a particular bin. There is a zero-error line in the graph, and more than 80% of the errors lie within +10 Watt. It is typically assumed that any algorithm, which could predict the output, where 80% of the error lying within 10%.

The training set, Figure 10 consists of three different graphs: the gradient graph, whose gradient value (which is a measure of change in all weights with respect to change in error) at epoch 12 is 0.56399. The Mu graph has a Mu value (a control parameter for algorithm used in the neural network) of 0.001 at 12 epochs. The validation check graph (an automatic check performed by computer to see if data entered is sensible and reasonable) is equal to 6 at epoch 12.

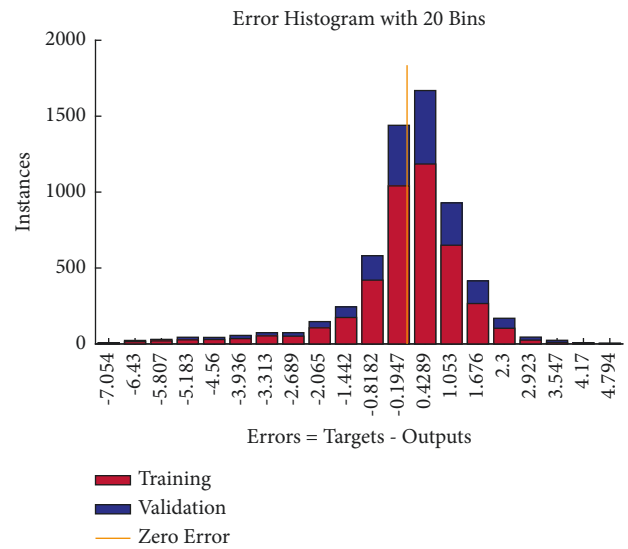

Figure 9: Error histogram.

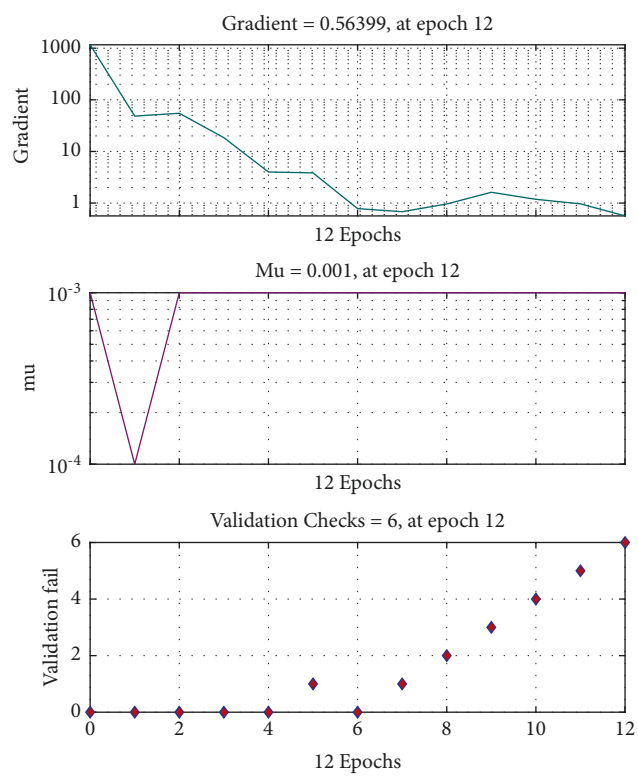

Figure 10: Graph depicting the gradient value, the Mu value, and the validation check value, respectively.

Figure 11 shows the relation between the original power output and the predicted power output, using the best epochs from the ANN. The dots represent the original power output; the blue, red, and green line is the best linearized predictive model derived from ANN, and the dotted line represents the best linear relation for the true target. However, the difference between the predictive model trend-line and the true trend-line was noticed for all features, which is evident in Figure 11.

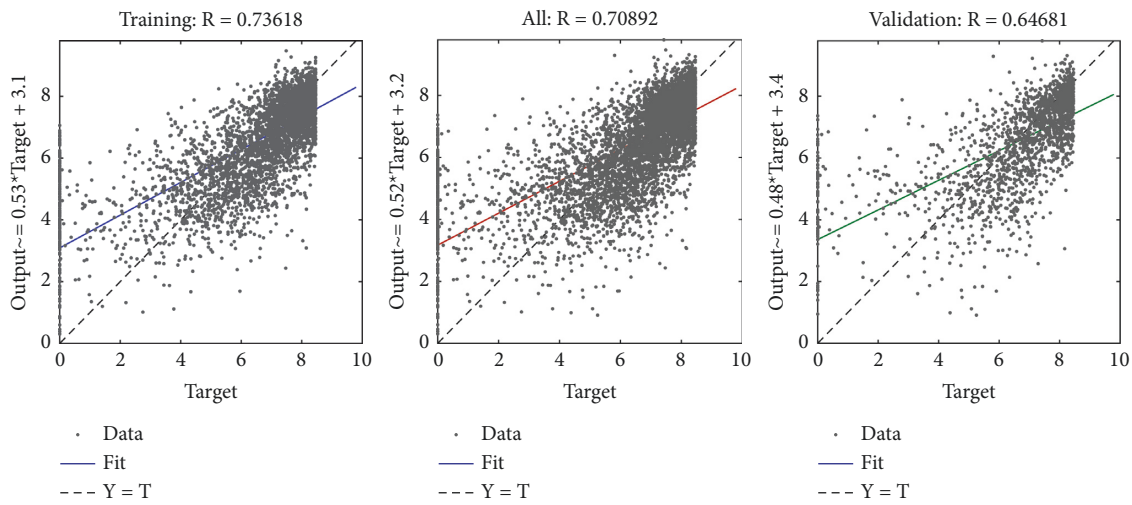

Figure 11: Graph depicting the gradient value, the Mu value, and the validation check value, respectively.

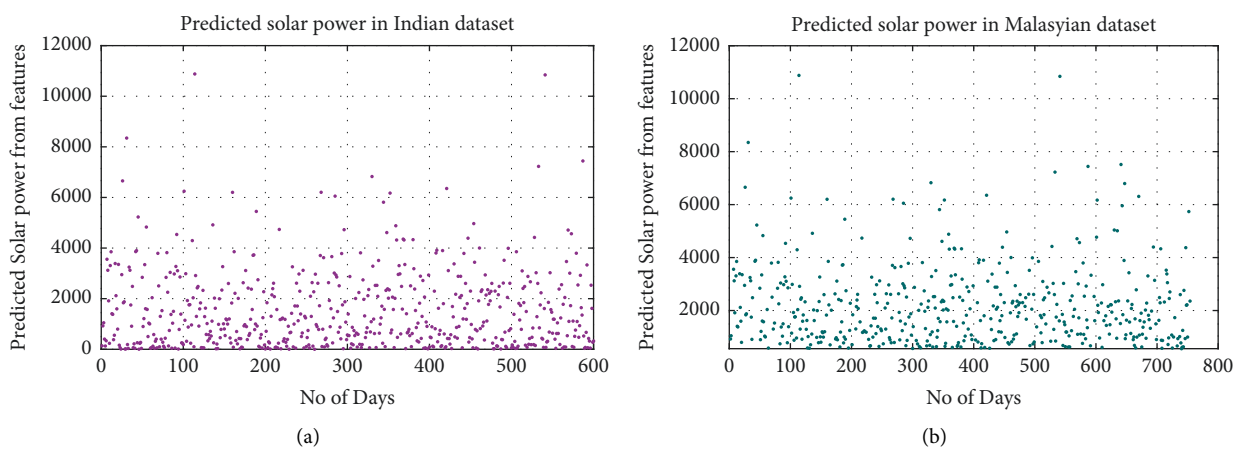

Figure 12: Predicted solar power in (a) India and (b) Malaysia.

Table 2: Comparison between proposed method and other methods.

Method	Parameter	Result
CFS	RMSE	06.1555
Relief	RMSE	5.5351
Proposed method	RMSE	1.5565

Finally, Figure 12 shows the result of the predicted power of the PV in countries such as India and Malaysia. It is divided into two different graphs, one for the predicted solar power in India, which is depicted in Figure 12(a), and other for the predicted solar power in Malaysia, which is illustrated in Figure 12(b). The x axis of the graph is labeled as the number of days ranging from 0–600 in India and 0–800 in Malaysia. The y axis is labeled as predicted solar power from given features, with a range of 0–18000 in India and Malaysia. A brief comparison among other prediction methods is presented in Table 2.

10. Conclusions

The predicting photovoltaic power is an important research field that employs various forecasting approaches to mitigate the consequences of solar output unpredictability. In smart grid and microgrid concepts, there is an increasing amount of photovoltaic (PV) generating penetration. PV power is intermittent and heavily dependent on irradiance, temperature, and humidity, due to the irregular nature of solar sources. Solar energy generation has a lot of potential in India. The country's geographic position is advantageous for solar energy generation. The reason for this is because India is a tropical nation that receives solar radiation practically all year, averaging 3,000 hours of sunlight. This equates to almost 5,000 trillion kWh. In the case of Malaysia, it will be a center for solar cell production by 2030, according to the Malaysian Solar PV Roadmap 2017. According to the Renewable Energy Policy and Action Plan, electricity generated from renewable sources such as solar PV, biomass, biogas, minihydro, and solid wastes could total to 11,227 GWh by

2020 (NREPAP). Solar power will generate a clean and green environment in the future, and by employing the tracking system, the power produced will be maximized. Solar power as a source of energy will also assist to minimize global warming and the greenhouse effect by reducing the usage of nonrenewable energy. When compared to other models, our model was more accurate in calculating the output power with a RMSE of 1.556.

(1) Our trained ANN model is simple and easy to understand, which can be used to calculate and predict the output power of PV system in India and Malaysia with performing complex calculations.

(2) Since the research was based for counties of India and Malaysia, it can help other researchers in these countries who can use our method and its performance for the prediction in their region.

For further research, we can acquire more PV and environmental data by setting up a physical system and collecting the data from it, this would help us acquire better data, which would help build more accurate models. This would help in making a more predictive model using the approach from this research and can be compared with other CNNs in the future. Cooling and cleaning effects can also be added in the future and can be used with a dataset being collected for five years, making a more accurate model.

Data Availability

The dataset used in the following research is available from the corresponding author on request. Additionally, the dataset for the countries mentioned and even other different countries can be downloaded in the form of a CSV file from the website mentioned in reference [14] by entering the latitude and longitude of the place along with the parameters required.

Conflicts of Interest

The authors declare that there are no conflicts of interest regarding the publication of this paper.

Acknowledgments

Thanks to Universiti Teknologi PETRONAS (UTP) and Valore Institute of Technology (VIT) for joint research collaboration for utilities of the resources.

References

[1] S. T. Meraj, N. Z. Yahaya, K. Hasan et al., "A filter less improved control scheme for active/reactive energy management in fuel cell integrated grid system with harmonic reduction ability," *Applied Energy*, vol. 312, Article ID 118784, 2022.

[2] M. S. Hossain Lipu, S. Ansari, M. SazalMiah et al., "A review of controllers and optimizations based scheduling operation for battery energy storage system towards decarbonization in microgrid: challenges and future directions," *Journal of Cleaner Production*, vol. 360, Article ID 132188, 2022.

[3] R. S. Phukan, "Solar Energy in India – Pros, Cons and the Future," Maps of India, India, 2014, https://www.mapsofindia.com/my-india/india/scope-of-solar-energy-in-india-pros-cons-and-the-future.

[4] A. W. Azhari, K. Sopian, A. Zaharim, and M. A. Ghoul, "A new approach for predicting solar radiation in tropical environment using satellite images – case study of Malaysia," *WSEAS Transactions on Environment and Development*, vol. 4, no. 4, pp. 373–378, 2008.

[5] Mordor Intelligence, *Malaysia solar energy Market - growth, Trends, COVID-19 Impact, and Forecasts (2022 - 2027)*, Mordor Intelligence, Hyderabad, India, 2021.

[6] M. Millán, J. Lobato, and P. Rodrigo, P. Cañizares and M. A. Rodrigo, Prediction and management of solar energy to power electrochemical processes for the treatment of wastewater effluents," *Electrochimica Acta*, vol. 335, Article ID 135594, 2020.

[7] M. Bouzerdoum, A. Mellit, and A. Massi Pavan, "A hybrid model (SARIMA-SVM) for short-term power forecasting of a small-scale grid-connected photovoltaic plant," *Solar Energy*, vol. 98, pp. 226–235, 2013.

[8] L. A. Fernandez-Jimenez, A. Muñoz-Jimenez, A. Falces et al., "Short-term power forecasting system for photovoltaic plants," *Renewable Energy*, vol. 44, pp. 311–317, 2012.

[9] P. Bacher, H. Madsen, and H. A. Nielsen, "Online short-term solar power forecasting," *Solar Energy*, vol. 83, no. 10, pp. 1772–1783, 2009.

[10] D. L. King, J. A. Kratochvil, and W. E. Boyson, *Photovoltaic Array Performance Model*, US- Department of Energy, Washington, DC, USA, 2004.

[11] F. Jawaid and K. N. Junejo, "Predicting daily mean solar power using machine learning regression techniques," in *Proceedings of the 2016 Sixth International Conference on Innovative Computing Technology*, August 2016.

[12] R. Ahmed, V. Sreeram, Y. Mishra, and M. Arif, "A review and evaluation of the state-of-the-art in PV solar power forecasting: techniques and optimization," *Renewable and Sustainable Energy Reviews*, 109792, vol. 124, , 2020.

[13] F. Bucci, M. De Felice, E. Maggioni et al., "Deterministic and stochastic approaches for day-ahead solar power forecasting," *Journal of Solar Energy Engineering*, vol. 139, no. 2, 2016.

[14] N. Ahmad, A. Khandakar, A. El-Tayeb, K. Benhmed, I. Atif, and F. Touati, "Novel design for thermal management of PV cells in harsh environmental conditions," *Energies*, vol. 11, no. 11, p. 3231, 2018.

[15] M. K. Behera, I. Majumder, and N. Nayak, "Solar photovoltaic power forecasting using optimized modified extreme learning machine technique," *Engineering Science and Technology, an International Journal*, vol. 21, no. 3, pp. 428–438, 2018.

[16] K. S. Ria and M. Samykano, "Performance of utility scale PV plant in Malaysia and India: a comparative study," in *Proceedings of the 4th Int. Conf. Electr. Energy Syst*, pp. 106–110, ICEES, Chennai, India, February 2018.

[17] A. KhareSaxena, S. Saxena, and K. Sudhakar, "Energy performance and loss analysis of 100 kWp grid-connected rooftop solar photovoltaic system," *Building Service Engineering Research and Technology*, vol. 42, no. 4, pp. 485–500, Mar. 2021.

[18] A. Gopi, K. Sudhakar, N. W. Keng, A. R. Krishnan, and S. S. Priya, "Performance modeling of the weather impact on a utility-scale PV power plant in a tropical region," *International Journal of Photoenergy*, vol. 2021, Article ID 5551014, 10 pages, 2021.

[19] S. P. Mishra and P. K. Dash, "Short term wind power forecasting using Chebyshev polynomial trained by ridge extreme learning machine," in *Proceedings of the 2015 IEEE Power, Commun. Inf. Technol. Conf. PCITC 2015*, pp. 173–177, Bhubaneswar, India, October 2016.

[20] J. Li, J. K. Ward, J. Tong, L. Collins, and G. Platt, "Machine learning for solar irradiance forecasting of photovoltaic system," *Renewable Energy*, vol. 90, pp. 542–553, 2016.

[21] A. Moosa, H. Shabir, H. Ali, R. Darwade, and B. Gite, "Predicting solar radiation using machine learning techniques," in *Proceedings of the 2nd Int. Conf. Intell. Comput. Control Syst*, pp. 1693–1699, ICICCS, Madurai, India, June 2019.

[22] A. Khosravi, R. Koury, L. Machado, and J. Pabon, "Prediction of hourly solar radiation in Abu Musa Island using machine learning algorithms," *Journal of Cleaner Production*, vol. 176, pp. 63–75, 2018.

[23] H. Sheng, J. Xiao, Y. Cheng, Q. Ni, and S. Wang, "Short-term solar power forecasting based on weighted Gaussian process regression," *IEEE Transactions on Industrial Electronics*, vol. 65, no. 1, pp. 300–308, 2018.

[24] T. Hiyama and E. Karatepe, "Investigation of ANN performance for tracking the optimum points of PV module under partially shaded conditions," in *Proceedings of the 2010 Conference Proceedings IPEC*, pp. 1186–1191, Singapore, October 2010.

[25] D. O'Leary and J. Kubby, "Feature selection and ANN solar power prediction," *J. Renew. Energy*, vol. 2017, Article ID 2437387, 7 pages, 2017.

[26] A. Khandakar, M. E. H. Chowdhury, M. Khoda Kazi et al., "Machine learning based photovoltaics (PV) power prediction using different environmental parameters of Qatar," *Energies*, vol. 12, no. 14, p. 2782, 2019.

[27] T. M. Hossain, J. Watada, I. A. Aziz, M. Hermana, S. T. Meraj, and H. Sakai, "Lithology prediction using well logs: a granular computing approach," *Int. J. Innov. Comput. Inf. Control*, vol. 17, no. 1, pp. 225–244, 2021.

[28] A. Murata, H. Ohtake, and T. Oozeki, "Modeling of uncertainty of solar irradiance forecasts on numerical weather predictions with the estimation of multiple confidence intervals," *Renewable Energy*, vol. 117, pp. 193–201, 2018.

[29] M. Abuella and M. B. Chowdhury, "Hourly probabilistic forecasting of solar power," in *Proceedings of the 2017 North American Power Symposium*, pp. 7–9, Morgantown, WV, USA, September 2017.

[30] R. Singh and I.S. I. Singh, "Power performance analysis of solar tracking system in UTP," *Advanced Methods for Processing and Visualizing the Renewable Energy*, Springer, Berlin, Germany, pp. 47–57, 2020.

[31] B. H. Truong, P. Nallagownden, K. H. Truong, R. Kannan, D. N. Vo, and N. Ho, "Multi-objective search group algorithm for thermo-economic optimization of flat-plate solar collector," *Neural Computing & Applications*, vol. 33, no. 19, pp. 12661–12687, 2021.

[32] P. Stackhouse, *NASA POWER | Data Access Viewer"*, Power.larc.nasa.gov, Washington, D.C, USA, 2022.

Hindawi
Mathematical Problems in Engineering
Volume 2022, Article ID 8390433, 9 pages
https://doi.org/10.1155/2022/8390433

Research Article

State Evaluation Method of Distribution Terminal Based on Deep Reinforcement Learning

Fei Xue, Xutao Li, Xiaoli Wang, Hongqiang Li, and Bei Tian

Electric Power Research Institute of State Grid Ningxia Electric Power Co., Ltd, Yinchuan 750001, China

Correspondence should be addressed to Fei Xue; tjuxf1010@126.com

Received 1 April 2022; Revised 19 June 2022; Accepted 25 June 2022; Published 13 July 2022

Academic Editor: Mohammad Yaghoub Abdollahzadeh Jamalabadi

The reliable operation of the distribution terminal is a key link to realize distribution automation. It is particularly important to efficiently and accurately evaluate the operation state of the distribution terminal. In order to realize accurate state perception of distribution terminals, a state evaluation method based on deep reinforcement learning is proposed to support the reliable operation of the distribution network. First, the fault causes of terminal equipment and the collected datasets are introduced. On this basis, the multilayer network structure is used to analyze the terminal state. Q-reinforcement learning network is used to optimize the convolution neural network, solve the overfitting problem of the deep network model, and continuously extract the data features. At the same time, in order to increase the objectivity and reliability of the evaluation method, the membership function optimization is also introduced into the model to further ensure the accuracy of the state analysis method. Simulation results show that the recognition accuracy of the proposed method is 94.23%, which shows excellent evaluation performance.

1. Introduction

With the accelerating pace of distribution network construction, the coverage of distribution terminals is also increasing year by year [1–3]. The distribution terminal is used for the monitoring and controlling of switching post, section switch on the column, ring network cabinet, distribution transformer, line voltage regulator, and reactive power compensation capacitor in medium voltage distribution network. Its operation stability and reliability directly affect the operation stability and reliability of the whole distribution network [4].

However, the vast majority of distribution terminals are directly installed outdoors or in a simple sheltered area, which is easy to be affected by external force damage, and various unexplained abnormalities often occur [5]. In addition, due to the large number and wide distribution of distribution terminals, the workload of manual normalization inspection is huge. In particular, the distribution terminals and communication equipment on the column are installed at a high place, so it is extremely inconvenient for manual on-site inspection and maintenance. All the above factors pose great challenges to the state detection and fault analysis of distribution terminals [6]. Therefore, it is urgent to propose an efficient and accurate state evaluation method of distribution terminals.

The traditional state identification method of the distribution terminal adopts the mode of postmaintenance or regular maintenance [7]. Postmaintenance refers to the maintenance only when the equipment fails and cannot continue to operate, which will directly reduce the operation reliability of the distribution network. The maintenance method of regular maintenance, which only disassembles the equipment to a certain extent according to the specified time interval, will inevitably produce "excess maintenance" [8].

The emergence of a deep learning network provides a new solution for on-line detection and evaluation of power equipment status. The deep network can be used for continuous feature extraction and model training of the data collected by the distribution terminal, to build a reliable distribution terminal state sample database, and then to realize accurate distribution terminal state evaluation. However, due to the deep network structure, the current multilayer network has the problem of overfitting the large data sample set, and the state analysis model is difficult to

maintain the same stability in the whole cycle, which also makes most of the current network models have the problem of low state recognition accuracy.

Aiming to support the reliability of the terminal state, a method based on in-depth learning of terminal state analysis is proposed. The innovation of this method is mainly composed of two parts as follows:

(1) Considering the time-series characteristics of power grid state data, this study uses the convolutional neural network (CNN) to construct a terminal state evaluation network and introduces Q-reinforcement learning network to solve the overfitting problem of multilayer network, which can strengthen the network's perception and decision-making ability, achieve high-precision identification of different states, and improve the accuracy and stability of the evaluation network model.

(2) At the same time, considering the complexity of the distribution terminal data, this study also introduces the membership function to optimize the model, which increases the objectivity and reliability of terminal state evaluation methods, and further ensures the accuracy and accuracy of output state evaluation results.

2. Related Research

The state evaluation of distribution terminal can timely and correctly diagnose various abnormal states or alarm information of the terminal, so as to prevent or eliminate faults and ensure the safe [9].

In the era of rapid development of distribution internet of things, the original working mode of distribution operation and maintenance is difficult to cope with the pressure brought by the large-scale access of distribution terminals [10, 11]. The number of operation and maintenance personnel is limited, the technical level is uneven, and the construction scale and the number of distribution terminals are large. There are various factors causing the defects of distribution terminals, resulting in the difficulty and complexity of operation and maintenance work. At present, the operation and maintenance personnel only record and classify a large number of terminal defect data, and conduct postevent human analysis and defect elimination according to the operation and maintenance experience for terminal defects. Passive operation and maintenance have low operation and maintenance efficiency [12].

Aiming to support the stable state of the system after large-scale access to distribution terminals, it is urgent to mine the required laws from a large number of terminal data generated by distribution network operation, effectively analyze the reasons behind the defects, provide ideas for terminal state evaluation, and improve the efficiency and ability of distribution terminal operation and maintenance.

Data mining technology has penetrated into many fields of power system and promoted the development of distribution network in the direction of intelligence [13, 14]. At present, the fuzzy theory modeling method is usually used for equipment state evaluation to evaluate the fuzziness and uncertainty of the characteristic quantity of the thing itself, in order to accurately measure the influence of each state quantity on the equipment state [15, 16]. Although the method of mathematical modeling can support the distribution network to realize the self-detection of the terminal state to a certain extent, the data of the distribution terminal are too large and the cause of fault is too complex [17–19], which makes the establishment of state model particularly difficult and cannot well support the distribution network to realize the timely perception and identification of terminal equipment state.

The fault identification and analysis method based on the multilayer network model gradually break through the limitations of traditional methods. Through continuous training and learning of sample data, a complete and reliable equipment state database is established, and finally, effective distribution terminal operation state identification is realized [20–22]. However, it should be noted that there is less research on realizing the state perception of distribution terminal based on deep learning, but many scholars have effectively perceived the operation state of power equipment or mechanical equipment with the help of the powerful learning ability of multilayer network. Reference [23] will continuously train and learn the sample data obtained from the fan SCADA system through the convolution neural network to realize the health monitoring and state recognition of the fan; reference [24] realizes end-to-end abnormal state detection of steam turbine mechanism equipment based on deep convolution neural network; reference [25] proposed a new defect diagnosis method combining least squares support-vector machine and Bayesian network decision tree to realize the state recognition of secondary equipment such as remote terminal unit and merging unit; reference [26] uses the superposition denoising automatic encoder model in deep learning to directly extract feature information from microgrid power equipment and introduces clustering algorithm to determine the state of electrical equipment. However, it should be noted that for the deep network, the deeper network structure can indeed improve the network efficiency of the state identification model, but there is also the problem that the identification accuracy is reduced due to the overfitting of the model, which makes the stability of the distribution terminal state analysis network model open to discussion.

In this study, the Q-reinforcement learning network model is used to optimize the CNN network while ensuring the recognition accuracy of the state analysis model. Through continuous learning of the data before and after the time, the problem of CNN network overfitting can be solved, which can well support the operation state evaluation and analysis of distribution terminal equipment.

3. Multidimensional Evaluation Method of Distribution Terminal State Based on Deep Reinforcement Learning

3.1. State Perception of Distribution Terminals and Analysis of Influencing Factors. Complete and reliable state data

acquisition is the premise to realize the state evaluation of the distribution terminal. In this study, with the help of the key circuits inside the heterogeneous distribution terminal equipment, combined with the hardware detection technology and software verification method, the internal operation state monitoring is realized, and the inspection results are sent through the communication channel, so that the internal operation key parameters and self-inspection results of the distribution terminal are in a "visual" state.

The main acquisition contents of the power distribution terminal are shown in Figure 1.

As shown in Figure 1, the power distribution terminal as a whole mainly includes the control circuit, board, and program operation status. Monitoring the key components can timely find out whether the terminal program, hardware, and power supply are normal, so as to determine whether the collected information is available and quickly locates the terminal fault.

At the same time, it should be noted that the defects and fault causes of distribution terminals are complex and diverse. This study summarizes and analyzes the key factors causing terminal defects through the fault types and causes counted by the actual power supply company, as shown in Table 1.

In this study, distribution terminal faults are mainly divided into internal causes and external causes. Most of the internal causes are equipment source characteristics, and the external causes are environmental impact characteristics.

As shown in Figure 2, this study first divides the collected data sample set into the corresponding training dataset and test sample set. Then, based on the training sample set, the network model of fault diagnosis of deep Q-network is built until the corresponding iteration conditions are met. Finally, based on the deep Q-network, the terminal state of the distribution network is accurately evaluated and analyzed.

3.2. Distribution Terminal State Feature Extraction. Unlike the primary equipment with special state indicators, the distribution terminal is an electronic equipment with a complex failure mechanism. The characteristic quantities deeply related to various faults are often hidden in the hardware. However, the existing terminal's own state sensing means are lacking, so it is impossible to directly obtain the characteristic quantity reflecting the terminal hardware state like a primary device.

In view of the above situation, this study selects three operation indexes as the state characteristic quantity, namely, abnormal reporting frequency f_{ab}, contradiction reporting frequency f_{con}, and terminal offline frequency f_{off}.

An abnormal report refers to the record describing the abnormality of the terminal body in the alarm event uploaded by the terminal, such as encryption verification failure and battery activation abnormality. The abnormal report frequency can directly reflect the overall operation

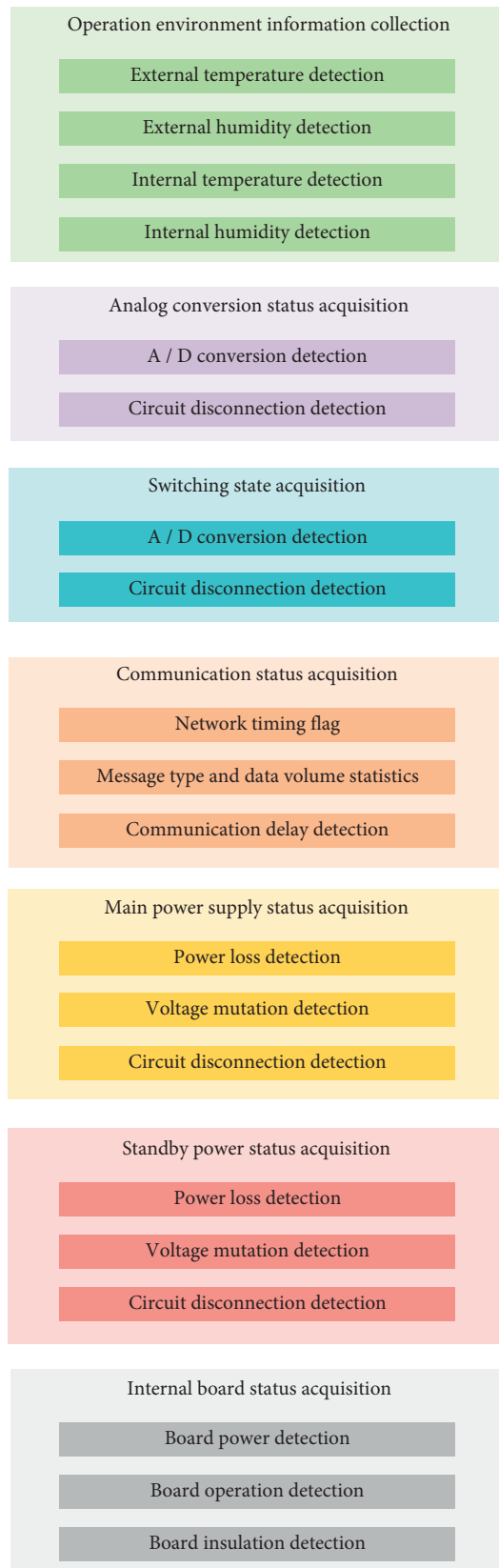

Figure 1: Status detection of distribution terminal.

Table 1: Multidimensional influencing factors of distribution terminal fault.

Type		Project
External factors		Environmental temperature and humidity change Wireless signal quality Power failure Improper human operation Primary equipment impact
Internal factors	Running state	Maintenance history Software running status Equipment upgrade and commissioning
	Maintenance history	Equipment family defects Troubleshooting history Long service life

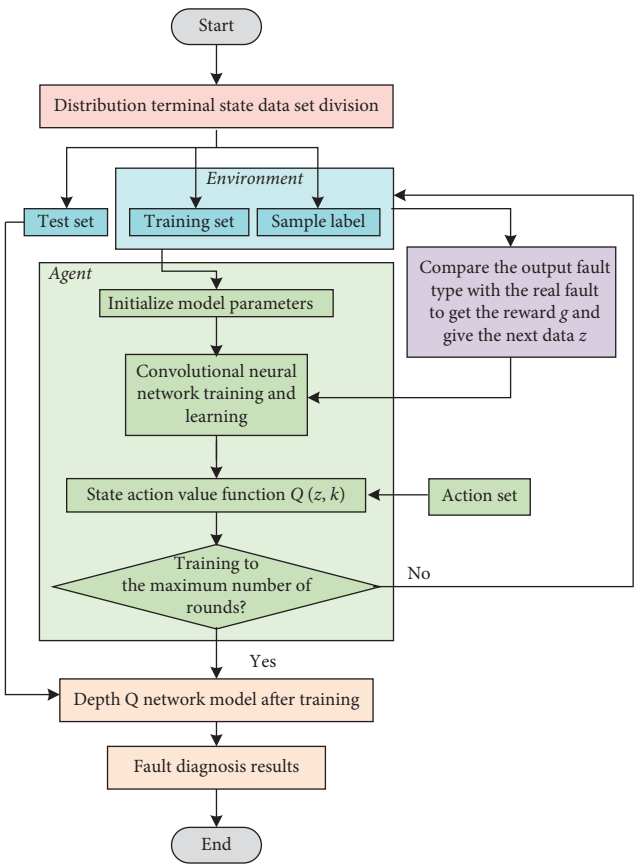

Figure 2: Fault diagnosis flowchart of deep Q-network.

status of the terminal, and its calculation method is shown in equation (1)as follows:

$$f_{ab} = \frac{N_{ab}}{T}, \tag{1}$$

where T represents the statistical duration; N_{ab} indicates the number of abnormal reports within the statistical time.

Some information uploaded by the terminal needs to conform to certain logic; for example, after the terminal power supply line fault trips, it must follow the AC power loss report, etc. If there are too many reports N_{con} that do not conform to the logical relationship within the statistical duration T, it indirectly indicates that the terminal has the trend of failure. Therefore, the frequency of introducing conflict reports is as follows:

$$f_{\text{con}} = \frac{N_{\text{con}}}{T}. \tag{2}$$

A considerable part of terminal faults gradually develops from short-term disconnection to long-term offline. Therefore, the off-line frequency of the terminal also has certain significance for reflecting the terminal state, and its calculation method is shown in equation (3).

$$f_{\text{off}} = \frac{M_{\text{off}}}{T}, \tag{3}$$

where M_{off} represents the number of terminal drops in the statistical time T.

3.3. State Evaluation of Distribution Terminal Based on Deep Reinforcement Learning. Deep reinforcement learning is a trial and error algorithm, which makes the network have both perception ability and decision-making ability. This study realizes the state evaluation of distribution terminals based on a deep reinforcement learning network.

3.3.1. Deep Reinforcement Learning. The research shows that a convolutional neural network has strong feature learning and expression ability, better robustness, and faster calculation speed. It can input the sample dataset into the CNN model for training and use the trained network to distinguish different distribution terminal feature information, so as to achieve high-precision recognition of different states. Therefore, we adopt the basic network structure as the state evaluation network.

The CNN network adopts a cognitive mechanism of imitating biological natural vision.

The rectangular convolution kernel of CNN is used to convolute with the local receptive domain of the input signal, and the convolution check with the same numerical weight is used to scan the input data, so that its parameters can be shared. The mathematical model of convolution operation is as follows:

$$z_{i+1} = u_i \otimes z_i + d_i, \tag{4}$$

where z_i is the current input eigenvector; z_{i+1} represents the eigenvector after convolution calculation; $\otimes$ is the symbol of convolution operation; u_i is the weight of convolution kernel; and d_i is offset.

After the convolution operation is completed, the nonlinear transformation is realized through the activation function to improve the expression ability of the model. The expression is as follows:

$$v_i = f(z_{i+1}). \tag{5}$$

Pooling operation can effectively preserve feature information. In this study, the maximum pool method is used to deal with it, and its mathematical expression is as follows:

$$\begin{aligned} &\text{maxpooling}(f[i-1], f[i], f[i+1]) \\ &= \max(f[i-1], f[i], f[i+1]), \end{aligned} \tag{6}$$

where maxpooling represents the maximum pool(); $f[i]$ is the i value; $f[i-1]$ is the $i-1$ value; $f[i+1]$ is the $i+1$ value; and max indicates the maximum value.

At the same time, we should see that the data collected by the distribution terminal have the characteristics of time series. In order to make the CNN network better extract the characteristic information of the sample dataset, the Markov decision-making method is used to strengthen the network.

The Markov decision process includes four tuples $\langle Z, K, p, g\rangle$, in which Z is a state-space set; $z \in Z$ is a state in the state-space set; K is the action-space set; $k \in K$ is an action in the action-space set; p is the current time state after the action k is executed by the agent: the probability of transforming to the next time state z'; and g is the reward obtained by converting the current time state to the next time state z after the action Z is executed by the agent.

In the fault identification task of this study, the status z is the sample data uploaded by the terminal; action k is the category of the operation state of the distribution terminal; and whether the model recognition result is consistent with the terminal state type is an important standard for awarding g. When the sample type is consistent with the recognition result, g is taken as $+1$; otherwise, g is taken as -1; and for the state transition probability p, although there is no correlation between each state, the training data samples will be randomly disrupted and the number of training data samples will be evenly distributed during network operation. The state transition probability will become $p = 1/R$, in which R is the number of fault categories.

Due to the problems of local minimum and overfitting in the traditional depth neural network, the accuracy of the model after training is not high and the stability is poor. To solve this problem, we choose to add a Q-learning strategy to the deep neural network to enhance the recognition stability.

The fault diagnosis process of the deep Q-network is shown in Figure 2. The model realizes the intelligent fault diagnosis through the interaction between the environment and the agent. First, the environment inputs the initial data z to the agent. After the CNN network fitting, the state-action value function $Q(z, k)$ outputs the action k, compares it with the fault type of data z in the environment, and then gives the agent reward to make the model achieve the expected effect.

3.3.2. State Evaluation of Distribution Terminals. Through the above analysis, we define the sample dataset collected by the distribution terminal as shown in Table 2. At the same time, this study takes it as the input data of the evaluation model of deep reinforcement learning.

Then, the proposed evaluation model is introduced for learning and training. The learning process of the proposed deep reinforcement learning model is as follows:

(1) We initialize the weight parameter τ of the fitting Q-value function;

(2) We repeat the experience track from 1 to UU;

Initialization status (sample data of distribution terminal);

(3) We observe whether the output action is consistent with the sample label corresponding to the fault data in the environment. If it is consistent, $z = +1$; otherwise, $z = -1$;

(4) We input the state z' at the next time and use $y = g + \vartheta \max Q(z', k'; \tau)$ to calculate the target Q-value function y;

(5) The gradient descent algorithm is used to update the network parameters for $(y - Q(z', k'; \tau))^2$.

Figure 3 shows the selected membership function. Considering the complexity of distribution terminal data, the membership function of a triangle combined with the semi-trapezoid is relatively simple and accurate, so this method is used to calculate the membership degree in this study.

The membership function calculation formula of triangle combined with semi-trapezoid is shown in equations (7) to (10).

$$c_1(q) = \begin{cases} 1, & q \le Q_1, \\ \dfrac{Q_2 - q}{Q_2 - Q_1}, & Q_1 < q \le Q_2, \\ 0, & q > Q_2, \end{cases} \tag{7}$$

$$c_2(q) = \begin{cases} \dfrac{q - Q_2}{Q_2 - Q_1}, & Q_1 < q \le Q_2, \\ \dfrac{Q_3 - q}{Q_3 - Q_2}, & Q_2 < q \le Q_3, \\ 0, & \text{else}, \end{cases} \tag{8}$$

Table 2: Distribution terminal status dataset.

Type	Data category	Data number
Operation environment information collection	External temperature detection	z_1
	External humidity detection	z_2
	Internal temperature detection	z_3
	Internal humidity detection	z_4
Analog conversion status acquisition	A/D conversion detection	z_5
	Circuit disconnection detection	z_6
Switching state acquisition	A/D conversion detection	z_7
	Circuit disconnection detection	z_8
Communication status acquisition	Network timing flag	z_9
	Message type	z_{10}
	Communication delay detection	z_{11}
Main power supply status acquisition	Power loss detection	z_{12}
	Voltage mutation detection	z_{13}
	Circuit disconnection detection	z_{14}
Standby power status acquisition	Power loss detection	z_{15}
	Voltage mutation detection	z_{16}
	Circuit disconnection detection	z_{17}
	Residual capacity detection	z_{18}
Internal board status acquisition	Board power detection	z_{19}
	Board operation detection	z_{20}
	Board insulation detection	z_{21}

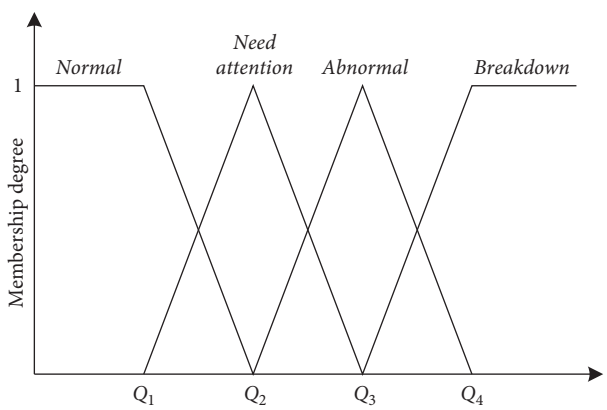

Figure 3: Membership function diagram of a triangle and semi-trapezoid combination.

$$c_3(q) = \begin{cases} \dfrac{q - Q_2}{Q_3 - Q_2}, & Q_2 < q \le Q_3, \\ \dfrac{Q_4 - q}{Q_4 - Q_3}, & Q_3 < q \le Q_4, \\ 0, & \text{else}, \end{cases} \tag{9}$$

$$c_4(q) = \begin{cases} 0, & q \le Q_3, \\ \dfrac{q - Q_3}{Q_4 - Q_3}, & Q_3 < q \le Q_4 \ , \\ 1, & q > Q_4, \end{cases} \tag{10}$$

where q represents the terminal deterioration evaluation value according to the evaluation index; $c_j(q)$ is the membership function under each state evaluation, which is to determine the state evaluation results of distribution terminals.

4. Experiment Analysis

Aiming to present the experimental simulation analysis with the best effect, the experiment is completed on the machine of Ubuntu 16.04 system, and the analysis network is built by relying on the open-source machine learning platform of PyTorch deep learning framework. The specific experimental platform settings are shown in Table 3.

4.1. Experimental Dataset and Evaluation Index. Using the distribution terminal state analysis method proposed in this study, we take the sample dataset of power distribution terminal operation markers collected by a power grid from Electric Power Research Institute (a total of 15000 data, covering 13 terminal-related state quantities) as an example. The sample dataset is divided into training sample dataset and test sample dataset according to the ratio of 4 : 1.

The RMSE indicates the overall reliability of the prediction.

Aiming to quantify the evaluation efficiency, we use the general evaluation index as the indicator of the quality of the results, that is, the root mean square error (RMSE) E_R, and its calculation formula is shown in equation (11)as follows:

$$E_R = \sqrt{\frac{1}{N}\sum_{i=1}^{N}\left(y_i - \hat{y}_i\right)^2}. \tag{11}$$

Table 3: Setting of recognition experimental analysis platform.

Project	Parameter
Operating system	Ubuntu 16.04
CPU	Inter(R) Core(TM) i5-7200 CPU
GPU	GeForce RTX2080 TI
RAM	16 GB
Development language	Python
Development platform	PyTorch
Development tool	PyCharm

4.2. Training Process Analysis of the Proposed Model. In the proposed network model, the convolution kernel size of the first convolution layer is 128×1. The step size is 8, and the larger convolution kernel can effectively extract the characteristics of time-domain signals on a large scale. The second and third convolution layers are used to better extract the deep features of the signal. The size of the convolution kernel is 8×1. The output of the network at this position is pooled, and the layer has local invariance. By using maximum pooling for the output characteristics of convolution, the network can reduce the amount of data while maintaining the essence of the signal. The width of pool nuclei is 5×1, and the step size is 4.

The full-connection layer can connect these features. The full-connection layer can enhance the ability of the network to learn features, including 256 and 32 neurons, respectively.

Aiming to characterize the excellent ability of the improved prediction model, we first compare the traditional CNN network with the improved network. The prediction results can be obtained from Tables 4 and 5.

As shown in Tables 4 and 5, under the same experimental background and network parameters, the network performance of the deep reinforcement learning network model proposed is significantly improved. When the network parameters are set to learning rate = 0.150 and training parameters = 20 000, the network accuracy of the improved CNN prediction model is the best, that is, E_R is 232.99.

In each round of training, the steps of the deep reinforcement learning model proposed in this study are 512 in each round, and a total of 3000 rounds are trained. At the same time, we average the loss value and draw it, as shown in Figure 4.

From Figure 4, we can see that after each round of training, the low accuracy and poor stability of the model after training can be solved due to the addition of a Q-learning strategy so that the evaluation model has good antinoise performance, which can support the loss value of the terminal state analysis model proposed in this study to remain in a relatively low state, indicating that the model can maintain a high learning efficiency in every round of training. Therefore, the feasibility of this method in distribution network terminal state identification analysis is verified.

4.3. Performance Analysis of the Evaluation Model. In order to verify that the distribution terminal state analysis method proposed in this study has the optimal performance of state identification, reference [23] and reference [26] are used as comparison methods to realize simulation experiment analysis in the same operation scenario.

Table 4: Prediction performance of the traditional CNN network.

Learning rate	Training parameters	E_R
0.050	10000	337.36
0.100	10000	312.72
0.150	10000	278.87
0.050	20000	305.25
0.100	20000	299.87
0.150	20000	268.78

Table 5: Prediction performance of the proposed network model.

Learning rate	Training parameters	E_R
0.050	10000	298.01
0.100	10000	286.32
0.150	10000	240.95
0.050	20000	279.19
0.100	20000	257.03
0.150	20000	232.99

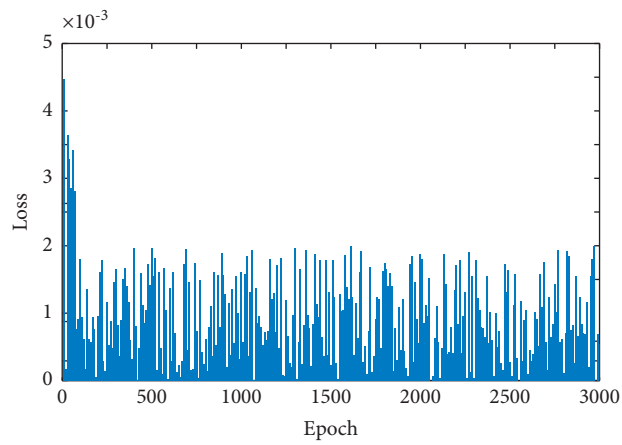

Figure 4: Loss value change curve of the evaluation model.

Figure 5 shows the analysis results of test datasets under different methods.

As shown in Figure 5, the state evaluation performance of the method proposed in this study is better than that of the comparison method. The recognition accuracy of the proposed method is 94.23%, which is 1.1% and 0.9% higher than that of reference [23] and reference [26], respectively. The evaluation index of the proposed method is 249.3, which is 7.96 lower than reference [26] and 12.66 lower than reference [23].

The reason is that reference [23] ignores the time-series characteristics of distribution terminal equipment data, and only roughly extracts and learns the state data from the deep network. However, reference [26] ignores the problem of poor stability of the deep network model, and cannot achieve stable and efficient state evaluation and analysis throughout the cycle.

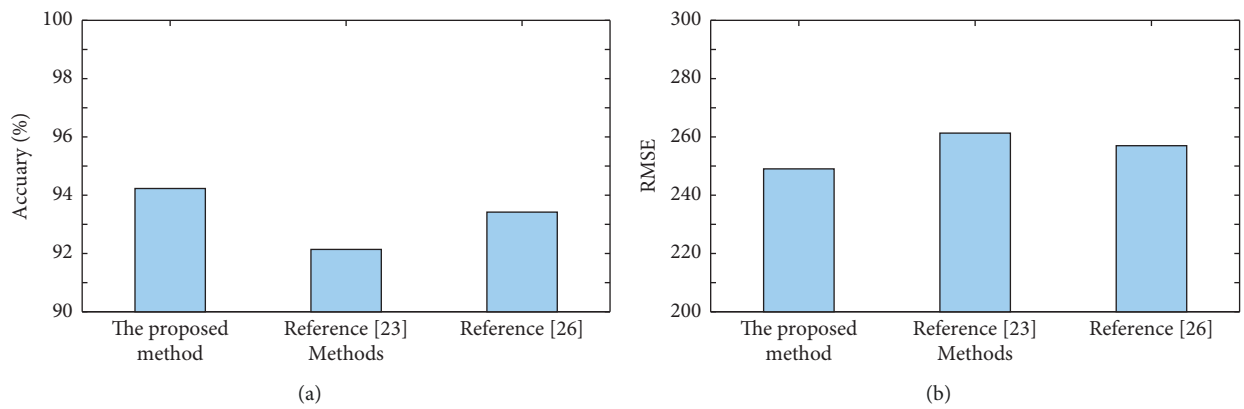

Figure 5: State evaluation diagram of distribution terminal. (a) State recognition accuracy. (b) Root mean square error E_R.

Due to the existence of the Q-reinforcement learning network, the proposed method can enhance the perception and decision-making ability of the network, make the antinoise ability of the state evaluation model better, and can effectively improve the state analysis performance of the model. In addition, the existence of a membership function increases the objectivity and reliability of the terminal state evaluation method so that the proposed distribution terminal state analysis model has better recognition and evaluation ability.

5. Conclusions

Accurately monitoring and evaluating the operation status of distribution terminals are the basic means to realize the safe and reliable operation of the distribution network. Therefore, this study proposes a distribution network state evaluation method using a deep reinforcement learning model. The proposed terminal state evaluation model is composed of the Q-reinforcement learning network and convolutional neural network, which has the strong model antinoise ability and effectively extracts the characteristic information of the sample dataset. At the same time, triangle and semi-trapezoid membership functions are introduced to support the reliability. The simulation experiment is based on the actual sample dataset of the distribution terminal. The experiment proves that the recognition accuracy and root mean square error E_R of the proposed method are 94.23% and 232.99, respectively, which can accurately and stably evaluate the operation status of distribution terminals.

Although the method proposed can accurately identify the distribution station area data l data, its parameters are fixed values, which are difficult to automatically adjust according to the data characteristic information. The next research work is to introduce the parameter adaptive algorithm into the model to enhance the ability of parameter optimization and further improve the evaluation efficiency.

Data Availability

The data used to support the findings of this study are included within the article.

Conflicts of Interest

The authors declare that they have no conflicts of interest.

References

[1] G. J. Xiong, X. F. Yuan, A. W. Mohamed, J. Chen, and J. Zhang, "Improved binary gaining-sharing knowledge-based algorithm with mutation for fault section location in distribution networks," *Journal of Computational Design and Engineering*, vol. 9, no. 2, pp. 393–405, 2022.

[2] G. Y. Chen, W. X. Mo, and H. B. Wang, "Efficient cloud-based digital-physical testing method for feeder automation system in electrical power distribution network," *Archives of Electrical Engineering*, vol. 69, no. 3, pp. 545–559, 2020.

[3] Z. Nie, J. N. Zhang, and H. W. Fu, "Key technologies and application scenario design for making distribution transformer terminal unit being a containerized edge node [J]," *Automation of Electric Power Systems*, vol. 44, no. 3, pp. 154–161, 2020.

[4] S. Chen, S. Liang, and S. Li, "Assessment of Electrical equipment status in distribution network based on multi-source data fusion," *IOP Conference Series: Earth and Environmental Science*, vol. 632, no. 1, pp. 1–6, 2021.

[5] X. Zhang, Y. Tang, and Q. Liu, "A fault analysis method based on association rule mining for distribution terminal unit," *Applied Sciences*, vol. 11, no. 11, pp. 1–14, 2021.

[6] G. Zhang, X. Ji, and Y. Li, "Power-based non-intrusive condition monitoring for terminal device in smart grid," *Sensors*, vol. 20, no. 13, pp. 1–19, 2020.

[7] L. J. Ge, Y. L. Li, and J. Yan, "Smart distribution network situation awareness for high-quality operation and maintenance: a brief review," *Energies*, vol. 15, no. 3, pp. 1–24, 2022.

[8] J. Zhang, H. Wang, and Y. Hu, "Design of intelligent inspection system for distribution network based on circular multi-agent structure," *IOP Conference Series: Earth and Environmental Science*, vol. 218, no. 1, pp. 1–8, 2019.

[9] J. Fang, H. B. Wang, F. A. Yang et al., "A data-driven fault location method in distribution network based on PMU data," *IEEJ Transactions on Electrical and Electronic Engineering*, vol. 17, no. 3, pp. 325–334, 2021.

[10] S. Y. Shao, X. Ma, and W. Yuan, "Research on Construction and Application of Power Distribution Internet of Things," in *Proceedings of the 3rd International Conference on Computer Information Science and Application Technology (CISAT)*,

pp. 1–7, ELECTR NETWORK, Daqing, China, December, 2020.

[11] S.-C. Chu, J. C.-W. Lin, and J. Li, "Genetic and Evolutionary Computing," in *Proceedings of the Fourteenth International Conference on Genetic and Evolutionary Computing (ICGEC)*, Jilin, China, October, 2021.

[12] Y. B. Ye, M. Xie, and T. G. Huang, "A state assessment method for intelligent substation secondary equipment based on grey theory and cloud model," *Power System Protection and Control*, vol. 47, no. 9, pp. 105–111, 2019.

[13] W. Zhang, W. X. Sheng, and S. H. Du, "Architecture and technology implementation of massive data based distribution network operation analysis system," *Automation of Electric Power Systems*, vol. 44, no. 3, pp. 147–153, 2020.

[14] D. Renga, D. Apiletti, D. Giordano et al., "Data-driven exploratory models of an electric distribution network for fault prediction and diagnosis," *Computing*, vol. 102, no. 5, pp. 1199–1211, 2020.

[15] G. Y. Chen, J. J. Li, and Y. Chen, "Data-driven and interactive fault diagnosis of distribution switches," *Advanced Technology of Electrical Engineering and Energy*, vol. 38, no. 3, pp. 10–17, 2019.

[16] H. Sun, G. Zhuang, and B. Gao, "Fuzzy comprehensive evaluation of relay protection equipment status in intelligent substations based on combination weighting method," *Electrical Measurement & Instrumentation*, vol. 57, no. 7, pp. 23–28, 2020.

[17] H. Y. Li, Y. Y. Wang, and X. H. Liang, "Fault Prediction of Power Transformer by Association Rules and Markov," in *Proceedings of the 2018 IEEE International Conference on High Voltage Engineering and Application (ICHVE)*, pp. 1–4, Athens, December, 2018.

[18] W. Huang, J. Chen, and C. Q. Liu, "Research on Line-Loss Correlation Analysis Technology of Distribution Network Based on Apriori Algorithm," in *Proceedings of the 2020 5th Asia Conference on Power and Electrical Engineering (ACPEE)*, pp. 1399–1403, Chengdu, China, August, 2020.

[19] D. Q. Liu, X. J. Zeng, and Y. N. Wang, "Security situation assessment of intelligent distribution transformer terminal unit based on information entropy," *Southern Power System Technology*, vol. 14, no. 1, pp. 18–23, 2020.

[20] K. Zhao, H. K. Jiang, and K. B. Wang, "Joint distribution adaptation network with adversarial learning for rolling bearing fault diagnosis," *Knowledge-Based Systems*, vol. 222, no. 1, pp. 1–12, 2021.

[21] Z. Zhang, W. Jiang, J. Geng, X. Deng, and X. Li, "fault diagnosis based on non-negative sparse constrained deep neural networks and dempster-shafer theory," *IEEE Access*, vol. 8, no. 1, Article ID 18182, 2020.

[22] J. Dai, J. Wang, W. Huang, J. Shi, and Z. Zhu, "Machinery health monitoring based on unsupervised feature learning via generative adversarial networks," *IEEE*, vol. 25, no. 5, pp. 2252–2263, 2020.

[23] C. Xiao, Z. J. Liu, and T. L. Zhang, "Deep learning method for fault detection of wind turbine converter [J]," *Applied Sciences-Basel*, vol. 11, no. 3, pp. 1–22, 2021.

[24] C. Y. Wang, Z. L. Zhen, and T. Y. Liu, "Research on detection method of steam turbine rotor unbalance and misalignment fault based on convolution neural network," *Proceedings of the CSEE*, vol. 41, no. 7, pp. 2417–2426, 2021.

[25] Y. T. Jia, L. M. Ying, D. H. Wang, and J. Zhang, "Defect prediction of relay protection systems based on LSSVM-BNDT," *IEEE Transactions on Industrial Informatics*, vol. 17, no. 1, pp. 710–719, 2021.

[26] F. Xu, X. Shu, X. Li, and X. Zhang, "Data-Driven bearing fault diagnosis of microgrid network power device based on a stacked denoising autoencoder in deep learning and clustering by fast search without data labels," *Complexity*, vol. 2020, no. 1, Article ID 5013871, 29 pages, 2020.

Hindawi
Mathematical Problems in Engineering
Volume 2022, Article ID 1854365, 9 pages
https://doi.org/10.1155/2022/1854365

Research Article

Analysis of Smart Grid Using Multimedia Sensor Networks with Effective Resource Allocation

Yuvaraja Teekaraman,[1] **Irina Kirpichnikova**,[1] **Hariprasath Manoharan**,[2] **Ramya Kuppusamy**,[3] **and Arun Radhakrishnan**[4]

[1]*Faculty of Energy and Power Engineering, South Ural State University, Chelyabinsk 454 080, Russia*
[2]*Department of Electronics and Communication Engineering, Panimalar Institute of Technology, Chennai 600 123, India*
[3]*Department of Electrical and Electronics Engineering, Sri Sairam College of Engineering, Bangalore 562 106, India*
[4]*Faculty of Electrical & Computer Engineering, Jimma Institute of Technology, Jimma University, Jimma, Ethiopia*

Correspondence should be addressed to Yuvaraja Teekaraman; teekaramani@susu.ru and Arun Radhakrishnan; arun.radhakriahnan@ju.edu.et

Received 11 February 2022; Revised 2 March 2022; Accepted 31 March 2022; Published 18 May 2022

Academic Editor: Saeid Jafarzadeh Ghoushchi

In recent days, for smart grid network updates, video sensors are used where each node needs to be compressed before transmission. This is very much useful for developing countries as in future the smart grid communication process will play a major role in entire society. Therefore, in this article, minimization of power, energy consumption, and delay for wireless video sensor networks have been computed by providing better quality of service at a similar period. Also, the problem of optimizing transmission and delivery rate has been studied. For solving the aforementioned problems, the intuitive migrant algorithm has been implemented for providing better energy consumption. Additionally, modified larvae optimization tool has been integrated for providing better convergence rate, where all the nodes will be compressed at a better rate with necessary quality of service. The simulation results show that by applying algorithms in two folds, and each video sensor node is compressed by satisfying necessary constraints with fast convergence rate.

1. Introduction

It is well known that there are a lot of interconnecting devices that have been integrated with personal computers through Internet with secured connection. However, it is not possible to say that these connections will be secured all time because the competency of various objects is surrounding each individual. Therefore, wireless sensor networks (WSN) can be used for both detection and data communication in wireless medium. The WSN in this medium can be regarded as smart object due to its nature, and it can be used by a lot of people all over the world in an apparent way [1]. A lot of emerging technologies have been established following the perception indicated in [1], and they are denoted as Internet of Things (IoT) [2]. Recently, with advancements in image sensors, it is highly possible to create images, where the resolution of image will be higher with less cost. In line with the above concern, it is much possible on creating smart objects for capturing image and video with high-quality pixels [3].

Correspondingly, multimedia content is becoming more popular on Internet, and therefore, it is vital that difficulties on wireless video sensor networks (WVSN) have to be solved by utilizing the energy effectively with common supply. Likewise, the interest on various green energies that transforms the output to expand wireless networks has been emerging with long-term sustainability. This curiosity has made several researchers [4–7] to exploit the green energy by providing sufficient sustainability on entire network. Further, it is discussed [8] that for designing effective WSN to transform energy, resource allocation plays an important role. Correspondingly, WSN supports a wide range of applications by providing diverse quality of service as per

requirements, and it is not possible that each user can access it directly through air transmission [9].

For establishing commercial WSN, each user laptop needs to be connected with hotspot for providing services at different levels by using a particular network with good quality of service such as availability of service, improved bandwidth, and reduction in data loss [10]. Generally, the performance of every network will be measured in terms of bandwidth and latency. For measuring the aforementioned metrics, data bits will be transmitted in a particular time, where each user can predict delivery of data from their end. Identically, an algorithm that is used for allocating the channel defines interference range with corresponding node number for minimizing intrusions [11, 12]. The correlation considering interference using improved game-based channel allocation algorithm has been propounded [13] by placing the target node more closely to interference source.

However, the disadvantage in this model [13] is that it does not follow any actual rule for minimizing interference. Additionally, the same model has been used with Nash equilibrium with a physical model and also considering breadth first channel search algorithm [14, 15]. Both models in [14, 15] form a loss function by providing linkage for achieving maximum throughput. In correlation with the models in [14, 15], a channel allocation strategy for instantaneous data flow in entire network has been proposed [16–18]. Similarly, a wireless channel network for accepting other nodes by utilizing energy efficiently using multiple channels has been established with necessities in negotiating high synchronization time with huge overhead cost [19].

The problem on resource allocation has been handled by providing feedback in OFDM-based mesh networks [20], where designing quantization codebook with equal probability distribution, amount of power distributed, etc. will be considered as parameters for allocating subcarriers by utilizing Lagrange multipliers with restrictions on feedback. Conversely, for supporting traffic in different modules (flexible and inflexible modes), an algorithm on resource allocation is deliberated [21] by providing calculations on first-order Lagrangian techniques in addition to utilities for nonconvex problems, which is finally converted to convex one. This type [21] of problem can be solved using decomposition method by applying it in two folds. At the final stage, integration of the projected resource allocation framework has been accomplished adaptively for both modes. However, the difficulty [21] is that the method does not provide any global solution under different networking conditions.

As an alternative of [21], a bio-inspired method using multihop desynchronization algorithm with time division multiple access has been projected [22], which is entirely based on resource allocation in distributed networks. This type of algorithm is able to calculate data transmission rate that attempts to act as reference source for allocating resources in addition to collision detection. By implementing [22], the problem on hidden nodes in multihop networks is resolved effectively by sharing resources with nodes that are located adjacently. Identical to [21, 22], for providing good performance, a resource-aware task scheduling method is implemented [23] for exploiting weight exponentially with exploitation to track all relevant applications on WSNs. The algorithm integrated in [23] will also track the quality and consumption of energy by using some learning techniques.

Comparatively, the resources have been allocated based on priority for sharing primary resources [24] between multiple networks in wireless medium. Also, the algorithm that has been integrated is premeditated by arranging the mechanisms that adhere to IEEE 802.15.6 standards. By doing this, the entire traffic will be under control with specified parameters. Thus, the transfer rate on each network will be derived based on priority. Furthermore, for monitoring multiple stages in production lines, industrial WSNs are used [25] with cascaded topology by considering necessary characteristics and prerequirements. In this kind of process, minimizing the resource allocation problem has been studied by formulating proper channel allocation problem within each field network.

For proving better quality on robotic images, the author in [26] has applied a sonographic system for ultrasound scan. The primary thought in this type of implementation [26] is that there is no need for any physicians to go for onsite monitoring. Moreover, for accessing and compressing the quality of medical images, a new technique for storing the required information has been anticipated [27–29]. Incorporating the sensor nodes by optimizing the lifetime of ad-hoc networks with energy efficient topology has been discussed [30]. Using the same method [30], effective resources have been allocated to multimedia sensor networks for increasing the throughput with maximized energy [31, 32]. In addition, multipath routing protocols for supporting multimedia data for improving quality of service have been deliberated [33]. Recently, analysis has been carried out in operating characteristics of receiver for designing required prototype, and this type can be extensively used for assessing the performance with adequate support on providing conditions in diagnosis. Ultimately, for significant dynamic range metrics has been assessed in perceptual quality by compressing intensity with individual counting for proportions that are paired. In current generation, a new cognitive model has been designed as an alternative of sensor networks as handheld remote operations can be assured [34]. In the abovementioned model, a Zigbee technology is integrated with high control mechanisms using distinct algorithms where high quality of service is attained. However, the use of cognitive networks in smart grid environment is highly cost effective, and several constraints have to be measured before infrastructure installation process. Therefore, as an alternate to cognitive models, the researchers [35] have suggested introduction of 5G networks as high operation of network speed with edge computing technologies are enabled. By enabling high-speed infrastructure security of smart grid is also transformed as high-end technologies.

1.1. Research Gap and Motivation. Even though high effective measures and resources are allocated for converting the grid to be smart, only few researchers have addressed the problem in a precise way [1–33]. In recent networking structure [34, 35], research gap on smart grid networks with

high cost of installation is observed, and in other developed models, a crucial task on minimization of power with better quality of service with constraints such as distortion and transmission delivery rates has not been solved in an accurate manner. However, all the procedures enumerated [1–33] grieves from any one drawback. Therefore, the entire system thus needs an effective methodology for assimilating the channel model thus satisfying the consistency desires. Therefore, to decipher many challenging errands, the gap has been solved using the integrated system model with IMO algorithm.

As an outcome of providing effectual and high-quality videos by observing the entire network performance, an IMO algorithm that improves the consumption of power through clustering technique has been projected. In the proposed model, a unified assessment will be performed by integrating the algorithms in twofolds for the purpose of increasing power consumption in entire network. Subsequently, the MLO technique has been smeared to compute for fast convergence with less number of parameters.

1.2. Objectives. To the best of author's knowledge, there has been no prior exertion on adjoining the manifold objectives such as minimization of (i) power, (ii) energy consumption of nodes, and (iii) delay and maximization of throughput. Therefore, the prime objective of the proposed exertion is to select best nodes thus satisfying the above-mentioned objectives by integrating the algorithms in twofolds and then applying MLO tool for virtuous decision-making (check for better convergence). In addition, the projected model prominently expands the performance of video in a less computational time even for large networks.

2. Problem Formulation

The proposed method focuses on minimization on consumption of power for video sensors by optimizing both transmitted and encoded power at each node. The channel model with probability outage [3] for such networks can be given from:

$$\text{Power}_{n,m}^{\text{outage}} = 1 - e^{\left(-\delta G_0 w_{nm}/T_n^k\right)}, \tag{1}$$

where $\text{Power}_{n,m}^{\text{outage}}$ represents the probability of outage transmitted from node n to m, δ indicates the signal-to-noise ratio threshold and it is defined according to application of sensors $G0$ designates Gaussian variation in noise, Wnm signifies the distance between the nodes n and m, and T_n^k shows the power transmitted from node n.

For characterizing both success and failure on reception of messages, the outages should be lesser than certain threshold values. For each video node, the messages will be delivered at a rate P_n^e/L_t, which is given in seconds. For video sensors, the distortion will be taken into account with two components (source and channel) where the process will consist of compression and encoding. Thus, distortion of video sensors [2] can be computed from:

$$\text{Distortion}_n^p = \alpha^2 e^{\left(-\eta P_n^e \text{Power}_{n,m}^{2/3}\right)}, \tag{2}$$

where η represents the efficiency of encoding process and $\alpha 2$ signifies average variance on input side.

2.1. Minimization of Power. Another important element that should be resolved for video sensors is the problem of channel distortion where in this case the video frames will be transmitted in a parallel way that causes several errors, while transmission of signals and this type of distortion depend on packet loss rate. In the projected model, first, the information will be passed to sink node. This is done for two path networks in order to make the loss rate almost equal to corresponding outage probabilities. Thus, for ith node, the channel distortion [3] will be calculated from:

$$\text{Channel Distortion}_i = \mu_i \alpha_i \frac{\sigma_i}{1 - \sigma_i}, \tag{3}$$

where μ_i represents the corresponding model parameter that entirely depends on encoding parameters and αi is the average time difference between two frames.

(3) can be modified for calculating entire video distortion as follows:

$$TD_i = \mu_i \alpha_i \left(e^{\varphi d_o} \left(\frac{D_i^{\varphi}}{p_i} \right) - 1 \right). \tag{4}$$

Here, the total distortion represents the sum of distortion caused by both channel and source [12]. Thus,

$$TD_i = \text{Distortion}_i^{\text{source}} + \text{Distortion}_i^{\text{channel}}. \tag{5}$$

The primary objective on minimizing the total power that is consumed by each node can be calculated by optimizing the transmitted and encoded power in addition to source rate at each node. Also, high quality of video can only be achieved if the power consumption is increased at all corresponding nodes, which is not discussed and calculated in [34]. The objective of power minimization is given in:

$$\min p_{i,j} = \left(\sum_{i=1}^{N} P_i^{\text{source}} + P_i^{\text{channel}} \right) + \sum_{j=1}^{N} P_j^{\text{channel}}. \tag{6}$$

In case if node priority is considered, then the nodes will be ranked based on weighted sum as given in Equation (6) and is subject to the following constraints.

2.1.1. Total Distortion. For minimizing the power that is consumed by each node, the distortion at transmitter, channel, and receiver end should always be low. In the proposed method, the threshold distortion value for real set of data will be given as input, and if any deviation (error) occurs, then there is a need to increase the power of sensor nodes. (7) indicates that the total distortion must be always less than or equal to threshold distortion [3].

$$\text{Distortion}_i^{\text{source}} + \text{Distortion}_i^{\text{channel}} \leq \text{Distortion}_i^t, \tag{7}$$

where distortion^t represents the threshold at ith node.

2.1.2. Transmission Rate

$$TR_i^{\text{source}} \leq z_i TR_i^{\max}, \tag{8}$$

where $TR^{\max}$ represents the maximum transmission rate and (8) indicates that the source transmission rate should be less than or equal to maximum transmission rate.

2.1.3. Constraint Based on Sensor Node. (9) specifies that for each sensor node set of constraints will be implemented. The sensor node set is indicated by Z_i, and it should not be greater than 1. If any interference occurs in sensor nodes, then that node will not be allowed for transmitting the information in same channel.

$$\sum_{i=1}^{N} Z_i \leq 1, \tag{9}$$

where Z_i represents the set of nodes and the nodes that are interfering cannot be transmitted in same channel.

2.1.4. Decision Variables. In the proposed method, the decision variables are used for defining the major objective, which is called power factor of sensors. In decision variables, maximum power will be predefined as input and it should not go beyond specified threshold value. It can be seen from (10) that the power transmitted at source and channel should not go beyond least value (zero).

$$P_i^{\text{source}}, P_i^{\text{channel}}, P_j^{\text{channel}}, TR_i \geq 0. \tag{10}$$

2.2. Quality of Service

2.2.1. Delivery Rate. Combinations of both variable and invariable traffic will be generated while transmission and compression of video where the sensor inclines to behave badly if it is heterogeneous in nature. Due to this, the data rate will be affected that does not make the constraints (equations (8)–(10)) satisfied. In case of variable traffic of the data rate is lesser than the required rate, then all invariable traffic will reach zero, and this will not satisfy the constraint as given in (10). Therefore, the quality of service is an important factor while testing the efficiency of multiple services.

$$DQ_i\left(\left[p_i^t - P_i^t, p_i^t\right]\right) = \frac{RA_i\left(\left[p_i^t - P_i^t, p_i^t\right]\right)}{RV_i\left(\left[p_i^t - P_i^t, p_i^t\right]\right)}, \tag{11}$$

where DQ_i represents the delivery rate during certain time period, RA_i indicates the packets that is sent to node, and i RV_i designates the number of valid packets.

2.2.2. Energy. There are lots of probabilities of producing error while compressing the video using required sensors. In such cases, the energy should be as high as possible; therefore, the efficiency of entire network can be automatically improved and is given in (12). In the proposed method, if video has been compressed at transmitter end, then energy transmitted through channel should always be higher. If the node energy is higher, the quality of service at the receiver end will be much higher. Therefore, for this process, energy will be sensed, and it will be informed at the transmitter where the sensed energy at the transmitter will be sent to the receiver as shown in:

$$\text{Total Energy}_i = \begin{cases} \text{Energy}_{\text{sense}} + \text{Energy}_{\text{transmiited}} \text{if energy is sensed from node } i, \\ \text{Energy}_{\text{transmitted}} + \text{Energy}_{\text{recieved}} \text{if } z \in Z_i, \\ 0, \text{Otherwise.} \end{cases} \tag{12}$$

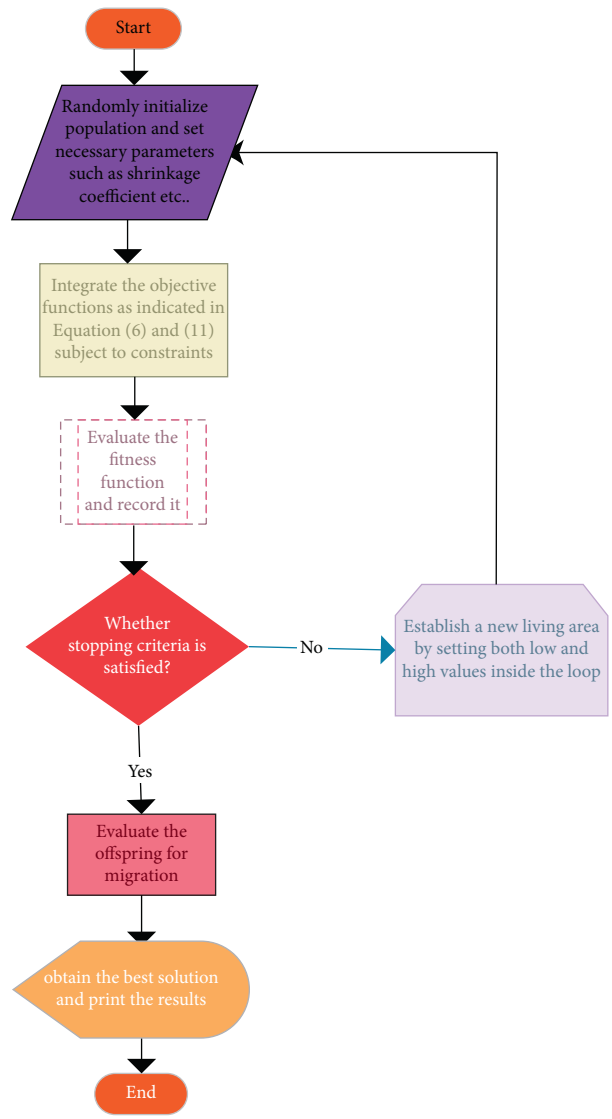

Figure 1: Implementation of IMA for smart surveillance.

3. Optimization Algorithms

The foremost advantage of the proposed model is that it minimizes the power by maintaining good quality of service that is not focused on existing literature. Therefore, for

analyzing the performance of projected model, the algorithms are integrated in two folds. In first phase, an intuitive migrant algorithm (IMA) is applied for improving consumption of energy through clustering techniques. In second stage, modified larvae optimization (MLO) algorithm is integrated for allocating resources to multiple users [36].

3.1. IMA for Smart Surveillance. IMA is one of the famous algorithms that is considered for optimization problems. This type of nature-inspired algorithm will search for optimum solutions within less computational time. Here, the main role of IMA is that during migration it should mimic the behavior of animals for searching best food and shelter. In general, there are two important steps in IMA, and they are as follows:

(i) Migration by replacing the existing location with newer ones

(ii) Updating the population

In step 1, if the animal changes from one position to other, then it must obey three rules they are (i) collision prevention, (ii) moving in same direction, and (iii) endure closer. During migration, there is a chance of adding new animals if existing ones gets unrestrained. Finally, if the topology is created, then a random neighbor will be selected and each individual position will be updated by following equation (13), and the implementation flow chart is shown in Figure 1.

$$NP(i+1) = NP(i) + \eta\left(CP_i^{\text{neighbourhood}} - CP_i\right), \tag{13}$$

where $NP(i+1)$ and $NP(i)$ represents old and new positions of ith individual and CP_i indicates the current position of ith individual.

As shown in Figure 1, the process of relocation and population updating is necessary for finding an optimal solution. After integrating the objective functions, each individual with best fitness value is established and then they are migrated from one location to other. At the first stage, if there are i number of animals that are doing their random process, then the best position is calculated. However, as the process continues, the amount of work that the animals are doing gradually reduces; therefore, the animals should be migrated to other areas, which are having high amount of natural components. The global optimal solution thus obtained nearby is always treated as best solution (current solution). After executing each iteration, the area will be reduced further and as a result acceleration process will be started for determining convergence and to test precise nature of the algorithm. The boundary values can be calculated using:

$$\begin{aligned} \text{low}_i &= CS_{\text{best}} - LAR, \\ \text{up}_i &= CS_{\text{best}} + LAR, \end{aligned} \tag{14}$$

where CS_{best} represents the best current solution and LAR signifies the amount of radius.

Since both upper and lower boundaries are provided ((14)), the intuitive migrant algorithm has the ability to converge earlier. In other algorithms for each sensor nodes, there will be no boundary conditions, and the loop will execute constantly where the convergence time will be much higher. However, due to best fitness value in the search space and boundary conditions of sensor nodes, the algorithm will converge earlier. The best individual in each case is obtained by calculating the fitness function as given in:

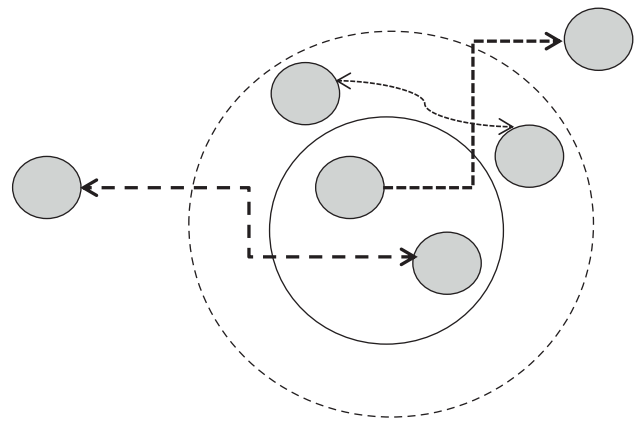

Figure 2: Expansion and migration of larvae.

$$\text{fitness}_i^{\text{best}} = \sum_{i=1}^{N} \min \left\| x_i - d_i \right\|^2, \tag{15}$$

where d_i represents the distance between two individuals.

3.2. Modified Larvae Optimization. The primary advantage on integrating MLO is that it has only less parameters and it is able to achieve convergence at the earliest. This type of algorithm is mainly observed for all routing, sensor problems, etc. and in line with the above concern the MLO has been integrated as second fold in this article. At the starting stage, each larvae will start exchanging the necessary information by updating its position during each iteration. This is done by sending a short beam to all its neighbors that are positioned within the search space. At the same time, each larvae will start moving from one position to another to choose the best one.

In MLO, each individual attraction is proportional to intensity and also it is inversely proportional to distance between them, which is given in:

$$Z_i^l = (1-\delta) Z_i (l-1) + \mu J\left(y_i^l\right), \tag{16}$$

where y_i represents the position of yth individual separated by a distance l at regular time intervals μ that indicates the corresponding updating coefficient.

Following (16), the position of each individual is updated as

$$Z_{i+1}^l = Z_j^l + r\left(\frac{Z_i - Z_j}{\left\| Z_i - Z_j \right\|}\right). \tag{17}$$

If the number of individuals is high, then the local solution will be affected since concentration of each individual

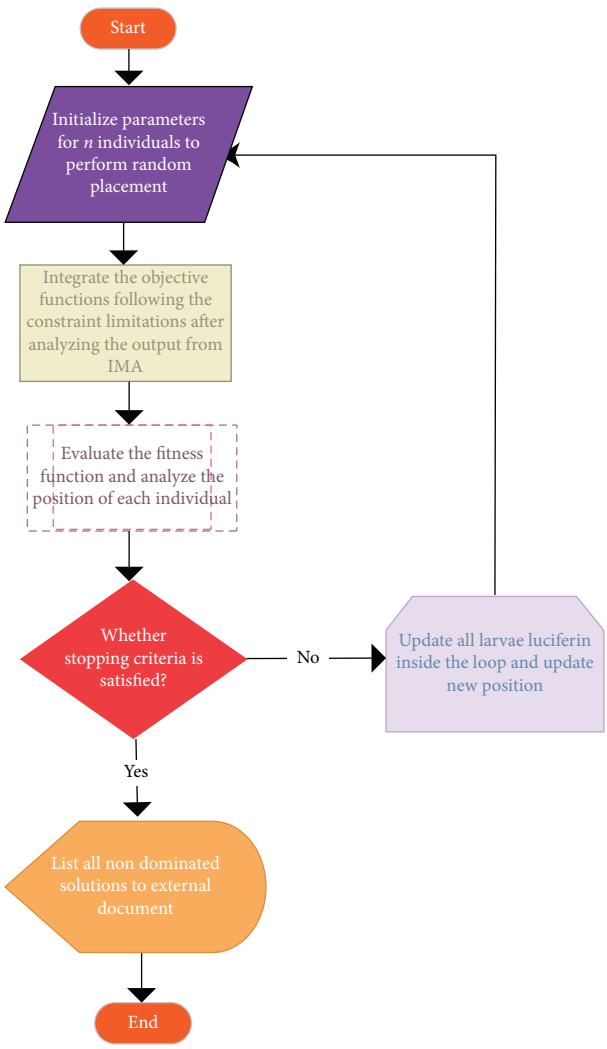

Figure 3: Integration of MLO for better convergence.

tends to lower its neighboring radius. So if the density is high, then it directly reflects the radius range that will be reduced at the final stage as shown in Figure 2. Moreover, in MLO, the larvae will be ranked in a particular order for calculating the fitness value as shown in Figure 3, which includes both coding and decoding schemes with varying step values. Both schemes are preferred for reducing the difficulties where the constraints will not be considered at this stage. The reason behind such considerations is to improve the efficiency of the proposed model. At initial stage, both upper and lower bounds are assigned by following the description on finding the first node for calculating the fitness value.

4. Results and Discussion

The outcome of the proposed MLO algorithm is examined using different test conditions. The transmission range of sensor nodes is 100 m and sensing range is 30 m. The initial energy of sensor nodes is 1.4 to 4.9 Mbps, the initial power consumption of transmitting circuit is 0.51 W, and the receiving circuit is 0.25 W, as indicated in Table 1. The performance of the proposed method is compared with the existing [31, 32] methods by considering four parametric scenarios.

Table 1: Simulation parameters.

Parameters	Values
Number of nodes	10 to 100
Data rate	516 to 994 bits per second
Network area	$103 \times 103\ m^2$
Energy of sensor nodes	1.4 to 4.9 mbps
Initial power consumption of transmitting circuit	0.51 W
Initial power consumption of receiving circuit	0.25 W

4.1. Scenario 1. In this scenario, the power supplied to the sensor nodes has been calculated from (1). Figure 4 shows the calculation of power where the number of sensor nodes has been varied from 10 to 100. It can be seen from Figure 4 that power supplied to the sensor nodes in the proposed method is much lesser than the existing method [31]. For example, if the number of sensor node is 40, then power supplied will be 0.25 W, whereas for existing method [31], the power will be much higher that is equal to 0.56 W. Also, the power supplied in the proposed method will become constant during less sensor nodes implementation (equal to 40), but for the existing method [31], power will become constant at high sensor node implementation that is equal to 70. This proves that the proposed method with MLO proves to be more efficient in terms of power.

4.2. Scenario 2. In this scenario, energy saving of each sensor node that is one of the important parameter in wireless networks is calculated from equation (12) and is simulated. For a virtuous sensor, energy consumed by each node should be as low as possible. Figure 5 specifies the energy consumption where for each sensor node separate energy values are calculated. It can be seen from Figure 5 that proposed method conserves very less energy when compared to the existing method [31]. For example, if the number of sensor node is 60, then the energy consumed by the proposed method will be 3.1 megabits per second, whereas for the existing method [31], it is 4.2 megabits per second. This proves that energy consumed from transmitter to receiver is much lesser in the proposed method than the existing method [31].

4.3. Scenario 3. Once the energy consumed by sensor nodes is low, then it is also necessary that the delay of each node should be lesser. Delay can be defined as the amount of time required for each aggregated data to reach the receiver. Figure 6 represents the delay caused by channel that is represented in milliseconds. For a good data network, the delay should be lesser that is obtained by the proposed method. It can be seen from Figure 6 that the delay caused by the proposed method for transmitting the data during each

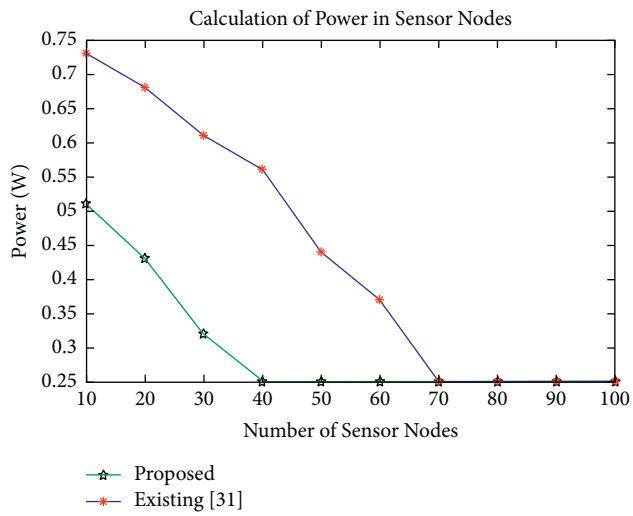

Figure 4: Calculation of power in sensor nodes.

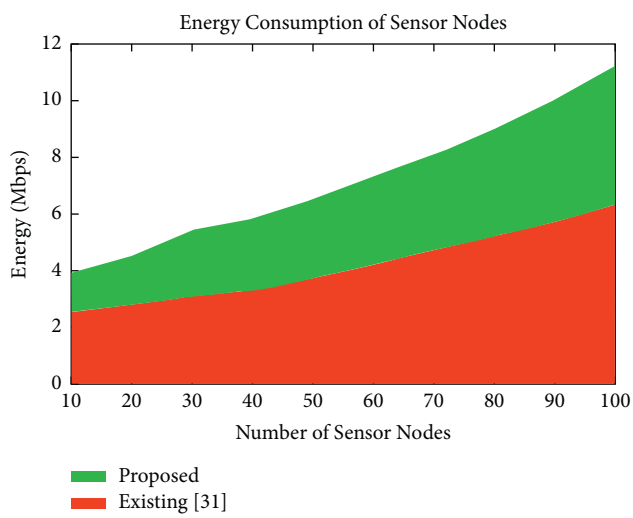

Figure 5: Energy consumption of sensor nodes.

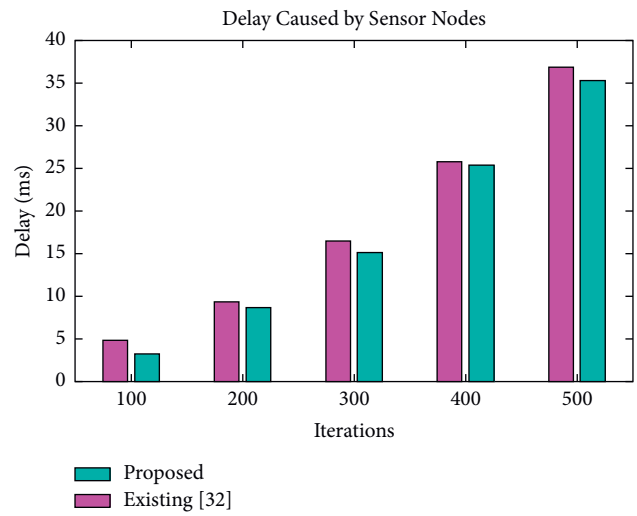

Figure 6: Calculation of delay.

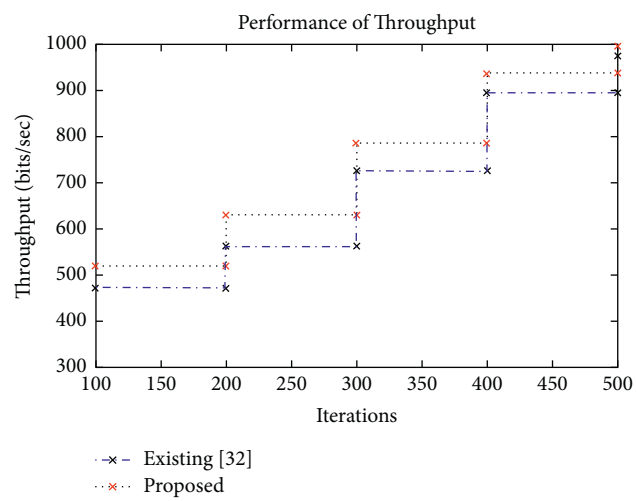

Figure 7: Performance of throughput.

iteration is much lesser when compared to the existing method [32]. For example, if iteration is equal to 300, then data sent from transmitter to receiver will suffer by a delay of 15 ms, whereas for existing method, the data delay will be higher that is equal to 16.5 ms. This proves that projected method proves to be more efficient in terms of delay.

4.4. Scenario 4. After minimizing all necessary parameters such as energy consumption, delay, and power, the throughput of entire network will be automatically maximized. Figure 7 shows the performance of throughput, which is represented in bits per second. The step values obtained during each iteration proves that throughput from transmitter to receiver and vice versa is much higher in the proposed method than the existing method [32]. It can be seen from Figure 7 that each iteration is increased to a much higher extent. For example, if iteration is equal to 300, then throughput for proposed method will be 783 bits per second, whereas for existing method it is lesser that is equal to 724 bits per second. This scenario proves that throughput of multimedia data networks is maximized at higher extent.

5. Conclusions

In this article, an investigation has been carried out for compressing video sensor nodes by minimizing the power in smart grid communication networks thus retaining necessary quality of service constraints. This novel technique has been carried out to meet the demand of future updating smart grid networks. If the nodes are properly compressed, then the need of virtual reality applications will be satisfied. An efficient algorithm that provides better energy consumption and fast convergence rate has been applied in twofold. The simulation results have been compared with other existing techniques where very low throughput with high power and energy consumption of nodes has been achieved [31, 32]. However, the projected method achieves

better quality of service (Throughput) with less power and energy consumption.

Furthermore, the proposed model will be able to support more number of users (nodes) without any reduction in efficiency. In future, the proposed work can be extended by using wireless nodes to monitor smart cities without any attack from external sources, and the delivery of data will be maximized from the transmitter end.

5.1. Policy Implications. The proposed multimedia video sensors can be applied in industry 4.0 for monitoring the following.

(i) Presence and absence of surrounding objects

(ii) Record measurements in production units, and

(iii) Checking the quality of products

Data Availability

The data used to support the findings of this study are available from the corresponding author upon request.

Conflicts of Interest

The authors declare that they have no conflicts of interest.

References

[1] H. Arjmandi and F. Lahouti, "Resource optimized distributed source coding for complexity constrained data gathering wireless sensor networks," *IEEE Sensors Journal*, vol. 11, no. 9, pp. 2094–2101, 2011.

[2] P. Del Fiorentino, C. Vitiello, V. Lottici et al., "Resource allocation in short packets BIC-UFMC transmission for Internet of Things," *Proceedings of the IEEE Globecom Work GC Wkshps 2016*, , Washington, DC, USA, December 2016.

[3] Z. He and W. Dapeng, "Resource allocation and performance analysis of wireless video sensors," *IEEE Transactions on Circuits and Systems for Video Technology*, vol. 16, no. 5, pp. 590–599, 2006.

[4] J. Zou, H. Xiong, C. Li, R. Zhang, and Z. He, "Lifetime and distortion optimization with joint source/channel rate adaptation and network coding-based error control in wireless video sensor networks," *IEEE Transactions on Vehicular Technology*, vol. 60, no. 3, pp. 1182–1194, 2011.

[5] C. Li, J. Zou, H. Xiong, and C. W. Chen, "Joint coding/routing optimization for distributed video sources in wireless visual sensor networks," *IEEE Transactions on Circuits and Systems for Video Technology*, vol. 21, no. 2, pp. 141–155, 2011.

[6] M. Imran, K. Khursheed, N. Lawal, M. O'Nils, and N. Ahmad, "Implementation of wireless vision sensor node for characterization of particles in fluids," *IEEE Transactions on Circuits and Systems for Video Technology*, vol. 22, no. 11, pp. 1634–1643, 2012.

[7] M. Imran, N. Ahmad, K. Khursheed, M. A. Waheed, N. Lawal, and M. O'Nils, "Implementation of wireless vision sensor node with a lightweight bi-level video coding," *IEEE Journal on Emerging and Selected Topics in Circuits and Systems*, vol. 3, no. 2, pp. 198–209, 2013.

[8] X. Lu, P. Wang, D. Niyato, and Z. Han, "Resource allocation in wireless networks with RF energy harvesting and transfer," *IEEE Network*, vol. 29, no. 6, pp. 68–75, 2015.

[9] P. D. Diamantoulakis, *Resource Allocation in Wireless Networks with Energy Constraints*, pp. 68–75, 2018.

[10] I. Loumiotis, T. Stamatiadi, E. Adamopoulou, K. Demestichas, and E. Sykas, "Dynamic backhaul resource allocation in wireless networks using artificial neural networks," *Electronics Letters*, vol. 49, no. 8, pp. 539–541, 2013.

[11] M. Peltomaki, J. M. Koljonen, O. Tirkkonen, and M. Alava, "Algorithms for self-organized resource allocation in wireless networks," *IEEE Transactions on Vehicular Technology*, vol. 61, no. 1, pp. 346–359, 2012.

[12] R. J. J. Green, H. Joshi, M. D. D. Higgins, and M. S. S. Leeson, "Recent developments in indoor optical wireless [Optical wireless communications]," *IET Communications*, vol. 2, pp. 3–10, 2008.

[13] N. Dowler and C. J. Hall, "Safety issues in telesurgery - summary," *IEE Colloquium on `Towards Telesurgery'*, , London, UK, June 1995.

[14] Y. B. Choi, J. S. Krause, H. Seo, K. Capitan, and C. Kyusuk, "Telemedicine in the USA: standardization through information management and technical applications," *IEEE Communications Magazine*, vol. 44, no. 4, pp. 41–48, 2006.

[15] R. S. H. Istepanian, E. Jovanov, and Y. T. Zhang, "Guest editorial introduction to the special section on M-health: beyond seamless mobility and global wireless health-care connectivity," *IEEE Transactions on Information Technology in Biomedicine*, vol. 8, no. 4, pp. 405–414, 2004.

[16] N. Golmie, D. Cypher, and O. Rebala, "Performance analysis of low rate wireless technologies for medical applications," *Computer Communications*, vol. 28, no. 10, pp. 1266–1275, 2005.

[17] S. Sneha and U. Varshney, "Enabling ubiquitous patient monitoring: model, decision protocols, opportunities and challenges," *Decision Support Systems*, vol. 46, no. 3, pp. 606–619, 2009.

[18] D. J. Vergados, D. D. Vergados, and I. Maglogiannis, "NGL03-6: applying wireless DiffServ for QoS pmet," *IEEE Globecom 2006*, pp. 4–8, 2006.

[19] D. Cypher, N. Chevrollier, N. Montavont, and N. Golmie, "Prevailing over wires in healthcare environments: benefits and challenges," *IEEE Communications Magazine*, vol. 44, no. 4, pp. 56–63, 2006.

[20] J. Esch, "A Survey on ambient intelligence in healthcare," *Proceedings of the IEEE*, vol. 101, no. 12, pp. 2467–2469, 2013.

[21] L. Xu, Y. Yang, and Y. Li, "Resource allocation of limited feedback in clustered wireless mesh networks," *Wireless Personal Communications*, vol. 75, no. 2, pp. 901–913, 2014.

[22] B. Q. Han, G. F. Feng, and Y. F. Chen, "Heterogeneous resource allocation algorithm for ad hoc networks with utility fairness," *International Journal of Distributed Sensor Networks*, vol. 11, no. 1, Article ID 686189, 2015.

[23] Y. J. Kim, H. H. Choi, and J. R. Lee, "A bioinspired fair resource-allocation algorithm for TDMA-based distributed sensor networks for IoT," *International Journal of Distributed Sensor Networks*, vol. 12, no. 4, Article ID 7296359, 2016.

[24] M. I. Khan, "Resource-aware task scheduling by an adversarial bandit solver method in wireless sensor networks," *EURASIP Journal on Wireless Communications and Networking*, vol. 2016, no. 1, p. 10, 2016.

[25] S. Kim and B. K. Song, "A prioritized resource allocation algorithm for multiple wireless body area networks," *Wireless Networks*, vol. 23, no. 3, pp. 727–735, 2017.

[26] F. Lin, C. Chen, T. He, K. Ma, and X. Guan, "A separation principle for resource allocation in industrial wireless sensor

networks," *Wireless Networks*, vol. 23, no. 3, pp. 805–818, 2017.

[27] R. S. H. Istepanian, N. Philip, M. G. Martini, N. Amso, and P. Shorvon, "Subjective and objective quality assessment in wireless teleultrasonography imaging," in *Proceedings of the 30th Annual International Conference of the IEEE Engineering in Medicine and Biology Society*, pp. 5346–5349, Vancouver, BC, Canada, August 2008.

[28] K. Vidhya and S. Shenbagadevi, "Performance analysis of medical image compression," in *Proceedings of the International Conference Signal Process Syst ICSPS*, Kathmundu, Nepal, November 2009.

[29] A. Arar, A. Mohamed, A. A. El-Sherif, and V. C. M. Leung, "Optimal resource allocation for green and clustered video sensor networks," *IEEE Systems Journal*, vol. 12, no. 3, pp. 2117–2128, 2018.

[30] P. Yan, S. Choudhury, F. Al-Turjman, and I. Al-Oqily, "An energy-efficient topology control algorithm for optimizing the lifetime of wireless ad-hoc IoT networks in 5G and B5G," *Computer Communications*, vol. 159, pp. 83–96, 2020.

[31] F. Al-Turjman, B. D. Deebak, and L. Mostarda, "Energy aware resource allocation in multi-hop multimedia routing via the smart edge device," *IEEE Access*, vol. 7, Article ID 151203, 2019.

[32] F. Al-Turjman, M. Z. Hasan, and H. Al-Rizzo, "Task scheduling in cloud-based survivability applications using swarm optimization in IoT," *Transactions on Emerging Telecommunications Technologies*, vol. 30, no. 8, pp. 1–20, 2019.

[33] M. Z. Hasan, H. Al-Rizzo, and F. Al-Turjman, "A survey on multipath routing protocols for QoS assurances in real-time wireless multimedia sensor networks," *IEEE Commun Surv Tutorials*, vol. 19, no. 3, pp. 1424–1456, 2017.

[34] E. Ogbodo, D. Dorrell, and A. Abu-Mahfouz, "Energy-efficient distributed heterogeneous clustered spectrum-aware cognitive radio sensor network for guaranteed quality of service in smart grid," *International Journal of Distributed Sensor Networks*, vol. 17, no. 7, Article ID 155014772110283, 2021.

[35] R. Borgaonkar, I. Anne Tøndel, M. Zenebe Degefa, and M. Gilje Jaatun, "Improving smart grid security through 5G enabled IoT and edge computing," *Concurrency and Computation: Practice and Experience*, vol. 33, no. 18, pp. 1–16, 2021.

[36] X. Li, J. Zhang, and M. Yin, "Animal migration optimization: an optimization algorithm inspired by animal migration behavior," *Neural Computing & Applications*, vol. 24, no. 7-8, pp. 1867–1877, 2014.

Hindawi
Mathematical Problems in Engineering
Volume 2022, Article ID 1259131, 11 pages
https://doi.org/10.1155/2022/1259131

Research Article

Specific Surface Area Characterization of Spinel Ferrite Nanostructure Based Compounds for Photocatalysis and Other Applications Using Extreme Learning Machine Method

Miloud Souiyah,[1] Taoreed O. Owolabi,[2] Saibu Saliu,[2] Talal F. Qahtan,[3] Nahier Aldhafferi,[4] and Abdullah Alqahtani[4]

[1]*Department of Mechanical Engineering, College of Engineering, University of Hafr Al Batin, P.O. Box 1803, Hafr Al Batin 31991, Saudi Arabia*
[2]*Physics and Electronics Department, Adekunle Ajasin University, Akungba Akoko 342111, Ondo State, Nigeria*
[3]*Physics Department, College of Science and Humanities in Al-Kharj, Prince Sattam Bin Abdulaziz University, Al-Kharj 11942, Saudi Arabia*
[4]*Computer Information Systems Department, College of Computer Science and Information Technology, Imam Abdulrahman Bin Faisal University, Dammam 31441, Saudi Arabia*

Correspondence should be addressed to Taoreed O. Owolabi; owolabitaoreedolakunle@gmail.com

Received 11 February 2022; Revised 15 March 2022; Accepted 9 April 2022; Published 26 April 2022

Academic Editor: Ramin Ranjbarzadeh

Nanocrystalline spinel ferrite based compounds are technological driven materials with interesting potentials in photocatalysis for renewable energy generation, gas sensing for pollution control, magnetic drug delivery, rod antennas, storage media (high density) and supercapacitive materials, among others. Specific surface area of spinel ferrite based compounds contributes immensely to the application of this semiconductor in industrial domains. Experimental determination of specific surface area is laborious and costly and consumes appreciable time. Compositional substitutions in crystal structure effectively improve physical properties and enhance specific surface area through alteration of moment distribution between tetrahedral oxygen sites and octahedral coordination. With the aid of distorted lattice parameters due to compositional substitution and the spinel ferrite nanocrystallite size as model descriptors, this present work models the specific surface area of spinel ferrite nanomaterial through extreme learning machine (ELM) based intelligent modeling method. The developed sigmoid activation function-based ELM (S-ELM) model shows superior performance over genetic algorithm based support vector regression (GBSVR) and stepwise regression (STWR) models existing in the literature with performance improvement of 61.31% and 70.01%, respectively, using root mean square error performance metric. The significances of cobalt and lanthanum compositional substitution on the specific surface area of spinel ferrite nanomaterials were investigated using S-ELM model. Ease of implementation of S-ELM model as compared with the existing GBSVR model, coupled with the demonstrated improved performance and persistent closeness of its predictions with the experimental values, would be highly meritorious for quick and precise characterization of specific surface area of spinel ferrite nanomaterials for various desired applications.

1. Introduction

Spinel ferrite nanomaterials have recently attracted significant attention due to their unique and fascinating chemical, physical, magnetic, electrical, and optical properties [1, 2]. These properties are useful in a variety of technological advancements and applications, which include photocatalysis for renewable energy generation [3], cancer treatment [4], agents for antibacterial [5], electromagnets [6], gas sensors, biomedicine [7], switching devices [8], drug delivery [9, 10], magnetic recording [11], water splitting [12], magnetic resonance imaging [13], multilayer chip inductors

[14], supercapacitors [15], and spintronics, among others. Recent significant attention on nanomaterial based magnetic materials such as spinel ferrite nanomaterials can be attributed to their unique properties, which include the ability to adjust their optical, structural, magnetic, and electronic properties through doping as well as vacancy creation [16–19]. By altering the size, shape, manufacturing technique, dopant ions, and their concentration, various physical properties of a system containing nanoparticles can be changed [20–22]. Large specific surface area, excellent calcination ability, quantum confinement effect, and smaller crystal size render spinel ferrite based compound indispensable for many applications [23]. The size difference between a nanoparticle and its surface area is a vital aspect of nanotechnology since the smallest particle has a characteristic larger surface area. The inverse relation between the size of the nanoparticle and the surface area creates a dramatic change between the electronic structure of the bulk particle and that of the nanoparticle [24]. This work employs crystallite size and lattice distortion to model the specific surface area of spinel ferrite nanomaterial.

The ferrite family is classified as garnets, hexagonal, and spinel ferrite using crystal structure as a criterion [25]. Spinel ferrites are distinguished from other ferrite family members by their distinctive features, which have led to their deployment for many technological applications [9, 26, 27]. Spinel ferrites have the general chemical formula MFe_2O_4, with M denoting divalent ions such as Fe^{2+}, Co^{2+}, Zn^{2+}, Mg^{2+}, Mn^{2+}, and Ni^{2+}, among others [28]. There are two types of interstitial sites characterizing spinel crystal structure: the tetrahedral (A) and octahedral (B) sites. Spinel can further be grouped into three categories based on its crystal structure: inverse spinel, normal spinel, and complex spinel [29]. Fe(III) and M(II) occupy octahedral sites and tetrahedral, respectively, in normal spinel, and ZnFe2O4 is a typical example [30]. Because the interstitials of octahedral sites are often larger than those of tetrahedral sites, cations with lesser radii are more likely to be found at M sites. In contrast, those with larger radii are more likely to be found at Fe(III) sites. In inverse spinel, half of the Fe(III) is located in tetrahedral sites, whereas the M(II) and the remaining Fe(III) are found in octahedral sites, such as NiFe2O4 [31]. In complex spinel, M(II) and Fe(III) occupy tetrahedral and octahedral sites in a random order [12]. The features of spinel ferrites are compositional dependence, distribution of cations over sites available, and their preparation techniques [32]. To enhance their specific surface area for the desired application, several metal ions, including Ni, Gd, Sr, Zn, Co, Cd, etc., have been used to dope ferrite nanoparticles [25, 33–39], which alter the crystal lattice properties of the spinel ferrite at various nanoparticle sizes. The crystallite size and lattice parameter are utilized in this work to model specific surface area of spinel ferrite through an intelligent algorithm based on an extreme learning machine.

Extreme learning machine (ELM) is an enhanced version of a single hidden layer feedforward network with conventional potentials to adjust network weights (such as the output and input weights) and biases using traditional gradient descent approach [40, 41]. However, this approach consumes appreciable training time with characteristic less efficiency [42]. Extreme learning machine algorithm trains single hidden layer feedforward network using amazing trick in which the values of the biases and input weights are chosen randomly and arbitrarily. Hence, generalized inverse operation is purposely employed for output weight computation to minimize the generalized error while the system becomes simplified as linear systems [43]. Moreover, the ELM algorithm determines only the output weight with the circumvention of a descent-based approach known to be slow. Therefore, the computational techniques utilized by ELM algorithm lead to minimized training error, reduced computational time, and enhanced generalization ability due to minimization of output weight norm. These unique features of ELM algorithm have widened its application domain in varieties of fields and specialization [44–47]. The uniqueness of ELM algorithm is harnessed in this contribution to model specific surface area of spinel ferrite based compounds while the existing models in the literature determine specific surface area of the same compounds using stepwise regression (STWR) model and hybrid genetic algorithm based support vector regression (GBSVR) model [27]. The deficiency of STWR based model comes from its inability to account for nonlinearity between the descriptors and the measured specific surface area [27]. The existing GBSVR model shows better performance over STWR model due to its ability to adopt nonlinear mapping function for feature space data transformation coupled with hyperparameters optimization using genetic algorithm. The empirical risk minimization principle which formulates the mathematical background of ELM based model strengthens its universal approximation capacity over the structural risk minimization principle adopted by GBSVR model. The superiority of ELM has been demonstrated in this contribution by comparing the estimates of ELM based model with the existing models in the literature. The obtained performance enhancement of the ELM based model compared with other existing intelligent models in the literature is due to the universal approximation feature of ELM through Moore-Penrose generalized inverse implementation.

Novelties of the developed sigmoid activation function-based ELM (S-ELM) model over the existing models in the literature include the ease of implementation and better generalization capacity on the basis of performance metrics. The developed S-ELM model can be easily implemented using Excel or standard calculator while the implementation of the existing genetic algorithm based support vector regression (GBSVR) model [27] is restricted to MATLAB environment. S-ELM model has demonstrated enhanced performance of 4.67% (using correlation coefficient, CC), 5.28% (using mean absolute error, MAE), and 58.22% (using root mean square error, RMSE) over the existing GBSVR model [27] for training set of data samples while it achieves improved performance of 11.64% (using CC metric), 61% (using MAE metric), and 61.31% (using RMSE metric) for testing set of data samples. In the same vein, the developed S-ELM model shows performance improvement of 58.29% (using CC metric), 87.66% (using MAE metric), and 84.12% (using RMSE metric) over the existing stepwise regression

(STWR) model [27] on training set of samples while it demonstrates improved performance of 18.28% (using CC metric), 67.05% (using MAE metric), and 70.01% (using RMSE metric) for testing set of samples.

The roadmap of this work entails Section 2 (which presents the background of ELM, data acquisition, and computational methodology) and Section 3 (which shows and discusses results with comparison to the existing models in the literature).

2. Empirical Study and Computational Methodology

The mathematical background and extreme learning machine description are presented in this section. The section also includes the computational strategies and physical description of the dataset.

2.1. Extreme Learning Machine Intelligent Method. Extreme learning machine (ELM) is an intelligence based algorithm with single-layer feedforward network architecture and characteristic single hidden layer [40, 48, 49]. The algorithm randomly maps the hidden layer and ultimately assigns values for the biases and input weights with the goal of output weight computation using least-square approach. ELM algorithm conserves training time compared with the conventional backpropagation algorithm. At the same time, the characteristic stochastic choice of the input weights and the biases ensures universal approximation of the relationship between the target and descriptors. Consider a training set (ψ_r, S_r) of spinel nanoferrite based compounds of M number of samples in which the measured specific surface area of the magnetic semiconductor is defined as $S_r = [s_{r1}, s_{r2}, \ldots.., s_m]^T$ while the crystallite size and the lattice distortion which serve as the model descriptors are defined as $\psi_r = [\psi_{r1}, \psi_{r2}, \ldots..\psi_m]^T$. ELM algorithm models and approximates function linking (ψ_r, S_r) of spinel nanoferrite based compounds with σ hidden nodes and $\chi(\psi)$ activation function with an output presented in equation (1) [50].

$$\begin{aligned}\delta_r &= \sum_{r=1}^{\sigma} \varnothing_r \chi_r(\psi_i) \\ &= \sum_{r=1}^{\sigma} \varnothing_r \chi_r(\gamma_r \psi_r + \lambda_r),\end{aligned} \tag{1}$$

where $r = 1, 2, 3, \ldots, M$ $\gamma_r = [\gamma_{r1}, \gamma_{r2}, \ldots.., \gamma_m]^T$ is the weight vector linking hidden nodes with the input nodes, $\varnothing_r = [\varnothing_{r1}, \varnothing_{r2}, \ldots., \varnothing_m]^T$ is the weight vector joining hidden nodes with the output nodes, and λ_r represents the threshold of r hidden nodes. Supposing that the ELM algorithm approximates M-spinel nanoferrite based compound samples with minimum error, parameters $\varnothing_r$, γ_r, and λ_r exist, so that equation (2) is satisfied.

$$\sum_{r=1}^{\sigma} \varnothing_r \chi_r(\gamma_r \psi_r + \lambda_r) = S_{\text{pred}}, \tag{2}$$

where the estimated specific surface area using ELM algorithm is defined as S_{pred}. The matrix representation of the expression contained in equation (2) is shown in the following equation:

$$H\varphi = S_{\text{pred}}, \tag{3}$$

where $\mathbf{H} = \begin{bmatrix} \chi(\gamma_1\psi_1 + \lambda_1) & \cdots & \chi(\gamma_\sigma\psi_1 + \lambda_\sigma) \\ \vdots & \cdots & \vdots \\ \chi(\gamma_1\psi_M + \lambda_1) & \cdots & \chi(\gamma_\sigma\psi_M + \lambda_\sigma) \end{bmatrix}$,

$\boldsymbol{\varphi} = \begin{bmatrix} \varphi_1^{\mathbf{T}} \\ \vdots \\ \varphi_\sigma^{\mathbf{T}} \end{bmatrix}_{\boldsymbol{\sigma}\mathbf{xn}}$ and $\mathbf{S}_{\text{pred}} = \begin{bmatrix} \mathbf{S}_{\text{pred1}}^{\mathbf{T}} \\ \vdots \\ \mathbf{S}_{\text{pred}\sigma}^{\mathbf{T}} \end{bmatrix}_{\mathbf{Mxn}}$

The parameters γ_r and λ_r of the hidden layer are selected randomly, while the parameter $\varnothing_r$ of the output layer is computed through Moore-Penrose generalized inverse as presented in equation (4) [51].

$$\varnothing = H^T\left(HH^T\right)^{-1} S_{\text{pred}}. \tag{4}$$

2.2. Spinel Ferrite Nanomaterial Data Samples for Modeling and Simulation. The dataset samples utilized for modeling ELM based model that estimates specific surface area of doped spinel ferrite nanomaterials consist of the crystallite size and lattice parameter (along the crystallographic direction) as descriptors, while the desired target is the specific surface area after dopant incorporation. The entire samples for modeling are extracted from available forty different compounds of spinel ferrite nanomaterials in [52–58]. Introduction of dopants such as zinc into spinel ferrite nanomaterial crystal structure influences the specific surface area of the parent compound and further expands the crystal lattice without causing a disturbance on the lattice symmetry [59]. Similarly, crystallite size contributes to structural disorder on nanoparticle surface due to the significance of spin disorder as the ratio of the surface and volume is altered [60].

The correlation cross-plot between crystallite size, lattice parameter, and specific surface area is shown in Figure 1 purposely to deduce the trend of linear relationship between the specific surface area of spinel ferrite nanomaterials and the descriptors. The coefficients of a linear relationship between crystallite size and lattice parameter are −26.67% and −26.58%, respectively, which strongly indicates that the lattice constant and crystallite size are not linearly correlated with the specific surface area despite the established physical discretional relation [60–62]. To establish a relationship for specific surface area of spinel ferrite nanomaterial, hybrid genetic algorithm based support vector regression (GBSVR) and stepwise regression (STWR) models were proposed recently with acceptable performance metrics [27]. The present developed model based on ELM has characteristic ease of implementation and further shows superior performance as compared with the existing models.

2.3. Computational Method and Details. Extreme learning machine (ELM) based model for spinel ferrite nanomaterial specific surface area prediction was developed using

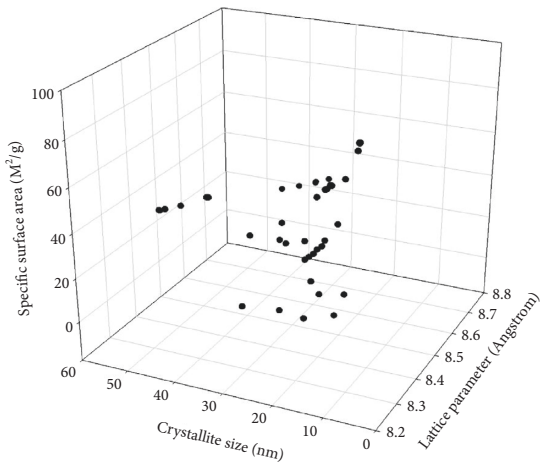

Figure 1: Three-dimensional cross-plot between the descriptors and specific surface area of doped spinel ferrite nanomaterial.

MATLAB computing environment. Randomization of forty samples of spinel ferrite nanomaterial based compounds was conducted while 4 : 1 ratio of data separation into training and testing phase followed. Randomization strengthens model efficiency and saves computational time in such a manner that model enjoys validation on approximated patterns during training phase. The generalization and predictive capacity of the proposed ELM based model were further enhanced through grid search approach of model parameters. The model parameter is the number of hidden nodes for different activation functions. However, these parameters could be optimized using metaheuristic algorithms [63–67], manual method [68], and grid search approach [69]. The choice of grid search approach in this work is due to a few numbers of model parameter (which is only the hidden node) which makes the choice of heuristic algorithm computationally noneconomical. Computational steps for the ELM based model are described as follows:

Step 1: *Initialization of Mersenne Twister Generator:* input weights and biases are generated using Mersenne Twister Generator within MATALAB. This pseudo-random generator further preserves the reproducibility of the model.

Step 2: *Number of hidden node optimization through a grid search approach for each of the chosen activation functions:* with the search space spanning between 1 and 100 for hidden node selection, one activation function was selected at a time from different available functions such as sigmoid function, triangular basis function, sine function, radial basis function, and hardlim function.

Step 3: *Hidden layer output matrix computation:* Deployment of training set of data on equation (3) yields the output matrix of the hidden layer.

Step 4: *Calculation of output weights connecting the hidden layer with the output layer:* Implementation of Moore-Penrose generalized inverse using equation (4) computes the output weights.

Step 5: *Validation stage and performance metrics computation:* The computed output matrix and the randomly generated input weights as well as the biases are employed using ELM operational principles to determine the specific surface area of spinel ferrite nanomaterial compounds that were excluded during training phase. The predictions of ELM based models developed were compared with the known experimental values of specific surface area while performance metrics such as mean absolute error (MAE), correlation coefficient (CC), and root mean square error (RMSE) were computed. The model with characteristic lowest value of MAE and RMSE was assigned the best model. The weights corresponding to the best model were also saved for subsequent deployment. The computational illustration of every step is presented in Figure 2.

3. Results and Discussion

The results of S-ELM model for specific surface area estimation is contained in this section. The comparison of the prediction strength of S-ELM model with the two existing models in the literature is further discussed.

3.1. Extreme Learning Based Functions for Specific Surface Area Prediction. The empirical equation generated through implementation of ELM algorithm for prediction of specific surface area of doped spinel ferrite nanomaterials is shown in equation (5). The obtained relation extends equation (4) with the sigmoid activation function.

$$S_{pred} = \sum_{r=1}^{\sigma} \varnothing_r / 1 + \exp\{-(\gamma_r \psi_i + \lambda_r)\}. \quad (5)$$

Several activation functions were explored while the sigmoid function demonstrated superior performance. The output weights ($\varnothing_r$), bias (λ_r), and input weights (γ_r) for each of the descriptors are presented in Table 1 for each of the hidden node. As presented in the table, the optimum number of hidden node is thirty-four. Ease of implementation of equation (5) contributes to its superiority (over the existing hybrid intelligent model in [27]) in addition to the enhanced performance demonstrated by the developed S-ELM model.

3.2. Model Performance Comparison. Performance of S-ELM model developed in this work is compared with GBSVR (2021) [27] and STWR (2021) [27] existing models in the literature and shown in Figure 3. Using mean absolute error (MAE) shown in Figure 3(a), S-ELM model outperforms GBSVR (2021) and STWR (2021) model with performance improvement of 5.28% and 87.66%, respectively, while percentage improvements of 4.67% and 58.30% were, respectively, obtained using correlation coefficient (CC) as presented in Figure 3(b).

Similar comparison on the basis of root mean square error (RMSE) presented in Figure 3(c) shows performance improvement of 58.21% and 84.12%, respectively. During

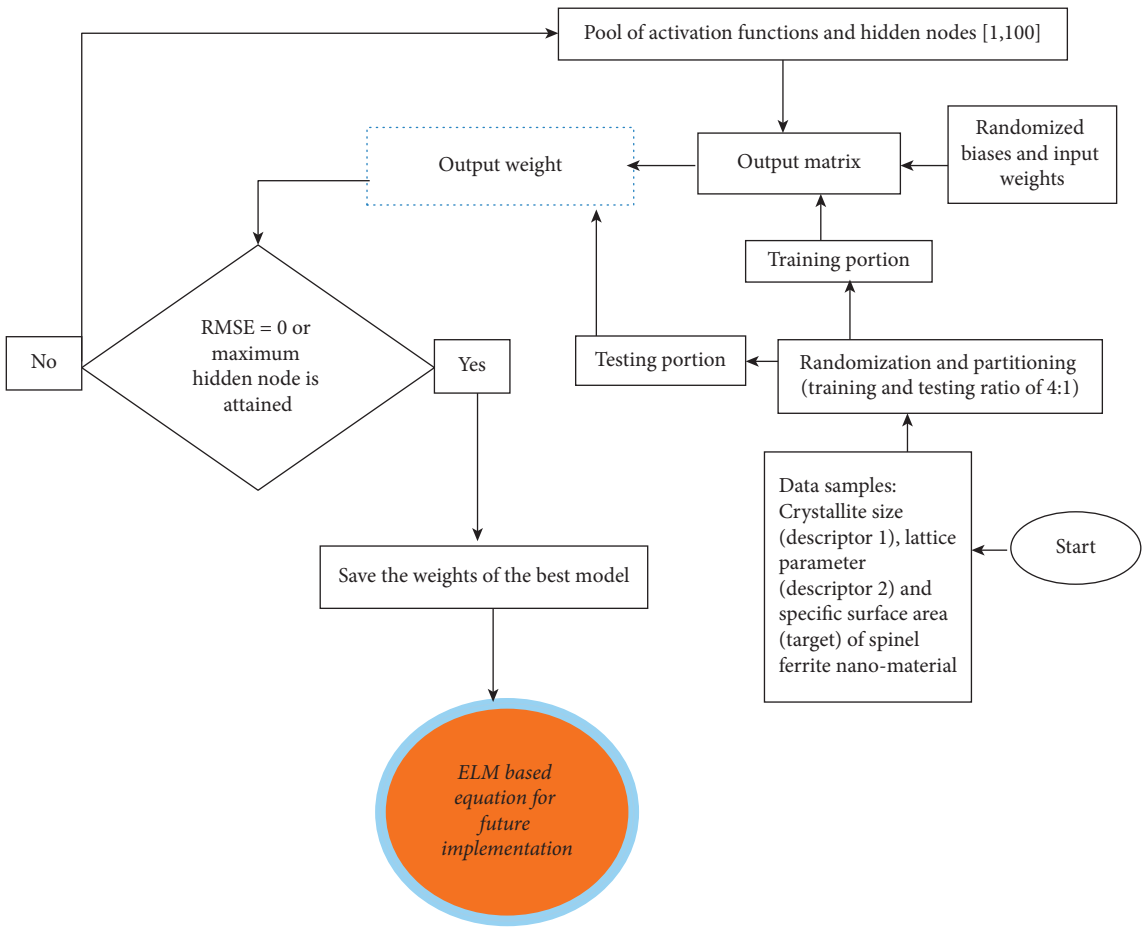

Figure 2: ELM based model flowchart for specific surface area of spinel ferrite nanomaterial estimation.

testing stage of model development, S-ELM model outperforms GBSVR (2021) [27] and STWR (2021) [27] existing models with performance improvement of 61.0% and 67.06% on the basis of MAE presented in Figure 3(d), and 11.64% and 18.28% on the basis of CC presented in Figure 3(e), 61.31% and 70.1% on the basis of RMSE presented in Figure 3(f), respectively. Table 2 presents the values of each of the parameters' measuring performance as well as the performance superiority of the present S-ELM model over the existing models.

3.3. Predictions of the Present and Existing Models. The results of the influence of different dopants on specific surface area of spinel ferrite nanomaterials are presented in Table 3. Cobalt-based spinel ferrite shows enhanced surface area at various crystallite sizes of nanomaterials with reduced crystal lattice constant [52]. The variation in lattice constant which manifested into enhanced surface area is due to smaller ionic radius of cobalt as compared with the copper ions. Site preference for each of the metal ions results in enhanced surface area, as can be observed in manganese, copper, and codoping systems presented in Table 3. The significances/effects of other different kinds of dopants on surface area of spinel ferrite nanomaterials are presented in Table 3. The estimates of S-ELM model show consistent and persistent closeness with the measured values compared with the estimates of the two existing GBSVR (2021) and STWR (2021) models. The precision characterizing the developed S-ELM model can also be inferred from the lowest MAE value and highest CC value for the entire spinel ferrite nanomaterials presented in Table 3. The universal approximation power of ELM algorithm through Moore-Penrose generalized inverse implementation contributes immensely to its superior performance. The result of yttrium substitution for cadmium in $Cd_{1-x}Y_xFe_2O_4$ ferrite compound is presented in Table 3. There is alteration in cation distribution since yttrium and cadmium ions occupy the tetrahedral site during the substitution while the octahedral site is occupied by the iron [54]. The observed ions distribution leads to gradual reduction in the value of the compound's specific surface area as the yttrium concentration increases while the results of the developed S-ELM model capture the majority of the observed experimental trends. The estimated specific surface area for gadolinium (rare Earth metal) substitution in spinel ferrite compound using S-ELM model is also presented in Table 3. Gadolinium ions in lattice structure of $Zn_{0.5}Mg_{0.5}Fe_{2-x}Gd_xO_4$ ferrite cause interstitial site stretching in octahedral and tetrahedral sublattice and further promote cations redistribution which alters the specific surface area of the compound [55]. The empirical risk minimization principle governing the employed ELM

Table 1: ELM parameters for empirical equation implementation.

Hidden node (r)	$\varnothing_r$	λ_r	γ_r (lattice parameter)	γ_r (crystallite size)
1	−0.62274	−0.09551	0.662722	$-2.2E+09$
2	0.945422	0.888646	0.396684	$5E+12$
3	−0.57982	0.29738	0.507116	$-4.8E+07$
4	−0.8383	−0.51232	0.65382	$-3E+13$
5	−0.14263	−0.9731	0.825833	$-9.3E+11$
6	0.732903	−0.37844	0.361	−1669932
7	−0.04152	0.070403	0.559194	425195.2
8	0.445617	−0.23035	0.746379	5102536
9	−0.68086	−0.28236	0.693861	$1.38E+11$
10	0.240922	−0.3114	0.324664	$-3E+08$
11	0.250907	0.186269	0.344454	$1.54E+10$
12	0.17992	−0.55345	0.807188	$-2.9E+09$
13	0.935471	0.408186	0.118581	$-1.2E+13$
14	−0.4163	0.231036	0.123533	26047114
15	0.020411	0.840614	0.373485	$-6.4E+12$
16	−0.56299	0.54586	0.000409	$-5.7E+08$
17	0.085264	0.700882	0.376104	$-4.3E+12$
18	−0.36751	−0.1255	0.329068	$1.06E+09$
19	0.577621	−0.22523	0.785514	434085.8
20	0.247755	0.230884	0.351277	$1.09E+10$
21	0.437797	−0.95321	0.661203	$1.99E+11$
22	−0.71626	−0.62271	0.015629	$-1.1E+13$
23	−0.77069	0.949419	0.086171	$-1.7E+10$
24	0.911439	0.232516	0.903004	$3.4E+12$
25	−0.34473	−0.20198	0.030566	$4.1E+10$
26	0.351874	−0.82816	0.117889	$-7.1E+11$
27	0.956593	0.165212	0.633875	$1.81E+10$
28	−0.9117	−0.42496	0.101884	$8.58E+12$
29	0.716314	0.082483	0.388419	$-4.1E+09$
30	−0.25616	−0.87667	0.23045	$-1.1E+12$
31	−0.81234	0.208952	0.366493	−98509.6
32	0.89921	0.692168	0.754947	$5.48E+12$
33	0.867543	−0.79842	0.374596	$5.58E+08$
34	0.988284	0.566743	0.021894	$8.37E+12$

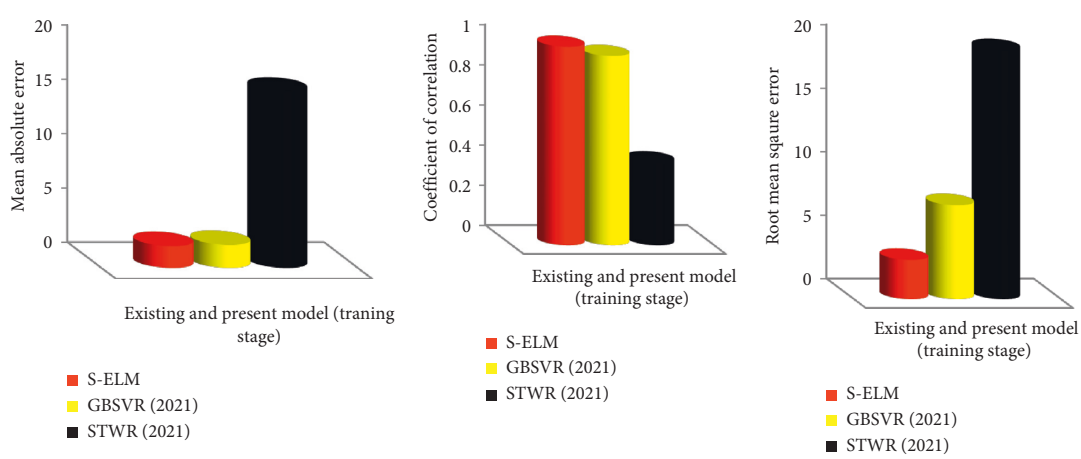

(a) (b) (c)

Figure 3: Continued.

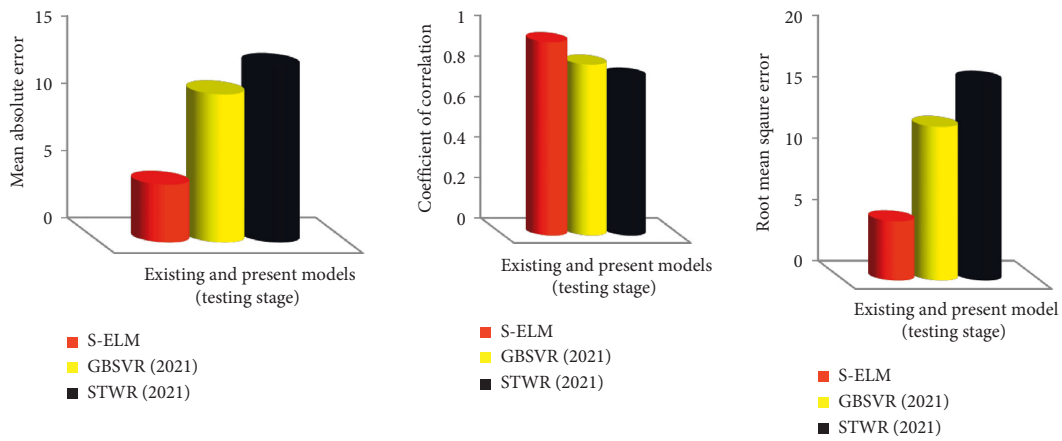

(d) (e) (f)

Figure 3: Comparison of S-ELM model and GBSVR (2021) and STWR (2021) models: (a) based on a mean absolute error on training dataset; (b) based on coefficient of correlation on training dataset; (c) based on root mean square error on training dataset; (d) based on mean absolute error on testing dataset; (e) based on coefficient of correlation on testing dataset; (f) based on root mean square error on testing dataset.

Table 2: Comparison of model performance as well as the performance superiority.

	Training			Testing		
	CC	MAE	RMSE	CC	MAE	RMSE
S-ELM	0.9902	2.0029	3.1181	0.9566	4.3021	4.8494
GBSVR (2021) [27]	0.9440	2.1146	7.4631	0.8452	11.0318	12.535
STWR (2021) [27]	0.4130	16.2313	19.6192	0.7817	13.0592	16.2186
% superiority of S-ELM over GBSVR	4.6726	5.2819	58.2192	11.6454	61.0032	61.3127
% superiority of S-ELM over STWR	58.2962	87.6602	84.1066	18.2793	67.0573	70.0991

Table 3: Specific surface area of different spinel ferrite based nanomaterials as obtained from experimental values and developed S-ELM model as well as the existing GBSVR (2021) and STWR (2021) models. All values of specific surface area are measured in (M^2/g).

Spinel ferrite nanomaterial	Measured specific surface area	S-ELM	Residual	GA-SVR (2021)	Residual	SWR (2021)	Residual
$CoFe_2O_4$	23.500 [52]	23.598	0.098	23.600	0.100	46.054	22.554
$CuFe_2O_4$	8.900 [52]	3.754	5.146	9.000	0.100	48.881	39.981
$MnFe_2O_4$	0.400 [52]	1.035	0.635	36.117	35.717	34.528	34.128
$MN_{0.4}Co_{0.6}Fe_2O_4$	11.900 [52]	11.906	0.006	12.000	0.100	35.832	23.932
$Mn_{0.4}Co_{0.4}Cu_{0.2}Fe_2O_4$	8.800 [52]	10.793	1.993	28.379	19.579	34.361	25.561
$Mn_{0.4}Co_{0.2}Cu_{0.4}Fe_2O_4$	4.000 [52]	4.770	0.770	4.100	0.100	38.662	34.662
$MN_{0.4}Cu_{0.6}Fe_2O_4$	1.400 [52]	6.734	5.334	1.500	0.100	34.932	33.532
$Mg_{0.25}Ni_{0.15}Cu_{0.25}Co_{0.35}Fe_{2-x}La_xO_4$ ($x = 0$)	40.047 [53]	40.656	0.609	40.046	0.001	27.126	12.921
$Mg_{0.25}Ni_{0.15}Cu_{0.25}Co_{0.35}Fe_{2-x}La_xO_4$ ($x = 0.03$)	43.503 [53]	46.320	2.817	40.436	3.067	29.593	13.910
$Mg_{0.25}Ni_{0.15}Cu_{0.25}Co_{0.35}Fe_{2-x}La_xO_4$ ($x = 0.06$)	48.562 [53]	51.320	2.758	48.462	0.100	32.158	16.404
$Mg_{0.25}Ni_{0.15}Cu_{0.25}Co_{0.35}Fe_{2-x}La_xO_4$ ($x = 0.09$)	49.071 [53]	44.652	4.419	46.434	2.637	32.337	16.734
$Mg_{0.25}Ni_{0.15}Cu_{0.25}Co_{0.35}Fe_{2-x}LaxO_4$ ($x = 0.12$)	40.067 [53]	33.590	6.477	40.167	0.100	28.269	11.798
$Mg_{0.25}Ni_{0.15}Cu_{0.25}Co_{0.35}Fe_{2-x}La_xO_4$ ($x = 0.15$)	39.361 [53]	43.102	3.741	39.461	0.100	27.573	11.788
$Cd_{1-x}Y_xFe_2O_4(x = 0)$ [54]	32.180 [54]	32.539	0.359	32.280	0.100	19.719	12.461
$Cd_{1-x}Y_xFe_2O_4(x = 0.125)$	29.900 [54]	37.289	7.389	30.000	0.100	25.880	4.020
$Cd_{1-x}Y_xFe_2O_4(x = 0.250)$	30.420 [54]	22.383	8.037	30.320	0.100	25.393	5.027

Table 3: Continued.

Spinel ferrite nanomaterial	Measured specific surface area	S-ELM	Residual	GA-SVR (2021)	Residual	SWR (2021)	Residual
$Cd_{1-x}Y_xFe_2O_4(x=0.375)$	25.440 [54]	25.637	0.197	25.540	0.100	39.862	14.422
$Cd_{1-x}Y_xFe_2O_4(x=0.5)$	28.740 [54]	28.238	0.502	28.840	0.100	31.757	3.017
$Zn_{0.5}Mg_{0.5}Fe_2O_4$	24.860 [55]	23.746	1.114	40.292	15.432	35.567	10.707
$Zn_{0.5}Mg_{0.5}Fe_{1.98}Gd_{0.02}O_4$	25.524 [55]	24.207	1.317	38.006	12.482	34.715	9.191
$Zn_{0.5}Mg_{0.5}Fe_{1.96}Gd_{0.04}O_4$	26.756 [55]	26.820	0.064	26.856	0.100	34.053	7.297
$Zn_{0.5}Mg_{0.5}Fe_{1.94}Gd_{0.06}O_4$	28.250 [55]	32.117	3.867	28.350	0.100	33.331	5.081
$Zn_{0.5}Mg_{0.5}Fe_{1.92}Gd_{0.08}O_4$	29.497 [55]	32.109	2.612	29.480	0.017	32.559	3.062
$Zn_{0.5}Mg_{0.5}Fe_{2-x}Gd_xO_4$ $(x=0.1)$	31.837 [55]	30.688	1.150	31.937	0.100	31.884	0.047
$Zn_{0.5}Co_{0.05}La_xFe_{2-x}O_4$ $(x=0)$	33.300 [56]	27.141	6.159	40.083	6.783	34.896	1.596
$Zn_{0.5}Co_{0.05}La_xFe_{2-x}O_4$ $(x=0.025)$	55.500 [56]	54.887	0.613	55.400	0.100	38.741	16.759
$Zn_{0.5}Co_{0.05}La_xFe_{2-x}O_4$ $(x=0.05)$	58.800 [56]	50.000	8.800	58.700	0.100	38.286	20.514
$Zn_{0.5}Co_{0.05}La_xFe_{2-x}O_4$ $(x=0.075)$	59.200 [56]	53.848	5.352	59.300	0.100	38.330	20.870
$Zn_{0.5}Co_{0.05}La_xFe_{2-x}O_4$ $(x=0.1)$	60.900 [56]	60.363	0.537	39.996	20.904	38.324	22.576
$Zn_{0.5}Co_{0.05}La_xFe_{2-x}O_4$ $(x=0.125)$	60.800 [56]	61.102	0.302	43.691	17.109	38.333	22.467
$Co_{0.9}Ni_{0.1}Fe_2O_4$	41.800 [57]	41.418	0.382	41.700	0.100	34.085	7.715
$Co_{0.7}Ni_{0.3}Fe_2O_4$	64.700 [57]	64.691	0.009	64.600	0.100	39.379	25.321
$Co_{0.5}Ni_{0.5}Fe_2O_4$	79.500 [57]	79.488	0.012	79.400	0.100	45.148	34.352
$Co_{0.3}Ni_{0.7}Fe_2O_4$	85.200 [57]	85.195	0.005	85.100	0.100	51.574	33.626
$Co_{0.1}Ni_{0.9}Fe_2O_4$	92.700 [57]	92.695	0.005	92.600	0.100	73.049	19.651
$Cu_{0.5}Cd_{0.25}Co_{0.25}Fe_2O_4$	25.349 [58]	29.527	4.178	25.449	0.100	31.361	6.012
$Cu_{0.5}Cd_{0.25}Co_{0.25}Fe_{1.9875}O_4$	26.311 [58]	23.605	2.706	34.640	8.329	32.075	5.764
$Cu_{0.5}Cd_{0.25}Co_{0.25}Fe_{1.975}O_4$	29.266 [58]	29.984	0.718	40.431	11.165	31.776	2.510
$Cu_{0.5}Cd_{0.25}Co_{0.25}Fe_{1.9625}O_4$	37.102 [58]	35.063	2.040	37.002	0.100	33.245	3.857
$Cu_{0.5}Cd_{0.25}Co_{0.25}Fe_{1.95}O_4$	41.808 [58]	47.090	5.282	41.708	0.100	33.760	8.049
		MAE	2.463		3.898		15.597
		CC	0.986		0.916		0.461

algorithm strengthens its universal approximation capacity and translates to improved performance as compared with structural risk minimization principle utilized by the existing GBSVR model. The deviations between the estimates of S-ELM model and the measured values can be reduced further through implementation of advanced intelligent algorithms such as sensitivity linear learning method of neural networks, metaheuristically optimized extreme learning method, and gravitational search algorithm based support vector regression, among others.

4. Conclusion

Extreme learning machine (S-ELM) based model was developed for predicting the specific surface area of spinel ferrite based nanomaterials using the lattice distortion (due to the incorporated dopants) and the size of nanoparticle crystallite as descriptors. S-ELM model has demonstrated enhanced performance of 4.67% (using CC metric), 5.28% (using MAE), and 58.22% (using RMSE metric) over the existing GBSVR model for training set of data samples while it achieves improved performance of 11.64% (using CC metric), 61% (using MAE metric), and 61.31% (using RMSE metric) for testing set of data samples. Similarly, S-ELM model shows performance improvement of 58.29% (using CC metric), 87.66% (using MAE metric), and 84.12% (using RMSE metric) over the existing STWR model on training set of samples while it demonstrates improved performance of 18.28% (using CC metric), 67.05% (using MAE metric), and 70.01% (using RMSE metric) for testing set of samples. The developed S-ELM model investigates the influence of cobalt, yttrium, magnesium, nickel, and cadmium on specific surface areas of spinel ferrite nanomaterials. Aside from the ease of implementation of S-ELM model, its enhanced performance further contributes to its uniqueness. The precision demonstrated by S-ELM model would strengthen quick, efficient, and precise characterization of the specific surface area of spinel ferrite based compounds with circumvention of time demanding experimental procedures. Advanced intelligent algorithms such as sensitivity linear learning method of neural networks, metaheuristically optimized extreme learning method, and gravitational search algorithm based support vector regression could be developed for spinel ferrite specific surface area modeling in future works.

Data Availability

The needed raw data for reproducing the presented findings are available in the cited references in Section 2.2 of the manuscript.

Conflicts of Interest

The authors declare no conflicts of interest.

Acknowledgments

This research work was funded by the contributing authors and no external fund was received.

References

[1] P. Lavanya Rathi and S. Deepa, "Structural, magnetic, thermal and optical properties of Sn2+ cation doped magnetite nanoparticles," *Ceramics International*, vol. 46, no. 3, pp. 2969–2978, 2020.

[2] Y. Slimani, B. Unal, M. A. Almessiere et al., "Investigation of structural and physical properties of Eu3+ ions substituted Ni0.4Cu0.2Zn0.4Fe2O4 spinel ferrite nanoparticles prepared via sonochemical approach," *Results in Physics*, vol. 17, Article ID 103061, 2020.

[3] K. K. Kefeni and B. B. Mamba, "Photocatalytic application of spinel ferrite nanoparticles and nanocomposites in wastewater treatment: Review," *Sustainable Materials and Technologies*, vol. 23, Article ID e00140, 2020.

[4] K. K. Kefeni, T. A. M. Msagati, T. T. Nkambule, and B. B. Mamba, "Spinel ferrite nanoparticles and nanocomposites for biomedical applications and their toxicity," *Materials Science and Engineering: C*, vol. 107, Article ID 110314, 2020.

[5] A. Samavati and A. F. Ismail, "Antibacterial properties of copper-substituted cobalt ferrite nanoparticles synthesized by co-precipitation method," *Particuology*, vol. 30, pp. 158–163, 2017.

[6] A. Sharma, K. M. Batoo, E. H. Raslan, S. F. Adil, and G. Kumar, "Structural and magnetic study of Mn0.5Zn0.5CuxFe2-xO4 nanoferrites synthesized via solution combustion method," *Vacuum*, vol. 157, pp. 422–427, 2018.

[7] K. Srinivasan, N. Zebardast, P. Krishnamurthy et al., "Comparison of new visual disturbances after superior versus nasal/temporal laser peripheral iridotomy," *Ophthalmology*, vol. 125, no. 3, pp. 345–351, 2018.

[8] A. Sharma, K. M. Batoo, E. H. Raslan, and G. Kumar, "Effect of chromium ions on the structural, magnetic, and optical properties of manganese-zinc ferrite nanoparticles," *Journal of Materials Science: Materials in Electronics*, vol. 31, no. 19, Article ID 16959, 2020.

[9] S. B. Kale, S. B. Somvanshi, M. N. Sarnaik, S. D. More, S. J. Shukla, and K. M. Jadhav, "Enhancement in surface area and magnetization of CoFe2O4 nanoparticles for targeted drug delivery application," *AIP Conference Proceedings*1953 pages, 2018.

[10] N. N. Al-Rawi, B. A. Anwer, N. H. Al-Rawi, A. T. Uthman, and I. S. Ahmed, "Magnetism in drug delivery: the marvels of iron oxides and substituted ferrites nanoparticles," *Saudi Pharmaceutical Journal*, vol. 28, no. 7, pp. 876–887, 2020.

[11] R. Sharma, P. Thakur, M. Kumar et al., "Improvement in magnetic behaviour of cobalt doped magnesium zinc nanoferrites via co-precipitation route," *Journal of Alloys and Compounds*, vol. 684, pp. 569–581, 2016.

[12] K. K. Kefeni, B. B. Mamba, and T. A. M. Msagati, "Application of spinel ferrite nanoparticles in water and wastewater treatment: a review," *Separation and Purification Technology*, vol. 188, pp. 399–422, 2017.

[13] N. Alghamdi, J. Stroud, M. Przybylski et al., "Structural, magnetic and toxicity studies of ferrite particles employed as contrast agents for magnetic resonance imaging thermometry," *Journal of Magnetism and Magnetic Materials*, vol. 497, 2019.

[14] T. Krishnaveni, B. R. Kanth, V. S. R. Raju, and S. R. Murthy, "Fabrication of multilayer chip inductors using Ni-Cu-Zn ferrites," *Journal of Alloys and Compounds*, vol. 414, no. 1, pp. 282–286, 2006.

[15] S. S. Kumbhar, M. A. Mahadik, V. S. Mohite, Y. M. Hunge, K. Y. Rajpure, and C. H. Bhosale, "Effect of Ni content on the structural, morphological and magnetic properties of spray deposited Ni-Zn ferrite thin films," *Materials Research Bulletin*, vol. 67, pp. 47–54, 2015.

[16] E. Petrova, D. Kotsikau, and V. Pankov, "Structural characterization and magnetic properties of sol-gel derived Zn x Fe 3-x O 4 nanoparticles," *Journal of Magnetism and Magnetic Materials*, vol. 378, pp. 429–435, 2015.

[17] D. Kotsikau, M. Ivanovskaya, V. Pankov, and Y. Fedotova, "Structure and magnetic properties of manganese-zinc-ferrites prepared by spray pyrolysis method," *Solid State Sciences*, vol. 39, pp. 69–73, 2015.

[18] M. Satalkar, S. N. Kane, M. Kumaresavanji, and J. P. Araujo, "On the role of cationic distribution in determining magnetic properties of Zn 0.7-x Ni x Mg 0.2 Cu 0.1 Fe 2 O 4 nano ferrite," *Materials Research Bulletin*, vol. 91, pp. 14–21, 2017.

[19] K. Kombaiah, J. J. Vijaya, L. J. Kennedy et al., "Effect of Cd2+ concentration on ZnFe2O4 nanoparticles on the structural, optical and magnetic properties," *Optik*, vol. 135, pp. 190–199, 2017.

[20] D. Carta, M. F. Casula, A. Falqui et al., "A structural and magnetic investigation of the inversion degree in ferrite nanocrystals MFe2O4(M = Mn, Co, Ni)," *Journal of Physical Chemistry C*, vol. 113, no. 20, pp. 8606–8615, 2009.

[21] S. B. Darling and S. D. Bader, "A materials chemistry perspective on nanomagnetism," *Journal of Materials Chemistry*, vol. 15, no. 39, pp. 4189–4195, 2005.

[22] D. Chaudhary and B. Kumar, "Cost optimized hybrid genetic-gravitational search algorithm for load scheduling in cloud computing," *Applied Soft Computing*, vol. 83, Article ID 105627, 2019.

[23] M. A. Almessiere, A. Demir Korkmaz, Y. Slimani, M. Nawaz, S. Ali, and A. Baykal, "Magneto-optical properties of rare earth metals substituted Co-Zn spinel nanoferrites," *Ceramics International*, vol. 45, no. 3, pp. 3449–3458, 2019.

[24] D. S. Mathew and R. S. Juang, "An overview of the structure and magnetism of spinel ferrite nanoparticles and their synthesis in microemulsions," *Chemical Engineering Journal*, vol. 129, no. 1, pp. 51–65, 2007.

[25] G. L. Jadhav, S. D. More, C. M. Kale, and K. M. Jadhav, "Effect of magnesium substitution on the structural, morphological, optical and wettability properties of cobalt ferrite thin films," *Physica B: Condensed Matter*, vol. 555, pp. 61–68, 2019.

[26] M. Houshiar, F. Zebhi, Z. J. Razi, A. Alidoust, and Z. Askari, "Synthesis of cobalt ferrite (CoFe2O4) nanoparticles using combustion, coprecipitation, and precipitation methods: a comparison study of size, structural, and magnetic properties," *Journal of Magnetism and Magnetic Materials*, vol. 371, pp. 43–48, 2014.

[27] T. O. Owolabi, T. A. Saleh, O. Olusayo, M. Souiyah, and O. E. Oyeneyin, "Modeling the specific surface area of doped spinel ferrite nanomaterials using hybrid intelligent computational method," *Journal of Nanomaterials*, vol. 2021, Article ID 9677423, 2021.

[28] S. Dasgupta, B. Das, Q. Li et al., "Toward on-and-off magnetism: reversible electrochemistry to control magnetic phase transitions in spinel ferrites," *Advanced Functional Materials*, vol. 26, no. 41, pp. 7507–7515, 2016.

[29] Q. Zhao, Z. Yan, C. Chen, and J. Chen, "Spinels: controlled preparation, oxygen reduction/evolution reaction application, and beyond," *Chemical Reviews*, vol. 117, no. 15, Article ID 10121, 2017.

[30] Y. Li, Y. Li, X. Xu et al., "Structural disorder controlled oxygen vacancy and photocatalytic activity of spinel-type minerals: a case study of ZnFe2O4," *Chemical Geology*, vol. 504, pp. 276–287, 2019.

[31] M. Nawaz, A. Shahzad, K. Tahir et al., "Photo-Fenton reaction for the degradation of sulfamethoxazole using a multi-walled carbon nanotube-NiFe2O4 composite," *Chemical Engineering Journal*, vol. 382, Article ID 123053, 2020.

[32] A. Sankaramahalingam and J. B. Lawrence, "Structural, optical, and magnetic properties of MgFe2O4 synthesized with addition of copper," *Synthesis and Reactivity in Inorganic Metal-Organic and Nano-Metal Chemistry*, vol. 42, no. 1, pp. 121–127, 2012.

[33] Z. K. Heiba, M. B. Mohamed, H. H. Hamdeh, and M. A. Ahmed, "Structural analysis and cations distribution of nanocrystalline Ni1−Zn Fe1.7Ga0.3O4," *Journal of Alloys and Compounds*, vol. 618, pp. 755–760, 2015.

[34] M. Satalkar, S. N. Kane, A. Ghosh et al., "Synthesis and soft magnetic properties of Zn0.8-xNixMg0.1Cu0.1Fe2O4 (x = 0.0-0.8) ferrites prepared by sol-gel auto-combustion method," *Journal of Alloys and Compounds*, vol. 615, no. 1, pp. 313–316, 2015.

[35] S. N. Kane and M. Satalkar, "Correlation between magnetic properties and cationic distribution of Zn0.85−x Ni x Mg0.05Cu0.1Fe2O4 nano spinel ferrite: effect of Ni doping," *Journal of Materials Science*, vol. 52, no. 6, pp. 3467–3477, 2017.

[36] K. Rajasekhar Babu, K. R. Rao, and B. Rajesh Babu, "Cu 2+ -modified physical properties of Cobalt-Nickel ferrite," *Journal of Magnetism and Magnetic Materials*, vol. 434, pp. 118–125, 2017.

[37] A. Hajalilou, H. M. Kamari, and K. Shameli, "Dielectric and electrical characteristics of mechanically synthesized Ni-Zn ferrite nanoparticles," *Journal of Alloys and Compounds*, vol. 708, pp. 813–826, 2017.

[38] M. A. Almessiere, Y. Slimani, M. Sertkol et al., "Ce-Nd Co-substituted nanospinel cobalt ferrites: an investigation of their structural, magnetic, optical, and apoptotic properties," *Ceramics International*, vol. 45, no. 13, Article ID 16147, 2019.

[39] M. P. Ghosh, S. Datta, R. Sharma, K. Tanbir, M. Kar, and S. Mukherjee, "Copper doped nickel ferrite nanoparticles: jahn-Teller distortion and its effect on microstructural, magnetic and electronic properties," *Materials Science and Engineering: B*, vol. 263, Article ID 114864, 2021.

[40] G. B. Huang, Q. Y. Zhu, and C. K. Siew, "Extreme learning machine: theory and applications," *Neurocomputing*, vol. 70, no. 1, pp. 489–501, 2006.

[41] A. Alqahtani, "Engineering the energy gap of cupric oxide nanomaterial using extreme learning machine and stepwise regression algorithms," *Journal of Nanomaterials*, vol. 2021, Article ID 4797686, 2021.

[42] X. Liu, Q. Ge, X. Chen, J. Li, and Y. Chen, "Extreme learning machine for multivariate reservoir characterization," *Journal of Petroleum Science and Engineering*, Article ID 108869, 205 pages, 2021.

[43] U. Safder, J. Loy-benitez, H.-T. Nguyen, and C. Yoo, "A hybrid extreme learning machine and deep belief network framework for sludge bulking monitoring in a dynamic wastewater treatment process," *Journal of Water Process Engineering*, vol. 46, Article ID 102580, 2022.

[44] O. E. Oyeneyin, B. S. Obadawo, A. A. Olanrewaju et al., "Predicting the bioactivity of 2- alkoxycarbonylallyl esters as potential antiproliferative agents against pancreatic cancer (MiaPaCa-2) cell lines," *GFA-based QSAR and ELM-based models with molecular docking*, vol. 19, 2021.

[45] Y. Li, Y. Zeng, Y. Qing, and G.-B. Huang, "Learning local discriminative representations via extreme learning machine for machine fault diagnosis," *Neurocomputing*, vol. 409, pp. 275–285, 2020.

[46] Y. Ma, L. Wu, Y. Guan, and Z. Peng, "The capacity estimation and cycle life prediction of lithium-ion batteries using a new broad extreme learning machine approach," *Journal of Power Sources*, vol. 476, no. 56, Article ID 228581, 2020.

[47] W. Ahmed, H. Ma, X. Ouyang, and D. Y. Mo, "Prediction of aircraft trajectory and the associated fuel consumption using covariance bidirectional extreme learning machines," *Transp. Res. Part E*, vol. 145, Article ID 102189, 2021.

[48] E. Han and N. Ghadimi, "Model identification of proton-exchange membrane fuel cells based on a hybrid convolutional neural network and extreme learning machine optimized by improved honey badger algorithm," *Sustainable Energy Technologies and Assessments*, vol. 52, Article ID 102005, 2022.

[49] S. M. I. Shamsah and T. O. Owolabi, "Modeling the maximum magnetic entropy change of doped manganite using a grid search-based extreme learning machine and hybrid gravitational search-based support vector regression," *Crystals*, vol. 10, no. 4, 310 pages, 2020.

[50] S. M. Sulaiman, P. A. Jeyanthy, D. Devaraj, and K. V. Shihabudheen, "A novel hybrid short-term electricity forecasting technique for residential loads using Empirical Mode Decomposition and Extreme Learning Machines," *Computers & Electrical Engineering*, vol. 98, Article ID 107663, 2022.

[51] T. O. Owolabi, "Extreme learning machine and swarm- based support vector regression methods for predicting crystal lattice parameters of pseudo-cubic/cubic perovskites Extreme learning machine and swarm-based support vector regression methods for predicting crystal lat," *Journal of Applied Physics*, vol. 127, Article ID 245107, 2020.

[52] M. Co, O. Fe, V. Verma, M. Kaur, and J. Marc, "Tailored structural, optical and magnetic properties of ternary nano-hybrid," *Ceramics International*, vol. 45, no. 8, Article ID 10865, 2019.

[53] N. Cu, C. Fe, A. Aslam et al., "Physica B: physics of Condensed Matter Study of structural, optical and electrical properties of La 3 + doped Mg 0.25," *Phys. B Phys. Condens. Matter*, vol. 602, Article ID 412565, 2021.

[54] N. Amin, M. S. Ul Hasan, Z. Majeed et al., "Structural, electrical, optical and dielectric properties of yttrium substituted cadmium ferrites prepared by Co-Precipitation method," *Ceramics International*, vol. 46, no. 13, Article ID 20798, 2020.

[55] S. B. Somvanshi, S. A. Jadhav, M. V. Khedkar, P. B. Kharat, S. D. More, and K. M. Jadhav, "Structural, thermal, spectral, optical and surface analysis of rare earth metal ion (Gd3+) doped mixed Zn-Mg nano-spinel ferrites," *Ceramics International*, vol. 46, no. 9, Article ID 13170, 2020.

[56] A. Aslam, A. U. Rehman, N. Amin et al., "Lanthanum doped Zn0.5Co0.5LaxFe2−xO4 spinel ferrites synthesized via co-precipitation route to evaluate structural, vibrational, electrical, optical, dielectric, and thermoelectric properties," *Journal of Physics and Chemistry of Solids*, vol. 154, Article ID 110080, 2021.

[57] P. A. Vinosha, A. Manikandan, R. Ragu et al., "Impact of nickel substitution on structure, magneto-optical, electrical and acoustical properties of cobalt ferrite nanoparticles,"

Journal of Alloys and Compounds, vol. 857, Article ID 157517, 2021.

[58] K. Hussain, N. Amin, and M. I. Arshad, "Evaluation of structural, optical, dielectric, electrical, and magnetic properties of Ce3+ doped Cu0.5Cd0.25Co0.25Fe2-xO4 spinel nano-ferrites," *Ceramics International*, vol. 47, no. 3, pp. 3401–3410, 2021.

[59] A. Tony Dhiwahar, M. Sundararajan, P. Sakthivel, C. S. Dash, and S. Yuvaraj, "Microwave-assisted combustion synthesis of pure and zinc-doped copper ferrite nanoparticles: structural, morphological, optical, vibrational, and magnetic behavior," *Journal of Physics and Chemistry of Solids*, vol. 138, Article ID 109257, 2020.

[60] Y. Slimani, H. Güngüne, M. Nawaz, A. Manikandan, H. S. El Sayed, and M. A. Almessiere, "Magneto-optical and microstructural properties of spinel cubic copper ferrites with Li-Al co-substitution," *Ceramics International*, vol. 44, Article ID 14242, 2018.

[61] N. Ghazi, H. Mahmoudi Chenari, and F. E. Ghodsi, "Rietveld refinement, morphology analysis, optical and magnetic properties of magnesium-zinc ferrite nanofibers," *Journal of Magnetism and Magnetic Materials*, vol. 468, pp. 132–140, 2018.

[62] H. Javed, A. Rehman, S. Mussadiq et al., "Reduced graphene oxide-spinel ferrite nano-hybrids as magnetically separable and recyclable visible light driven photocatalyst," *Synthetic Metals*, vol. 254, pp. 1–9, 2019.

[63] B. S. Yildiz and A. R. Yildiz, "Comparison of grey Wolf, whale, water cycle, ant lion and sine-cosine algorithms for the optimization of a vehicle engine connecting rod," *Materials Testing*, vol. 60, no. 3, pp. 311–315, 2018.

[64] N. Pholdee, S. Bureerat, and A. R. Yildiz, "Hybrid real-code population-based incremental learning and differential evolution for many-objective optimisation of an automotive floor-frame," *International Journal of Vehicle Design*, vol. 73, no. 1, pp. 20–53, 2017.

[65] S. Karagoz and A. R. Yildiz, "A comparison of recent metaheuristic algorithms for crashworthiness optimisation of vehicle thin-walled tubes considering sheet metal forming effects," *International Journal of Vehicle Design*, vol. 73, no. 1, pp. 179–188, 2017.

[66] N. M. Sabri, M. Puteh, and M. R. Mahmood, "A review of gravitational search algorithm," *International Journal of Advances in Soft Computing and Its Applications*, vol. 5, no. 3, 2013.

[67] R. Samala and M. Kotapuri, "Optimal DG sizing and siting in radial system using hybridization of GSA and Firefly algorithms," *Modelling, Measurement and Control A*, vol. 91, no. 2, pp. 77–82, 2018.

[68] O. E. Oyeneyin, B. S. Obadawo, D. S. Metibemu et al., "An exploration of the antiproliferative potential of chalcones and dihydropyrazole derivatives in prostate cancer via androgen receptor: combined QSAR, machine learning, and molecular docking techniques," *Phys. Chem. Res.*vol. 10, no. 2, pp. 211–223, 2022.

[69] O. Olubi, E. Oniya, and T. Owolabi, "Development of predictive model for radon-222 estimation in the atmosphere using stepwise regression and grid search based-random forest regression," *Journal of the Nigerian Society of Physical Sciences*, vol. 3, pp. 132–139, 2021.

Hindawi
Mathematical Problems in Engineering
Volume 2022, Article ID 1713657, 12 pages
https://doi.org/10.1155/2022/1713657

Research Article

Performance Analysis of FFBP-LM-ANN Based Hourly GHI Prediction Using Environmental Variables: A Case Study in Chennai

N. B. Sushmi and D. Subbulekshmi

School of Electrical Engineering, Vellore Institute of Technology, Chennai 600127, Tamil Nadu, India

Correspondence should be addressed to N. B. Sushmi; sushmi.nb2018@vitstudent.ac.in and D. Subbulekshmi; subbulekshmi.d@vit.ac.in

Received 7 February 2022; Accepted 5 April 2022; Published 23 April 2022

Academic Editor: Araz Darba

Sun is the sustainable and abundantly available alternative resource on the planet Earth. The uncertain nature of the source caused due to various environmental factors increases the need to quantify the irradiation potential at the targeted location, especially for power smoothing processes, solar-fed electrical applications, and the utility grid. The irradiation measuring devices lead to appropriate maintenance and more expenses and are ineffective under dynamically varying irradiation conditions. Hence, a robust ML-based forecasting technique is sufficient to predict GHI under dynamically varying irradiation profiles caused by various environmental factors. Therefore, this study focuses on short-term (hourly) GHI forecasting using the FFBP-LM-ANN approach. In most of the related articles, the selection of independent variables and designing the network is being a challenge and obstacle in attaining fast and efficient prediction. Such a scenario increases the overall computation complexity and understanding. Hence, this study was intended to use a simple process to crucially select 5 environmental factors and to optimally choose the number of neurons for designing the network for better irradiation prediction. Thus, the network is designed with an input layer of 5 selected environmental variables and one hidden layer with 20 neurons, and hourly GHI in the output layer is performed. The approach is trained using the Levenberg-Marquardt BP algorithm in MATLAB toolbox, with the help of a 4-year dataset received for the rooftop panels of VIT University, Chennai, from NREL. The performance of the model during training and testing was validated and analyzed using 9 performance matrices. As a result, FFBP-LM-ANN satisfactorily predicts hourly GHI for the targeted location based on rRMSE of 7.21%, MAE of 0.042, MBE of 0.000492, R of 0.96, MAPE of 44.4%, MRE of 9.5%, and NSE of 94% obtained under testing process. Moreover, the model has performed much better when compared with 9 related models that exist in literature based on the input variables used, network design, epoch, and RMSE. Subsequently, such a predictor will be adaptable and more suitable for the explicit prediction of hourly GHI for different regions across the world having varying climatic conditions, since the study model is designed for locations facing robust climatic nature. More importantly, the designed model is superior with only environmental variables, which are rarely found in the article, rather than geographical variables, which are predominantly used in most of the related literature.

1. Introduction

The drastic increase in greenhouse gases and energy demand has taken a new revolution in energy production over a few decades [1]. As a result, the usage of fossil fuel-based resources is getting depleted day by day. This shoots up the popularity of using renewable energy sources worldwide, and also, this paved the way to tackle the power crisis issues faced by more developing and developed nations [2]. Among the renewables, solar power generation creates attention among researchers, industrialists, and rural developments due to clean, sustainable, and abound availability. As the solar generators are purely dependent on irradiation as the main parameter for energy production, the irradiation is uncertain and nonstationary due to highly varying environmental conditions. Hence, highly sensitive measuring

instrument should be essential in PV sites, which are expensive, causes maintenance issues, and are less effective during dynamically varying environmental conditions. But accessing the availability of exact irradiation at the desired location should be accurately known for the power smoothing process, solar-fed electric vehicles/appliances, and also to tackle various grid-related problems [3]. Therefore, the knowledge of knowing short-term irradiation potential is essential to designers for the effective utilization of resources before building a panel for the appropriate applications [4, 5]. There are numerous reviews that have been conducted on various Machine Learning-based irradiation forecasting techniques in the development of solar PV systems [6–16]. It summarizes that ANN predictor finds superior performance under all climatic and environmentally varying conditions when efficient training algorithm, architecture, and specifically selected attributes were incorporated. It also has the dominating features of performing faster computation and handling highly nonlinear datasets compared with other approaches [17, 18]. Therefore, this article was intended to focus on effective training algorithm, simple attributes selection process, and the quicker network design for ANN in attaining the efficient prediction were discussed.

The training algorithms used in the backpropagation process of ANN are Gradient Descent (GD), Bayesian Regularization (BR), Levenberg–Marquardt (LM), and scaled conjugate gradient (SCG) [19]. Some of the neural networks, which undergone analysis with various backpropagation training algorithms, are as follows [20]: conducted FFBP-ANN model to predict daily average GSR using metrological data such as maximum ambient air temperature, minimum ambient air temperature, minimum relative humidity, and day of the year for the site in Madura city, Tamil Nādu. Here, 3 ANN models were designed with different combinations of features mentioned above using two backpropagation training algorithms such as LM and GD. Finally, it was concluded that the FFBP-LM model with minimum air temperature and day of the year outperforms the other models based on MAPE and MSE obtained. Reference [21] proposed two FFBP-ANN with different combinations of the dataset for prediction monthly average GSR using 9 metrological variables such as latitude, longitude, altitude, year, month, mean ambient air temperature, mean station level pressure, mean wind speed, and mean relative humidity for 5 different locations in India (Bangalore, Chennai, Kolkata, New Delhi, and Mumbai). The models were designed with different BP training algorithms such as GD, LM, RP, and SCG. The optimal architecture was designed based on minimum MSE and higher R-value attained by checking the performance with a different number of neurons in the hidden layer. It is concluded that both ANN models outperform well using the LM training process with better MAE, RMSE, and R values. In [22], the average daily solar radiation prediction in Kuwait City was performed by the FFBP-ANN model. The dataset for 5 years was received from 5 different sites in Kuwait. For better generalization and to avoid overfitting issues, the ANN model with GD and LM algorithm for 10 neurons in the hidden layer is developed and gets MAPE = 86.3 and MAPE = 85.6, respectively. Further, the model with neurons of 1460 has been designed and obtained a MAPE of 94.75. Hence, it is finalized that better performance has been achieved in the case of the LM-ANN model. Likewise, the research proved the effectiveness of the Levenberg–Marquardt (LM) based learning process used in backpropagation. Therefore, it has been taken under consideration by more researchers and industrialists in using LM based backpropagation algorithm for ANN in the irradiation forecasting fields. Some of its contributions are as follows [23]: it performed FFBP-LM-ANN with multiple hidden layers for monthly average GSR prediction in Nigeria using 5 metrological variables such as min and max temperature, mean relative humidity, wind speed, and sunshine hours. The performance was evaluated using statistical tools such as RMSE, R^2, and MAPE. Reference [24] conducted FFBP-LM-ANN-based GHI prediction for new Delhi using Latitude, Longitude, Elevation, and meteorological parameters such as Months of a year, Days of a month, Temperature, Atmospheric Pressure, Humidity, and Wind Speed. The performance was evaluated using MSE and R. [25] proposed a hybrid Boruta Algorithm and FFBP-NN for hourly global radiation prediction using 13 features such as the month of the year, day of the month, an hour of the day, air temperature, relative humidity, surface pressure, wind speed at 3 meters, wind direction, peak wind direction at 3 meters, diffuse horizontal irradiance, direct normal irradiance, azimuth angle, and solar zenith angle of Buraydah in Saudi Arabia. Here, the feature selection process is performed by dividing the entire dataset into three sets of input features by which the optimal input features set is retrieved by the Boruta Algorithm based on the prediction accuracy obtained by a neural network. The performance is evaluated using MAPE, MSE, RMSE, and R^2. Reference [26] performed FFBP-LM-ANN method with multiple hidden layers for hourly GSR prediction using 5 (selected variable using Cosine Amplitude Method (CAM)) metrological variables such as hourly actual pressure, wind speed, wind direction, relative humidity, and average temperature. To reduce the variance and increase the prediction accuracy, the optimal parameters of the network were chosen based on the trial-and-error method. It was performed by designing 20 ANN models with different combinations of parameters and functions, whose performance is evaluated using correlation coefficient and MSE. Reference [27] conducted spatial, temporal, annual, and 2-year (2018 and 2019) ahead solar radiation prediction using FFBP-LM-ANN approach by considering input variables such as latitude, longitude, day of the year, and year collected for 36 data points in Nigeria from 1979 to 2014. The optimal design of the model was chosen based on the RMSE value attained during testing. The performance of the model was evaluated using R^2. In [28], the daily solar radiation prediction using the FFBP-LM-ANN model was performed for the site in Hamirpur, Himachal Pradesh. The optimal design with minimum error and high R-value is obtained by considering three network models with different combinations of input variables and neurons. Finally, the model with temperature, humidity,

barometric pressure, rainfall, and sunshine hours has outperformed the others with $R = .86$ and MAPE = 16.45%. Reference [29] performed prediction of hourly GSR using FFBP-LM-ANN using metrological parameters for the site in Kathmandu, Nepal. For obtaining the optimal design and performance, five models of ANN were designed based on considering the different combinations of input variables. Hence, the model with average temperature, relative humidity, sunshine duration, and rainfall amount has outperformed the other model based on good MBE = 0.0368, MPE = 0.1243, RMSE = 0.2781, and $R = 0.9880$. In [30], the daily GSR forecasting was performed by FFBP-LM-ANN with multiple hidden layers using metrological variables and particulate matters for the site in Tehran. The 12 ANN model was designed with different combinations of activation functions. The model with max and min daily temperature, relative humidity, wind speed, and particulates of matter with tansig-logsig-purelin has outperformed with MAPE = 3.13, RMSE = 0.077, and $R^2 = 0.97$. Reference [31] performed 6 ML-FFBP-LM-Neural Networks with 32 different combinations of input features such as minimum temperature, maximum temperature, the difference in temperature, sunshine hours, theoretical sunshine hours, and extraterrestrial radiation for predicting monthly average GSR for the site in India. It is confirmed that ANN with DT, H_o, S_o and DT, H_o outperforms well in predicting GSR based on MAPE = 4.19%, MPE = 3.30, RRMSE = 4.90 and MAPE = 2.61%, MPE = 1.32, and RRMSE = 3.96, respectively, when compared with other ANN models and 4 empirical models.

The works related to FFBP-LM-ANN reveal that every model can predict irradiation with satisfactory error measures. It is to be noted that, for every location, the independent variables considered should not be similar for accurate irradiation prediction. It varies depending on climatology, environmental conditions around the location of the PV site. Therefore, in every article, the feature variables were manually taken or performed several network models with different combinations of input features for obtaining a better model with the minimum error or used complex feature selection algorithms incorporated with the network design. Such scenarios lead to inaccurate prediction, increase the computational complexity in terms of processing time and data storage, several experimentation processes, and increase the overall complexity of the system. Moreover, no mathematical expression was explicitly provided in any article for choosing the number of neurons in the hidden layer [20, 27]. Generally, they use the trial-and-error method with the consideration of producing minimum statistical error measures. Hence, the attributes and number of neurons should be crucially selected without compromising the performance.

The ultimate goal of this study is to develop a data-driven based irradiation forecasting model for accessing the irradiation potential during a dynamic change in irradiation conditions due to environmental factors without the use of any costly instruments. Therefore, the contribution of the study is as follows: (1) extract the hourly metrological data of 4 years (2016–2019) from the National Renewable Energy Laboratory (NREL) for the targeted location of VIT University, Chennai. (2) Apply Pearson correlation coefficient as the feature selection process, which helps in the better selection of 5 important features among 18 feature variables. (3) Use a mathematical expression to optimally design the number of neurons for the application as per the dataset availability. (4) Focus on the most powerful Feedforward Backpropagation Levenberg-Marquardt ANN-based solar irradiation prediction model for finding hourly GHI under dynamically irradiation conditions due to various environmental parameters for the rooftop panels of VIT University, Chennai. (5) Performance of the prediction model was evaluated by comparing the obtained GHI with the actual GHI for the corresponding dataset using statistical tools.

The article is organized as follows: the first section covers the overview of the technique performed, description of study location, data collection, and preprocessing procedure, attribute selection, and network design used for prediction process in this study, which were discussed elaborately. The second section concentrates on analyzing the performance of the model and comparison with similar existing works that are effectively performed. The final section projected the overview of the study made with added future ideas.

2. Materials and Methods

2.1. Artificial Neural Network. ANN is the data-driven based learning process that got inspired by the information exchange process carried out in the human brain. It is unique and flexible in solving underlying complex nonlinear functions with high accuracy and faster learning. The basic principle behind every NN is artificial neurons. It constitutes the process element, which receives the input signal and generates the output for the neighboring process after performing with activation function and associated weights [32]. Figure 1 illustrates the architecture of a simple artificial neuron.

The neurons receive the input signal called the independent variable ($x_1, x_2, \ldots x_n$) and receive the output Y. The output is expressed by the following equation [33]:

$$Y = f(v(w, x)), \tag{1}$$

$$v(w, x) = \sum_{k=1}^{n} w_k x_k + b = W'X + b. \tag{2}$$

"v" is the function used for representing the weights associated with each input and the sum of bias, where $w_1, w_2, \ldots, w_n$ are the weights associated with each connection. The vector representation of weight is given as ($W' = w_1, w_2, \ldots, w_n$), the input vector is given by ($X = x_1, x_2, \ldots x_n$), and "b" represents the bias expressed in equation (2). "f" represents the activation function, through which the output is generated from the immediate previous proceeded layer, which is chosen based on the presence of node in the hidden or output layer and the type of problem stated. Some of the commonly used activation functions in the literature are logistic sigmoid function, hyperbolic tangent

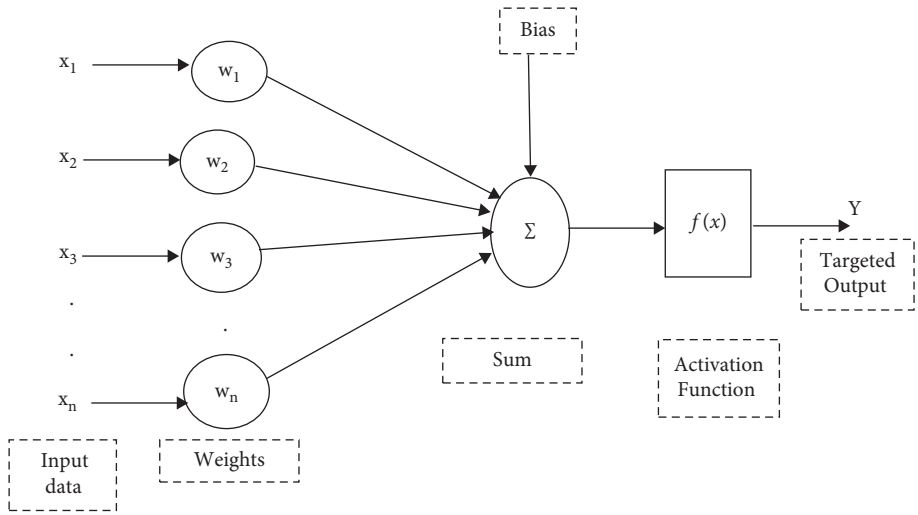

Figure 1: Architecture of an artificial neuron.

sigmoid function, Gaussian radial basic function, linear Unipolar step function, Bipolar step function, Unipolar linear function, and Bipolar linear function [34], and their illustration is given in [35].

2.2. Feedforward Backpropagation Process. It is a two-way process, used to train the model for attaining the desired output by reducing the error. The first way includes forward computation of input weights, and the second way includes the backward process of updating weights based on error obtained [36]. The basic structure of the Feedforward network includes an input layer, a hidden layer, an output layer, and their connection associated with its adoptable synaptic weights. Each layer is made up of a specific number of neurons or nodes, by which the information exchange and decision-making take place. Each node receives input from its previous nodes with the weighted sum of their input and added bias. Then, its result proceeded to activation function at each layer for producing the targeted prediction. The procedure is repeated for several iterations with randomly generated weights until the desired output is attained. As it is a black box model [37], the technique finds the useful and complex relationship between the input and output variables in attaining the targeted output. Hence, the learning and generalization have been carried out effectively. Therefore, ANN is especially used in classification, prediction, and especially handling complex and noisy data [38]. Moreover, a neural network with one hidden layer is sufficient and more common than multiple hidden layers-based networks [39, 40].

Later, in advance, to reduce overfitting, convergence at local maxima, and the convergence rate, the back-propagation learning process has been exhibited. This process starts from the output layer and migrates toward the first layer with the updated weights. Here, based on the input signal, the network generates an output. Then, the error is calculated according to the difference between the obtained and actual target. With the note of reducing the error and to get the desired output, the weights are modified and adjusted using a training algorithm. Hence, the process is repeated on every iteration until the error reaches the predetermined range. The general expression used to calculate the partial derivative of error at the nth layer is given by the following equation:

$$E_n = \frac{1}{2} \sum (Y_n - T_n)^2, \tag{3}$$

where Y_n represents the actual output at the nth layer, T_n denotes the targeted output at the nth layer, and E_n denotes the error generation at the nth layer. Figure 2 illustrates the schematic of the multilayer FFBP-ANN process used in the study with five input features, 20 neurons, and hourly GHI as the output [41].

2.3. Levenberg-Marquardt Training Algorithm. The powerful and widely used algorithm for training the neural network is the LM algorithm for adjusting the weights in accordance with the error calculated. Hence, the error obtained will be minimized within a tolerable range, within less iteration, and in a faster manner. The uniqueness of LM algorithm performance is due to the combined design of the Steepest descent algorithm and the Gauss-Newton algorithm. The computation of the LM algorithm related to the Hessian matrix and the Jacobian matrix is expressed using the following equation:

$$w'_{n+1} = w'_n - \left[J_n^T J_n + \mu I\right]^{-1} J_n^T e_n, \tag{4}$$

where

$$H = J_n^T J_n. \tag{5}$$

Based on the parameter μ, the training process switches between the Steepest descent algorithm and the Gauss-Newton algorithm. When μ is small or close to zero, the Gauss-Newton algorithm is performed. It is expressed using the following equation:

$$w'_{n+1} = w'_n - \left[J_n^T J_n\right]^{-1} J_n^T e_n. \tag{6}$$

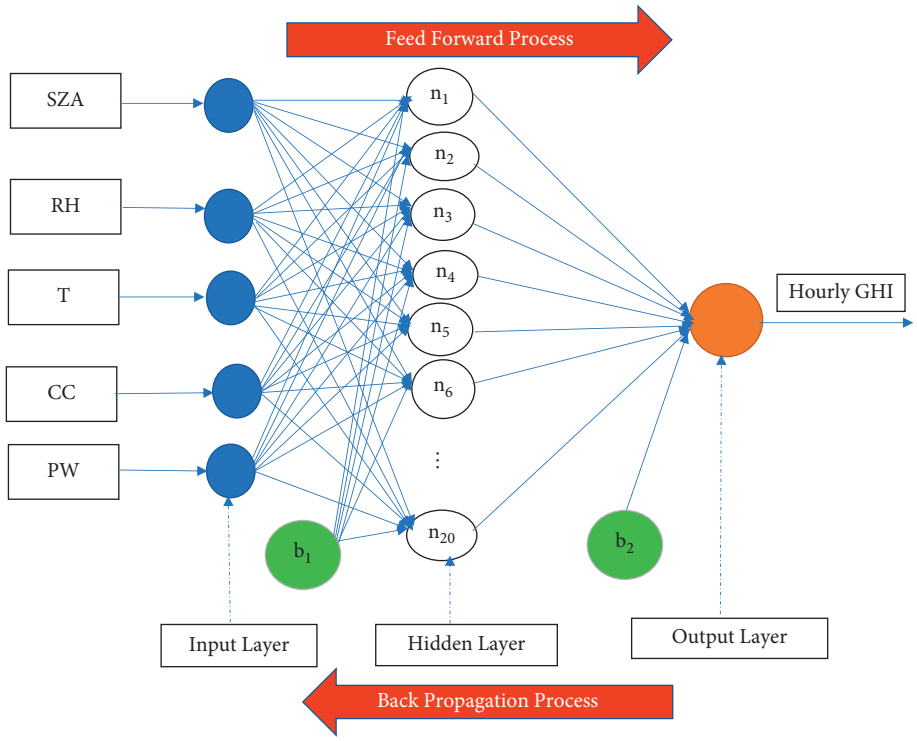

Figure 2: Schematic representation of multilayer FFBP-ANN used in the study.

When μ is very larger, the steepest descent algorithm will be carried out. It is expressed using the following equation:

$$w'_{n+1} = w'_n - \alpha g. \tag{7}$$

When μ is still larger, then consider $\alpha = 1/\mu$. In this way, the performance function gets reduced during every iteration, where w'_{n+1} →Weight of next iteration, w'_n -Weight of current iteration, J-Jacobian matric (has the derivative of the network error concerning weight and bias), e_n- Vector of the network error, μ-Combination coefficient, g- Gradient, H-hessian matrix, and I-Identity matrix [34, 42–45].

2.4. Case Study Region. The network model is designed for the Rooftop solar panels of VIT University, Chennai, with a total capacity of 550 KW whose Latitude and Longitude are 12.8406°N, 80.1534°E, respectively, as shown in Figure 3. While looking at the geographical and climatic nature, the region is situated at the southeast coast of India and the northeast corner of Tamil Nadu. It is characterized by tropical wet and dry climate as it is located at the Eastern coastal plane. Moreover, the city lies on the thermal equator, which helps in preventing extremely varying seasonal temperatures. Hence, the City receives a minimum temperature of 18–20 degrees Celsius and a maximum temperature of 38–42 degrees Celsius. Generally, the weather is hot and humid, and the seasons are pleasant (November–February), hot (March–June), and Heavy rainfall (July–September) every year.

2.5. Data Collection. In this study, a 4-year dataset with 18 features, namely, Year, Month, Day, Hour, Temperature,

Figure 3: Arrangement of Rooftop solar panels of VIT University, Chennai.

Cloud Type, Dew Point, DHI, DNI, Relative Humidity, Solar Zenith Angle, Surface Albedo, Pressure, Precipitable Water, Wind Direction, Wind Speed, Cell Temperature, and GHI was obtained for the abovementioned location from National Renewable Energy Laboratory (NREL) with the granularity of one hour. The dataset of years 2016, 2017, and 2018 was used for preparing the model. The effectiveness of the design in irradiation prediction is validated by checking the model using the dataset 2019.

2.6. Data Preprocessing. Before processing the data into the model, some of the preprocessing steps, such as removal of outliers and filling the missing data using the most expected GHI values, are performed to improve accuracy and faster response. The outliers were removed from the dataset using the "isoutliers" command to prevent wrong prediction and

skewing of the ML model. Hence, the night data were removed from the entire dataset. Because the power generation from solar panels is performed only during the presence of sunlight, therefore, the data were considered only from 7 am to 5 pm, and others were removed as outliers. The second most important preprocessing step taken is data normalization. It is used to transform the different ranges of the variable between 0 to 1. This process helps improve the accuracy and training process and make a better correlation between features. They are formulated using the following equation:

$$X_{\text{Normalized}} = \frac{x_{\text{Act}} - Min(x)}{Max(x) - Min(x)}. \tag{8}$$

Once the training and testing using the normalized value are over, then for verification and validation of model performance, the obtained predicted GHI and the target GHI values were generated and denormalized using the following equation:

$$x_{\text{Act}} = X_{\text{Normalized}}\left[\text{Max}(x) - \text{Min}(x)\right] + \text{Min}(x), \tag{9}$$

where x_{Act} represents the present value of data, Max(x) and Min(x) represent the maximum and minimum value of the dataset, and $X_{\text{Normalized}}$ ranged from 0 to 1 obtained using equation (8).

2.7. Feature Selection Process. As the model is highly dependent on feature variables for reliable prediction, the most significant features for attaining hourly GHI among metrological data are ranked using the Pearson correlation coefficient. It numerically expresses the relation between the independent variable and the dependent one. The mathematical equation for calculating the coefficient is expressed in the following equation:

$$r = \frac{\sum(x_k - \overline{x})(y_k - \overline{y})}{\sqrt{\sum(x_k - \overline{x})^2 \sum(y_k - \overline{y})^2}}, \tag{10}$$

where, r-Correlation coefficient, x_k-Value of the input variable, $\overline{x}$ - mean value of input variable, y_k-values of the output variable, and $\overline{y}$ -mean value of output variable. The 'corrplot' is the MATLAB command used for calculating the Pearson correlation coefficient between each input and output variable. Hence, the computational complexity, cost, and forecasting error get decreased. To avoid overfitting problems in the ML model, only training data are used to find the correlation rank. However, our goal is to predict GHI under dynamically varying irradiation profiles especially due to various environmental factors. Hence, cell temperature, DHI, and DNI ranked in the first 3 places in correlation calculation, whose regression fit is .99902 when considered, as the features for the network are purposefully not considered for this study application. So, we are considering the rest of the superior environmental variables from the Pearson ranking. Therefore, after analyzing the database, the model was designed using selected features such as Solar Zenith angle ($r = -0.88456$), Relative Humidity ($r = -0.65959$), Temperature ($r = 0.55199$), Cloud cover ($r = -0.21625$), and Precipitable water ($r = -0.65959$) for better prediction without sacrificing accuracy. It is to be observed that a higher negative correlation coefficient value also has a more significant relation to GHI prediction. All these preprocessing procedures were carried out in the same MATLAB version mentioned.

2.8. Design of FFBP-LM-ANN Used in the Study. FFBP-LM-ANN-based forecasting mechanism is developed in MATLAB 2020b platform using "nntool" to predict short-term (hourly) GHI under dynamically varying environmental conditions especially using environmental data. Furthermore, for the prediction of hourly GHI, the ANN is designed with 3 layers, such as the input layer, one hidden layer, and the output layer. The number of neurons in the hidden layer whose lower and upper limits are calculated based on equation (11)is as follows [46]:

$$2(n_i + n_o) \le n_1 \le \frac{K(n_i + n_o) - n_o}{n_i + n_0 + 1}, \tag{11}$$

where n_i indicates the number of input variables, n_o represents the number of output variables, and K represents the number of instances. Usually, for any complex applications, it is enough to have the number of hidden layers that is chosen to be one for a better and simple design [21]. In this work, for the calculation of the number of neurons in the hidden layer, we have considered n_i as 5, n_o as 1, and K as 13198. Therefore, the number of neurons in the hidden layer ranges from 12 to 11312.4, respectively, according to equation (10). For simple and faster access in identifying the number of neurons in the hidden layer, we have considered the neurons that were chosen in the related work with five independent variables. Thereby, the optimal number of hidden layers and number of neurons in the hidden layer are decided during the learning state after performing several trials by considering the criterion MSE, time taken for training, number of Epochs, and best fit R-value. Hence, the ANN model used here is Feedforward Backpropagation Neural Network with five independent variables, a single hidden layer with 20 neurons, and one dependent variable GHI as output. Also, we used Levenberg-Marquardt Backpropagation optimizer as the training algorithm for updating the weights. Even though the memory consumed is more, satisfactory processing at a very faster rate also makes the error within the tolerable range. More significantly, the optimizer stops functioning when there is no improvement in generalization, which are indicated by an increase in the MSE value of the validation samples. The inclusion of the activation function in the network plays a major role in transforming or mapping the complex input to the response variable and decides whether the neuron is to be activated and proceeds as the input to the consecutive layer or not. The most effective activation function used in the hidden layer is "tansig," and "purelin" is used in the output layer [28, 32, 47]. Because "tansig" is the nonlinear activation function used for solving a complex problem in a single layer network, it transfers the real value of input between −1 and +1 and supports well under the backpropagation process.

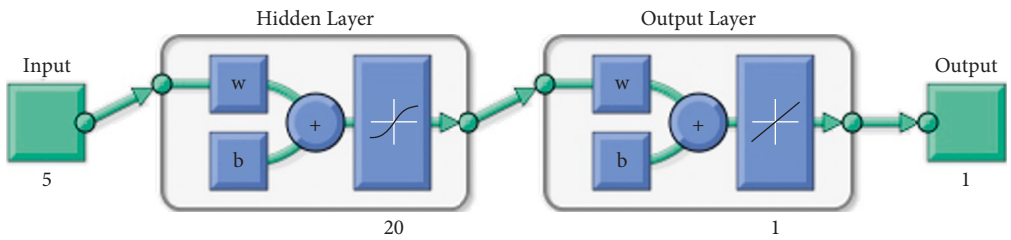

Figure 4: The architecture of the designed ANN.

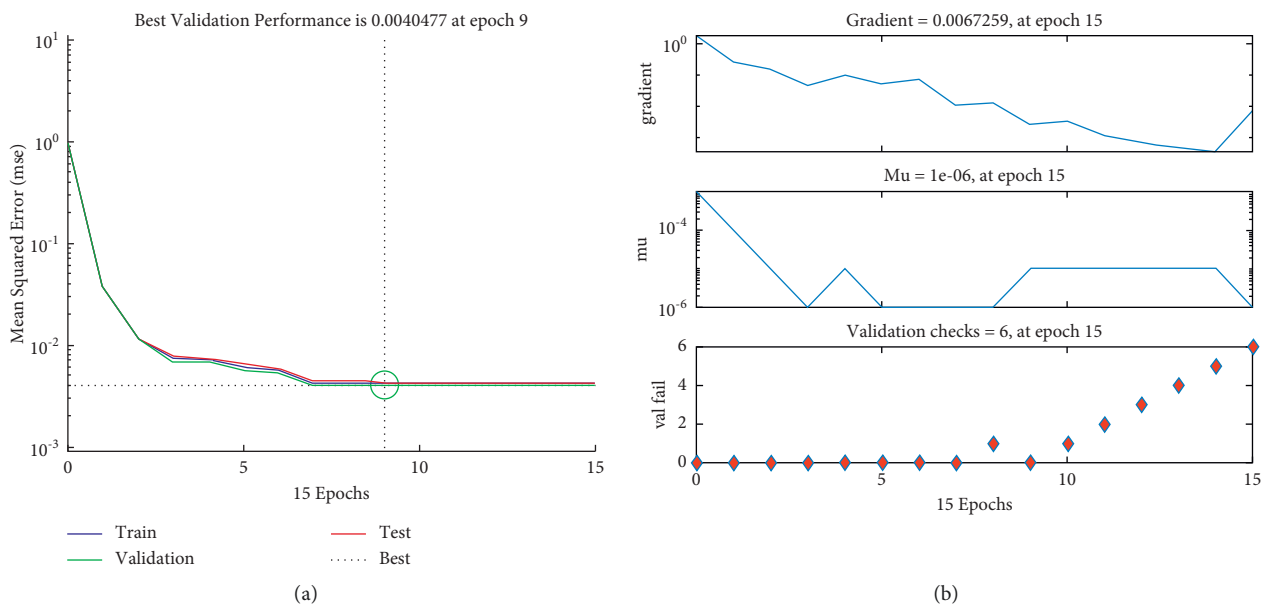

Figure 5: (a) MSE plot. (b) Performance of gradient, mu and validation check during the training process of designed FFBP-LM-ANN model for the collected dataset.

Also, it has the capability of strongly mapping the negative input value as negative and also producing zero centered output for the zero-input data compared with the sigmoid function. The "purelin" is the linear activation function that produces the responses between -infinitive to + infinitive. Here, it is preferred in the output layer, since the output is not confined within any range.

The model is processed by considering the dataset of the year 2016, 2017, and 2018 for preparing the model. Among them, it utilizes 75% of data for training, 15% for validation, and 15% for testing. Finally, the 2019 dataset was used for validating the effectiveness of the designed model. In order to observe the performance of the model under all climatic conditions at the targeted location, the data of the entire year are used to train and test the network. Figure 4 illustrates the Architecture of the designed ANN using MATLAB 2020b software.

3. Results and Discussion

3.1. Performance Analysis. The MSE plot of the designed FFBP-LM-ANN model obtained during the training, validation, and testing process related to Epochs is illustrated in Figure 5(a). It shows that once the input is processed, the network produces the predicted output. Then, that output will be compared with the target with the determination of MSE at the end of each iteration. Once the target and prediction are matched, then the learning process ends, and MSE reaches the minimum value. Thus, the plot reported that as the iteration increases, MSE gradually decreases. Therefore, MSE plays a vital role in checking the performance of the model. It is observed that, after 9 epochs, the system fails six times during training according to the validation check provided. Thereby, the best performance with a minimum Mean Square Error target is achieved at 15 epochs within a second. Figure 5(b) demonstrates the performance of gradient, mu, and validation check steps during the training process of the designed model. The first two plots show the attained values of gradient and mu at every epoch. Hence, the optimal values of gradient and mu are achieved at 15 epochs. The validation plot explains that, after seven epochs, the system fails once, and then the system corrects itself. Further, the system fails six times after nine epochs, thereby the training process stops.

Figure 6 shows the regression plots of the correlation coefficient obtained by the LM-ANN model during training, validation, and testing whose values are $R = 0.97401$, $R = 0.97509$, and $R = 0.97298$, respectively. It shows how closely the target and the output were related. It is observed that the overall regression correlation coefficient obtained is

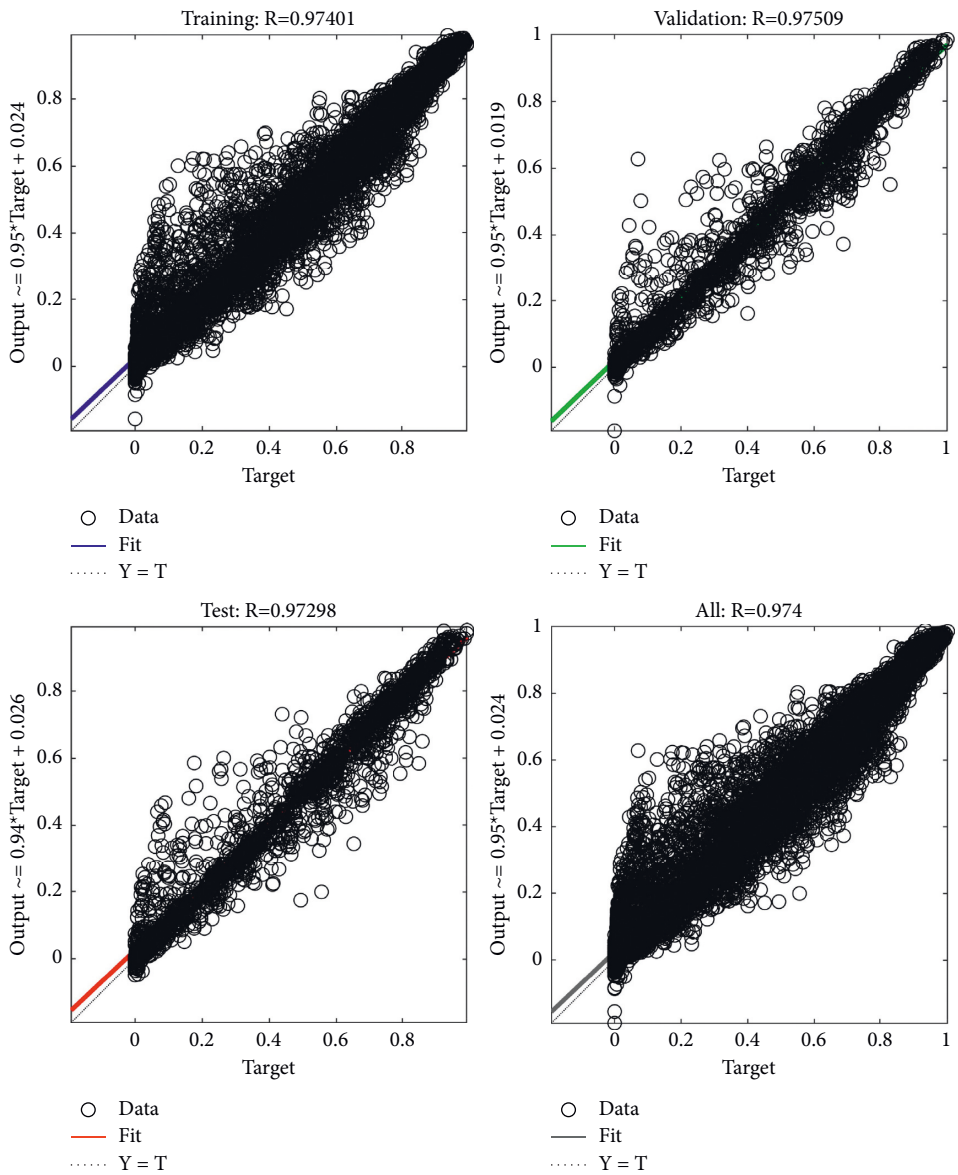

Figure 6: Regression plots of FFBP-LM-ANN model during training, testing, and validation process.

$R = 0.974$, which resembles that the output has good relation with the target.

The performance of the designed LM-ANN model was visualized by comparing the actual hourly GHI and the predicted hourly GHI obtained for the targeted location. Hence, Figure 7 shows the actual and predicted hourly GHI during the training process for the VIT site under the corresponding years 2016, 2017, and 2018 (total instances 13198) as illustrated. Then, the difference between the actual and the predicted GHI obtained during the training process is calculated and called an error, as shown in Figure 8. It can be seen that the predicting model can track the actual value firmly, because the notable number of errors is purposely maintained for better generalization during test data and to avoid overfitting problems.

The effectiveness/generalization of the design used in training is evaluated by subjecting the model to a new dataset with the same 5 features used in training, but for the year 2019, 4410 samples were collected from the exact location where the training data were collected. Figure 9 shows the performance comparison of actual hourly GHI with the predicted hourly GHI produced by the designed model for the corresponding year 2019 for the VIT site are illustrated. The difference between actual and predicted hourly GHI was calculated and graphically visualized as an error in Figure 10. It is observed from the error plot that, in the first half of every year, the prediction is much better; after that, it seems to be more fluctuating. It is due to the monsoon faced by the city every year. Hence, it is confirmed that the design was significantly working well in the hourly GHI prediction for the targeted location of Chennai.

The responses obtained by the FFBP-LM-ANN model during training and testing using selected hourly environmental variables such as Solar Zenith Angle, Relative

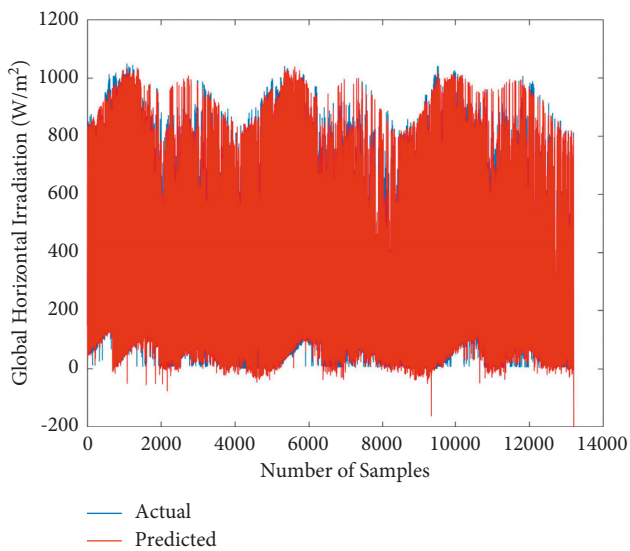

Figure 7: Performance comparison of actual and predicted hourly GHI obtained by FFBP-LM-ANN model during the training process.

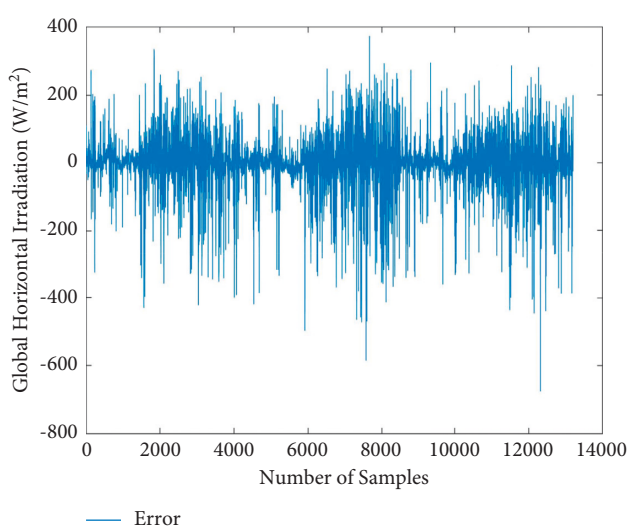

Figure 8: Error obtained during the training process of FFBP-LM-ANN.

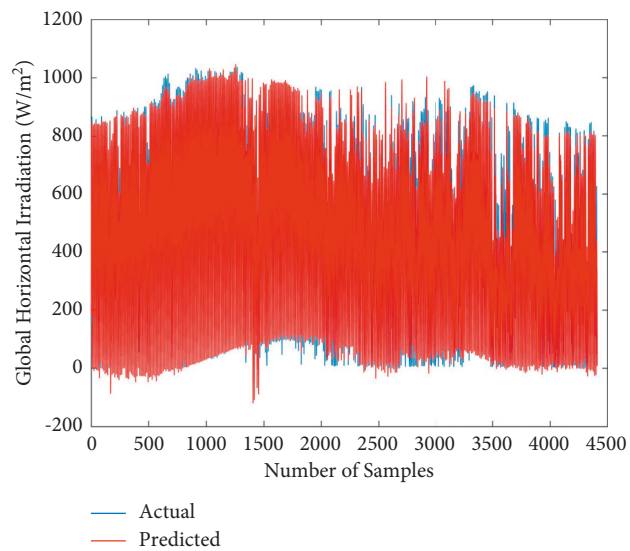

Figure 9: performance comparison of actual and predicted hourly GHI by FFBP-LM-ANN model during the testing phase.

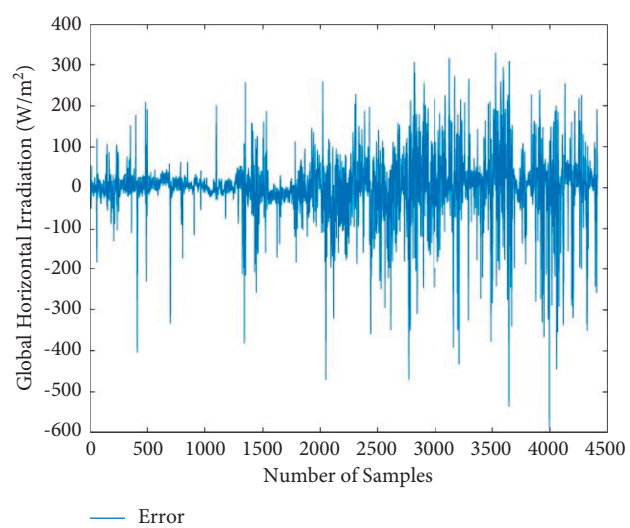

Figure 10: Error obtained during the testing process of FFBP-LM-ANN.

Humidity, Ambient Temperature, Cloud cover, and precipitate of VIT University, Chennai ,were analyzed. The performances are validated by computing the performance matrices from the actual, predicted, and error values obtained [48–51].

The performance of the study model was evaluated by the most commonly used statistical indicators such as MSE, RMSE, rRMSE, MAE, rMAE, MAPE, MBE, R^2, MRE, and NSE, which are calculated and displayed in Table 1. According to the range of rRMSE specified in [31], this model attains excellent rRMSE in both training and testing as 6.562% and 7.21%, respectively. Likewise, the ranges of MAPE were specified in [28]. The model receives satisfactory MAPE under training and testing conditions whose values are 0.386397 and 0.44432, respectively. The MBE shows very small values of bias, in both training and testing; it shows that the model makes a very closer prediction with minor error based on actual and predicted values. The other indicators, such as rMAE and MRE, have got values within the tolerable range. The designed LM-ANN model has attained a correlation coefficient of 0.96 and Nash Sutcliffe efficiency (NSE) of 94% during the testing process. Overall, the model has attained satisfactory performance based on most of the error indicators.

4. Comparison of Study Model with Existing Similar Models

The performance of the study model is compared with other similar existing works performed all over the world mentioned in the literature, which are presented in decreasing

Table 1: The statistical performance measure of the FFBP-LM-ANN model during training and testing.

Model/Input features	Performance index	Expression	Training/(2016, 2017, 2018)	Testing/(2019)
FFBP-LM-ANN/SZA, RH, T, CC, Pp	MSE	$1/N \sum_{i=1}^{n} (G_{\text{ANN}} - G_{\text{Actual}})^2$	0.004306	0.005078
	RMSE	$\sqrt{1/N \sum_{i=1}^{n} (G_{\text{ANN}} - G_{\text{Actual}})^2}$	0.06562	0.07126
	rRMSE	$\text{RMSE} \times 100/G_{\text{Actual (Max)}}$	6.562%	7.21%
	MAE	$1/N \sum_{i=1}^{n} \lvert G_{\text{ANN}} - G_{\text{Actual}} \rvert$	0.039332	0.042448
	rMAE	$\text{MAE}/\overline{G_{\text{Actual}}} \times 100$	8.7336%	9.4829%
	MAPE	$1/N \sum_{i=1}^{n} \lvert G_{\text{ANN}} - G_{\text{Actual}} \rvert / G_{\text{Actual}} \times 100$	38.6397%	44.432%
	MBE	$1/N \sum_{i=1}^{n} (G_{\text{ANN}} - G_{\text{Actual}})$	0.00004002301	0.000492
	R	$\sqrt{1 - \sum_{i=1}^{n} (G_{\text{Actual}} - G_{\text{ANN}})^2 / \sum_{i=1}^{n} (G_{\text{Actual}} - \overline{G_{\text{ANN}}})^2}$	0.961542	0.959541
	MRE	$1/N \sum_{i=1}^{n} \lvert G_{\text{ANN}} - G_{\text{Actual}} \rvert / G_{\text{total}} \times 100$	8.73336%	9.5566%
	NSE	$1 - 1/N \sum_{i=1}^{n} (G_{\text{Actual}} - G_{\text{ANN}})^2 / 1/N \sum_{i=1}^{n} (\overline{G_{\text{Actual}}} - G_{\text{ANN}})^2$	0.95	0.94

Table 2: Performance comparison of study model with similar existing work.

References	Location	Variables	Network	Epochs	RMSE
[25]	Buraydash/Saudi Arabia	DNI, SZA, DHI, hours	4-5-1	-	30.23
[45]	India	Hourly climate data	13-20-1	36	7.591
[27]	Nigeria	Lat, long, day of the year, year	4-20-1	46	3.98
[21]	Mumbai/India	Lat, log and altitude, year and month, mean ambient temperature, mean station level pressure, mean wind speed, mean relative humidity.	6-24-1	1000	3.6461
[23]	Makurdi/Nigeria	Min. Temperature, max. Temperature, relative humidity, wind speed, sunshine hours	5-5-5-4-1	1000	0.98831
[17]	Utter Pradesh/India	Lat, long, altitude, max. Temperature, min. Temperature, humidity, wind speed, sunshine, solar radiation	9-10-1	33	0.1936
[26]	Adane/Turkey	Actual pressure, wind speed, wind direction, relative humidity, average temperature	5-10-30–1	124	0.1543
[24]	New Delhi/India	Lat, long, elevation, the month of the year, day of the month, temperature, atmospheric pressure, humidity, wind speed	9-10-1	1000	0.09441
[30]	Tehran	Temperature, relative humidity, wind speed, particulate matter	5-12-24–1	-	0.0773
Present study	**Chennai/India**	**SZA, RH, T, CC, PW**	**5-20-1**	**15**	**0.07126**

order in Table 2. Their performances are compared in terms of the most commonly used matrices called RMSE, epoch, network design, and the input variables used. It is noted that the study model has the exact fit of predicted value to actual data points with a minimum RMSE of 0.07126 than other related works. In addition to that, the model performs the prediction within 15 epochs, which resembles the simple network structure, and an optimal number of neurons were considered, which highlights the superiority of the models compared with other FFBP-LM-ANN designs. Ultimately, the effective environmental feature related to dynamic irradiation profiles considered in this study makes the prediction process more precise when compared with other similar works. More importantly, it is observed that the irradiation can be predicted well under environmental factors rather than geographical features such as latitude, longitude, altitude, elevation, and time zone, which are considered in [17, 21, 24, 27, 45] whose RMSE values and computational complexity are predominantly higher.

5. Conclusion

The hourly Global Horizontal Irradiation prediction was performed by FFBP-LM-ANN using a 4-year database received from NREL for the rooftop panels of VIT University, Chennai. The article discussed a fast and powerful LM-Backpropagation training algorithm for error minimization in the network. The model utilized a simple feature selection process and effective mathematical expression for calculating the optimal hidden layer neurons without compromising the performance. The performance of the model was evaluated using rRMSE, MAE, MBE, R, NSE, MAPE, and MRE of 7.21%, 0.042, 0.000492, 0.96, 94%, 44.43, and 9.5%, respectively. The effective comparison was made with 9 related existing works to show the superiority of the model based on input variables, network design, epoch, and RMSE. Consequently, such a predictor will be reliable and suitable for quantifying the irradiation potential using environmental variables at any location across the world facing dynamic climatic conditions.

In the future, this work will be enhanced by developing the model hybrid with an optimization algorithm for hyperparameter tuning in improving the performance of irradiation forecaster with increased prediction accuracy. In addition to that, the very short-term prediction and seasonal performance of the model should be analyzed.

Data Availability

The data used to support the findings of this study are included in the article. Further data or information required is available from the corresponding author upon request.

Conflicts of Interest

The authors declare that there are no conflicts of interest regarding the publication of this paper.

Acknowledgments

The authors sincerely acknowledge "National Renewable Energy Laboratory (NREL)" for providing a sufficient dataset in the development of our model. Special thanks are due to VIT University, Chennai, for granting facilities and support during the preparation of the manuscript.

References

[1] S. Manabe, "Role of greenhouse gas in climate change∗∗," *Tellus A: Dynamic Meteorology and Oceanography*, vol. 71, no. 1, pp. 1–13, 2019.

[2] V. Manieniyan, M. Thambidurai, and R. Selvakumar, "Study on energy crisis and the future of fossil," in *Proceedings of the SHEE 2009, Engineering Wing, DDE, Annamalai University*, Chidambaram, Tamil Nadu, pp. 7–12, 2009.

[3] A. El Hendouzi and A. Bourouhou, "Solar photovoltaic power forecasting," *Journal of Electrical and Computer Engineering*, vol. 2020, Article ID 8819925, 21 pages, 2020.

[4] Z. E. Mohamed, "Using the artificial neural networks for prediction and validating solar radiation," *Journal of the Egyptian Mathematical Society*, vol. 27, no. 1, 2019.

[5] A. Alzahrani, P. Shamsi, C. Dagli, and M. Ferdowsi, "Solar irradiance forecasting using deep neural networks," *Procedia Computer Science*, vol. 114, pp. 304–313, 2017.

[6] R. Ahmed, V. Sreeram, Y. Mishra, and M. D. Arif, "A review and evaluation of the state-of-the-art in PV solar power forecasting: techniques and optimization," *Renewable and Sustainable Energy Reviews*, vol. 124, Article ID 109792, 2020.

[7] P. Singla, M. Duhan, and S. Saroha, "A comprehensive review and analysis of solar forecasting techniques," *Frontiers in Energy*, 2021.

[8] S. Ghimire, R. C. Deo, N. J. Downs, and N. Raj, "Global solar radiation prediction by ANN integrated with European Centre for medium range weather forecast fields in solar rich cities of Queensland Australia," *Journal of Cleaner Production*, vol. 216, pp. 288–310, 2019.

[9] H. Ghoddusi, G. G. Creamer, and N. Rafizadeh, "Machine learning in energy economics and finance: a review," *Energy Economics*, vol. 81, pp. 709–727, 2019.

[10] A. Kumar, M. Rizwan, and U. Nangia, "A hybrid intelligent approach for solar photovoltaic power forecasting: impact of aerosol data," *Arabian Journal for Science and Engineering*, vol. 45, no. 3, pp. 1715–1732, 2020.

[11] A. Qazi, H. Fayaz, A. Wadi, R. G. Raj, N. A. Rahim, and W. A. Khan, "The artificial neural network for solar radiation prediction and designing solar systems: a systematic literature review," *Journal of Cleaner Production*, vol. 104, pp. 1–12, 2015.

[12] G. M. Yagli, D. Yang, and D. Srinivasan, "Automatic hourly solar forecasting using machine learning models," *Renewable and Sustainable Energy Reviews*, vol. 105, pp. 487–498, 2019.

[13] J. Fan, L. Wu, F. Zhang et al., "Empirical and machine learning models for predicting daily global solar radiation from sunshine duration: a review and case study in China," *Renewable and Sustainable Energy Reviews*, vol. 100, pp. 186–212, 2019.

[14] A. K. Yadav and S. S. Chandel, "Solar radiation prediction using Artificial Neural Network techniques: a review," *Renewable and Sustainable Energy Reviews*, vol. 33, pp. 772–781, 2014.

[15] K. B. Debnath and M. Mourshed, "Forecasting methods in energy planning models," *Renewable and Sustainable Energy Reviews*, vol. 88, pp. 297–325, 2018.

[16] A. Alfadda, S. Rahman, and M. Pipattanasomporn, "Solar irradiance forecast using aerosols measurements: a data driven approach," *Solar Energy*, vol. 170, no. June, pp. 924–939, 2018.

[17] A. Choudhary, D. Pandey, and S. Bhardwaj, "Artificial neural networks based solar radiation estimation using back-propagation algorithm," *International Journal of Renewable Energy Resources*, vol. 10, no. 4, pp. 1566–1575, 2020.

[18] E. A. Ahmed, "Statistical comparison between empirical models and artificial neural network method for global solar radiation at qena, Egypt," *J. Multidiscip. Eng. Sci. Technol.*, vol. 2, no. 7, pp. 1899–1906, 2015.

[19] M. Al-Shamisi, A. Assi, and H. Hejase, "Estimation of global solar radiation using artificial neural networks in Abu Dhabi city, United Arab Emirates," *Journal of Solar Energy Engineering*, vol. 136, no. 2, 2014.

[20] J. Zhu, B. Arsovska, and K. Kozovska, "Acupuncture treatment in osteoarthritis," *Int. J. Recent Sci. Res.*, vol. 11, no. 02, pp. 37471-37472, 2020.

[21] N. Premalatha and A. Valan Arasu, "Prediction of solar radiation for solar systems by using ANN models with different back propagation algorithms," *Journal of Applied Research and Technology*, vol. 14, no. 3, pp. 206–214, 2016.

[22] M. Bou-Rabee, S. A. Sulaiman, M. S. Saleh, and S. Marafi, "Using artificial neural networks to estimate solar radiation in Kuwait," *Renewable and Sustainable Energy Reviews*, vol. 72, pp. 434–438, 2017.

[23] A. Kuhe, V. T. Achirgbenda, and M. Agada, "Global solar radiation prediction for Makurdi, Nigeria, using neural networks ensemble," *Energy Sources, Part A: Recovery, Utilization, and Environmental Effects*, vol. 43, no. 11, pp. 1373–1385, 2021.

[24] A. Choudhary, D. Pandey, and S. Bhardwaj, "Overview of solar radiation estimation techniques with development of solar radiation model using artificial neural network," *Advances in Science, Technology and Engineering Systems Journal*, vol. 5, no. 4, pp. 589–593, 2020.

[25] M. A. A.-H. Abdulatif Aoihan Alresheedi, "Hybrid artificial neural networks with Boruta algorithm for prediction of global solar radiation: case study in Saudi arabia," *Lecture Notes in Computer Science*, vol. 9, no. 2, pp. 19–27, 2020.

[26] O. Goncu, T. Koroglu, and N. F. Ozdil, "Estimation of hourly global solar radiation using artificial neural network in Adana province, Turkey," *Journal of Thermal Engineering*, vol. 7, no. 14, pp. 2017–2030, 2021.

[27] I. G. Friday, B. C. Udochukwu, T. Igbawua, T. Alaxander, and O. J. Ndubuisi, "Assessment of global solar radiation at selected points in Nigeria using artificial neural network model (ANNM)," *International Journal of Environment and Climate Change*, vol. 9, no. 7, pp. 376–390, 2019.

[28] S. Kumar and T. Kaur, "Development of ANN based model for solar potential assessment using various meteorological parameters," *Energy Procedia*, vol. 90, pp. 587–592, 2016.

[29] M. Mohandes, S. Rehman, and T. O. Halawani, "Estimation of global solar radiation using artificial neural networks," *Renewable Energy*, vol. 14, no. 1–4, pp. 179–184, 1998.

[30] M. Vakili, S.-R. Sabbagh-Yazdi, K. Kalhor, and S. Khosrojerdi, "Using artificial neural networks for prediction of global solar radiation in tehran considering particulate matter air pollution," *Energy Procedia*, vol. 74, pp. 1205–1212, 2015.

[31] D. V. S. K. Rao K, M. Premalatha, and C. Naveen, "Analysis of different combinations of meteorological parameters in predicting the horizontal global solar radiation with ANN approach: a case study," *Renewable and Sustainable Energy Reviews*, vol. 91, pp. 248–258, 2018.

[32] H. Ghritlahre, "Development of feed-forward back-propagation neural model to predict the energy and exergy analysis of solar air heater," *Trends in Renewable Energy*, vol. 4, no. 2, pp. 213–235, 2018.

[33] M. O. Moreira, P. P. Balestrassi, A. P. Paiva, P. F. Ribeiro, and B. D. Bonatto, "Design of experiments using artificial neural network ensemble for photovoltaic generation forecasting," *Renewable and Sustainable Energy Reviews*, vol. 135, Article ID 110450, 2021.

[34] M. A. Jallal, S. Chabaa, S. Chabaa, and A. Zeroual, "Half-hour global solar radiation forecasting based on static and dynamic multivariate neural networks," *Journal of Engineering Research*, vol. 9, no. 2, pp. 203–217, 2021.

[35] A. P. Yadav and L. Behera, "Solar radiation forecasting using neural networks and wavelet transform," *IFAC Proceedings Volumes*, vol. 47, no. 1, pp. 890–896, 2014.

[36] N. B. Shaik, S. R. Pedapati, S. A. A. Taqvi, A. R. Othman, and F. A. A. Dzubir, "A feed-forward back propagation neural network approach to predict the life condition of crude oil pipeline," *Processes*, vol. 8, no. 6, p. 661, 2020.

[37] A. Ibnelouad, A. E. L. Kari, H. Ayad, and M. Mjahed, "Multilayer artificial approach for estimating optimal solar PV system power using the MPPT technique," vol. 30, no. December, pp. 109–120, 2021.

[38] A. Mosavi, M. Salimi, S. Faizollahzadeh Ardabili, T. Rabczuk, S. Shamshirband, and A. Varkonyi-Koczy, "State of the art of machine learning models in energy systems, a systematic review," *Energies*, vol. 12, no. 7, p. 1301, 2019.

[39] H. Pourpasha, P. Farshad, and S. H. Zeinali, "Modeling and optimization the effective parameters of nanofluid heat transfer performance using artificial neural network and genetic algorithm method," *Energy Reports*, vol. 7, pp. 8447–8464, 2021.

[40] N. Suresh, G. T. Nhinda, V. Hashiyana, P. Veerabhadram, and A. Limbo, "Use of Artificial Neural Network (ANN) to Predict the Output of a Photovoltaic (PV) System," 2020.

[41] F. A. Makinde, C. T. Ako, O. D. Orodu, and I. U. Asuquo, "Prediction of crude oil viscosity using feed-forward back-propagation neural network (FFBPNN)," *Pet. Coal*, vol. 54, no. 2, pp. 120–131, 2012.

[42] P. B. Duttagupta and D. Roy, "ANN based techniques for short term load forecasting," *Indian Institute of Technology, Kharagpur 721302*, pp. 327–330, 2002.

[43] A. Sarfuddin and A. Tiwari, "A comparative study of forecasting solar irradiation of indore city using different machine learning techniques," vol. 6, no. 6, pp. 27–32, 2018.

[44] B. Plangklang and J. Nantaphunkul, "ANN application for solar radiation forecasting using levenberg-marquardt algorithm," vol. 1, no. 1, 2015.

[45] A. Choudhary and V. Chauhan, "Solar energy prediction using ANN," vol. 21, no. 1, pp. 1–9, 2014.

[46] Nastaran Reza Nazar Zadeh, https://www.udemy.com/course/artificial-neural-network-and-machine-learning-using-matlab/learn/lecture/21837724#overview, 2021.

[47] F. J. Diez, L. M. Navas-Gracia, L. Chico-Santamarta, A. Correa-Guimaraes, and A. Martínez-Rodríguez, "ANNs for the daily prediction of horizontal global solar irradiation in an agrometeorological station with mediterranean warm summer climate," *Prime Archives in Agronomy*, Vide Leaf, Hyderabad, India, pp. 1–37, 2020.

[48] M. K. Behera, I. Majumder, and N. Nayak, "Solar photovoltaic power forecasting using optimized modified extreme learning machine technique," *Engineering Science and Technology, an International Journal*, vol. 21, no. 3, pp. 428–438, 2018.

[49] A. Takilalte and S. Harrouni, "Daily direct normal irradiance forecasting by support vector regression case study: in ghardaia-Algeria," in *Proceedings of the 2019 Int. Conf. Adv. Electr. Eng. ICAEE 2019*, pp. 1–6, Algiers, Algeria, November 2019.

[50] Z. U. R. Tahir, M. Azhar, P. Blanc et al., "The evaluation of reanalysis and analysis products of solar radiation for Sindh province, Pakistan," *Renewable Energy*, vol. 145, pp. 347–362, 2020.

[51] O. Kisi, S. Heddam, and Z. M. Yaseen, "The implementation of univariable scheme-based air temperature for solar radiation prediction: new development of dynamic evolving neural-fuzzy inference system model," *Applied Energy*, vol. 241, pp. 184–195, 2019.

Hindawi
Mathematical Problems in Engineering
Volume 2022, Article ID 4877422, 12 pages
https://doi.org/10.1155/2022/4877422

Research Article

Energy-Efficient Hybrid Power System Model Based on Solar and Wind Energy for Integrated Grids

Nishant Jha,[1] **Deepak Prashar**,[1] **Mamoon Rashid**,[2] **Zeba Khanam**,[3] **Amandeep Nagpal**,[1] **Ahmed Saeed AlGhamdi**,[4] **and Sultan S. Alshamrani**[5]

[1]*School of Computer Science and Engineering, Lovely Professional University, Jalandhar 144411, India*
[2]*Department of Computer Engineering, Faculty of Science and Technology, Vishwakarma University, Pune 411048, India*
[3]*College of Computing and Informatics, Saudi Electronic University, Dammam, Saudi Arabia*
[4]*Department of Computer Engineering, College of Computer and Information Technology, Taif University, P.O. Box 11099, Taif 21994, Saudi Arabia*
[5]*Department of Information Technology, College of Computer and Information Technology, Taif University, P.O. Box 11099, Taif 21944, Saudi Arabia*

Correspondence should be addressed to Mamoon Rashid; mamoon873@gmail.com

Received 10 October 2021; Revised 15 January 2022; Accepted 26 January 2022; Published 21 February 2022

Academic Editor: Araz Darba

Global energy needs have risen in recent years, and traditional energy sources such as fossil fuels are no longer viable. To meet the growing electricity demand, attention has moved to renewable energy sources such as solar and wind energy. Furthermore, the development of clean energy is vital for combating climate change. Various studies have shown the effectiveness of using hybrid systems (combination of solar photovoltaic and wind energy systems) for generating power. However, a significant amount of energy gets wasted. To prevent the wastage of energy, a dual-energy generation system for integrated grids has been suggested in this paper. The load data have been collected from various regions in Rajasthan, India. An optimal grid system configuration is designed using net present cost and cost per unit of energy. Other factors such as the tilt angle of PV array optimization, wind energy, and inverter optimization have also been used for increasing the reliability and stability of the system. Sensitivity analysis has been performed to analyze the effective variations of the capital costs on the developed system economy. The results obtained from the simulations show that the overall costs of generating electricity from diesel systems and nongrid-based systems have been reduced to 20% at 10% annual capacity shortage allowance. Upon cost analysis, we found that the total cost for installing the suggested system is 49,500 USD, whereas for other systems, the costs came out as 66,000 USD, 56,500 USD, and 56,300 USD, respectively.

1. Introduction

Hybrid energy systems have received worldwide attention for remote locations where grid supply is not feasible [1]. In remote areas, various renewable energy technologies such as standalone solar systems and minigrids have been introduced to achieve an efficient energy supply [2]. However, many of them do not offer real versatility to the end user or are not practical when they are launched, usually due to the lack of sales to offset product replacement and operating and repair costs. Furthermore, in the light of global grid growth, the concern that grid arrival at a particular location will render off-grid systems useless has recently spread among energy system investors [2, 3]. Climate change has become a major environmental concern in recent years as Green House Gas (GHG) emissions have increased [4]. As a result, it has been urged to look for alternative energy sources that can produce electricity [4], and wind and solar energy have been proven to be effective in producing cost-effective electricity [4]. In older times, only solar energy was used for generating electricity. Using only solar energy systems is having some challenges. These systems are not capable of

generating maximum power during cloudy or rainy days [5]. People who use this system will be without power until the battery has been discharged [5]. Maximum power can be produced by combining solar and wind energy production techniques [5]. For electric power generation systems, these kinds of integrated systems guarantee a pollution-free and accident-free inventory [5]. Various off-grid methodologies, such as hydroenergy and geothermal energy, have been tried in the past few years to improve power supply reliability, but they have failed [6, 7]. The key cause for such strategies' inability is their high energy prices, which are unaffordable on a broader scale [6, 7]. The system presented in this paper is based on various optimization techniques for enhancing the efficiency of the system, which can provide continuous power at lower costs, thus reducing the financial pressure on people living in rural areas. Integrating solar and wind energy into hybrid power generation systems will minimize induced power volatility relative to single Variable Renewable Energy (VRE) systems, increasing overall system efficiency and reliability [7]. As a result, the amount of capacity used in the device can be decreased significantly, resulting in significant cost savings [7]. The major contributions of the paper are as follows:

(i) In this paper, a hybrid and effective system for harnessing power is suggested based on IoT and a combination of solar and wind energy

(ii) The aim of this paper is to find the solution to the challenges in resolving carbon emission and enhancing power efficiency, along with the focus on predicting the cost of energy from the system

The remainder of the paper is organized as follows. The associated work is covered in Section 2. The importance of the research is explained in Section 3. The proposed architecture and optimization methods are explained in Section 4. Section 5 summarizes the research findings, and Section 6 concludes the paper. Section 7 explains the limitation of the current study and future scope of work.

2. Related Work

Due to increased awareness regarding climate change and other environmental issues, the expectations for generating power from renewable sources of energy have increased [8]. Various studies have been conducted to suggest cost-effective and efficient systems for generating electricity. In [8], the authors have suggested a novel analysis technique for pumped storage and thermal power generator with a detailed introduction of renewable energy sources (RESs). For addressing operational planning for thermal power generators and output decisions for pumped storage, this paper uses Tabu search and interior point methods [9, 10]. The authors of [11] gave a high-level overview of the functional integration of hybrid renewable energy systems (HRES) in multienergy buildings. The paper discussed the most commonly used HRES solutions in the residential sector, as well as an investigation of HRES integration with thermal and electrical loads in residential apartments, which were then connected to external energy grids. The authors of [12] demonstrated the advantages of expanding the integration of renewable energy sources in the insular system. The main focus of this paper is on profit maximization, cost efficiency, GHG reduction, and time consumption in power generation. The authors of [13] submitted a review of different control strategies used by battery storage systems for smoothing the output power of wind turbines in order to improve future energy applications. The authors of [14] applied model predictive control to a three-phase inverter and used another model to estimate future system voltage forecasts for a given set of voltages. The method presented in this paper avoids the use of linear and nonlinear controllers by avoiding the use of a modulator, and it was found to be effective and simple to implement. The authors used an integrated approach in [15], combining spatially explicit resource potential analysis with high spatial resolution modeling of the US electricity system. Various wind supply curves, reflecting variations in siting regimes such as regulatory, physical, and social land-use factors, are analyzed in this study to determine the impact of potential wind growth. In [16], the authors have optimized a hybrid energy system for catamaran ship. The authors have discussed PV performance, generator performance, dual-input buck boost, and simulation. In [17], the authors have suggested an economic day-ahead scheduling technique for a sustainable cogeneration system. A dynamic programming model was developed for which the goal is to minimize fuel consumption. In [18], the authors have focused on the design and performance analysis of dual-axis tracking solar systems. The authors have also conducted a detailed review of various types of solar tracking systems and types of solar PV cells. The performance analysis for various solar PV systems suggested by other authors as per the literature reviewed is compared in Table 1. Recent development also focuses on developing efficient battery technology for energy storage in smart grid systems. In [26], the authors have developed a power management system, which is capable of controlling the power flow for an integrated system. However, using this technology as a storage system will make the overall system more expensive, which might not be affordable for low-income countries. We want to keep the system as simple as possible through which we can cover both high-income and low-income countries. The authors of [27] have discussed finding an effective solution to replace natural gas for power generation with wind and solar energy. This study has also discussed the different cases of carbon-dioxide emission and the total cost of energy. However, the scope of the study is limited as in countries like Yemen and Saudi Arabia, natural gas is the most widely used for power generation, and it is not possible to extract the full potential of the integrated grid systems in these regions. So we have to develop a low-cost system to avoid wastage of investments in installing integrated systems under these conditions.

In [28], the authors have suggested a model for calculating tariffs at charging stations for electric vehicles. This paper also suggests the use of solar energy for charging electric vehicles (EVs). The approach suggested in this paper is unique, but various factors that affect the efficiency of the system such as tilt angle of the PV array have not been

Table 1: Comparison between performances of various PV systems.

Reference	Performance of the model suggested
[19]	The peak power for the solar PV system was computed to be 1928 wp.
[20]	The output efficiency of the PV system was largely affected by the rise in temperature.
[21]	The total energy generated from the system to fulfill the required load was 26% from grid, 32% from fuel cells, and 42% from solar PV.
[22]	The energy costs for a standalone system with a reformer were computed to be 0.164–0.233 USD/kWh. The addition of fuel cells to the hybrid systems will also increase these costs by 33–37%.
[23]	The annual power generated by the system suggested by the authors and deployed on highways of China has reached 356GWh.
[24]	Two hybrid power systems were suggested. Both the electrical efficiency and fuel economy have increased up to 2% and 12%, respectively.
[25]	Emission of GHG for hybrid energy systems with supercapacitor energy storage systems decreases by 814,428 gallons of the same diesel.

discussed. In [29], the authors have suggested a trigeneration system that produces ammonia, hydrogen, and electricity through the integrated solar system. This system can be fully implemented in high-income and middle-income countries, but in low-income countries, implementing this technique would be challenging as ammonia is a harmful substance and might cause respiratory diseases to the person who is operating the energy system or living nearby the system.

Upon analysis of the literature, we found that most of the works focus on developing complex systems which might affect the efficiency of the system and are not feasible for low-income or poor nations. Through this paper, we have tried to improve the system through various optimization techniques so that the system would be feasible for all.

3. Significance of Work

In contrast to conventional fossil fuel-based resources, renewable energy sources play a critical role in maintaining the country's economy and quality of life [30]. Due to the increase in severe problems as a result of climate change, this research may be useful in addressing the issues to some extent. Using an integration of solar energy and wind energy will cause zero pollution, low greenhouse emissions, and fewer challenges related to waste management [31]. The system suggested in this paper is a better alternative for nuclear energy for fulfillment of 100% of electricity needs of the world [31]. The solution suggested in this paper will help in achieving a continuous power supply without the risk of harming nature or humans. Various studies have shown only a single renewable energy source for producing electricity, either solar energy or wind energy. Single renewable sources, on the other hand, become problematic in terms of operational costs and energy yield due to the intermittent nature of renewable sources [32]. Two or more renewable sources are combined to form a hybrid energy system (HES) based on these drawbacks [32]. The main aim of implementing such a system is to maximize power production, lower operating costs, and increase system productivity [32]. The hybrid system proposed in this paper can be quickly introduced to provide end users with highly efficient and reliable power. An HES may be used as a standalone system or as part of a grid [32]. Standalone systems, on the other hand, need a lot of storage to handle the load [32]. In grid-connected systems, the storage can be small, which can decrease the efficiency of the system. So, it is advised to use HES in standalone modes for generating high power. The energy produced from the suggested system is stable without causing any type of pollution. With the current challenge of not having enough space to construct power plants as the world's population grows, it is critical to make efficient use of land used to produce electricity and to think carefully when constructing a power plant. The power plant must be located near the power availability area to avoid power transmission losses and low power transit costs [31]. Thus to increase the reliability of power generation, integrated systems are used. Furthermore, to increase the dependency of the overall system only on one technique, either solar/wind energy, the size of the storage battery is needed to be reduced and using integrated systems would help in achieving this.

4. System Architecture

There has been an increase in demand for renewable energy sources as the prices of nonrenewable energy sources have risen [33]. As a result, this paper proposes that electricity is generated using hybrid systems based on solar and wind energy. The windmills start rotation and generate electricity with the help of magnetic coupling between a rotating magnetic coil and a stationary magnetic coil when enough wind is available at the area where the system is supposed to be installed. This technique harnesses both wind and solar energy [33]. The working of the system is shown in Figure 1.

The wind turbine generator is used to charge the battery in Figure 1, and the ATMega 328 Microcontroller is used for smart sensing and charging of the batteries, with the output displayed on the LCD screen. The solar panels mounted on the revolving plates ensure optimum daylight visibility for producing enough power for charging the batteries. This system is a good example of how the natural resources can be effectively used for producing electricity at cheaper rates [33]. The internal working of the system can be explained as follows. The photovoltaic (PV) subsystem consists of PV modules connected in series or parallel according to the requirements. Power is generated by ultraviolet (UV) rays from the sun. Direct Current (DC) is produced, and then it is converted to Alternating Current (AC) with the help of an inverter [34–36]. For maximizing the power generation,

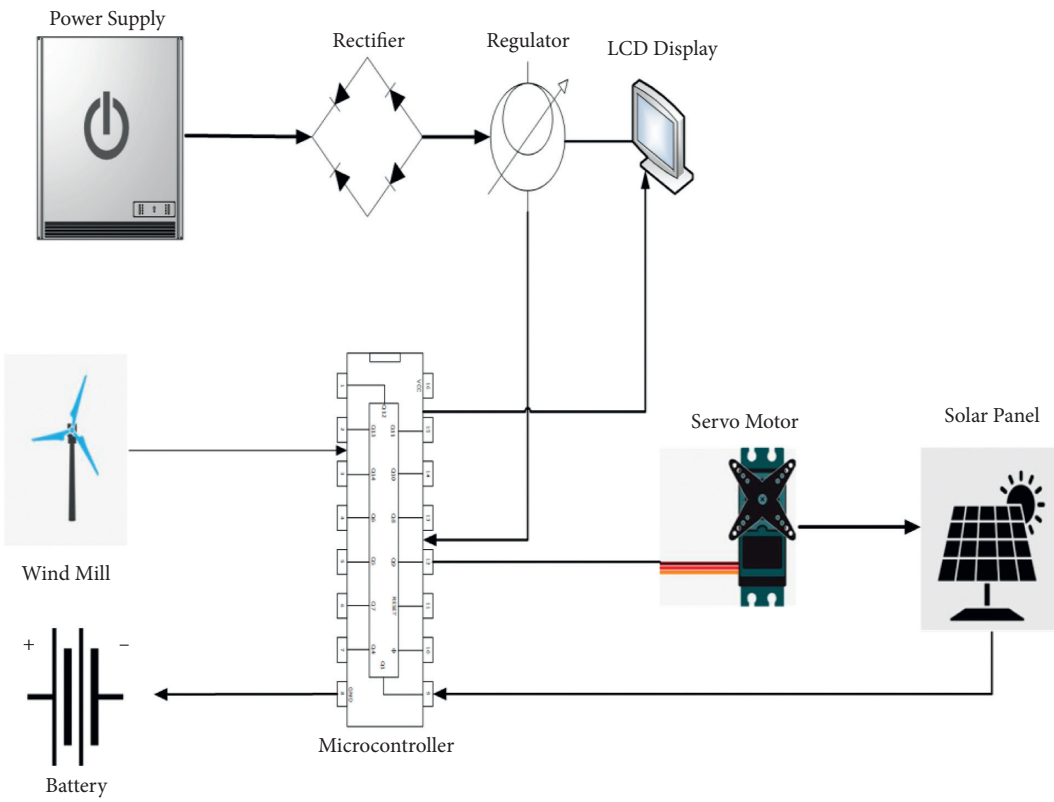

Figure 1: System working representation.

Maximum Power Point Technique (MPPT) [36] is used. The output power can be calculated as given in equations (1) to (7) [37, 38].

$$Z_{\mathrm{MPPT}}(t) = J_{\mathrm{MPPT}}(t) * K_{\mathrm{MPPT}}(t), \tag{1}$$

$$J_{\mathrm{MPPT}}(t) = J_s\left[1 - \alpha\left(exp\left\{\frac{K_{\max}}{\beta * K_c}\right\}\right)\right] + \Delta T(t), \tag{2}$$

$$K_{\mathrm{MPPT}}(t) = K_{\max} + \phi J_c.\Delta T(t), \tag{3}$$

$$\alpha = \left(1 - \frac{J_{\max}}{J_s}\right) * \exp\left(-\frac{K_{\max}}{\beta * K_c}\right), \tag{4}$$

$$\beta = \left(\frac{J_{\max}}{J_c} - 1\right) * \left[\ln\left(1 - \frac{J_{\max}}{J_s}\right)\right]^{-1}, \tag{5}$$

$$\Delta J(t) = J_s\left(\frac{IR(t)}{R_{\mathrm{ref}}} - 1\right) + \theta_{1,s} * \Delta T(t), \tag{6}$$

$$\Delta T(t) = T_x - T_{x,\mathrm{ref}}, \tag{7}$$

where J_c is the voltage of open circuit, J_s is the short-circuit current, $K_{\max}$ and $J_{\max}$ are the voltage and current at the maximum output power, $\theta_{1,s}$ is the temperature coefficient of power, IR(t) is the incident radiation on the PV surface, T_x(t) is the cell temperature that varies with ambient temperature and solar radiation, and $T_{x,\mathrm{ref}}$ is the PV temperature under normal conditions. Control systems are used for maintaining an equilibrium between the power supply and load. When the power is generated in excess, then it is stored in the storage system and when the power demanded is in excess, then it provides the backup [34–36]. Charge controllers are also used for maintaining a balance between charging and discharging to enhance the life of batteries [36]. The charging and discharging of the batteries are given as [37, 38]

$$\begin{aligned} S_f &= S(t-1) * (1-\sigma) + \left[X(t) - \frac{XJ(t)}{\phi}\right] * \phi_{\mathrm{charge}}, \\ S_f &= S(t-1) * (1-\sigma) + \left[X(t) - \frac{XJ(t)}{\phi}\right] * \phi_{\mathrm{discharge}}, \end{aligned} \tag{8}$$

where $S(t)$ and $S(t\text{-}1)$ are the charging and discharging states, σ is the discharging speed of the battery for 1 hour, $XJ(t)$ is the power of the load, $X(t)$ is the output power of the renewable sources, and $\phi_{\mathrm{discharge}}$, ϕ, and ϕ_{charge} are the efficiency of the inverter and batteries for both the charging and discharging states. In the wind energy subsystem, the generation of power depends upon the speed of the wind and sometimes it is unstable and produces a variable AC. Variable AC is converted to fixed DC with the help of a rectifier, and then fixed DC is converted to fixed AC with the help of a converter to stabilize the system [36]. Batteries are used as a storage system used for storing excess power and regulating the voltage of the system and are used as a backup in case of inefficient generation of power by the system

[35, 36]. The output power generated by the wind subsystem is calculated by [36]

$$Z_P = \frac{\left(\alpha \lambda x y^3\right)}{2}, \tag{9}$$

where Z_P is the output power, α is the power coefficient, λ is the ratio of tip speed, y is the wind speed, and x is the frontal area of the wind turbine.

The presented architecture in Figure 1 is the general architecture, and various studies have been conducted on this architecture. Now our goal is to optimize this architecture so that maximum power can be generated from the system. This can be done by applying optimization techniques and genetic algorithm, which are discussed as follows. The grid system is presented in Figure 2.

4.1. Optimization of Tilt Angle of the PV Array. The amount of solar energy collected is affected by the orientation and tilt of the solar panels [39]. As a result, solar panels must be installed at optimal angles in order to obtain the greatest amount of solar energy in a given area [39]. One of the methods to achieve this task is to install a sun tracker. However, sun tracker increases the complexity and costs of the system. Instead of installing sun trackers, changing the orientation angles seasonally, monthly, or yearly could be a better alternative [39]. The total solar radiation falling on a tilted surface (T) is made up of direct/beam solar radiation T_{direct}, diffuse radiation $T_{diffuse}$, and ground reflected radiation T_{refer} by considering isotropic reflection. Then, the average daily solar radiation on a tilted surface is given as [40]

$$T = T_{\text{direct}}\lambda_x + \frac{T_{\text{diffuse}}}{2} + (1 + \cos\phi) + \frac{T\psi}{2}(1 - \cos\phi), \tag{10}$$

where λ_x is the ratio of the average beam radiation on the tilted surface to that of the horizontal surface and ψ is the function of transmittance of the atmosphere. If the surface is facing the equator [40], then

$$\lambda_x = \frac{\cos(\alpha - \beta)\cos\gamma\sin\sigma + (\pi/180)\sigma\sin(\alpha - \beta)\sin\gamma}{\cos\alpha\cos\gamma\sin\sigma + (\pi/180)\sigma\sin\phi\sin\gamma}, \tag{11}$$

where γ is the sunset hour angle, given by [40]

$$\begin{aligned} \gamma &= \min[\gamma = \arccos(-\tan\alpha\tan\gamma)], \\ \gamma &= \min[\arccos(-\tan(\alpha - \beta)\tan\gamma)], \end{aligned} \tag{12}$$

where min is the smallest value of the items in the brackets.

4.2. Optimization of Microgrid Services like Storage, Batteries, Inverter, and Wind Power. Because photovoltaic (PV) units have low maintenance costs, inverter size must be optimized to achieve system productivity. The rated power of the PV system must be optimally matched with the rated power of the inverter to achieve maximum power [41]. The optimal inverter sizing is determined by the amount of solar radiation received locally, the ambient temperature, and the inverter's performance [41]. The PV array only produces a portion of its rated power when solar radiation levels are low, and the inverter, therefore, operates at a lower efficiency [41]. The rated capacity of the inverter is lost under overloading conditions [41], which is why optimum PV array sizing is required. Not every area is suitable for wind energy systems. The amount of kinetic energy present in the wind increases with wind speed, but not all of the kinetic energy can be converted into another source of energy while passing through a wind turbine. Since the wind current begins after the rotor, a portion of its initial kinetic energy persists in the wind, causing it to continue to flow [3, 6]. The ratio of kinetic energy (KE), when divided by the KE available in the wind, can be converted into wind turbines called power coefficient [3, 6, 42]. The power coefficient is dependent on the downstream and upstream ratio of the turbine to wind velocity. The density of the wind power is defined as the quantitative measure of the wind energy available in a particular geographical area. It is often considered the critical indicator of the potential of wind energy [3, 6, 42]. The major indicators of wind speed with optimization [42, 43] are defined as follows:

$$s_v = x\left[1 - \frac{1}{y}\right]^{(1/y)}, \tag{13}$$

where S_V is the portable wind speed. The highest energy-carrying speed of the wind is defined as follows [42–44]:

$$s_{\max} = x\left(1 + \frac{2}{y}\right)^{(1/y)}. \tag{14}$$

The density of the power of the wind evaluates the wind available in a particular area and is given as follows [44]:

$$\frac{L}{A} = \frac{1}{2}\sigma v^3. \tag{15}$$

This equation can also be written as Weibull Parameters [45] as follows:

$$\left(\frac{L}{A}\right)_w = \int_0^\infty \frac{1}{2}\sigma V^3 f v^3 \mathrm{d}V = \frac{1}{2}\sigma C^3 \Gamma\left(1 + \frac{3}{y}\right), \tag{16}$$

where L is the density of wind power represented in Watt/m^2, A is the area swept in m^2, $f(v^3)$ is the probability distribution function, and vis the speed of wind in m/s.

5. Results' Analysis

The software Hybrid Optimization of Multiple Energy Resources (HOMER) [46] was chosen for simulations and system design. We chose this software because it can perform essential tasks like optimization, simulation, and sensitivity analysis. After the users' data have been simulated, HOMER determines the best setup based on the lowest net present cost (NPC) [46]. Sensitivity analysis is carried out to ensure that only the best components are used in the system design. We chose the rural areas of Rajasthan, India, for system testing because the state is covered in desert, allowing ample solar energy to be harnessed. The community consumes 165.59 kWh per day, with a peak demand

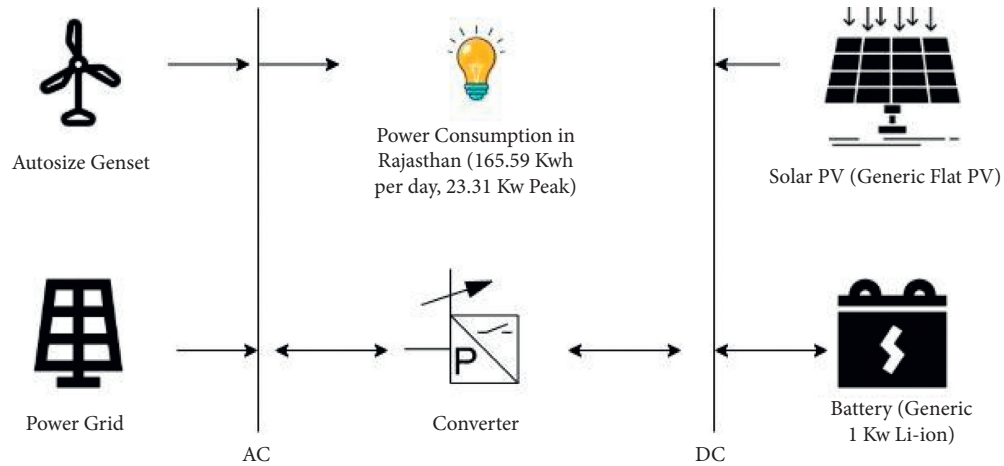

Figure 2: Grid system internal structure.

of 23.31 KW. The load profiles were created using public databases [47, 48] and a poll conducted by the Government of Rajasthan in India. The random variability from one day to the next is 10%, and the variability from one-time step to the next is 20%. Summer demand (May–July) was found to be moderate, and winter demand was found to be low (November–January). Electrical service can need a distribution system, whether the system is self-contained or connected to the grid [46]. A grid connection system would need an 11 KV/220V step-down transformer as well as an automatic transfer switch to resolve any power distribution anomalies. The seasonal load profile generated is shown in Figure 3.

The components used for designing the system are explained in Tables 2–5, respectively.

The purpose of using the Autosize Genset generator is that this generator automatically adjusts itself according to the load. The capacity of the generator is small so that it cannot produce capacity shortages in cases of sensitivity and in the future if the multiyear analysis is used. This generator is also capable of adjusting its fuel curve to match its size (source: http://www.homerenergy.com).

Generic 10 kW wind turbine is used for our study. Table 3 lists the wind turbines' various parameters, while Figure 4 depicts the power curve. The turbine's predicted lifespan was discovered to be 20 years. Although the initial investment is low, replacement costs are high. However, when compared to high-quality wind turbines during the project's lifetime, the HOMER simulation findings show that the turbine contributes to a less net present cost (NPC) due to its low capital cost [46]. The surface area criteria are based on National Renewable Energy Lab (NREL) standards [46]. According to NREL, the capacity per unit area is $3.0 \pm 1.7\,\mathrm{MW/km^2}$. Therefore, the area required for 10 kW wind turbine is $2500\,\mathrm{m^2}$. The capacity of the wind turbines can be optimized by a genetic algorithm [49] given as Algorithms 1 and2, respectively. Upon analysis of HOMER, we found that the lifetime of the overall system would be in the range of 20–30 years, which is a good sign.

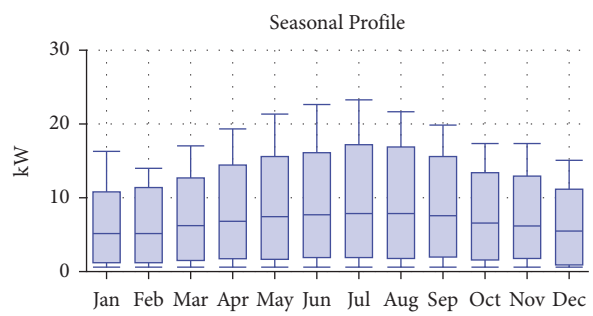

Figure 3: Season-based load profile obtained for the suggested installation location.

Table 2: Generator specifications.

Type	Autosize Genset
Size (kW)	1.2 kW
Capital cost (INR)	500 INR
Restoration cost (INR)	500 INR
O&M cost (per operational hour)	0.030 INR

Table 3: Wind turbine specifications.

Type	Generic 10 kW
Hub height	24 meters
Capital cost (INR)	50000 INR
Restoration cost (INR)	50000 INR
O&M cost (per operational hour) lifetime	500 INR/year 20 years

Due to the seasonal nature of renewable energy sources, energy storage devices are necessary to ensure a constant supply of energy from renewable sources. We have considered the load following strategy [46] in developing our model. Due to the sudden increase or decrease in power supply, hybrid systems require additional reserves to tackle the challenges related to sudden increase or decrease. The operating reserve was considered as 10% of the hourly load

Table 4: Storage battery specifications.

Type	Generic 1 kWh Li-ion
Lifetime	15 years
Capital cost	550 USD
Restoration cost	550 USD
O&M cost (per operational hour)	10 USD/year
Throughput	3000 kWh

Table 5: Solar PV specifications.

Type	Generic flat PV
Derating factor	80%
Capital cost	2500 USD
Restoration cost	2500 USD
O&M cost (per operational hour)	10 USD/year
Lifetime	25 years

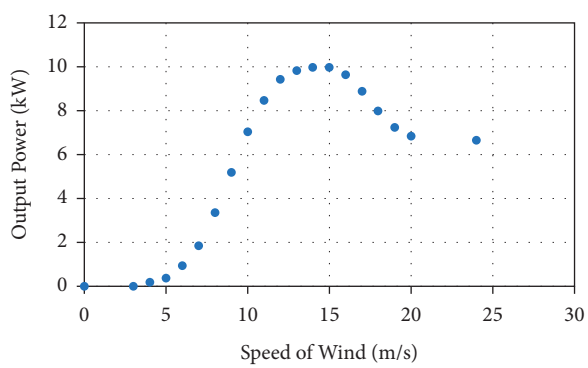

Figure 4: Scatter plot of the wind turbine in terms of power.

(1) Initialize GA ∈ [0,1], POS ∈ f(V)//*Particle swarm optimization, f(V) = Functional Decision Variables*
(2) If
(3) POS optimizes w(f(n)) ∈ NIS//*NIS = noninferior solutions, w(f(n)) = weighted single objective function*
(4) **Then**
(5) Use Crowding Distance Method for the solutions Obtained in step 3
(6) **If**
(7) User submitted = true, terminate the algorithm and Solutions = accepted
(8) **Else**
(9) Values recorded
(10) Evaluate Fitness for each individual, do Genetic Operations
(11) Return Values recorded
(12) Evaluate Fitness for each individual, do Genetic Operations
(13) Return to Step 2

Algorithm 1: Optimization of the capacity of wind turbines.

as recommended by [46] for maximizing efficiency. The specifications for the solar PV and storage devices are given in Tables 4 and 5, respectively.

5.1. Simulations and Analysis. For the evaluation of the proposed system, various configurations such as grid-only systems, renewable energy sources (RES) systems, and Grid-RES hybrid systems are analyzed. The optimization results are recorded in Table 6.

The HOMER findings show that the RES only setup is achievable with the available resources. This result was achieved after numerous trials, mistakes, and the removal of inefficient data in order to reduce simulation time. This system is economically feasible at 10% shortage. The monthly production of power is shown in Figure 5. In Grid-

(1) Initialize $u = 0\,\mathrm{m/s}^2 \in$ POS in decision making variables//u= initial velocity
(2) Evaluate Fitness Values, Extreme Points
(3) New_u and position updated
(4) **If**
(5) Steps 1,2,3 = True, conditions satisfied
(6) Algorithm terminated
(7) **Else**
(8) Go to step 2 again

Algorithm 2: For noninferior solutions.

Table 6: RES configuration optimization result.

PV (kW)	Wind turbine	Battery	Conv (kW)	Initial capital	Operating cost (USD/year)	Net NPC	Coe ($/kWh)	Renewable factor	Capacity shortage
26	10	100	25	$63,531	$16,405	$84,413	0.118	0.028	0.10
------	11	120	25	$77,762	$21,375	$83,201	0.156	0.028	0.10

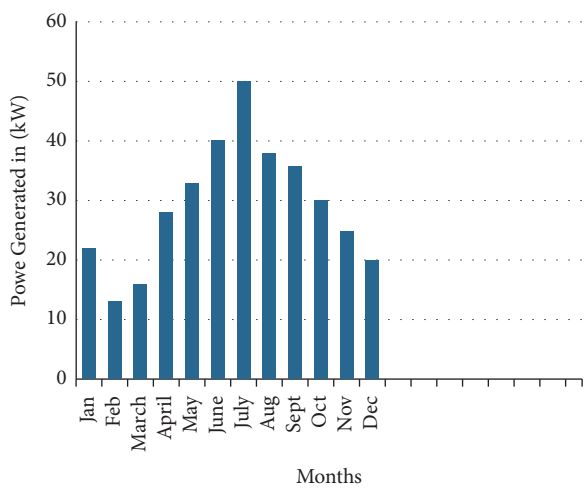

Figure 5: Monthly power production at 10% shortage.

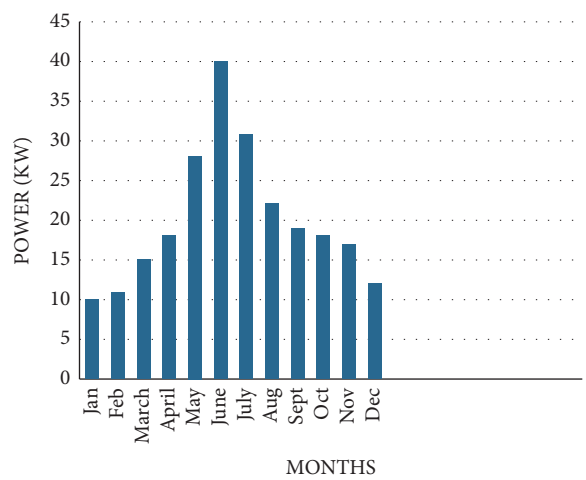

Figure 6: Monthly power production of Grid-RES system.

RES systems, it has been found from HOMER simulations that these systems are feasible with currently available renewable resources. This type of system is also economically efficient. Upon optimization, it has been found that the system gives a net present cost (NPC) of $3,45,198. The renewable factor for this type of configuration is 77.6%. In this type of configuration, battery and inverter are not necessary as the grid network acts as a backup for the system. The monthly power production is given in Figure 6.

5.2. Sensitivity Analysis. The control parameters of a system can be varied in sensitivity analysis to examine the effect of these parameters on the system's effectiveness [46]. This aids the designer in creating a system that is effective. A sensitivity analysis is often performed to ensure that the system is reliable. Because the aim is to protect 100 percent of the load, the energy system would be expensive. A sensitivity analysis of the capacity constraints for the system will provide the details about how much amount is to be paid by the customers for more effective system in terms of hours of reliability. Values from 0 to 15% with a phase of 2% were given as capacity constraints inputs. In addition, a sensitivity analysis was carried out to research the conditions under which the available findings are true for PV modules and battery prices and how much the cost of the device would differ with the variance of these prices. A sensitivity analysis was performed to evaluate all possible scenarios between these rates, where capital cost multipliers of 1.5 to 3.5 were given for the solar PV capital cost, and multipliers of 1 to 2 were given for the battery capital cost. For running the simulations, the time step was set to 40 minutes (instead of the default 60 minutes in HOMER) to effectively adjust the load and output of electricity. The maximum number of simulations per optimization was set to 25,000. This implies that simulations would be discarded if they have not been completed until the value has been achieved. Increasing this value therefore dramatically increases the simulation time. The device design accuracy and the NPC accuracy were

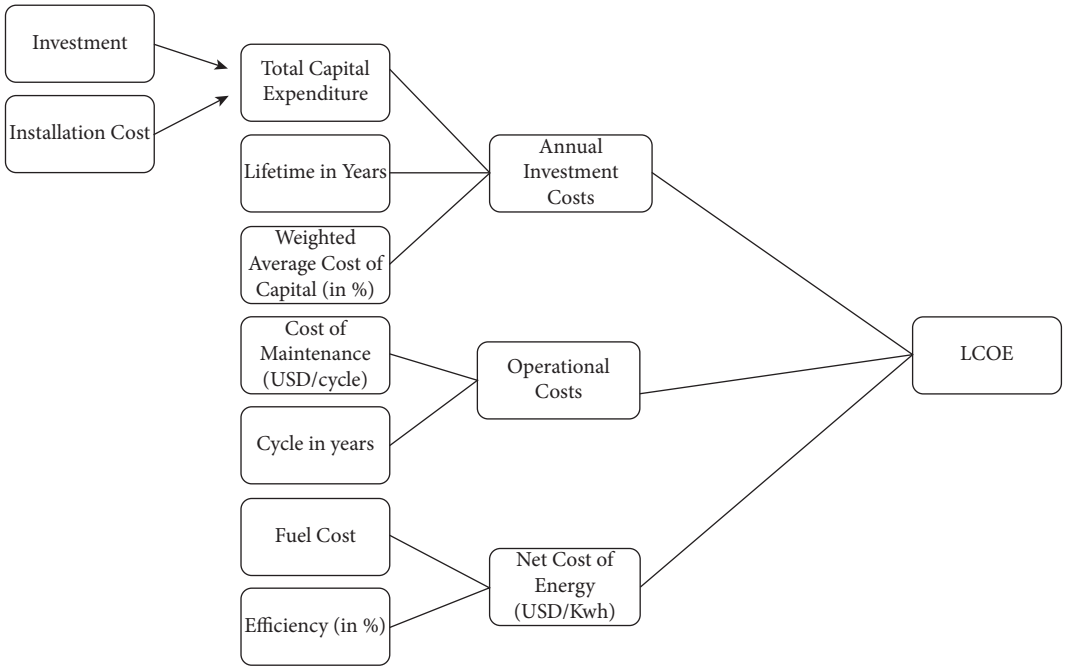

Figure 7: Flowchart for calculation of LCOE.

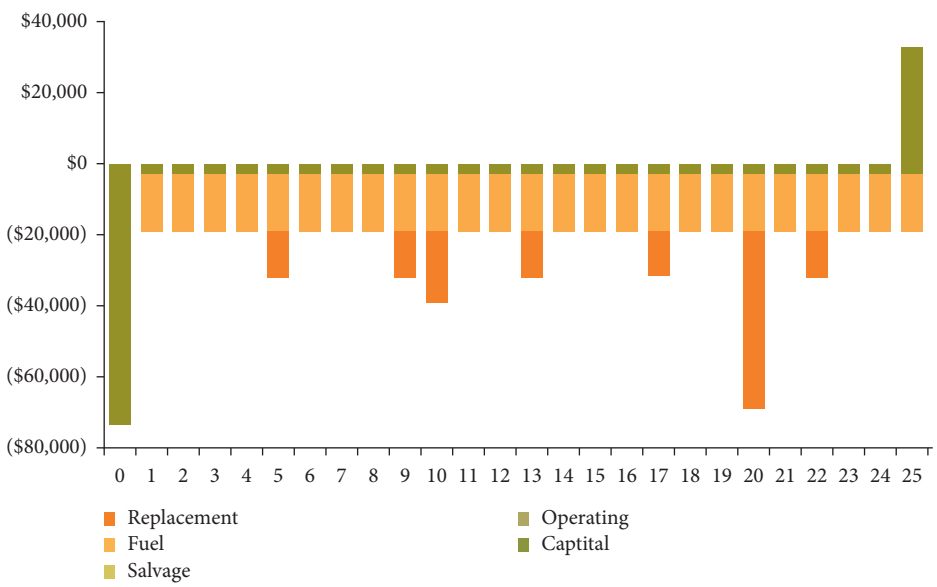

Figure 8: Cash flow diagram showing the cost efficiency of the suggested system.

Table 7: Cost analysis between various systems.

System configuration	PV array number	Number of wind generators	Battery quantity	PV converter	Cost (in USD)
Single PV	50	0	10	15	$66,000
Single wind	0	10	5	0	$56,650
Nonoptimized	20	5	6	8	$56,300
Suggested system	15	6	6	6	$49,500

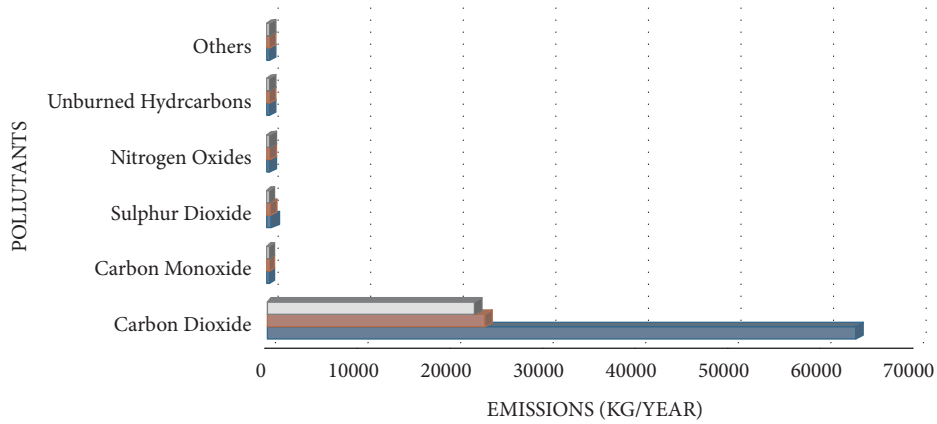

Figure 9: Comparison between greenhouse emissions of various systems. Blue bar indicates a grid-only system, orange bar indicates grid-wind system, and grey bar indicates grid-wind-PV system, which is suggested.

defined by maximum simulation errors set at 1% and 2%, respectively.

The efficiency of the system is shown in Figure 7, Figure 8, Table 7, and Figure 9, respectively, with a comparison between various systems in terms of cost analysis and greenhouse emissions. The flowchart for the calculation of LCOE (levelized cost of heat) [50] is given in Figure 7.

Clearly, we can see from Figure 8 that the system suggested in this paper is efficient. It can also be seen that the optimized PV system is more cost-effective than other systems. It can also be inferred from the results that most of the energy is supplied by wind.

6. Conclusion

Due to the growth of population and environmental pollution, the demand for efficient production of electricity has increased. Utilizing solar and wind energy for electricity production will help in resolving the challenges such as climate change and greenhouse emissions and can emerge as the best solution for resolving the energy crisis. The hybrid energy system suggested in this paper has advantages such as continuity in power supply, high efficiency, low maintenance cost, optimized utilization of the resources, and load management. The results given in this paper show that the use of hybrid PV-wind power generation units could save up to 10%–20% of the cost of current systems. This study encourages the use of hybrid systems in India and abroad in order to improve electricity production sustainability. Hybrid systems will provide a viable, secure power supply to rural areas while also providing a pool of funding for community grid maintenance and economic development. Ultimately, these systems will help to increase the usage of renewable energy for generating electricity globally and thereby contribute to resolving the environmental problems currently facing the world.

7. Limitations and Future Scope of the Work

Solar energy and wind energy undoubtedly come to people's mind when we talk about renewable energy. In an hour, the sun emits enough energy, which can cover human needs for a year. This property makes solar energy the best form of energy to be integrated with other energy forms. However, with the current technology, we are unable to extract the full potential of the integrated systems. Some amount of energy gets wasted due to inefficient operation. According to recent reports [51], it has been shown that the PV panels have a median degradation rate of 0.5% per year. It may be high in hot climate areas and rooftop systems. The degradation rate of 0.5% shows that the energy production from solar PV will decrease at the rate of 0.5% per year. This will make the system inefficient over time. Furthermore, the unpredictability and intermittency of solar energy make the solar PV panel less reliable. Solar panels require additional inverters to convert DC to AC energy in order to be used on the power network, which makes the system complex and increases the installation time and circuit development costs. For a continuous supply of electricity on grid connections, PV panels also require storage batteries along with inverters, which also increases the investment costs. Moreover, the installation of solar PV panels usually requires a large area of land for a period of more than 20 years. Also, solar PV is fragile and can be damaged easily, so insurance costs also increase the overall costs of the systems. Our future work will be based on resolving these challenges and the development of microenergy grids with micro-PV cells, which would require less complexity and installation area. This system will be further integrated with blockchain technology to increase the efficiency of the system.

Data Availability

The data used to support the findings of this study are available from the corresponding author upon request.

Conflicts of Interest

The authors declare that they have no conflicts of interest.

Acknowledgments

This research was supported by the Taif University Research Supporting Project no. TURSP-2020/311, Taif University, Taif, Saudi Arabia.

References

[1] S. Sanajaoba, "Optimal sizing of off-grid hybrid energy system based on minimum cost of energy and reliability criteria using firefly algorithm," *Solar Energy*, vol. 188, pp. 655–666, 2019.

[2] F. Husni, Y. Tan, and J. Yan, "Power and Methanol Production from Biomass Combined with Solar and Wind Energy : Analysis and Comparison," *Energy Procedia*, vol. 145, pp. 576–581, 2018.

[3] C. Mata Yandiola, *Feasibility Analysis of the Use of Hybrid Solar PV-Wind Power Systems for Grid Integrated Mini-Grids in India*, Dissertation, KTH, School of Industrial Engineering and Management (ITM). Selco Foundation, Stockholm, Sweden, 2017.

[4] Y. Kassem, H. Çamur, and R. A. F. Aateg, "Exploring solar and wind energy as a power generation source for solving the electricity crisis in Libya," *Energies*, vol. 13, no. 14, p. 370, 2020.

[5] S. Al-Mimar, *Integration of Solar and Wind Power at Lillgrundwind farm Wind Turbine Shadow Effect on Solar Farm atLillgrund Wind Farm*, Halmstad University, Halmstad, Sweden, 2015, http://www.diva-portal.org/smash/record.jsf?pid=diva2%3A817812&dswid=9794.

[6] F. Ueckerdt, *Integrating Variable Electricity Supply from Wind and Solar PV into Power Systems*, Technische Universität Berlin, Berlin, Germany, Berlin, 2014.

[7] G. Notton, "Hybrid wind-photovoltaic energy systems," in *Stand-Alone and Hybrid Wind Energy Systems*Woodhead Publishing, Sawston, UK, 2010.

[8] T. Mitani, M. Aziz, T. Oda, A. Uetsuji, Y. Watanabe, and T. Kashiwagi, "Annual assessment of large-scale introduction of renewable energy: modeling of unit commitment schedule for thermal power generators and pumped storages," *Energies*, vol. 10, p. 738, 2017.

[9] F. Tang, H. Zhou, Q. Wu, H. Qin, J. Jia, and K. Guo, "A Tabu search algorithm for the power system islanding problem," *Energies*, vol. 8, no. 10, pp. 11315–11341, 2015.

[10] F. Capitanescu and L. Wehenkel, "Experiments with the interior-point method for solving large scale Optimal Power Flow problems," *Electric Power Systems Research*, vol. 95, pp. 276–283, 2013.

[11] L. Canale, A. R. Di Fazio, M. Russo, A. Frattolillo, and M. Dell'Isola, "An overview on functional integration of hybrid renewable energy systems in multi-energy buildings," *Energies*, vol. 14, no. 4, p. 1078, 2021.

[12] G. J. Osório, M. Shafie-khah, J. M. Lujano-Rojas, and J. P. S. Catalão, "Scheduling model for renewable energy sources integration in an insular power system," *Energies*, vol. 11, p. 144, 2018.

[13] L. M. S. de Siqueira and W. Peng, "Control strategy to smooth wind power output using battery energy storage system: a review," *Journal of Energy Storage*, vol. 35, Article ID 102252, 2021.

[14] I. Akhtar and S. kirmani, "Design and implementation of model predictive control for microgrid energy system with power quality improvement features," *International Journal of Electronics*, vol. 108, no. 12, pp. 1977–1998, 2021.

[15] T. Mai, A. Lopez, M. Mowers, and E. Lantz, "Interactions of wind energy project siting, wind resource potential, and the evolution of the U.S. power system," *Energy*, vol. 223, Article ID 119998, 2021.

[16] B. Setiawan, E. S. Putra, I. Siradjuddin, and M. Junus, "Optimisation solar and wind hybrid energy for model catamaran ship," *IOP Conference Series: materials Science and Engineering*, vol. 1073, no. 1, Article ID 012044, 2021.

[17] L. Sun, Y. Jin, J. Shen, and F. You, "Sustainable residential micro-cogeneration system based on a fuel cell using dynamic programming-based economic day- ahead scheduling," *ACS Sustainable Chemistry & Engineering*, vol. 9, no. 8, pp. 3258–3266, 2021.

[18] A. Awasthi, A. K. Shukla, M. M. S.R. et al., "Review on sun tracking technology in solar PV system," *Energy Reports*, vol. 6, pp. 392–405, 2020.

[19] A. Ghafoor and A. Munir, "Design and economics analysis of an off-grid PV system for household electrification," *Renewable and Sustainable Energy Reviews*, vol. 42, pp. 496–502, 2015.

[20] M. Al-Addous, Z. Dalala, C. B. Class, F. Alawneh, and H. Al-Taani, "Performance analysis of off-grid PV systems in the Jordan Valley," *Renewable Energy*, vol. 113, pp. 930–941, 2017.

[21] Ghenai, Chouki, and M. Bettayeb, "Grid-tied solar PV/fuel cell hybrid power system for university building," *Energy Procedia*, vol. 159, pp. 96–103, 2019.

[22] M. A. V. Rad, R. Ghasempour, P. Rahdan, S. Mousavi, and M. Arastounia, "Techno-economic analysis of a hybrid power system based on the cost-effective hydrogen production method for rural electrification, a case study in Iran," *Energy*, vol. 190, Article ID 116421, 2020.

[23] L. Qi, P. Zheng, X. Wu, W. Duan, L. Li, and Z. Zhang, "A hybrid wind-photovoltaic power generation system based on the foldable umbrella mechanism for applications on highways," *Solar Energy*, vol. 208, pp. 368–378, 2020.

[24] N. Bizon and P. Thounthong, "Energy efficiency and fuel economy of a fuel cell/renewable energy sources hybrid power system with the load-following control of the fueling regulators," *Mathematics*, vol. 8, no. 2, p. 151, 2020.

[25] T. Salameh, M. A. Abdelkareem, A. G. Olabi, E. T. Sayed, M. Al-Chaderchi, and H. Rezk, "Integrated standalone hybrid solar PV, fuel cell and diesel generator power system for battery or supercapacitor storage systems in Khorfakkan, United Arab Emirates," *International Journal of Hydrogen Energy*, vol. 46, no. 8, pp. 6014–6027, 2021.

[26] V. A. Ani, "Development of an intelligent power management system for solar PV-Wind-Battery-Fuel-Cell integrated system," *Frontiers in Energy Research*, vol. 9, p. 31, 2021.

[27] Y. Noorollahi, A. Khatibi, and S. Eslami, "Replacing natural gas with solar and wind energy to supply the thermal demand of buildings in Iran: a simulation approach," *Sustainable Energy Technologies and Assessments*, vol. 44, Article ID 101047, 2021.

[28] P. D. Santos, A. C. Zambroni de Souza, B. D. Bonatto, T. P. Mendes, J. A. S. Neto, and A. C. B. Botan, "Analysis of solar and wind energy installations at electric vehicle charging stations in a region in Brazil and their impact on pricing using an optimized sale price model," *International Journal of Energy Research*, vol. 45, no. 5, pp. 6745–6764, 2021.

[29] O. Siddiqui and I. Dincer, "Optimization of a new renewable energy system for producing electricity, hydrogen and ammonia," *Sustainable Energy Technologies and Assessments*, vol. 44, Article ID 101023, 2021.

[30] Z. Qadir, S. I. Khan, E. Khalaji, H. S. Munawar, F. Al-Turjman, and M. P. Mahmud, K. Le, Predicting the energy output of hybrid PV–wind renewable energy system using feature selection technique for smart grids," *Energy Reports*, vol. 7, pp. 8465–8475, 2021.

[31] M. Ian, E. Gençer, and F. M. O'Sullivan, "A general model for estimating emissions from integrated power generation and energy storage. Case study: integration of solar photovoltaic power and wind power with batteries," *Processes*, vol. 6, no. 12, p. 267, 2018.

[32] S. M. Lawan and W. A. W. Z. Abidin, *A Review of Hybrid Renewable Energy Systems Based on Wind and Solar Energy: Modeling, Design and Optimization*, Wind Solar Hybrid Renewable Energy System, IntechOpen Limited, London, UK, 2020.

[33] J. Kaustubh, T. Shelar, S. Sanap, and N. Sangit, "Dual power generation solar plus windmill generator," *New Arch-International Journal of Contemporary Architecture*, vol. 8, no. 2, pp. 1002–1006, 2021.

[34] J. Godson, M. Karthick, T. Muthukrishnan, and M. S. Sivagamasundari, "Solar PV-Wind hybrid power generation System," *International Journal of Advanced Research in Electrical, Electronics and Instrumentation Engineering*, vol. 2, no. 11, pp. 5350–5354, 2013.

[35] J. Godson, M. Karthick, T. Muthukrishnan, and M. S. Sivagamasundari, "Solar PV-Wind hybrid power generation system," *International Journal of Advanced Research in Electrical, Electronics and Instrumentation Engineering*, vol. 2, no. 11, pp. 5350–5354, 2013.

[36] M. Srikanth, T. V. Muni, M. V. Vardhan, and D. Somesh, "Design and simulation of PV-wind hybrid energy system," *J Adv Res Dyn Control Syst*, vol. 10, pp. 999–1005, 2018.

[37] L. Zhang, R. Belfkira, and G. Barakat, "Wind/PV/diesel energy system: modeling and sizing optimization," in *Proceedings of the 2011-14th European Conference on Power Electronics Application (EPE 2011)*, pp. 1–10, Birmingham, UK, 2011.

[38] W. M. Hamanah, M. A. Abido, and L. M. Alhems, "Optimum sizing of hybrid pv, wind, battery and diesel system using lightning search algorithm," *Arabian Journal for Science and Engineering*, vol. 45, no. 3, pp. 1871–1883, 2020.

[39] T. Khatib, A. Mohamed, and K. Sopian, "Optimization of a PV/wind micro-grid for rural housing electrification using a hybrid iterative/genetic algorithm: case study of Kuala Terengganu, Malaysia," *Energy and Buildings*, vol. 47, pp. 321–331, 2012.

[40] A. Kumar, N. S. Thakur, R. Makade, and M. K. Shivhare, "Optimization of tilt angle for photovoltaic array," *International Journal of Engineering Science and Technology*, vol. 3, no. 4, pp. 3153–3161, 2011.

[41] T. Khatib, A. Mohamed, and K. Sopian, "A review of photovoltaic systems size optimization techniques," *Renewable and Sustainable Energy Reviews*, vol. 22, pp. 454–465, 2013.

[42] F. Fazelpour, E. Markarian, and N. Soltani, "Wind energy potential and economic assessment of four locations in Sistan and Balouchestan province in Iran," *Renewable Energy*, vol. 109, pp. 646–667, 2017.

[43] S. H. Pishgar-Komleh, A. Keyhani, and P. Sefeedpari, "Wind speed and power density analysis based on Weibull and Rayleigh distributions (a case study: firouzkooh county of Iran)," *Renewable and Sustainable Energy Reviews*, vol. 42, pp. 313–322, 2015.

[44] K. Mohammadi, O. Alavi, and J. G. Mcgowan, "Use of Birnbaum-Saunders distribution for estimating wind speed and wind power probability distributions: a review," *Energy Conversion and Management*, vol. 143, pp. 109–122, 2017.

[45] A. Keyhani, M. Ghasemi-Varnamkhasti, M. Khanali, and R. Abbaszadeh, "An assessment of wind energy potential as a power generation source in the capital of Iran, Tehran," *Energy*, vol. 35, no. 1, pp. 188–201, 2010.

[46] S. Podder, R. S. Khan, and S. M. A. Alam Mohon, "The technical and economic study of solar-wind hybrid energy system in coastal area of Chittagong, Bangladesh," *Journal of Renewable Energy*, 2015.

[47] P. W. Stackhouse and C. H. Whitlock, "The National Aeronautics and Space Administration," 2016, https://cleanenergysolutions.org/resources/surface-meteorology-solar-energy-website.

[48] *Finding Data to Run HOMER*, 2022, https://www.homerenergy.com/products/pro/docs/latest/finding_data_to_run_homer.html.

[49] T. Wei Sun and W. Sun, "Optimization of wind-PV hybrid power system based on interactive multi-objective optimization algorithm," in *Proceedings of the 2012 International Conference on Measurement, Information and Control*, pp. 853–856, Harbin, 2012.

[50] O. Gudmundsson, J. E. Thorsen, and L. Zhang, "Cost analysis of district heating compared to its competing technologies," *WIT Transactions on Ecology and the Environment*, vol. 176, pp. 3–13, 2013.

[51] B. Mow, *STAT FAQs Part 2: Lifetime of PV Panels*, 2022, https://www.nrel.gov/state-local-tribal/blog/posts/stat-faqs-part2-lifetime-of-pv-panels.html.

Hindawi
Mathematical Problems in Engineering
Volume 2022, Article ID 4225080, 10 pages
https://doi.org/10.1155/2022/4225080

Research Article

Discrete Fourier Transform (DFT)-Based Computational Intelligence Model for Urban Carbon Emission and Economic Growth

Chun Fu,[1] **Xiayun Gui**,[1] **and Farzana Akter**[2]

[1]*Management School, Nanchang University, Nanchang 330000, China*
[2]*Department of ICT, Bangabandhu Sheikh Mujibur Rahman Digital University, Kaliakair, Gazipur, Bangladesh*

Correspondence should be addressed to Xiayun Gui; gxy_crcm@163.com and Farzana Akter; farzana@ict.bdu.ac.bd

Received 1 December 2021; Accepted 5 January 2022; Published 4 February 2022

Academic Editor: Araz Darba

Economic development leads to the widespread use of energy, which results in carbon emissions. In order to determine the correlation between different urban carbon emissions and fiscal growth, a coupling and coordination model of urban carbon emissions and economic growth based on discrete Fourier transform (DFT) is constructed. According to the coupling and coordinated development characteristics of economic growth and carbon emissions, the evaluation index system of the regional economy and carbon emissions is constructed. This paper examines the proportion of primary energy consumption and the influencing factors of carbon emission in a city and constructs the economic growth computational intelligence model and urban carbon emission model. The coupling degree among economic growth, carbon emission, and energy consumption is studied; the coupling standard between economic growth and energy consumption carbon emission is determined; and the carbon emission factor under the method of DFT is introduced. The coupling coordination model between economic growth and carbon emission is constructed, and the interaction mechanism between carbon emission, economic development, and environmental protection is determined. The experimental findings demonstrate that when energy consumption intensity and carbon emission are relatively low, the model's change in the trend of coupling coordination index is comparable with the real/actual condition and the model is more reliable.

1. Introduction

Carbon emission and economic development have attracted great attention from all the research communities in the world [1]. During economic growth, energy needs to be consumed constantly by the industries across the world, but the energy generation resources are limited [2]. The energy generation process also produces greenhouse gases in the process of production that may pose a threat to the survival and development of humans [3]. The governing bodies around the globe are paying enough attention to carbon emission or carbon footprints to minimize the carbon emission that directly affects the breathing air and is meticulously related to the health of people [4]. Sustainable urban development is consuming renewable energy solutions that are converting energy from one form to another for reducing carbon dioxide (CO_2) emissions [5]. However, climate changes, global warming, and the rapid rise in demand for energy have contributed to the generation of more carbon emissions. A few quantitative estimates have been fabricated from the data obtained from countries across the world regarding CO_2 emissions [6]. Innovative solutions are required to address the needs of energy and to control the carbon emissions to provide a better environment for breathing and living [7]. Currently, it is unanimously recognized that urban growth can strongly impact the contribution of carbon emissions, global warming, and changes in the international weather [8]. It is naturally important to employ suitable techniques for designing innovative energy solutions by preserving the good health of the environment [9]. Therefore, the research on the coordinated development based on the computational intelligence model of the low-

carbon economy is considered in this paper, and an innovative technique is presented to provide the solutions for the aforesaid problem. The research results are the important decision-making basis for the expansion of low-carbon economy. From the current situation of urban and rural development, with the rapid growth of the regional economy, most regions in the world are also facing the grim situation of high carbon emissions [10]. The contradiction between energy conservation and emission reduction, economic development, and environmental protection is increasing prominently [11]. It is worth establishing a correlation between economic growth and carbon emissions and correlating these factors with each other for the sustainable development of the economy. At present, the world has reached a consensus on the concept of supportable development in the sustainable environment [12]. The core of this concept is to strive for a harmonious development among society, economy, resources, and environmental protection and integrate the concept of the development of the society and economy with the resources as well as environment. In the past 20–30 years, CO_2 emission and its effects on economic growth have become one of the most discussed topics nationally as well as internationally [13]. Many research efforts are made in this area to provide solutions at different levels related to water, air, and the entire environment [14]. Therefore, to deal with the relationship between carbon emission and economic development and to deal with global climate deterioration, it is mandatory to find renewable energy generation solutions. At present, the energy consumption is beyond words, and the carbon emission is proportionately high. There is an inverse correlation between economic progress and environmental protection. The solution for reducing carbon emissions while developing the economy and safeguarding the environment has become a key subject for economic growth.

Low carbon emission and green development have become the only way of social development along with economic development [15]. To reduce carbon emissions while developing the economy and protecting the environment, the key is to deal with the coordination between carbon emissions and economic growth, and hence, we are proposing the solution in this paper. In this context, it is necessary to establish coordination between energy generation solutions and environment protection solutions. By improving the efficiency of energy generation and aiming at reducing greenhouse gas emissions, the proposed method will gradually achieve the unification of energy and the environment. However, with the increasing carbon emissions in various provinces and regions in the world, the energy conservation and emission reduction goals are on the top charter for maintaining stable and rapid economic growth that focuses on the overall development of energy utilization and reduction in carbon releases. It has significant practical importance, and various approaches, such as heuristic approaches, fuzzy-based approaches, applied mathematics, and AI-based intelligent models, have been proposed to address these problems.

The key points of the proposed research are as follows:

(i) In this paper, DFT-based computationally intelligent model is proposed that is focused on showing the adverse effects of urban emission of carbon dioxide on the environment and its negative impacts on economic development

(ii) This model studies the proportion of energy consumption, carbon emission factors (CEF), and analysis of CEF

(iii) In this paper, the proportion of primary energy consumption and its influencing factors of carbon emission in urban cities are examined

(iv) Coupling division standard between economic expansion and energy utilization carbon emission is studied and presented

(v) Correlation among economic development, carbon emission (CE), and energy generation is also examined

(vi) The changes in the rate of carbon emission intensity are also examined with the proposed method to check the effectiveness of the proposed work

The paper is organized as follows: Section 1 discusses the historical context of carbon emissions as well as the models and approaches employed by various writers to detect and reduce carbon emissions. The discrete Fourier algorithm (DFT) is discussed in Section 2. Section 3 delves into the coupling and coordination computational intelligence model of urban carbon emissions and economic growth. Section 4 contains a comprehensive experimental analysis. In the conclusion part, the outcome of the paper is illustrated.

2. Proposed Work Based on DFT

The discrete Fourier transform (DFT) is the discrete form that considers both the time and frequency domains [16]. In DFT, the sequences of time and frequency domains are finite, but in fact, these two sets of sequences should be considered as the main value sequences of discrete periodic variables. Even if DFT is applied to a finite discrete variable, it must be considered as a transformation of its periodic extension. In practical application, DFT is usually calculated by Fourier transform (FT) that has been originally developed for continuous variables, that is, analog variables. It is a mathematical tool used to analyze variables in the frequency domain. When real or complex numerical simulation variables are applied, it generates correlation frequency-domain functions.

The purpose of spectrum analysis is that the variables can be formed into the weighted sum of the complex exponential function (spectrum component) under the condition of handling the constraints [17]. Each frequency weighting term is the complex amplitude, and the problem can be decomposed into the sum of the sinusoidal fundamental components as the high-order sinusoidal component is an essential manifold of the fundamental frequency. The second application of DFT is to find a system's frequency response from the system's impulse response, and vice versa [18]. This

allows the structures to be analyzed inside the frequency domain, in a similar way as the convolution allows structures to be analyzed in the time area. In this case study, the values of data using various time domains and frequency domains are determined. This assists in attaining the impulse responses and frequency responses with normalized values as well as actual values.

With the emergence of digital computers, especially microprocessors, this work can perform spectrum analysis tasks in the digital domain. However, the computer can only receive discrete sequences with limited time, so it is necessary to truncate the variables in the time domain, transmit them to the digital domain of the computer, and then solve the coupling relationship between participating variables through DFT.

A periodic sequence signal $s(x)$ and its spectrum $s(k\alpha_1) = G_K(\alpha_1 = 2\pi/N, K = 1, 2, \ldots, N-1)$ are set, and $s(x)$ is expanded by Fourier series:

$$s(x) = \sum_{K=0}^{N-1} s(k\alpha_1)\mathrm{e}^N. \tag{1}$$

Its spectrum is represented by

$$s(k\alpha_1) = \frac{1}{N}\sum_{K=0}^{N-1} s(x)\mathrm{e}^N. \tag{2}$$

The spectrum density of discrete sequence signal is given in the following equation:

$$Ns(k\alpha_1) = \sum_{K=0}^{N-1} s(x)\mathrm{e}^N, \tag{3}$$

where $Ns(k\alpha_1)$ is the spectral density of the periodic sequence set number $s(x)$. According to the definition of Fourier transform of a continuous signal and the idea of Fourier transform of continuous signal, the spectral density of discrete nonperiodic sequence signal is defined as discrete Fourier transform, so the definition of discrete Fourier transform is described by

$$s(k) = \sum_{K=0}^{N-1} s(x)e^N. \tag{4}$$

From the above transformation results, it can be seen that the length of the periodic sequence signal $s(x)$ is N, and its DFT $s(k)$ is still a frequency domain of finite length sequence with the length of N. According to the definition of DFT, it is limited between 0 and 1.

Therefore, based on the periodic sequence signal $s(x)$, a coupling coordination computational intelligence model of carbon emission and economic growth should be constructed. The main causes of the model errors are spectrum leakage and fence effect caused by asynchronous sampling. In order to improve the measurement accuracy, it is necessary to restrain spectrum leakage or synchronize as much as possible to reduce its impact on coordination accuracy.

3. Coupling and Coordination Model of Urban Carbon Emission and Economic Growth

According to the characteristics of the coordinated development of economic growth and carbon emissions and the purpose of a comprehensive evaluation, the establishment of the comprehensive evaluation index model adheres to the following principles:

(1) The principle of policy relevance and comprehensiveness: Policy relevance requires that the indicator system should play a supporting and guiding role in the decision-making. It should comprehensively and objectively reflect all aspects of the coordinated development of economic growth and carbon emissions. The defined objectives should be related to the existing policy objectives, in line with the objective connotation of the coordinated development of economic growth and carbon emissions. Comprehensiveness means that the index system of coordinated development of economic growth and carbon emission should have enough coverage. Therefore, in the proposed research, we have selected the representative indicators that can reflect the theme, avoid the repeated selection amongst the indicators, and stick to the characteristics of linking the evaluation objectives and indicators.

(2) The principle of scientificity and comparability: The so-called scientificity means that the index system should be established on the basis of scientific feasibility, the data source should be accurate, and the comparability principle specifies that the processing method and the data analysis conform to the statistical standards and comparable. The specific indicators should be able to objectively and truly reflect the state of the system, and the interrelationship between subsystems and indicators can be comparable and evaluable. It should be able to evaluate the degree of coordinated development of economic growth and carbon emissions. There are no obvious scientific problems in the structure and selection of index systems [18]. The index content in our proposed work is simple and clear, strong in generality, and easy to understand and accept.

(3) Applicability and operability principle: In this, the selection of indicators should start from the regional characteristics of the selected research area, and the selection of indicators that can reflect the coordinated development of economic growth and carbon emissions should be given more attention. The concept of indicators should be clear; the calculation method should be simple; and the acquisition cost should be low.

Based on the three principles we can determine the model into three basic indexes or models as mentioned in the following.

3.1. Regional Economy and Carbon Emission Evaluation Index. Building evaluation index model is the key to carbon emission quality evaluation. It is necessary to have a deep understanding and objective analysis of the factors and models that make up carbon emission in the evaluation area, so as to select and establish them in a targeted way [19]. Different regions have different natural conditions, forming a wide variety of natural ecosystems, and different ecosystem states have different suitability for human survival. The selection of evaluation indicators should consider the regional carbon emission quality status, characteristics, the natural background of carbon emission, and the changes in the environment due to human activities, so as to make the evaluation of carbon emission quality more comprehensive [20].

Based on the research work on carbon releases, economy and atmosphere, and relevant research outcomes, 7 pointers are designated to ascertain the complete index of carbon release, and 10 pointers are nominated to ascertain the complete index of economic expansion level from the perspective of economic scale and economic growth potential.

From the two aspects of environmental pollution and environmental governance, 10 indicators are selected to calculate the comprehensive index of environmental level. The evaluation index system is shown in Table 1:

According to the data availability and relevant results, the region is selected as the decision-making unit, and three-stage DEA is utilized to determine the carbon release efficiency. Three-index indicators of capital, energy, and labor force are nominated as the input system; GDP and carbon dioxide emissions are selected as expected output and unexpected output systems, respectively. Taking a certain year as the base period, the capital stock of each city in the region is calculated according to the constant price in ten years. The unit of capital stock is 100 million yuan; the number of employees at the end of each year is taken as the labor force element, and the unit of energy consumption is taken as the energy factor, and the unit is 10,000 tons of standard coal [18]. The expected output GDP is converted into the base period constant price by using the deflator index and adjusted to the real GDP. The selection of external environmental variables mainly considers the factors that have a significant impact on carbon dioxide emission efficiency but are not within the scope of subjective control. The proportion of fiscal expenditure in GDP is selected to represent the government's influence; the proportion of tertiary industry represents the industrial structure for carbon release; and the intensity of utilization of energy is determined with the base period as the constant price.

3.2. Construction of the Economic Growth Model. The energy consumption structure of cities dominated by coal makes the energy consumption more thoughtful. The total energy utilization has also increased substantially in the recent decade, and the carbon emission per unit GDP is also on a rapid rise, which reflects the contradiction between economic growth and carbon release [20]. The regional current situation of carbon emission, economy, and environment development is the basis of model construction. To study a city's 3E system comprehensively, it should be started from three directions. First of all, carbon emission is the main indicator to evaluate the carbon release status of a nation or a province. Through the calculation of carbon emission, the carbon emission intensity of a region can be inferred, so as to reflect the carbon emission status of a region. Therefore, it is necessary to explore the research of the 3E system from the perspective of carbon emission, economic development, and energy preservation.

In the development of the economy, the optimization of energy consumption structure has not been taken into account, resulting in an energy consumption structure that does not consider environmental constraints such as reduction in carbon emissions. Carbon dioxide mainly comes from coal combustion, while the proportion of oil and natural gas is relatively low. According to the IPCC greenhouse gas release record strategies, the emission of 1 ton of standard coal is about 2.45 tons, and the proportion of carbon dioxide produced by coal, natural gas, and oil under the same heat is about 5:4:3. Table 2 shows the proportion of primary utilization of energy in one city, namely, Nanchang.

From Table 2, it can be noticed that the energy consumption structure of the city is relatively simple. From 2008 to 2019, the proportion of raw coal consumption has been maintained between 60% and 70%, while the consumption of natural gas, hydropower, and new clean energy is less than 3%, resulting in excessive dependence on coal for economic development producing carbon dioxide, sulfur dioxide, and other gases. In addition, the lack of promotion and practical application of new clean energy and the simplification of energy consumption structure are also the main reasons for the high carbon emissions. From 2008 to 2019, the total energy consumption has not changed much, showing a stable upward trend. From 2008 to 2017, the total energy consumption increased steadily and reached a maximum value in 2016. Then, there was a short-term decline and reached a minimum value in 2017. During this period, due to the global economic crisis in 2018–2019, the total energy consumption has dropped again; the investment in ecological security has also increased; and consequently, the investment in ICT has been increased. The achievements in energy preservation and carbon discharge reduction are indeed remarkable. In addition, according to the data, it can be inferred that the energy consumption structure is developing in a good direction, in which the proportion of raw coal in primary energy consumption has decreased from 79.2% in 2008 to 61.2% in 2018, and the amount of oil and natural gas in prime energy utilization has increased from 19.0% and 1.5% in 2008 to 31.0% and 3.6% in 2019, respectively. The data show that the energy consumption structure is more reasonable, and it is developing towards high efficiency and green clean energy. According to this development

Table 1: Assessment index scheme of the provincial economy and carbon release.

Primary index	Secondary indicator	Tertiary index
Carbon emission	The efficiency of carbon emissions	Technical efficiency
		Pure technical efficiency
		Scale efficiency
	Status of carbon emissions	Per capita carbon footprint
		Carbon emission density
		Carbon intensity
		Carbon productivity
The economic development	Economies of scale	Per capita gross regional product
		Per capita nonrefundable income of city residents
		Per capita fixed asset investment
	Economic growth potential	Proportion of nonagricultural industry
		Per capita trade sales of customer goods
		Proportion of tertiary industry
		Proportion of fiscal expenditure
		The GDP growth rate
		The density of population
		Average salary of employees on the job
The environmental protection	The environmental pollution	Energy utilization per 10,000 yuan GDP
		SO_2 emission intensity of 10,000 yuan GDP
		Industrial smoke emission
	Environmental governance	Water resources per capita
		The average temperature
		Forest coverage
		Comprehensive utilization rate of industrial solid waste
		Industrial dust removal capacity
		Green coverage in built-up areas
		The proportion of environmental protection investment in GDP

Table 2: Proportion of primary energy consumption in a city.

Years	Total energy consumption (tons of standard coal)	Proportion of primary energy consumption (%)		
		The raw coal	Oil	Natural gas
2008	12,454.0	79.2	19.0	1.5
2009	12,883.3	71.3	24.1	1.5
2010	14,228.0	71.4	24.3	1.2
2011	15,757.9	73.2	22.6	1.2
2012	16,925.7	73.1	22.7	1.3
2013	18,172.5	73.0	22.5	1.2
2014	19,856.4	67.9	27.3	1.3
2015	21,492.1	65.3	29.0	2.4
2016	22,313.9	61.3	31.6	3.8
2017	20,499.6	62.5	28.2	5.0
2018	20,585.7	62.1	28.2	5.4
2019	20,522.1	61.2	31.0	3.6

trend, the future energy consumption structure will be more reasonable; the carbon emissions will be controlled; and the environmental level will be improved.

Based on the above, the economic growth model is determined by taking the carbon emission factor as the periodic sequence signal $s(x)$, as shown in the following equation:

$$Q = \max s(x)_1 \left[\beta E^{-1} + (1-\beta) I\right] s(x)_2, \tag{5}$$

where $s(x)_1, s(x)_2$, respectively, represent the row and column vectors of the collected signals of the economic growth cycle; β represents the input coefficient of annual economic final products; and E^{-1} represents the matrix of direct consumption coefficient.

The carbon emission and the economic growth can be calculated for a certain region using the above two models, but this paper focuses on the effects of emission on growth specifically in the urban areas.

3.3. Construction of the Urban Carbon Emission Model. Combined with the specific situation, the difference in carbon emission efficiency after eliminating environmental factors is more obvious [17]. Hence, the cities are divided into two categories according to carbon emission efficiency. Starting from economic factors, scientific and technological factors, institutional factors, industrial structure, economic

scale, to scientific and technological investment as the influencing factors of energy conservation and emission reduction, the influencing factors of carbon emission are analyzed. The results are displayed in Table 3.

The analysis of carbon emission is carried out using Table 3 that implies various factors affecting carbon emission in specifically category 2 areas. The factors that are used to calculate carbon emission are industrial structure, scale of economy, science and technology, and the degree of openness of that area to the outside world. On the basis of these factors, coefficients and standard errors are also calculated. According to the research results in the table, the following can be inferred:

(1) Industrial organization has an undesirable impact on the two types of regions, and the influence on the carbon release efficiency of the first type of regions exceeds the significance level of 1%, which indicates that the industrial structure dominated by the second industry is not encouraging to the development of carbon release efficiency of each region. For every 1 percentage point increase in the industrial structure, the carbon emission efficiency of the first category of regions is reduced by 0.019 percentage points, and that of the second category is reduced by 0.007 percentage points, which indicates that proper adjustment of the proportion of the second industry is conducive to improving the carbon emission efficiency of each region. However, rendering to the applicable data, the quantity of the ancillary industry began to decline significantly in 2014, an overall decline of 73.3% compared with the previous year. On the surface, the adjustment of industrial structure has been effective, but the economic development has always relied on the secondary industry. Thus, it can be seen that the adjustment of industrial structure should be performed stepwise, not overnight.

(2) The impact of economic scale on the first category of areas is positive, and the impact on the second category of areas is negative, and the impact on the efficiency of carbon release of the second category of areas exceeds the significance level of 1%. For each percentage point increase in economic scale, the carbon emission efficiency of the first category of developed areas is increased by 0.007 percentage points, while that of the second category is decreased by 0.582 percentage points. The reason is that the first kind of regions with strong economic strength begin to pay attention to resource development and environmental problems after the economy reaches a certain level and gradually change the extensive economic development mode; while the second kind of underdeveloped regions focus on the pursuit of economic development, still they take the extensive economic development mode and ignore the resource and environmental problems. This is an inevitable stage in the process of development. Therefore, these regions should speed up economic development, and only after the economic development reaches a certain level can they change this mode.

(3) The impact of science and technology investment on the first and second categories of regions is positive, and the impact on carbon emission efficiency of the two categories of regions is more than 1% significant level, which shows that science and technology is an effective way to improve carbon emission efficiency. The scientific and rational input of final products has a greater impact on the first category of regions, which shows that the space for improving carbon emission efficiency in these regions is limited after the economic development reaches a certain level. Increasing product input, that is to say, accelerating economic growth is the most direct and effective way to improve carbon emission efficiency in the first category of regions.

(4) There is a negative impact on the two types of provinces, that is, the higher the degree of opening to the outside world, the lower the carbon release efficiency of each province.

Based on the above content, the urban carbon emission model is determined based on the carbon emission factor as the periodic sequence signal $s(x)$, as follows:

$$C = \max s(x)_{C1}\left[\beta E^{-1} + (1-\beta)I\right]s(x)_{C2}, \tag{6}$$

where $s(x)_{C1}$, $s(x)_{C2}$, respectively, represent the row and column vectors of the signal unit of the urban carbon emission cycle sequence.

The range standardization method is used to eliminate the order of magnitude and dimension of indicators, and AHP and differential coefficient of variation methods are comprehensively selected to prioritize the importance of the factors. The subjective and objective weights are taken as 0.5 to calculate the weight of each indicator, so as to complete the construction of economic growth and urban carbon emission model index model.

3.4. Construction of the Coupling Coordination Model. Let σ denote the coupling degree among economic expansion, carbon release, and energy utilization, and the value is between 0 and 1. When $C = 1$, it means that the three systems are in the best coupling state; when $C = 0$, it means that all elements in the system are independent, and the system develops disorderly. As an important indicator to reflect the coordinated development of the system coupling, coupling degree can be used to distinguish the coordinated degree of provincial energy utilization carbon releases and economic expansion coupling and the stage of coupling. At the same time, the coupling stage of economic growth and energy consumption carbon emission system is divided into five stages. See Table 4 for the specific division criteria.

Because the coupling degree only describes the interaction degree among economic growth, carbon release, and energy utilization and cannot reflect the level of coupling coordination, the carbon emission factor $s(x)$ under the

Table 3: Analysis of carbon emission factors.

Factors affecting	Category 1 area			Category 2 area		
	Coefficient	Standard error	Significant	Coefficient	Standard error	Significant
Constant term	1.2237	0.8687	***	0.8305	0.1663	***
The industrial structure	−0.0192	0.0157	ns	−0.0068	0.0033	ns
Economies of scale	0.0071	0.0054	***	−0.0582	0.0297	***
Science and technology	1.6870	0.2449	**	0.0700	0.3027	***
Degree of openness to the outside world	−0.0069	0.0010	ns	−0.0053	0.0027	ns

***Extremely significant. **Very significant. *Significant. ns: not significant.

DFT method is introduced. Because the constraint conditions of the economic growth model (5) and the city carbon emission model (6) are the same, if we pursue the maximum economic growth and the minimum carbon emission at the same time, therefore, the DFT method is used to build the coupling and coordination model of economic growth and carbon emissions represented in the following equation:

$$\lambda = \frac{Q}{C} = \frac{\max s(x)_1 \left[\beta E^{-1} + (1-\beta) I\right] s(x)_2}{\max s(x)_{C1} \left[\beta E^{-1} + (1-\beta) I\right] s(x)_{C2}}. \quad (7)$$

According to equation (7), the interaction and mutual restriction among carbon emission, economic growth, and ecological fortification can be determined, as shown in Figure 1.

First of all, economic development provides financial and technical support for carbon emissions, which is conducive to refining carbon releasing efficiency, improving carbon productivity, and encouraging energy preservation and emission reduction. On the other hand, carbon emissions react to the economy, which shows that if the GDP output per unit carbon emission is more (i.e., carbon emission efficiency), there would be lesser constraints on economic expansion, and these factors will be more conducive to the economic development. On the contrary, it means that economic development will consume more energy plus carbon emissions and restricts economic development. Economic development can reduce energy consumption, pollution, and pressure on the ecological environment by providing financial and technical support. However, economic development can also cause air, water, plants, and other pollution. The greater the degree of human intervention, the deeper the harm to nature will be. On the other hand, the ecological environment provides natural resources and material guarantees for economic development, which is the foundation of economic expansion. But, once the environment is polluted, the higher cost of environmental governance increases the economic burden. The higher the carbon emission is, the more fossil energy will be consumed. The carbon dioxide will produce a greenhouse effect, leading to a series of ecological environmental problems such as global warming, glacier melting, and water resource shortage. Therefore, controlling carbon emission becomes a necessary measure for environmental protection. On the other hand, the green plants in the natural environment convert the carbon dioxide absorbed into oxygen through photosynthesis, reducing the amount of carbon dioxide, and the natural seawater, soil, and other spheres can also absorb carbon emissions [19]. Therefore, the environment is the base of fiscal growth and carbon emission reduction; economic development is important support; and carbon emission is the key. Renewable energy solutions are necessary to protect the environment along with economic growth. It is of countless implications for promoting the sustainable development of the regional social economy to learn the coupling and harmonization relationship of carbon release, economic growth, and ecological protection.

4. Results and Discussion

In order to verify the effectiveness of the research on the coupling and coordination model of urban carbon emission and economic growth based on DFT, an experimental verification analysis is carried out.

4.1. Experiment Preparation. According to the prediction model, three cases of economic development Q, carbon emission C, and energy structure R gradient are designed, and the three parameters are combined in different cases, and a total of 27 combination results are obtained shown in the following equation:

$$S = (Q, C, R). \quad (8)$$

The specific combination is shown in Table 5.

In this study, through comparative analysis of each situation, we understand the possible carbon emission path in the future and seek a low-carbon economic development model that does not affect economic development and has low carbon emission.

4.2. Analysis of Experimental Results. Based on two cities (city "A" and city "B") in 2013 and 2018, the coupling and coordination effect of urban carbon emission and economic growth based on DFT is studied. The changing rate of carbon release intensity obtained by the two cities is shown in Table 6:

It can be seen from Table 6 that under different conditions, the two cities have given different rates of change of carbon emission intensity. According to the actual situation of the two cities, the change trend of the coupling coordination index of urban carbon emission and economic growth is obtained, as shown in Figures 2 and 3.

When the amount of economic change is positive, the coupling coordination index is smaller, and then the relationship between economic development and the environment is more harmonious. The larger the coupling coordination index is, the worse the relationship between them. According to the changing trend of coordination index, from 2014 to 2019, the coupling coordination index

Table 4: Coupling division standard between economic expansion and energy utilization carbon emission.

The value of C	Coupling phase	Detailed description
$\sigma = 0$	Uncoupled stage	There is no correlation between the systems.
$0 < \sigma \leq 0.3$	Low-level coupling	Lower economic growth and lower carbon emissions go hand in hand and are in the stage of no decoupling at a lower level.
$0.3 < \sigma \leq 0.5$	Rivalry phase	With the rapid development of the economy, carbon emissions are also growing at a relatively faster rate, and economic development and carbon emissions are in a stage of relatively decoupling from each other.
$0.5 < \sigma \leq 0.8$	Running-in and benign coupling stage	The rapid growth of carbon emissions leads to the strengthening of citizens' awareness of ecological safeguard and the slowdown of economic growth. The overall trend of higher economic growth and lower carbon emissions is parallel, and the two tend to be well coupled. At the same time, they are in the stage of developing from relative decoupling to absolute decoupling.
$0.8 < \sigma \leq 1$	High-level coupling	Economic development is absolutely decoupled from carbon emissions.

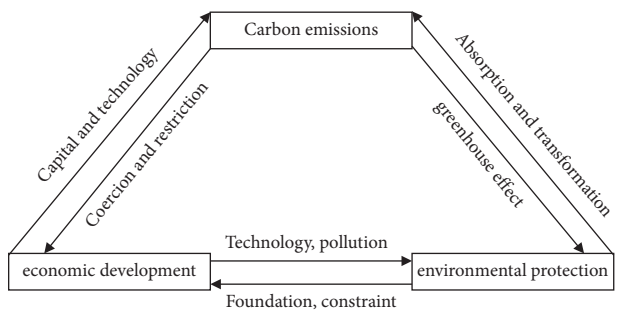

Figure 1: Interaction mechanism of carbon emission, economic development, and environmental protection.

Table 5: Combination results of three parameters in different situations.

Economic development	Carbon emission (CE)	Energy structure	Corresponding situation
Low output	Low CE efficiency	Low emission (LE)	Situation 1 (S1)
		Middle emissions (ME)	Situation 2 (S2)
		High emissions (HE)	Situation 2 (S2)
	Middle CE efficiency	LE	Situation 4 (S4)
		ME	Situation 5 (S5)
		HE	S6
	High carbon emission efficiency	LE	S7
		ME	S8
		HE	S9
Middle output	Low CE efficiency	LE	S10
		ME	S11
		HE	S12
	Middle carbon emission efficiency	LE	S13
		ME	S14
		HE	S15
	High carbon emission efficiency	LE	S16
		ME	S17
		HE	S18
High output	Low CE efficiency	LE	S19
		ME	S20
		HE	S21
	Middle carbon emission efficiency	LE	S22
		ME	S23
		HE	S24
	High carbon emission efficiency	LE	S25
		ME	S26
		HE	S27

Table 6: Change rate of carbon emission intensity.

Energy consumption emission		2013		2018	
		City A	City B	City A	City B
Low energy consumption	Low emission	−21.08	−18.34	−21.96	−20.11
	Middle emissions	−20.35	−17.62	−21.43	−19.86
	High emissions	−19.62	−16.90	−20.91	−19.11
Middle energy consumption	LE	−20.12	−19.44	−20.50	−19.42
	ME	−19.38	−18.34	−19.96	−18.62
	HE	−18.64	−17.66	−19.43	−18.22
High energy consumption	LE	−19.16	−18.32	−19.04	−17.94
	ME	−18.41	−17.69	−18.49	−17.23
	HE	−17.66	−16.70	−17.95	−16.89

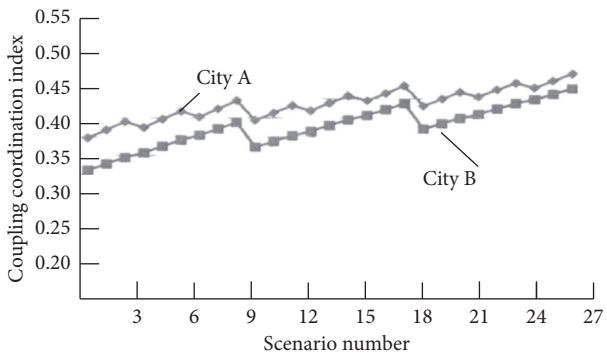

Figure 2: Change trend of coupling coordination index of two cities in 2013.

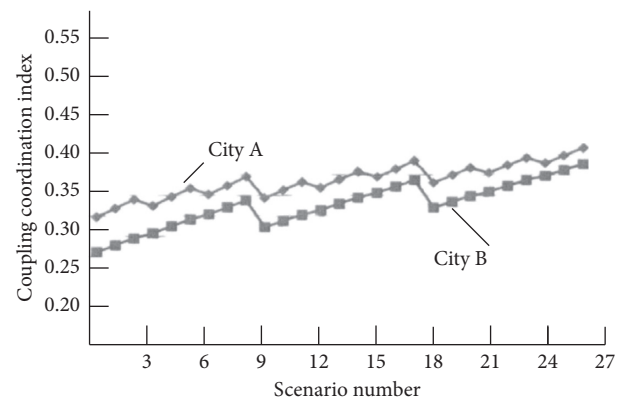

Figure 3: Change trend of coupling coordination index of two cities in 2018.

measured by city A is between 0.322 and 0.475. The lowest coupling coordination index belongs to case 1 in 2019, that is, low output, low energy consumption, and low emission. During 2014–2019, the coupling coordination index measured by city B is between 0.275 and 0.443. The lowest coupling coordination index belongs to case 1 in 2019. However, the experimental region is in the phase of quick expansion. Although the coupling and coordination index is low, it belongs to the situation of low output, and the economic output is relatively low, which is not the optimal development mode of the region. However, case 10, that is, low energy consumption and low emission of medium output, has a coupling coordination index of 0.373, which is not the lowest, but compared with other development models, this development model belongs to medium speed development with relatively fast development speed and relatively low energy consumption intensity with minimal carbon emission. This can be considered as the development path that can be selected for this region. Therefore, the coupling coordination index measured by city B is more suitable for this region.

The energy generation solutions and their impact on carbon emissions are directly proportional. Figure 4 presents the aggregate energy consumption of two cities and respective carbon emissions released from the energy solutions. It can be seen that the relationship is positively proportionate. As the consumption of energy increases, consequently, the carbon emissions are also increasing.

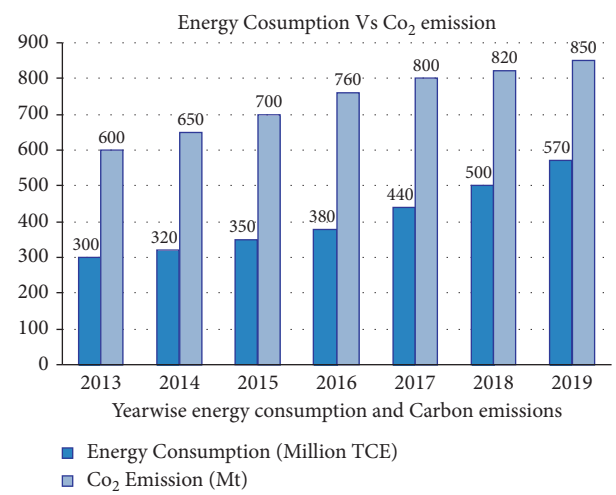

Figure 4: Year-wise energy consumption and carbon emissions for two cities in aggregated form.

5. Conclusions

Through index selection, this paper analyzes the influencing factors of urban carbon emission due to economic growth and industrialization. The coupling and coordination relationship between economic development and carbon emission is also established that provides theoretical guidance for the urban city to follow the low-carbon economic

development path. However, due to many uncertainties, changing policies, and a limited level of knowledge, there are still some constraints that have not been taken up in this research study, which may need further in-depth analysis. The work of this paper mainly focuses on the following aspects: (1) the influencing factors of carbon emissions are based on the selected parameters such as economic effect, population effect, energy effect, and technology effect, while the research on the influence of micro factors is not considered. (2) In order to improve the research of carbon emission reduction strategy, we have attempted to show the impact of influencing factors on energy generation and on reduction of carbon emission. (3) Carbon release reduction aim is essentially focusing on CO_2 release per unit of GDP, that is, carbon release intensity. However, there are very few domestic studies on the influencing factors of carbon emission intensity, but none of the study is considering all the possible factors that may influence energy generation solutions as well as CO_2 releases. Our proposed work provides index-based indicators that can help the urban area decide upon energy generation solutions by keeping the carbon emissions minimal.

Data Availability

Data are restricted to share, but the fields and output are available upon request to the corresponding author.

Conflicts of Interest

The authors declare that there are no conflicts of interest.

Acknowledgments

This research was partially supported by "Research on the Competitiveness of Green Development in Central China from the Perspective of Coordination."

References

[1] T. S. Adebayo, A. A. Awosusi, D. Kirikkaleli, G. D. Akinsola, and M. N. Mwamba, "Can CO_2 emissions and energy consumption determine the economic performance of South Korea? A time series analysis," *Environmental Science and Pollution Research*, vol. 28, no. 29, Article ID 38969, 2021.

[2] M. Alharthi, E. Dogan, and D. Taskin, "Analysis of CO_2 emissions and energy consumption by sources in MENA countries: evidence from quantile regressions," *Environmental Science and Pollution Research*, vol. 28, no. 29, Article ID 38901, 2021.

[3] Y. Li, X. Yang, Q. Ran, H. Wu, M. Irfan, and M. Ahmad, "Energy structure, digital economy, and carbon emissions: evidence from China," *Environmental Science and Pollution Research*, vol. 28, no. 45, Article ID 64606, 2021.

[4] R. Khoie, A. Bose, and J. Saltsman, "A study of carbon emissions and energy consumption of wind power generation in the Panhandle of Texas," *Clean Technologies and Environmental Policy*, vol. 23, no. 2, pp. 653–667, 2021.

[5] T. Güney and E. Üstündağ, "Wind energy and CO_2 emissions: AMG estimations for selected countries," *Environmental Science & Pollution Research*, 2021.

[6] X. Zhang, H. Zhang, and J. Yuan, "Economic growth, energy consumption, and carbon emission nexus: fresh evidence from developing countries," *Environmental Science and Pollution Research*, vol. 26, no. 25, Article ID 26367, 2019.

[7] M. Musah, Y. Kong, I. A. Mensah, S. K. Antwi, and M. Donkor, "The link between carbon emissions, renewable energy consumption, and economic growth: a heterogeneous panel evidence from West Africa," *Environmental Science and Pollution Research*, vol. 27, no. 23, Article ID 28867, 2020.

[8] M. K. Khan, M. I. Khan, and M. Rehan, "The relationship between energy consumption, economic growth and carbon dioxide emissions in Pakistan," *Financial Innovation*, vol. 6, no. 1, p. 1, 2020.

[9] A. Lajunen, "Evaluation of energy consumption and carbon dioxide emissions for electric vehicles in Nordic climate conditions," in *Proceedings of the 2018 Thirteenth International Conference on Ecological Vehicles and Renewable Energies (EVER)*, pp. 1–7, Monte Carlo, Monaco, April 2018.

[10] R. Rana and M. Sharma, "On the causality between electricity generation, energy consumption, investment patterns and CO_2 emissions in India," in *Proceedings of the 2018 2nd European Conference on Electrical Engineering and Computer Science (EECS)*, pp. 71–75, Bern, Switzerland, December 2018.

[11] C. Cappiello, S. Datre, M. Fugini et al., "Monitoring and assessing energy consumption and CO_2 emissions in cloud-based systems," in *Proceedings of the 2013 IEEE International Conference on Systems, Man, and Cybernetics*, pp. 127–132, Manchester, UK, October 2013.

[12] V. Kolev, I. Draganova-Zlateva, and D. Gospodinova, "Trends in energy efficiency and CO_2 emissions according to Bulgarian national energy efficiency plan," in *Proceedings of the 2019 11th Electrical Engineering Faculty Conference (BulEF)*, pp. 1–6, Varna, Bulgaria, September 2019.

[13] M. Katona and R. Radnai, "Primary energy consumption and CO_2 emission of internal combustion engine and electric vehicles," in *Proceedings of the 2017 6th International Youth Conference on Energy (IYCE)*, pp. 1–5, Budapest, Hungary, June 2017.

[14] M. Salari, R. J. Javid, and H. Noghanibehambari, "The nexus between CO_2 emissions, energy consumption, and economic growth in the U.S," *Economic Analysis and Policy*, vol. 69, pp. 182–194, 2021.

[15] L. Jiang, S. R. Sakhare, and M. Kaur, "Impact of industrial 4.0 on environment along with correlation between economic growth and carbon emissions," *International Journal of System Assurance Engineering*, 2021.

[16] M. Kaur and S. Kadam, "Discovery of resources over Cloud using MADM approaches," *International Journal for Engineering Modelling*, vol. 32, no. 2-4, pp. 83–92, 2019.

[17] D. Kirikkaleli, H. Güngör, and T. S. Adebayo, "Consumption-based Carbon Emissions, Renewable Energy Consumption, Financial Development and Economic Growth in Chile," *Business Strategy and Environment*, 2021.

[18] F. J. Hasanov, Z. Khan, M. Hussain, and M. Tufail, "Theoretical Framework for the Carbon Emissions Effects of Technological Progress and Renewable Energy Consumption," *Sustainable Development*, vol. 29, 2021.

[19] O. E Olubusoye, D Musa, and S Ercolano, "Carbon emissions and economic growth IN africa: are they related?" *Cogent Economics & Finance*, vol. 8, 2020.

[20] M. W. M. Roos, "Endogenous economic growth, climate change and societal values: a conceptual model," *Computational Economics*, vol. 52, no. 3, pp. 995–1028, 2018.

Hindawi
Mathematical Problems in Engineering
Volume 2022, Article ID 5321485, 14 pages
https://doi.org/10.1155/2022/5321485

Research Article

DCNN-GCM: A Deep CNN and Granger Causality Models for Forecasting Welfare Level of Energy-Producing Countries and Evaluating the Relationship between Energy Consumption and Sustainable Economic Welfare

Nasser Hoseinbor,[1] **Seyed Nematollah Mousavi**,[2] **and Abbas Aminifard**[3]

[1]*Department of Oil and Gaz Economics, Islamic Azad University, Marvdasht Branch, Shiraz, Iran*
[2]*Department of Agricultural Economics, Islamic Azad University, Marvdasht Branch, Shiraz, Iran*
[3]*Department of Economics, Islamic Azad University, Shiraz Branch, Shiraz, Iran*

Correspondence should be addressed to Seyed Nematollah Mousavi; snmousavi@miau.ac.ir

Received 24 October 2021; Revised 3 December 2021; Accepted 9 December 2021; Published 21 January 2022

Academic Editor: Saeid Jafarzadeh Ghoushchi

From the beginning of creation, human beings have realized the importance of energy for survival. They have always devoted a significant part of their energy to provide the required energy. Moreover, it can be said that energy resources have an essential role in the life and evolvement of societies. On the contrary, with the depletion of energy resources, severe environmental pollution caused by the consumption of petroleum products, and high cost of energy in the production cycle, allocating these resources must be carried out carefully. This paper aims to look at the connection between energy consumption and sustainable economic welfare in OPEC countries (Iran, Kuwait, Saudi Arabia, UAE, Ecuador, and Venezuela) during 2019–2009, utilizing the panel data method. Finally, we presented a CNN architecture for forecasting welfare levels in the case study countries. As a result, the relationship between energy consumption and economic growth among selected countries from energy-producing countries was compared in this analysis, which used the standard Granger causality test and the Granger causality test in several domains. The findings suggest that economic growth and inflation positively impact energy consumption in the countries studied. In addition, energy consumption positively impacts these countries' sustainable economic welfare, while inflation has a negative effect. In addition, the findings of the standard Granger causality test indicate a one-way causal association between energy consumption and economic development in Iran and Venezuela, as well as one-way causality from GDP to energy consumption in Ecuador, the United Arab Emirates, Saudi Arabia, and Kuwait. Also, based on the results of the CNN method, the RMSE are 1.75, 3.81, 1.39, 0.52, 0.69, and 1.72 for Ecuador, Emirates, Iran, Saudi Arabia, Kuwait, and Venezuela, respectively.

1. Introduction

Assessing sustainability and welfare is a contemporary issue of scientific and political importance. The Sustainable Development Goals of the United Nations aim to achieve a global transition to a world where all citizens experience high human well-being while not expanding the Earth's borders. More scientists argued as civilization developed that economic growth is the best way to accomplish the aims of sustainable development, with human welfare at its heart. Human well-being is a fundamental idea in human-nature interaction. The general population has largely agreed on the value of human well-being, influenced by social, environmental, and personal influences. Economic sustainability and energy use are essential considerations in achieving long-term social and economic development. Economic growth is often followed by energy consumption, which leads to socio-economic development and creates several environmental issues that offset the increase in human well-being. Using energy significantly improves

human well-being. Sustainable development has made energy, the environment, and the economy an essential issue for academia and global governments. Human well-being is a complicated, contentious, and ever-changing term. Economic, health, cultural, and social security are aspects of human well-being in the broadest sense. According to Wang et al. [1], human well-being serves as a connection between the natural world and human society. On the contrary, energy plays a critical role in human life and economic operations, serving as an indicator of well-being, economic and social progress, and a vital humanitarian need. As a result, per capita, energy consumption is an essential measure of a country's growth and economic progress. In the current time, energy is seen as a raw material for manufacturing and a strategic asset that shapes international affairs, the global economy, and politics. Energy supply conditions and challenges encountered during the procurement process significantly impact national and international competition. These factors also form country demand systems and are among the most important indices of essential economic variables. For all of these causes, electricity is one of the world's most pressing concerns today. Due to the importance of the subject, in the continuation of the work, we present the theoretical foundations and review the research background to introduce the model and related tests.

The expansion of a country's wealth allows it to continue to improve the well-being of its people. Some of the advantages of urban growth include improved nutrition, healthy lifestyle, increased life expectancy, increased adult literacy, lower child mortality rate, increased mobility, and increased recreation and leisure facilities. On the contrary, present economic growth should not result in higher environmental expenses since future development is dependent on it. While economic consumption by humans is called welfare, Max Neef [2] notes a threshold hypothesis in his research on economic growth and life quality. However, based on this person's desires and between increased consumption and increased wealth, a limit to economic development is reached. From this point on, certain luxury products' social and environmental costs tend to reverse human happiness. To put it in another way, environmental sustainability must be promoted to achieve stability. Since 1969, international organizations have released the Pearson Report, an overview of global growth that questions these development consequences and examines several causes, emphasizing that the long-term advantage of all economies, regardless of scale, is to make the most of human and material resources [3]. Around the same time, it expands the agriculture market and meets a broader range of people. Natural resources have the resources and environmental services that we depend on for our well-being, so green growth is the driving force behind sustainable growth and sustainability [4]. As a result, investment and creativity must be examined, as they would be the foundation for long-term development and the creation of new economic opportunities [5]. Some scholars, such as Miller [6], have concluded that human naivety and technological advancements make it easier to lessen the environmental harm generated by economic development. Seeking alternatives to finite resources and growing the Earth's capacity to sustain humanity are both reasonable options. As a result, achieving societal welfare is one of the most critical priorities of an economy [7]. However, there is disagreement about the various factors that affect these conditions. Indexes should be classified according to regional patterns. They should consider and enhance current data, covering all social, economic, environmental, and structural aspects [8] and [9]. Li et al. [10] have studied the effect of social and natural environmental elements on building energy. In another research, Qian et al. [11] have concluded a renewable energy accounting as an indicator of observation. Jafarzadeh-Ghoushchi et al. [12] have studied on seasonal storage solar energy system stage in Iran using a statistical model. According to Nodhaus and Tobin [13], the usual international standard of economic development lacks the essential elements of socio-economic security, natural resource utilization, and environmental quality. They developed a new method of calculating welfare that included per capita consumption (in which economic assets were increased and expenses were reclassified), recreation, and other nonmarket modes of activity, as well as deducting urbanization costs [14]. Most developed countries have made changes in health and education that have lasted almost two decades in advanced countries. However, GDP continues to be used to gauge welfare [15, 16]. The ISEW index was established by Costanza in 1990 and updated in 1993 to assess the long-term viability of people's perceived welfare standards. Economic, distributive, societal, and environmental variables are included. Guimaraes et al. [8], reflect on societal economics from the viewpoint of a capitalist economy that adheres to neoclassical theory and liberalism in practice. An alternative methodology to assessing economic development depending on real-world requirements proposes the development of the Index Sustainable Economic Welfare (ISEW), which includes variables such as income distribution, net capital growth, foreign and domestic capital, natural resource depletion, environmental damage, and the value of unpaid domestic work [14] and [17]. We have used the Granger causality model to compare the causality relationship between energy use and economic development in various realms in OPEC member countries, including Iran and Ecuador, the United Arab Emirates, Saudi Arabia, Kuwait, and Venezuela. In this study, with identifying the relationship between energy consumption and sustainable economic welfare in these nations, we will evaluate and compare the relationship between energy consumption and economic development in Iran and other countries. A CNN model was also presented for forecasting welfare levels in the research report countries.

2. Literature Review

In their report, Sánchez et al. [14] used data from Ecuador from 2001 to 2015 to quantify the ISEW. They also contrasted the ISEW to GDP as development indicators, emphasizing the distinction between stability and economic growth. The findings suggest that personal consumption is one of the most beneficial and essential components in

increasing long-term welfare. The destruction of natural resources negatively affects the welfare of Ecuador. The gap between sustainable welfare and GDP has been confirmed. In their study, Azami and Almasi [18] look at the connection between energy consumption and sustainable economic welfare in oil-producing countries. They look at the ISEW first and then connect energy consumption and sustainable economic welfare in these countries [19]. Personal consumption and energy reduction are considered components of sustainable welfare. The findings, calculated using Westerlund [20] test and taking cross-sectional dependency into account, show that energy use and Sustainable Economic Welfare have a long relation. The Granger causality test reveals a one-way relationship between sustainable economic welfare and energy use. This result has implications for energy and environmental policymakers. Wang et al. [21] used the PSR approach and factor weight ranking method to assess ecologically responsible development. Olubiyi [22] uses the Generalized System Torque (SYS-GMM) approach to analyze the link between energy consumption, carbon dioxide emissions, and welfare. The findings reveal a one-way causal relationship between coal use and per capita revenue. There was also evidence of one-way causality between death and coal use and carbon dioxide emissions. Furthermore, there is a two-way association between death and energy consumption. The findings of the SYS-GMM demonstrate that energy consumption has a wide range of consequences on welfare. Enhancement coal consumption lowers unemployment while raising energy consumption lowers infant mortality. The use of fossil fuels hastens death. Carbon dioxide emissions lower unemployment, but they boost child mortality rates. Infant mortality is often reduced as a result of increased energy intake. In their report, Roach and Meeus [23] look at the effect of energy policies on societal welfare. Energy strategies are mixed with the problem of product development management to meet their targets, resulting in a detailed model for development strategy from the perspective of a manufacturing organization. This method is applied in GAMS optimization applications using the BARON optimizer as a nonlinear mixed-integer (MINLP) solution. In addition, two alternative scenarios without the quota commitment strategy and its associated costs have been discussed to address the issue. The virtual price index is used to measure social security (VPI). The findings show that the subscriber welfare surplus increases in the long run, but it is lower than the short-term average. Furthermore, the introduction of the quota contribution scheme of tradable green certificates raised the penetration of clean energy sources (more than 60%) and the excess welfare (more than $ 107). In the second example, the cost of production falls as the number of cleaning services grows. Ahmadi et al. [24] have studied a new expert system model using programming in the industry [24].

In their research, Phoumin and Kimura [25] looked at the impact of energy shortages on household welfare in Cambodia. Household energy insecurity is described in this study as the current situation caused by inadequate energy intervention, which prevents the supply of specific household energy needs. Since energy insecurity differs from location to place, it can only be fully understood by local studies. Households with insufficient energy intake could be missing out on a plethora of other resources. The results show that energy poverty has a significant negative effect on household health, with an even greater impact on children's human capital development. There are many studies that have used artificial intelligence methods for predicting such as local wavelet and MLP methods for classification underwater targets [26] and wavelet convert for forecasting short-term PM10 condensation [27]. Blonz [28] identifies and determines the costs associated with an energy-efficient alternative to home appliances in his research. He points out that agents hired by the company are increasing their losses by misreporting to allow unauthorized refrigerators to be replaced deliberately. He also provides empirical estimates of the effects of these incentives on (1) the effectiveness of energy resilience and (2) welfare. Unqualified shifts are found to reduce welfare by an average of $ 106. Only half of the employees who follow the instructions save, increasing welfare by $ 60 per replacement. Sharifi et al. [29] have studied the influence of artificial intelligence and digital style on industry and energy during the pandemic. Ahmadi [30] has used computational modeling using GEP and logarithmic fuzzy preference programming to prioritize the economic growth factors. Also, in another research, Ghorbani et al. [31] have analyzed a statistical investment plan for call and put option pricing. Boughanmi et al. [32], in their research, evaluate the overall economic effects of rising energy prices in Oman through income distribution indices reflected in Gini coefficients and other inequality indices. The results show that the effects of a 50% reduction in energy subsidies will lead to a 0.62% increase in GDP, an increase in government savings of $ 2.9 billion, and a 3% decrease in household welfare. The main reason is the increase in the private consumer price index. However, the effect on the Gini coefficient is negligible. In the short run, income inequality is less sensitive to subsidy reform. In another study, Ghorbani et al. [33] have calculated an option pricing using investment plan with the haphazard interest price. In their study, Peng et al. [34] found that, while China's energy intensity has steadily decreased in recent years, the overall consumption of energy products has risen exponentially. One of the keys to managing energy demand is indirect energy taxes. In order to simulate indirect taxation in Jiangsu Province, one of China's most critical economic provinces with limited energy supplies, they established a computable general equilibrium model. The findings suggest that indirect taxes reduce energy consumption while direct energy taxes reduce economic and social welfare. When tax thresholds are 5%, 10%, and 15%, the GDP loss is 0.27 percent, 0.66 percent, and 1.13 percent. Qiao et al. [35] have used a wavelet transform for forecasting the disparity among natural gas producers and consumers in the United States on a monthly basis. Qiao et al. [36] have analyzed forecasting of US electricity production regarding a hybrid new model using artificial intelligence. Peng et al. [37] have investigated the impact of a blocked rectifier on metering efficiency in shale fossil fuel extraction. Peng et al. [38] have studied monthly oil and gas load forecasting using a wavelet cutoff

noise removal method and a mix of long-short-term memory. In the study of Agaa et al. [39], PV output power was predicted using CNN-LSTM and ConvLSTM models. The results demonstrate that the proposed strategies outperform a standard LSTM model in terms of accuracy. Sharifi et al. [40] have studied a novel model based on gene expression programming for predicting NOx emissions in engine diesel. Ahmadi et al. [41] have studied and designed a novel hybrid method for predicting GDP factors using artificial intelligence and statistical methods. The results show that the models forecast the factors with high accuracy. In the study of Khan et al. [42], a novel multistep forecasting model was suggested for power consumption. The proposed approach attains better predictive performance than existing methods, thereby confirming its effectiveness. Ahmadi and Taghizadeh [43] presented a GEP model for economy growth indicators using ARDL and PCA testing methods. The findings show that the models are applied for the assessment of the GDP and knowledge-based economy. Ghorbani and Korzeniowski [44] have analyzed an adaptive risk hedging for under Cox–Ingersoll–Ross bond yields. Also, in another research, Korzeniowski and Ghorbani [45] have analyzed a model investment for Hull–White bond yields. Taghizadech and Ahmadi [46] have studied a statistical analysis using Tukey and ARDL bound methods for assessment of knowledge-based economy factors on GDP in Iran. The findings suggest that statistical methods can evaluate the significance of the factors. Farsi et al. [47] used a novel method dubbed parallel LSTM-CNN on short-term load prediction. The findings suggest that deep CNN models, particularly PLCNet, are strong candidates for short-term prediction.

3. Methods and Materials

3.1. Theories of Sustainable Economic Welfare. Sustainable economic welfare has been related to an individual's degree of satisfaction by some authors, including Marshall [48], Hicks [49], and Pigou [50]. Economic welfare, in their opinion, refers to how satisfied people are in their purchases of goods and services. However, it is not all about material goods because "economic welfare and social welfare are intrinsically linked." This view is supported by recent studies such as Deaton [51] which claim that welfare is measured in ways other than income. It is interesting to note that "well-being" does not imply "consumption" or "economic prosperity," but rather "quality of life" [52]. Furthermore, influences affecting well-being include wages, income distribution, working environments, people's leisure time, production, and the environment [53–56]. Sen [57], for example, introduces a new definition of well-being that stresses the distinction between "being in a healthy situation" and "getting well-being." The desire to keep away from alien artifacts and luxury was among the first. In this case, welfare is linked to inner wishes that can be fulfilled with effort. He also agrees that social and economic conditions affect various classes of people and influence their choice of opportunities. The number of people living below the poverty line is a standard metric for measuring a country's welfare. However, it lacks the differing degrees of poverty among the poor. For this purpose, Sen [57] considers the well-being of individuals to measure the poverty index [14].

3.2. Dataset and Problem Formulation. The method of integrating time-series and cross-sectional data was used to examine the connection between GDP and energy usage, the general level of costs, etc., for the period 2009–2019. Also, the effect of the logarithm of GDP variables and the general level of prices in the countries is studied, and the logarithm of energy use and also the effect of the logarithm of energy consumption variables and the general level of prices on the logarithm of GDP using effect models, common, fixed effects, and random effects are analyzed. The data panel approach is used to analyze the association between economic welfare and energy consumption:

$$\mathrm{LOG}(E_{\mathrm{it}}) = \beta_{.} + \beta_1 \mathrm{LOG}(\mathrm{GDP}_t) + \beta_2 \mathrm{LOG}(P_t) + \beta_3 \mathrm{LOG}(\mathrm{GDP}_{t-1}) + \beta_4 \mathrm{LOG}(E_{t-1}) + \varepsilon_{\mathrm{it}}, \tag{1}$$

$$\mathrm{LOG}(\mathrm{GDP}_{\mathrm{it}}) = \beta_{.} + \beta_1 \mathrm{LOG}(P_{\mathrm{it}}) + \beta_2 \mathrm{LOG}(\mathrm{GDP}_{\mathrm{it}-1}) + \beta_3 \mathrm{LOG}(E_{\mathrm{it}}) + \varepsilon_{\mathrm{it}}. \tag{2}$$

In this regard, GDP represents economic welfare, which uses GDP as a measure of welfare. P also indicates the general level of prices, and ε is also a disturbance.

3.3. Convolutional Neural Network (CNN). CNN is a type of feedforward neural network that excels at computer vision and natural language understanding. It may be used to forecast time series with great success. CNN's local perception and local receptive may substantially limit the number of parameters, boosting model learning efficiency [58] and [59]. The convolution layer and the pooling layer are the two primary components of CNN [60]. Each convolution layer has several convolution kernels, and the method for calculating them is shown in equation (3). The features of the data are retrieved after the convolution operation of the convolution layer. However, the extracted feature sizes are pretty significant. Therefore, a pooling layer is applied after the convolution layer to lower the feature dimension and reduce the cost of training the network:

$$L_t = \mathrm{Tan}h(x_t k_t + b_t), \tag{3}$$

where L_t is the output of the convolution operator, x_t is the input time series, k_t is the weight values, and b_t is the bias value of the convolutional operator.

4. Results

4.1. Stationarity Analysis Test. In general, we know a random process, and related to it, a time-series stationary. If the variance and its mean are constant over time and the covariance between the two time periods t and $k+t$ depends only on the distance (delay or gap k) between the two time periods and not the actual period, t covariance. If one or more of the three stability conditions are not met, we call the random process, or time series, unstable. Based on the test results, most time-series variables are not stationary; instead, they are considered stationary with a definite trend with one-time differentiation. In such cases, the use of unstable time series causes R2, W-D, and t to lose their standard properties and thus cause problems for the econometric. The use of this data makes the results of regression unreliable and false. Due to this fact, before using the data, it is necessary to perform the necessary tests for the stability of this data by performing the necessary tests. Therefore, we used the generalized Dickey–Fuller test to evaluate the stability of variables, which are presented in the tables. According to Table 1, the hypothesis of a unit root test in the time series for all Ecuadorian variables at the level cannot be rejected. For all variables, it is rejected with a one-time differentiation. In other words, the levels of variables used in the model are unstable, which are stationary once differentiated.

Observing the results of Table 1, it can be concluded that the variables for Ecuador, UAE, Iran, Saudi Arabia, Kuwait, and Venezuela are at a nonstationary level, which is stationary with a one-time differentiation.

4.2. Model Regression Estimation. The results of estimating the above equations are presented in Tables 2 and 3. The fixed-effect model for the studied model was selected as the superior model compared to the expected effects and random effects. The width of different sources can better explain the differences between different countries in this model. The experimental findings of the stable impacts' method show that the logarithm of GDP of this period and the previous period has a beneficial impact on the logarithm of energy usage of the study countries. Therefore, the production capacities of countries are one of the factors affecting the consumption process of primary inputs in general and energy carriers in particular (as secondary inputs). Therefore, changes in production capacity in different sectors of the economy affect the levels of energy demand. Therefore, increasing production in each sector of the economy has overall direct and indirect effects on the energy carrier market. On the contrary, increasing the GDP of countries means increasing the production capacities of these countries. Therefore, increasing GDP in the study group has a positive effect on their energy consumption. Also, the logarithm of energy consumption variables in the previous period and the general level of prices positively affect the logarithm of energy consumption in all countries, with rising prices and the fact that, in the economy of OPEC countries, the energy supply is in the hands of the government, and the government pays energy subsidies for various reasons. It causes the price of energy to increase relatively less than the price of other institutions in the face of inflation, leading to a further increase in energy consumption. Based on F and LM tests' results, the fixed-effect model is selected as the superior method compared to other models. The results of the fixed-effect model indicate that the general level of prices has a negative effect on the GDP of the study countries. In other words, inflation in this group of countries has a negative impact on GDP. This result can be due to the decrease in demand for factors of

Table 1: Augmented Dickey–Fuller test.

Country	Stability	GDPP	OIL	ELEC	GAS	EC
Ecuador	In level	−1.291	−1.920	−0.603	−2.298	−2.188
	With difference	−3.428	−17.185	−2.158	−6.009	−4.521
Emirates	In level	−1.358	−2.159	−0.457	−2.349	−2.256
	With difference	−1.521	−3.310	−4.718	−4.412	−4.008
Iran	In level	−1.59	−2.124	−3.984	−4.385	−4.624
	With difference	−2.458	−2.124	−3.984	−4.385	−4.624
Saudi Arabia	In level	−0.048	−0.978	−2.551	−1.682	−2.151
	With difference	−3.175	−3.345	−6.782	−5.158	−4.785
Kuwait	In level	−0.548	−1.678	−2.781	−1.682	−2.151
	With difference	−2.145	−3.345	−6.542	−4.452	−4.103
Venezuela	In level	−1.675	−3.015	−2.195	−2.255	−1.726
	With difference	−2.572	−4.478	−3.951	−7.112	−4.123

Table 2: Results of estimating the panel data pattern: energy consumption variable.

Variables	Random effects	Fixed effects	Fixed effects
LGDP	0.05 (0.58)	0.05 (1.578)	−0.02 (−1.25)
LGDP (−1)	0.19 (3.72)	0.09 (2.63)	0.05 (0.59)
LP	0.51 (8.98)	0.08 (2.82)	0.01 (1.87)
LE (−1)	—	0.89 (23.4)	0.98 (55.92)
Determination coefficient	0.99	0.92	0.90
Durbin–Watson test	1.71	1.90	2.25

Table 3: Results of estimating the panel data pattern: GDP variable.

Variables	Random effects	Fixed effects	Fixed effects
LGDP (−1)	0.86 (148)	0.75 (12.8)	0.89 (158.8)
LE	−0.18 (−3.98)	0.15 (2.61	−0.07 (−0.91)
LP	−0.004 (0.218	−0.49 (−5.2	−0.05 (−0.89
Determination coefficient	0.99	0.92	0.90
Durbin–Watson test	1.71	1.90	2.25

production due to the increase in the price level of inputs, which ultimately leads to a decrease in GDP.

4.3. Granger Causality between Energy Consumption and Welfare. According to the stability of the variables, once the differentiation of the VAR model has estimated the difference for each of the selected countries, we performed the standard Granger causality test. The results of the Granger causality test are demonstrated in Table 4. In the Granger linear causality test performed in this section, the two zero hypotheses to be tested are as follows: Granger causality welfare is not energy consumption in selected countries and Granger energy consumption is not economic welfare.

Table 4 illustrates a one-way causal association between economic welfare and energy use in Ecuador, the United Arab Emirates, Saudi Arabia, and Venezuela. There is indeed a one-way relationship between energy use and economic welfare in Kuwait. There is a one-way causal link between energy use and welfare in Iran and Venezuela. Table 5 provides an overview of the findings:

Table 4: Granger causality results.

Country	GDP$\nRightarrow$EC	EC$\nRightarrow$GDP
Ecuador	3.378	5.215
Emirates	5.128	18.584
Iran	9.858	3.785
Saudi Arabia	0.758	16.850
Kuwait	0.685	8.714
Venezuela	14.485	0.448

Table 5: Summary of Granger causality results.

Country	Situation
Ecuador	There is a one-way causality from GDPP to EC
Emirates	There is a one-way causality from GDPP to EC
Iran	There is a one-way causality from EC to GDPP
Saudi Arabia	There is a one-way causality from GDPP to EC
Kuwait	There is a one-way causality from GDPP to EC
Venezuela	There is a one-way causality from EC to GDPP

4.4. Granger Causality between Selective Indexes and Economic Growth. Granger causality test between crude oil consumption, natural gas consumption, and electricity consumption with economic welfare was performed using Stata software. Its results are given in Table 6.

The Granger causality test shows one-way causality between crude oil use and economic welfare in Ecuador, the United Arab Emirates, Iran, and Kuwait, as seen in Table 6. There is a one-way causality from electricity consumption to economic welfare in Kuwait and Venezuela and a one-way trigger from economic welfare to electricity consumption in Saudi Arabia. In Ecuador, Iran, and Kuwait, the findings show a one-way causality of economic welfare in natural gas use. There is no causal link between crude oil consumption and economic welfare in Saudi Arabia, between electricity consumption and economic welfare in Ecuador, the UAE, and Iran, and between natural gas consumption and economic welfare in the UAE, Saudi Arabia, and Venezuela. As can be seen from the data, there is no causal relationship between crude oil consumption and economic welfare amongst these selected importing countries. In contrast, there is a one-way causal connection between crude oil consumption and economic welfare among the selected exporting countries, except for Saudi Arabia (see Table 7).

4.5. Granger Causality Test in Many Ranges between Energy Consumption and Welfare. According to Figure 1(a), it can be concluded that there is a causality relationship, in the long run, medium, and short term, from welfare to energy consumption in Iran.

Figure 1(b) shows no causality relationship for Iran in terms of energy consumption to welfare in any of the desired periods. Granger causality was also examined for other countries. However, only results are presented due to limitations. There is indeed a one-way causality connection between energy use and long- and medium-term welfare in Ecuador. In the long run, there is a one-way causality relationship between energy use and economic welfare in the UAE. However, in the medium and short term, there is none. In all three long-term, medium-term, and short-term cycles for Iran, there is a one-way causality association between economic welfare and energy use. There is a one-way causality relationship between energy use and economic welfare in Saudi Arabia and Kuwait in the medium term. There is a one-way causality link between economic welfare and long- and short-term energy use in Venezuela.

4.6. Granger Causality Test in Many Ranges between Selected Indexes and Economic Welfare. Figure 2(a) shows that, in the range 0 to 0.08, there is a Granger causality from the consumption of crude oil to the welfare of Iran. Because this interval includes the interval 0.01 to 0.05, this interval represents the long-term causality. Therefore, there is a long-term one-way causality of crude oil consumption for the welfare of Iran.

According to Figure 2(b), there is no causality relationship, in the long run, medium, or short term, from welfare to crude oil consumption for Iran. Figure 3 shows the lack of long-term, medium-term, and short-term causality of natural gas consumption to the welfare of Iran.

Figure 4(a) clearly shows the lack of long-term, short-term, and medium-term causality from the welfare of natural gas consumption for Iran. According to Figure 4(b), in the period of 0 to 0.4, there is a causality relationship between the consumption of electricity to welfare for Iran. Moreover, since this period includes the long-term range, so it can be said that there is a long-term causality from the consumption of electricity to the welfare of Iran. According to Figures 5(a) and 5(b), it can be concluded that there is no causal relationship in terms of welfare to electricity consumption in Iran in any period. Granger causality was also examined for other countries. However, due to limitations, only results are provided. In Ecuador, there is no causal connection between welfare and electricity consumption

Table 6: Granger causality test results for selected countries.

Country	OIL ⇏ GDPP	GDPP ⇏ OIL	ELEC ⇏ GDPP	GDPP ⇏ ELEC	GAS ⇏ GDPP	GDPP ⇏ GAS
Ecuador	4.658	0.680	0.329	3.453	2.125	7.265
Emirates	15.155	2.950	3.921	2.582	2.522	0.982
Iran	35.289	0.151	1.253	0.109	8.898	0.352
Saudi Arabia	0.085	0.108	0.932	15.251	0.695	0.238
Kuwait	6.868	0.0008	6.388	0.445	1.825	7.459
Venezuela	18.815	0.387	22.712	0.578	0.779	3.712

Table 7: Summary of Granger causality test results.

Country	Crude oil consumption	Electricity consumption	Natural gas consumption
	One-way causality from OIL to GDPP	There is no causality	One-way causality from GDPP to GAS
Emirates	One-way causality from OIL to GDPP	There is no causality	There is no causality
Iran	One-way causality from OIL to GDPP	There is no causality	One-way causality from GDPP to GAS
Saudi Arabia	There is no causality	One-way causality from GDPP to ELEC	There is no causality
Kuwait	One-way causality from OIL to GDPP	One-way causality from ELEC to GDPP	One-way causality from GDPP to GAS
Venezuela	One-way causality from OIL to GDPP	One-way causality from ELEC to GDPP	There is no causality

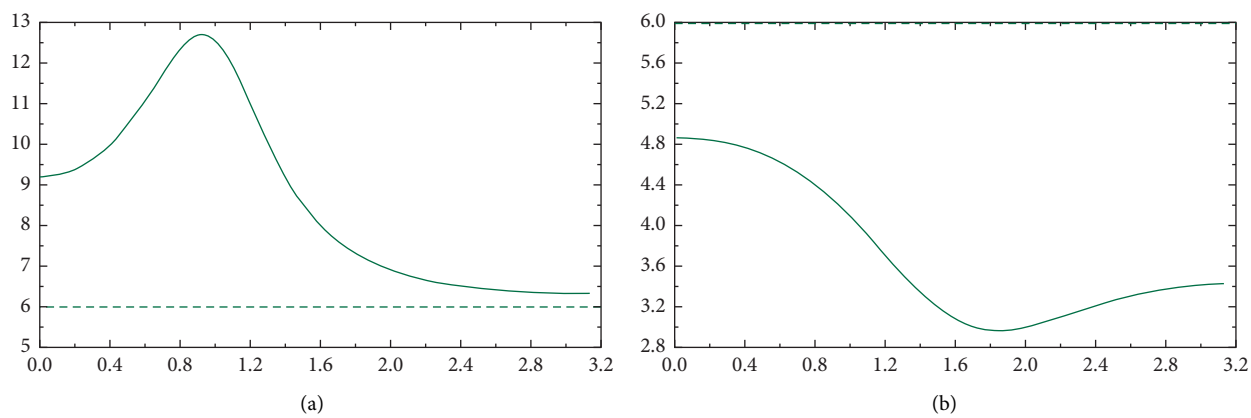

Figure 1: (a) Granger causality in the frequency domain from welfare to energy consumption in Iran. (b) Granger causality in a frequency domain from energy consumption to welfare.

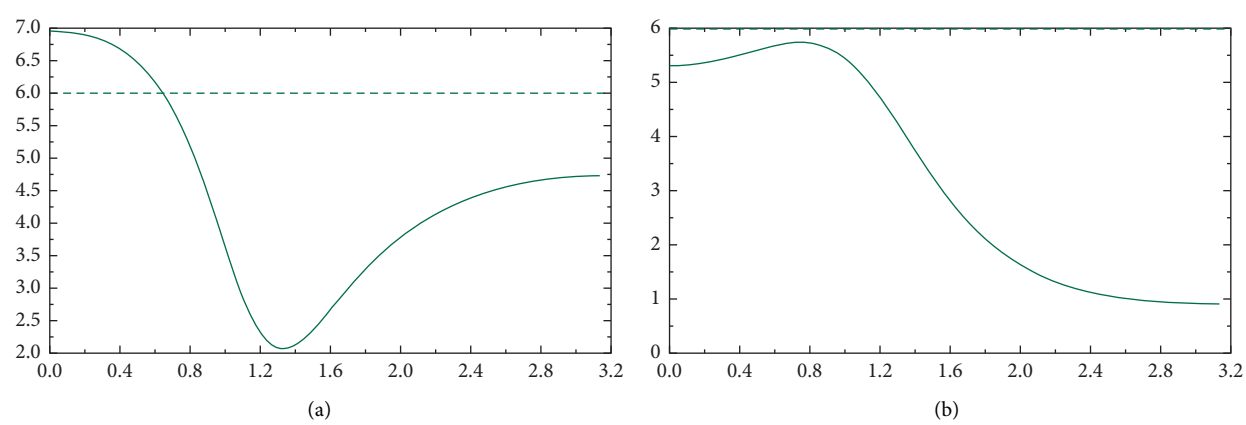

Figure 2: (a) Granger causality in a frequency domain from crude oil consumption to welfare for Iran. (b) Granger causality in a frequency domain of welfare to crude oil consumption for the variable of crude oil consumption in Iran.

and crude oil consumption in all three periods: long term, medium term, and short term, and between welfare and natural gas consumption, there is a one-way causality from welfare to natural gas consumption in the long and medium term. For the UAE, a causality relationship between welfare and electricity consumption and natural gas consumption in

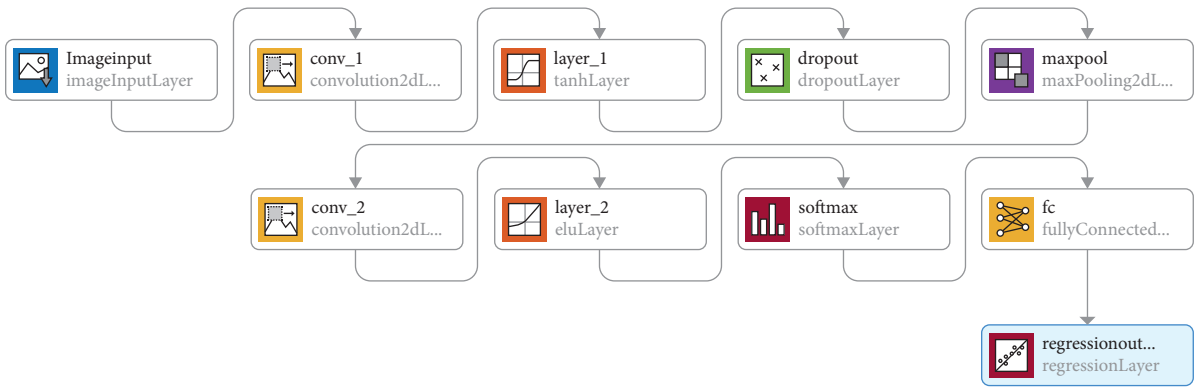

Figure 3: The architecture of the presented CNN method for forecasting time series.

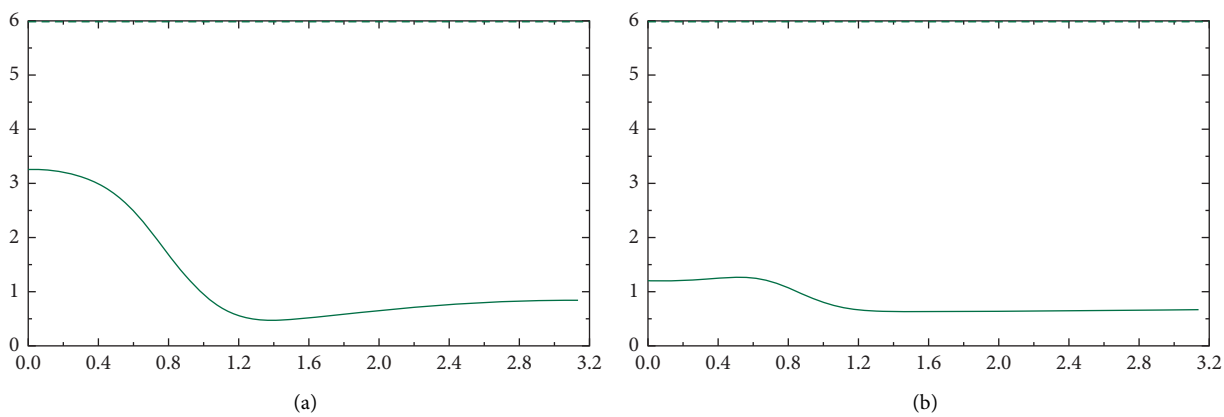

Figure 4: (a) Granger causality in a frequency domain from the consumption of natural gas to welfare for the natural gas variable in Iran. (b) Granger causality in the frequency domain of welfare to natural gas consumption for the natural gas variable in Iran.

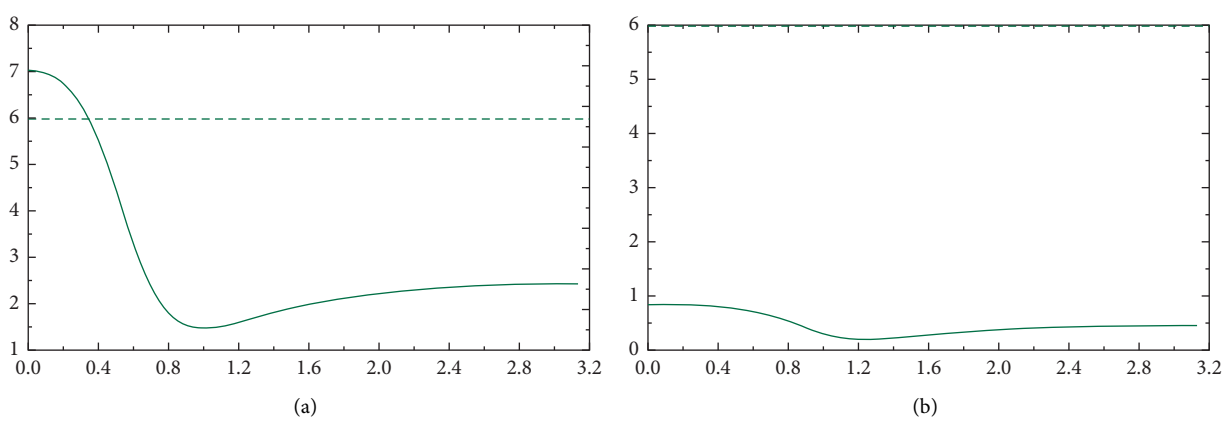

Figure 5: (a) Granger causality in a frequency domain from the consumption of electricity to welfare for the variable of electricity in Iran. (b) Granger causality in a frequency domain from welfare to electricity consumption in Iran.

all three periods, long-term, medium-term, and short-term, and between welfare and crude oil consumption does not exist; there is a one-way causality from crude oil consumption to welfare only in the long run.

In Iran, there is a long-term one-way causal relationship between welfare and energy use. There is a one-way causality relationship between crude oil consumption and welfare in the long term. There is no causal relationship between natural gas consumption and welfare in any of the three time periods. In the long term, there is a one-way causality link between welfare and natural gas consumption in Saudi Arabia, with natural gas consumption leading to welfare. There is a one-way causal link between welfare and crude oil usage in the long term, with crude oil consumption leading to welfare. In each of the desired cycles, there is no causal link between GDP and electricity usage. There is a one-way

causality relationship between GDP and natural gas consumption in Kuwait, with natural gas consumption leading to growth in the long run and prosperity leading to natural gas consumption in the medium and short term. There is no causal association between prosperity and energy use or crude oil use in all of the eras. There is a one-way causality relationship between healthcare and energy use in Venezuela at any point in time. There is a one-way causality relationship between welfare and natural gas consumption in the long term, with welfare leading to natural gas consumption. There is a one-way causality relationship from gas output to welfare to crude oil demand in the long and short terms. In the medium term, there is a two-way causality relationship.

4.7. Forecasting Welfare Using Convolutional Neural Network. In this paper, the CNN method is used to forecast the welfare in the countries based on time-series analysis (see Figure 3). The leading network consists of 10 layers of CNN operators. It includes two convolution operators of analysis (see Table 8).

The architecture and the properties of the layers are presented in Table 8 and Figure 3. The forecasting is evaluated with five lag and two activation functions. The results of forecasting using the CNN method are illustrated in Figure 6. Based on the training process of Figure 6, the stopping criteria of the model is RMSE that stops the iteration in 250 iterations. Based on the results of the CNN method, the RMSE are 1.75, 3.81, 1.39, 0.52, 0.69, and 1.72 for Ecuador, Emirates, Iran, Saudi Arabia, Kuwait, and Venezuela, respectively. The results of forecasting graphs are depicted with red color in Figure 6. Moreover, the RMSE value is represented in Figure 7.

5. Discussion and Limitation

The data imply that, in a few petroleum exporting countries, there is a one-way causation relationship between oil use and economic development. Finally, the results of the two fundamental Granger causality and Granger causality experiments are identical in certain fields. As a result, it is suggested as follows:

(i) Given that energy is one of the main factors in the country's future development and determining and implementing appropriate solutions in all areas related to energy will facilitate sustainable development in the country, despite all the historical events and realities, Iran should try not to consider oil and gas as tools in the political and social spheres. Furthermore, the energy sector as an independent sector to justify the existence of this relationship is expressed in such a way that the share of natural gas consumption in domestic consumption has been very high. Therefore, gas consumption in other parts will not have much impact on welfare.

(ii) Considering oil and gas to achieve other goals in the political sphere only leads to the fact that the conflicts of interest of the spheres will diminish the role of energy resources in itself and as an economic factor. In addition, the principle of using cost-benefit analysis should be embedded in all energy sector decisions. Unfortunately, in many cases, the actual costs of projects and their different dimensions are not taken into account. In the final analysis, we conclude that the cost of projects and policies has been much higher than its benefits. Also, reducing energy pollution is central, which should be considered in the future of energy. Finally, it is necessary to have a responsible approach to the exploitation of energy facilities, along with identifying resources, developing a strategy to motivate the emergence of alternative and renewable energy, meeting the capital needs of the energy sector, and dealing fairly with consumers and vulnerable businesses; the efficiency of energy production and consumption management must be planned. In this context, the replacement of fossil fuels is an inevitable prospect. Iran also needs a strategic policy in the energy sector that needs to be formulated and presented by an independent commission of experts, stakeholders, and the High Energy Council. The most crucial point that should be the focus of this policy is a responsible approach to energy use in the country. In short, in the future, the most important oil and gas producers in the world will be Saudi Arabia, Russia, Iraq, and Iran. Moreover, at the same time, due to the ups and downs in the price of energy carriers, the investment approach in this sector is increasing. However, due to the principle of the scarcity of financial resources and political approaches, the use of new investment requires the development of immediate plans for attracting foreign capital. Otherwise, other countries such as Saudi Arabia, Qatar, UAE, Russia, and Kuwait quietly drag the capital market into their borders and use them.

(iii) Medium to high growth of gas consumption in Iran according to the study of gas development indicators in different sectors shows, in recent years, the speed of development of gas subnetworks has been beyond the speed of development of national pipelines, gas refineries, and the upstream part of the gas producer. It shows an unfavorable trend in gas development. The following points are essential about gas production and consumption.

(iv) The country's gas production is growing with the implementation of various projects. Nevertheless, domestic consumption is growing rapidly. Most domestic gas production reaches domestic consumption (domestic, industrial, electricity generation, and injection into oil wells).

(v) Domestic gas consumption fluctuates seasonally, and the possibility of supplying gas to non-household sectors depends directly on the level of household consumption. In the cold winter months, the gas of power plants is cut off, and these units use alternative fuels.

Table 8: The layer properties of the presented CNN method for forecasting time series.

1	Input matrix	$5 \times 1 \times 1$ vector with "zerocenter" normalization
2	Convolution	3 1×1 convolutions with stride [1 1] and padding [0 0 0 0]
3	Tanh	Hyperbolic tangent
4	Dropout	50% dropout
5	Max pooling	1×1 max pooling with stride [1 1] and padding [0 0 0 0]
6	Convolution	3 1×1 convolutions with stride [1 1] and padding [0 0 0 0]
7	ELU	ELU with Alpha 1
8	Softmax	
9	Fully connected	One fully connected layer
10	Regression output	Mean squared error

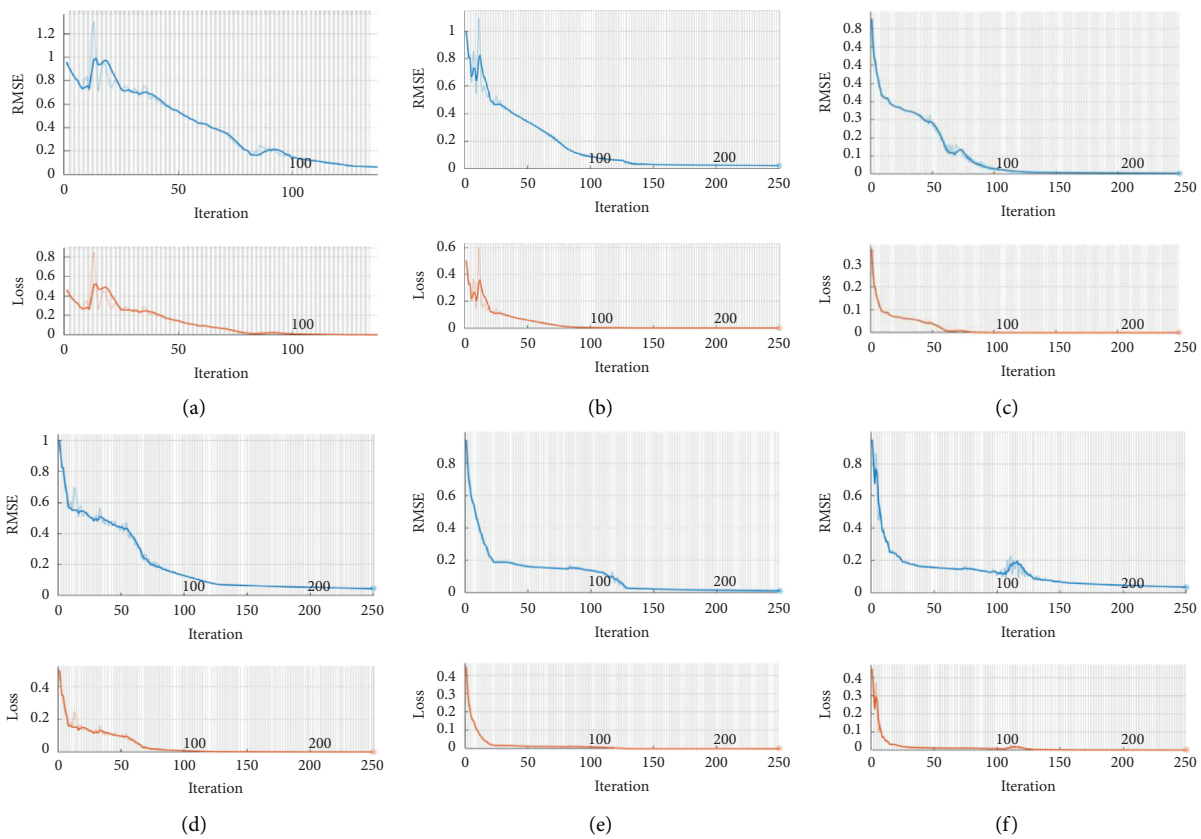

Figure 6: Training process of the CNN method. (a) Ecuador. (b) Emirates. (c) Iran. (d) Saudi Arabia. (e) Kuwait. (f) Venezuela.

(vi) Regarding the third selected indicator, it can be said that electricity is a component of energy carriers that, in many sectors, its use is irreplaceable. Many electrical devices do not allow switching with other energy carriers. Economic growth will increase household welfare, service, commercial units, industry development, and power consumption. Also, according to the results, it can be said that electricity consumption in most selected countries has not yet gained its position as an energy carrier.

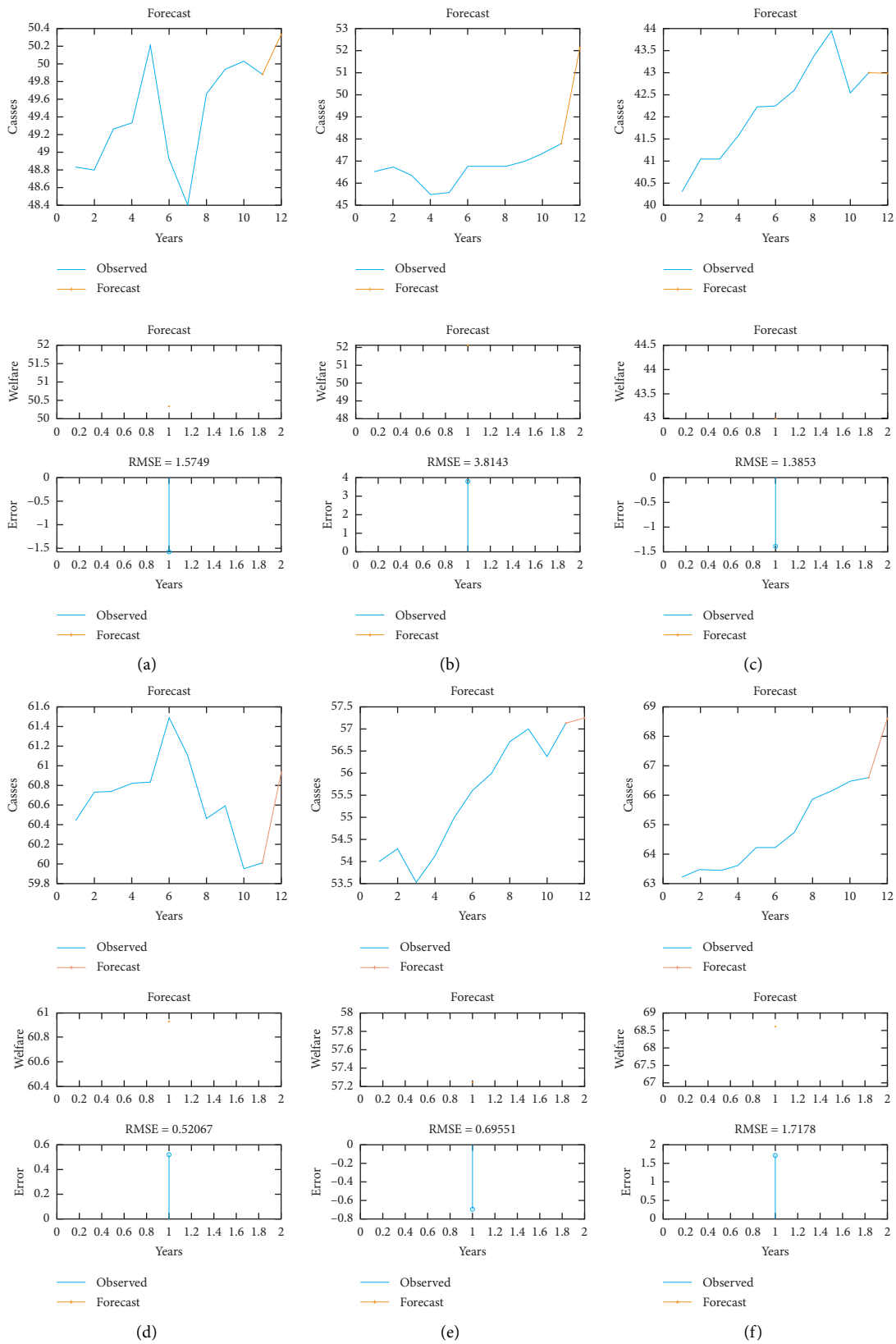

Figure 7: The results of forecasting using the presented CNN method. (a) Ecuador. (b) Emirates. (c) Iran. (d) Saudi Arabia. (e) Kuwait. (f) Venezuela.

6. Conclusion

In energy economics, the relationship between energy demand and economic development is crucial. Energy consumption can have different effects. The production and extraction of energy cause the destruction and pollution of the environment. It is an essential factor that doubles the need to study the relationship between energy production and consumption. These are the environmental issues that the countries of the world are facing. On the contrary, energy is presented as a production input that any restriction on its consumption limits production. Furthermore, since the main topic of economic growth is the growth of GDP, economic growth is accompanied by energy consumption. As a result, analyzing the relationship between economic development and energy demand is particularly important because it can better understand energy sector policies. As a result, we used the classical Granger causality model to analyze the causal association between energy use and economic development in this analysis. We have used the Granger causality model to compare the causality relationship between energy use and economic development in various realms in OPEC member countries, including Iran and Ecuador, the United Arab Emirates, Saudi Arabia, Kuwait, and Venezuela. We will analyze and compare the relationship between energy consumption and economic development in Iran and selected countries by determining the relationship between energy consumption and sustainable economic welfare in these countries. Based on the results, it can be hypothesized that there is a one-way causality relationship between energy use and economic development in Iran. Furthermore, in countries that use petroleum products, there is no two-way causality relationship between oil use and economic development. Finally, we presented a CNN architecture for forecasting welfare levels in the case study countries. The time-series plots represent the results.

Data Availability

The data used to support the findings of the study can be obtained from the corresponding author (snmousavi@miau.ac.ir).

Conflicts of Interest

The authors declare that they have no conflicts of interest.

References

[1] F. Wang, K. M. M. Jenny, and E. K. O. Lee, "The effects of qigong on anxiety, depression, and psychological well-being: a systematic review and meta-analysis," *Evidence-Based Complementary and Alternative Medicine*, vol. 2013, Article ID 152738, 16 pages, 2013.

[2] M. Max-Neef, "Economic growth and quality of life: a threshold hypothesis," *Ecological Economics*, vol. 15, no. 2, pp. 115–118, 1995.

[3] O. H. Pearson, L. Otto, L. Llerena, A. Molina, and T. Butler, "Prolactin-dependent rat mammary cancer: a model for man?" *Transactions of the Association of American Physicians*, vol. 82, pp. 225–238, 1969.

[4] M. J. Alier, "Decrecimiento sostenible: parís, abril del 2008," *Ecología Política: Cuadernos de Debate Internacional*, vol. 35, pp. 51–58, 2008.

[5] OECD, *Handbook on Constructing Composite Indicators: Methodology and User Guide*, OECD, Paris, France, 2008.

[6] G. T. A. MillerCiencia, "Desarrollo sostenible. Un enfoque integral Ministerio del Ambiente," *Estrategia Nacional de Cambio Climático del Ecuador 2012 –2015; 2012*, Cengage Learning Editores, Boston, MA, USA, 8th edition, 2007.

[7] B. B. Cuadrado, I. M. S. García, and M. G. S. Isabel, "Conditional factors of political budget cycles: economic development, media pressure, and political fragmentation," *Public Performance and Management Review*, vol. 41, no. 4, pp. 835–858, 2018.

[8] T. A. Guimaraes, E. B. A. Jairo, D. S. M. Magali, J. E. A. Borges, M. D. S. Machado, and M. R. M. Vargas, "Forecasting core competencies in an R&D environment," *R & D ManagementManagement*, vol. 31, no. 3, pp. 249–255, 2001.

[9] A. Ala, F. E. Alsaadi, M. Ahmadi, and S. Mirjalili, "Optimization of an appointment scheduling problem for healthcare systems based on the quality of fairness service using whale optimization algorithm and NSGA-II," *Scientific Reports*, vol. 11, no. 1, Article ID 19816, 2021.

[10] L. Li, W. Sun, W. Hu, and Y. Sun, "Impact of natural and social environmental factors on building energy consumption: based on bibliometrics," *Journal of Building Engineering*, vol. 37, Article ID 102136, 2021.

[11] A. Qian, X. Zhu, and F. Wang, "Economic loss dynamics of rare earth industry along the yellow river: taking renewable energy accounting as an observation indicator," *Journal of Coastal Research*, vol. 103, no. SI, pp. 101–106, 2020.

[12] S. G. Jafarzadeh, A. Sharifi, M. Ahmadi, and M. Maghami, "Statistical study of seasonal storage solar system usage in Iran," *Journal of Solar Energy Research*, vol. 2, no. 3, pp. 39–44, 2017.

[13] N. William and J. Tobin, *Is Growth Obsolete? Economic Growth*, National Bureau of Economic Research, MA, USA, 1972.

[14] S Mishell, W. O. Santiago, E. Toledo, and O. Jenny, "The relevance of index of sustainable economic wellbeing. Case study of Ecuador," *Environmental and Sustainability Indicators*, vol. 6, Article ID 100037, 2020.

[15] R. Costanza, G. Alperovitz, and H. Daly, "What would a sustainable and desirable economy-in-society-in-nature look like?, Creating a sustainable and desirable future," in *Creating a Sustainable and Desirable: Insights from 45 Global Thought Leaders*, pp. 33–49, World Scientific, Singapore, 2014.

[16] T. P. V. D. Matos, K. D. Mello, and R. A. Valente, "Protected areas and forest fragmentation: sustainability index for prioritizing fragments for landscape restoration," *Geology, Ecology, and Landscapes*, vol. 5, no. 1, pp. 19–31, 2021.

[17] J. Artin, V. Amin, M. Ahmadi, S. A. P. Kumar, and A. Sharifi, "Presentation of a novel method for prediction of traffic with climate condition based on ensemble learning of neural architecture search (NAS) and linear regression," *Complexity*, vol. 2021, Article ID 8500572, 13 pages, 2021.

[18] S. Azami and S. Almasi, "Energy consumption and sustainable economic welfare: new evidence of organization of petroleum exporting countries," *International Journal of Energy Economics and Policy*, vol. 10, no. 5, pp. 31–40, 2020.

[19] A. Varmaghani, M. A. Nazar, M. Ahmadi, A. Sharifi, S. J. Ghoushchi, and Y. Pourasad, "DMTC: optimize energy consumption in dynamic wireless sensor network based on fog computing and fuzzy multiple attribute decision-making," *Wireless Communications and Mobile Computing*, vol. 2021, Article ID 9953416, 14 pages, 2021.

[20] J Westerlund, "Testing for error correction in panel data," *Oxford Bulletin of Economics & Statistics*, vol. 69, no. 6, pp. 709–748, 2007.

[21] F. Wang, Y. Lu, and J. Ni, "Evaluating environmentally sustainable development based on the PSR framework and variable weigh analytic hierarchy process," *International Journal of Environmental Research and Public Health*, vol. 18, no. 6, 2021.

[22] E. A. Olubiyi, "Energy consumption, carbon emission, and well-being in africa," *The Review of Black Political Economy*, vol. 47, no. 3, pp. 1–24, 2020.

[23] M. Roach and L. Meeus, *The Welfare and Price Effects of Sector Coupling with Power-To-Gas*, European University Institute Robert Schuman Centre for Advanced Studies Florence School of Regulation, Fiesole FI, Italy, 2020.

[24] M. Ahmadi, "A review of using object-orientation properties of C++ for designing expert system in strategic planning," *Computer Science Review*, vol. 37, Article ID 100282, 2020b.

[25] H. Phoumin and F. Kimura, *The Impacts of Energy Insecurity on Household Welfare in Cambodia: Empirical Evidence and Policy Implications*Asian Development Bank Institute, Tokyo, Japan, 2019.

[26] W. Qiao, M. Khishe, and S. Ravakhah, "Underwater targets classification using local wavelet acoustic pattern and Multi-Layer Perceptron neural network optimized by modified Whale Optimization Algorithm," *Ocean Engineering*, vol. 219, Article ID 108415, 2021.

[27] W. Qiao, Y. Wang, J. Zhang, W. Tian, Y. Tian, and Q. Yang, "An innovative coupled model in view of wavelet transform for predicting short-term PM10 concentration," *Journal of Environmental Management*, vol. 289, Article ID 112438, 2021.

[28] J. A. Blonz, "The welfare costs of misaligned incentives: energy inefficiency and the principal-agent problem (2019-09-20)," 2019, https://ssrn.com/abstract=3473057.

[29] A. Sharifi, M. Ahmadi, and A. Ala, "The impact of artificial intelligence and digital style on industry and energy post-COVID-19 pandemic," *Environmental Science and Pollution Research*, vol. 28, no. 34, Article ID 46964, 2021.

[30] M.. Ahmadi, "A computational approach to uncovering economic growth factors," *Computational Economics*, vol. 58, pp. 1–26, 2020a.

[31] N. Ghorbani and A. Korzeniowski, "Call and put option pricing with discrete linear investment strategy," 2021, https://arxiv.org/abs/2110.04676.

[32] H. Boughanmi and A. K. Muhammad, "Welfare and distributional effects of the energy subsidy reform in the gulf cooperation council countries: the case of sultanate of Oman," *International Journal of Energy Economics and Policy*, vol. 9, no. 1, pp. 228–323, 2019.

[33] N. Ghorbani, "Option pricing with investment strategy under stochastic interest rates," The University of Texas at Arlington, TX, USA, Ph.D. dissertion, 2021.

[34] T. Peng, Z. Xiang, and H. Yanmin, "Economic and welfare influences of an energy excise tax in Jiangsu province of China: a computable general equilibrium approach," *Journal of Cleaner Production*, vol. 211, pp. 1403–1411, 2019.

[35] W. Qiao, W. Liu, and E. Liu, "A combination model based on wavelet transform for predicting the difference between monthly natural gas production and consumption of U.S." *Energy*, vol. 235, Article ID 121216, 2021.

[36] W. Qiao, Z. Li, W. Liu, and E. Liu, "Fastest-growing source prediction of US electricity production based on a novel hybrid model using wavelet transform," *International Journal of Energy Research*, 2021.

[37] S. Peng, Y. Zhang, W. Zhao, and E. Liu, "Analysis of the influence of rectifier blockage on the metering performance during shale gas extraction," *Energy and Fuels*, vol. 35, no. 3, pp. 2134–2143, 2021.

[38] S. Peng, R. Chen, B. Yu, M. Xiang, X. Lin, and E. Liu, "Daily natural gas load forecasting based on the combination of long short term memory, local mean decomposition, and wavelet threshold denoising algorithm," *Journal of Natural Gas Science and Engineering*, vol. 95, Article ID 104175, 2021.

[39] A. Agga, M. Labbadi, and Y. Houm, "Short-term self consumption PV plant power production forecasts based on hybrid CNN-LSTM, ConvLSTM models," *Renewable Energy*, vol. 177, pp. 101–112, 2021.

[40] A. Sharifi, M. Ahmadi, H. Badfar, and M. Hosseini, "Modeling and sensitivity analysis of NOx emissions and mechanical efficiency for diesel engine," *Environmental Science and Pollution Research*, vol. 26, no. 24, Article ID 25190, 2019.

[41] M. Ahmadi, S. G. Jafarzadeh, R. Taghizadeh, and A. Sharifi, "Presentation of a new hybrid approach for forecasting economic growth using artificial intelligence approaches," *Neural Computing & Applications*, vol. 31, no. 12, pp. 8661–8680, 2019.

[42] N. Khan, I. U. Haq, S. U. Khan, S. Rho, and M. Y. Lee, "DB-Net: a novel dilated CNN based multi-step forecasting model for power consumption in integrated local energy systems," *International Journal of Electrical Power & Energy Systems*, vol. 133, Article ID 107023, 2021.

[43] M. Ahmadi and R. Taghizadeh, "A gene expression programming model for economy growth using knowledge-based economy indicators: a comparison of GEP model and ARDL bounds testing approach," *Journal of Modelling in Management*, vol. 14, no. 1, 2019.

[44] N. Ghorbani and A. Korzeniowski, "Adaptive risk hedging for call options under cox-ingersoll-ross interest rates," *Journal of Mathematical Finance*, vol. 10, no. 4, pp. 697–704, 2020.

[45] A. Korzeniowski and N. Ghorbani, "Put options with linear investment for hull-white interest rates," *Journal of Mathematical Finance*, vol. 11, no. 1, pp. 152–162, 2021.

[46] R. Taghizadech and M. Ahmadi, "Statistical and econometrical analysis of knowledge-based economy indicators affecting economic growth in Iran: the new evidence of principal component analysis—Tukey and ARDL bound test," *Preprint: January*, vol. 10, 2019.

[47] B. Farsi, M. Amayri, N. Bouguila, and U. Eicker, "On short-term load forecasting using machine learning techniques and a novel parallel deep LSTM-CNN approach," *IEEE Access*, vol. 9, Article ID 31191, 2021.

[48] A. Marshall, "Consumer's surplus," *The Annals of the American Academy of Political and Social Science*, vol. 3, pp. 90–93, 1893, http://www.jstor.org/stable/1009153.

[49] J. R. Hicks, "The foundations of welfare economics," *The Economic Journal*, vol. 49, no. 196, pp. 696–712, 1939.

[50] A. C. Pigou, *Wealth and welfare*, Macmillan and Company, New York, NY, USA, 1912.

[51] A. Deaton, "Income, health, and well-being around the world: evidence from the gallup world poll," *The Journal of Economic Perspectives*, vol. 22, no. 2, pp. 53–72, 2008.

[52] T. Scitovsky, *The Joyless Economy: The Psychology of Human Satisfaction*, pp. 80–84, Oxford University Press, Oxford, UK, 1976.

[53] E. Liu, D. Li, W. Li et al., "Erosion simulation and improvement scheme of separator blowdown system–a case study of Changning national shale gas demonstration area," *Journal of Natural Gas Science and Engineering*, vol. 88, Article ID 103856, 2021.

[54] S. Peng, Q. Chen, and E. Liu, "The role of computational fluid dynamics tools on investigation of pathogen transmission: Prevention and control," *Science of The Total Environment*, vol. 746, Article ID 142090, 2020.

[55] M. Q. H. Abadi, D. Rahmati, A. Sharifi, and M. Ahmadi, "HSSAGA: designation and scheduling of nurses for taking care of COVID-19 patients using novel method of hybrid salp swarm algorithm and genetic algorithm," *Applied Soft Computing*, vol. 108, Article ID 107449, 2021.

[56] M. H. Nasirpour, A. Sharifi, M. Ahmadi, and S. J. Ghoushchi, "Revealing the relationship between solar activity and COVID-19 and forecasting of possible future viruses using multi-step autoregression (MSAR)," *Environmental Science and Pollution Research*, vol. 28, pp. 1–11, 2021.

[57] A. Sen, "On the development of basic income indicators to supplement the gnp measure," *United Nations Economic Bulletin for Asia and the Far East*, vol. 24, 1973.

[58] F. Farahanipad, M. Rezaei, A. Dillhoff, F. Kamangar, and V. Athitsos, "A pipeline for hand 2-D keypoint localization using unpaired image to image translation," in *Proceedings of the 14th PErvasive Technologies Related to Assistive Environments Conference*, pp. 226–233, Corfu, Greece, June 2021.

[59] M. Rezaei and N. Naderi, "Persian signature verification using fully convolutional networks," 2019, https://arxiv.org/abs/1909.09720.

[60] M. Ahmadi, T. Ali, D. Javaheri, A. Masoumian, S. J. Ghoushchi, and Y. Pourasad, "Dqre-scnet: a novel hybrid approach for selecting users in federated learning with deep-q-reinforcement learning based on spectral clustering," *Journal of King Saud University-Computer and Information Sciences*, 2021.